HIGH QUALITY INTEGRATED SILICON NITRIDE NANOPHOTONIC STRUCTURES FOR VISIBLE LIGHT APPLICATIONS

A Dissertation
Presented to
The Academic Faculty

by

Ehsan Shah Hosseini

In Partial Fulfillment
of the Requirements for the Degree
Doctor of Philosophy in
Electrical Engineering

School of Electrical and Computer Engineering
Georgia Institute of Technology
August 2011

HIGH QUALITY INTEGRATED SILICON NITRIDE NANOPHOTONIC STRUCTURES FOR VISIBLE LIGHT APPLICATIONS

Approved by:

Professor Ali Adibi, Advisor
School of Electrical and Computer Engineering
Georgia Institute of Technology

Professor Albert Bruno Frazier
School of Electrical and Computer Engineering
Georgia Institute of Technology

Professor Stephen Ralph
School of Electrical and Computer Engineering
Georgia Institute of Technology

Professor Phillip First
School of Physics
Georgia Institute of Technology

Professor John A. Buck
School of Electrical and Computer Engineering
Georgia Institute of Technology

Date Approved: Feb. 2011

To my Mother.

ACKNOWLEDGEMENTS

I wish to thank Prof. Ali Adibi for his guidance, support, and encouragement. He is a kind friend, and an incredibly supportive advisor

If it was not for the help and support of my great friends Billie Brown, and Mehrsa Raeiszadeh I might have not had survived the seemingly never ending graduate school.

I appreciate the great opportunity I had to be supervised by Dr. Siva Yegnanarayanan, with whom I started this research and hope to continue working one day. Also, I learned a great deal about photonics, physics, fabrication and most of all life in general from Dr. Mohammad Soltani and Dr. Babak Momeni. A large part of this thesis is indebted to collaborations with my dear friend Amir Hossein Atabaki. He has shown a great deal of patience sharing an office with me for the past five years.

The microfluidic, plasmonic and thermal parts of this thesis was done in collaboration with Mehrsa, Meysam and Payam. Also Dr. Devin Brown, with his professionalism, attention to details and support in fabrication helped this research greatly.

I would like to thank Omid, Arash, Reza, Saman, Majid, Saeed, Pejman, Payam, Qing, Farshid, Hossein, and Murtaza for their friendship and for their help and support. I am also grateful for the privilege to work with a wonderful group of colleagues at Professor Adibi's group. I would like to acknowledge my other friends, in particular, Ahmad, Pouya, Foad, Maryam, Amir, Mohammad, Navid, and Danie for making it an enjoyable experience to live in Atlanta.

The staff of the NRC at GaTech deserve the highest gratitude, specially Gary Spinner, Vinny Nguyen, and Eric Woods.

Finally, I especially would like to thank my family, specially my Mother.

TABLE OF CONTENTS

LIST OF TABLES

LIST OF FIGURES

LIST OF SYMBOLS OR ABBREVIATIONS

1D	One Dimensional.
2D	Two Dimensional.
3D	Three Dimensional.
AWG	Arrayed Waveguide Grating.
BOE	Buffered Oxide Etchant.
BOX	Burried Oxide.
CAD	Computer Aided Design.
CCW	Counterclockwise.
CMT	Coupled Mode Theory.
CW	Clockwise.
D	Displacement Vector.
DAQ	Data Acquisition.
E	Electric Field.
EBL	Electron Beam Lithography.
EM	Electromagnetic.
EOF	Electro-Osmotic Flow.
FC	Free-Carrier.
FCA	Free-Carrier Absorption.
FDTD	Finite-Difference Time-Domain.
FEM	Finite-Elements Methods.
FSR	Free-Spectral-Range.
HSQ	Hydrogen Silsequioxane.
HTO	High Temperature Oxide.
ICP	Inductively-Coupled Plasma.
LPCVD	Low-Pressure Chemical Vapor Deposition.

MiRC Microelectronic Research Center.

MOCVD Metal-Organic Chemical Vapour Deposition.

NIR Near Infra-Red.

NRC Nanotechnology Research Center.

PDF Pressure Driven Flow.

PDMS Polydimethylsiloxane.

PECVD Plasma-Enhanced Chemical Vapor Deposition.

PHASAR Phased Array.

PhC Photonic Crystal.

PMMA Polymethyl Methacrylate.

PUA Aliphatic Polyester-based Urethane Diacrylate Polymer.

PWE Plane Wave Expansion.

Q Quality Factor.

RIE Reactive ion etching.

TE Transverse Electric.

TIRS Temperature-Induced Resonance Shift.

TOC Thermo-Optic Coefficient.

TWR Traveling-Wave Resonator.

V Mode Volume.

SUMMARY

Optical microcavities confine light at resonant frequencies for extended periods of time and fundamentally alter the interaction of light with matter. The wavelength-scale optical confinement and low optical loss of nanophotonic devices dramatically enhance the interaction between light and matter within these structures, making them the basis of numerous applied and fundamental studies, such as cavity QED, nonlinear photonics and sensing. Optical microcavities can be characterized by two key quantities: an effective mode volume V_{eff}, which describes the per photon electric field strength within the cavity, and a quality factor Q, which describes the photon lifetime within the cavity. The quality factor Q is defined as $Q \equiv \omega_o/\delta\omega = \omega_o\tau/2$, in which ω_o is the resonant angular frequency, $\delta\omega$ is the resonance linewidth, and τ is the photon lifetime. Cavities with a small V_{eff} and a high Q offer an ideal building block for sensing applications, as any minute change in the vicinity of the cavity can be reflected in the resonance frequency shift or the quality factor change. Chip-based devices are particularly appealing, as planar fabrication technology can be used to make optical structures on a semiconductor chip that confine light to wavelength-scale dimensions, thereby creating strong enough electric fields that even a single photon can have an appreciable interaction with matter.

Two most investigated configurations for optical microresonators are photonic crystal and whispering gallery mode (WGM) resonators. High Q photonic crystal resonators, despite their smaller mode volumes compared to WGMs, suffer from the lack of an efficient in-plane coupling scheme. This, added to the relatively more complicated design and fabrication processes compared to WGMs, has lead us to devote most of this thesis proposal to cylindrical resonators, especially microdisks.

Realization of whispering gallery mode resonators in silicon-based material systems has great benefits, such as ease of fabrication, integrability with mature silicon (Si) electronics, and low cost. These novel structures have already been demonstrated on silicon oxide (SiO_2) [1], silicon [2], and silicon nitride (Si_3N_4) materials [3]. While SiO_2 micro-toroid and micro-sphere resonators have shown the highest Qs [1], their size and lack of chip-scale integrability (because of the bulky fiber taper coupling scheme) result in complications in using them for integrated photonics applications. On the other hand, Si microdisks on oxide substrates have recently been shown to be capable of achieving high quality factors ($Q > 10^6$) while being coupled to planar optical waveguides [4].

Integrated nanophotonics in the visible range of the spectrum could serve as a new platform for sensing and optical data processing applications. Photonic structures that guide and manipulate light in the visible spectral range are not as well investigated as their IR counterparts. Nevertheless, this spectral range is important for applications such as biological sensing (e.g., using fluorescence and surface enhanced Raman spectroscopy (SERS) [5, 6]), and visible wavelength reconfigurable optical signal processing (for applications such as LiDAR [7]). By adding light generation and detection in the visible range (using Si [8]) to the Si_3N_4 photonic device on the same substrate, it is possible to develop all visible nanophotonic components. The range of possible components includes sources, modulators, waveguides, and detectors on a monolithic CMOS-compatible photonic chips. Therefor, it is possible to form complete system-on-chip solutions based on Si/Si_3N_4 systems.

Despite their good performance in the infrared (IR) region, Si resonators suffer from significant material loss in the visible range of the optical spectrum, making them unsuitable for visible light applications. Unlike silicon, low-Si LPCVD Si_3N_4 offers a very low material loss throughout the optical range (wavelengths from 300 nm to several microns), and a moderately high refractive index ($n \approx 2$). Si_3N_4,

being a dielectric material, does not suffer from free carrier absorption, which is an important limiting factor in Si high-Q resonators. This makes the fabrication process more straightforward by eliminating the complicated surface treatment post processes necessary for high-Q silicon resonators [2]. On the other hand, having the absorption band edge located at approximately 300 nm wavelength, two photon absorption is not a limiting factor at high intensities at wavelengths larger than 600 nm. Thus, provided that the Si_3N_4 layer is optically isolated from the lossy Si substrate, it can guide the visible light without significant loss in this wavelength range. Nevertheless, most of the research on silicon nitride has been concentrated on infrared (IR) [9, 10, 11, 12, 13, 14] or near infrared (NIR) [15, 3] applications. The few reported works on Si_3N_4 photonic crystals [16, 17, 18, 19, 20, 21] and microring resonators [22] in the visible range were of considerably lower fabrication quality compared with their Si counterparts.

In this thesis, monolithic, high Q, compact Si_3N_4/SiO_2 resonators are demonstrated in the visible range, and critical coupling of the resonators to in-plane waveguides is also demonstrated (at λ=652-660 nm).

In chapter 2 the theoretical aspects are investigated. The mode structure of the microdisks is investigated, and the coupled mode theory is used to calculate the coupling between the resonators and the waveguides.

Details of fabrication of the devices are explained in section 3. The first demonstration of ultra high Q resonators is presented in 4.

The characterization setup and the experimental results are discussed in section 4.2. Coupling of high Q resonators to adjacent waveguides and its optimization are covered in section 4.3.

In chapter 5 a new coupling scheme for single mode coupling is presented. It will be shown that if the bus waveguide wraps around the microdisk, the coupling to only one of the microdisk modes will be enhanced. The structures presented in 4 and 5

will be integrated with micro/nano fluidic channels in 6

In section 7 the high resolution superprism spectrometers are investigated. Additionally, AWG spectrometers will be compared with superprisms in 8. The AWGs will be cascaded with microring resonators. This leads to wide-band, high-resolution spectrometers operating in the visible range.

In part 9 the possibility of fabrication of high Q and small mode volume photonic crystal cavities is presented. And finally in 10 it is shown that the structures shown all through the thesis can work without thermal perturbations.

CHAPTER I

BACKGROUND

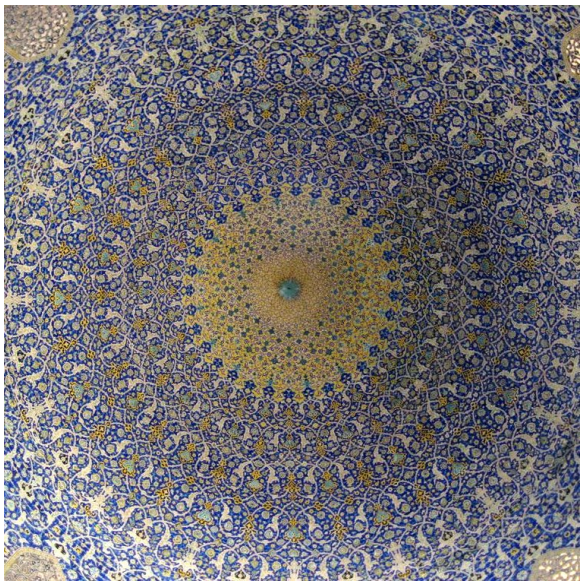

Figure 1: Whispering gallery dome in Esfehan, Iran.

In this chapter the background of the research in reviewed.

1.1 Early Works

The "whispering gallery" effect was analyzed as early as 1910 by Rayleigh [23]. His analysis of the channeling of acoustic waves is a precursor to the disk and ring resonators implemented in the microwave range starting in the 1960s. In the optical domain, integrated ring resonators were proposed in 1969 by Marcatili at Bell Labs [24]. The first guided optical ring resonator was demonstrated by Weber and Ulrich in 1971 [25]. This device consisted of a 5-mm-diameter coated glass rod to which light was coupled with a prism. The first structure to incorporate an integrated bus waveguide was demonstrated by Haavisto and Pajer in 1980 [26]. Most of the efforts through the 80s was concentrated on low index contrast, glass based, and large

diameter (> 1mm) resonators [27, 28, 29, 30]. Since the early efforts outlined above, there have been numerous works in various doped and undoped silica-based glasses [31, 32], Si based platform (Si, SiO_2, Si_3N_4, SiON) [33, 34, 35, 36], and polymers [37, 38] in the past decade. Many of these studies have reported multiring filters and also temperature-insensitive operation.

Microresonators constructed in III-V semiconductors were introduced in the early 1990s. Several groups demonstrated optically pumped microdisk lasers in both GaInAsP-InP and III-Nitrides using the whispering gallery modes (WGM) [39, 40, 41, 42, 43, 44, 45, 46, 47]. Most of these early efforts did not incorporate bus waveguides and relied on fibers to directly collect light from the disk. The first GaAs-AlGaAs microring resonator laterally coupled to a bus waveguide was demonstrated by Rafizadeh et al. in 1997 [48].

1.2 Integrated Structures

Initial efforts toward the fabrication of integrated ring resonators produced very large devices because the index contrast Δn between the core and cladding was small, and operation with large radii of curvature minimizes bending losses [24, 49]. For example, the device fabricated by Honda et al. had $0.052 < \Delta n < 0.067$ and a radius of 4.5 cm. Also, the device was multimode, and there was considerable mode mixing leading to a large background of non resonant light. On the other hand, the construction of microrings 10-μm or smaller requires high index contrast materials, and to make the structures single mode (in case of microrings), one needs to reduce the widths of the waveguides to submicron feature sizes. Narrower waveguides, in turn, lead to higher interaction with the sidewalls and require anisotropic and smooth etching. Moreover, large scale integration requires an accurate control of the coupling rates which can be accomplished laterally using high resolution lithography—e.g., electron beam lithography (EBL)—or vertically by material growth. In the past

decade, these technologies have reached maturity—especially taking advantage of CMOS compatible Si on insulator (SOI) technology—which has led to a variety of different functionalities. In particular, recent advances in Si photonics include the demonstration of high-speed optical modulators [50, 51, 52, 53, 54, 55, 56], Raman lasers [57, 58], WDM filters and buffers [59, 60], photodetectors [50, 61], wavelength conversion [62, 63], on-chip sensing [64, 65], optofluidics [66, 67], and optomechanics [68].

1.3 Sensing Applications

During the past two decades integrated optical sensors have been used extensively in sensitive (bio)chemical analysis. Optical biosensing can be carried out by using two different detection strategies: label-based and label-free detection. In the former protocol, target molecules are labeled with either fluorescence or light absorbing markers to detect and quantify the presence of a specific sample molecule of interest. In the label-free protocol, the target molecules are not labeled or modified, and their presence is revealed by methods such as refractometry, Raman spectroscopy, and optical detection of mechanical deflection of movable elements (e.g. a cantilever). These biosensors can be classified into two categories: mass sensors and fluorescence sensors. Mass sensors measure the presence of the captured analyte by detecting changes in absorption or refractive index, but are ineffective for analytes with small molecular weights and are sensitive to nonspecific binding. Fluorescence sensors measure the emission from an immobilized tracer molecule or fluorescently labeled analyte, and are generally more sensitive and more specific than mass sensors. Initially a number of mass/index sensors, e.g., uniform grating couplers [69], modal difference devices [70, 71], Mach-Zehnder [72], and Young [73] interferometers, have been proposed and successfully implemented.

The principle of grating sensors is based on highly accurate real-time measurement

of the changes in the coupling coefficients due to: (1) changes in the refractive index of a liquid sample covering the waveguide (differential refractometer); and (2) the adsorption or desorption of molecules out of a gaseous or liquid sample on the waveguide (gas or chemical sensor) [69]. The difference based sensors rely on the interference of two modes co-propagating along the same waveguide. These mode can be in two different polarizations (TE/TM) [70], or be parallel modes of a multimode waveguide [71]. The interferometric sensors, on the other hand, often consist of a reference arm—isolated from the sensing environment—and a sensing arm which interacts with the environment.

The Mach-Zehnder interferometer is a highly sensitive device. With the Mach-Zehnder interferometer a cladding index change of 10^{-4} to 10^{-8} can be identified, depending on the experimental configuration used. These double interference devices usually require large sampling areas (analyte volumes) and advanced detection electronics. Nevertheless, these disadvantages can be overcome by the introduction of multiple interference detectors.

Another approach to simultaneously increase the sensitivity and reduce the amount of the required analyte is to take advantage of the large effective interaction length in a microcavity mode [74, 75]. In 2002, Klunder et al. demonstrated the first integrated microcavity based sensor [15]. The device used (shown in Fig. 1.3) consisted of a microdisk resonator vertically coupled to a bus waveguide. The microdisk and the waveguide, both fabricated in silicon nitride, were separated by an oxide layer. The thickness of the oxide layer can accurately control the coupling. The spectrum of the scattered light from the microdisk was obtain through an out of plane collecting microscope in the 778 nm $< \lambda <$ 788 nm range. The multimode microdisk showed three main resonant features and the resonance with the highest Q was selected. The devices were then covered with water and alcohol and the change in the resonance frequencies were measured. The loaded Q of 4900 led to a sensitivity of 23 nm per unit

change in the refractive index. Moreover, the active volume of the fluid sample used in this experiment was less than 10 fL. This means that the number of molecules required for the microcavity sensor is orders of magnitude less than for the linear waveguide sensor. Since then, several groups have proposed sensing structures based on microdisk and microring resonators [76, 77].

Many of such resonator sensors belong to the class of sensors that do not require molecular tags; they rely on specific binding of target molecules to the sensor surface to produce a signal. Arrays of such integrated optics sensors, which can be easily produced, will enable pattern recognition techniques to be applied to improve recognition of biomolecules. Additionally, this makes it possible to separate the useful signal from the variations of the refractive index of the buffer solution and nonspecific binding [78]. A simple demonstration of these procedures is usually done with biotin (also known as vitamin H or B_7) coating, which causes the specific binding and immobilization of avidin. Typically, the surfaces are immersed in a 5% APTES (3-aminopropyltriethoxysilane) solution in isopropyl alcohol (IPA). APTES is used to deposit a buffer layer of silane (SiH_4), since silane is known to act as a bridge between biomolecules and inorganic surfaces such as silicon. The silane-biotin coating can form layers less than 3 nm in thickness, much thinner than the evanescent field region. Avidin is an egg-white derived protein with a molecular mass of 68 kDa (approximately equal to the mass of 68000 hydrogen atoms) and has an extraordinarily high affinity constant for biotin (greater than 10^{15} M^{-1}) [79, 80], which is one of the strongest known non-covalent bonds[1].

[1]A noncovalent bond is a type of chemical bond, typically between macromolecules, that does not involve the sharing of pairs of electrons, but rather involves more dispersed variations of electromagnetic interactions. The noncovalent bond is the dominant type of bond between supermolecules in supermolecular chemistry. Noncovalent bonds are critical in maintaining the three-dimensional structure of large molecules, such as proteins and nucleic acids, and are involved in many biological processes in which large molecules bind specifically but transiently to one another.

The affinity between a ligand (**L**) such as a biotin and a protein (**P**) such as avidin is commonly described by the dissociation constant (K_d), which is a measure of how tightly a ligand binds to a particular protein. The formation of a ligand-protein complex (**C**) can be described by a two-state

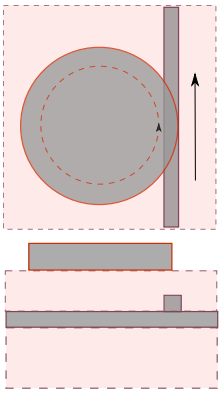

Figure 2: The configuration of the first optical microcavity based sensor. The waveguide is fabricated in the first round of lithography and the microdisk is aligned to it in the second step.

The avidin-biotin interaction displays biospecificity similar to antibody-antigen, DNA-DNA, and receptor-ligand recognition, all of which can be used in practical applications. The great strength of the noncovalent avidin-biotin bond—along with its resistance to breakdown—makes it an ideal model for demonstration of sensing of biomolecules.

The ultra high sensitivity of high Q microdisk microcavities motivated the investigation of other types of whispering gallery mode resonators. In 2003 Arnold et al. suggested the use of microspheres to detect bonding of single protein molecules [81, 82]. In 2007 Armani et al. suggested the use of microtoroids for ultra-high sensitivity single molecule sensors [83]. Microtoroids—introduced in 2003 by Vahala's group at CalTech [1]—are ultra-high-Q structures with smooth surfaces obtained by

---

process

$$\mathbf{C} \rightleftharpoons \mathbf{P} + \mathbf{L}\,, \tag{1}$$

for which the corresponding dissociation constant is defined as

$$K_d = \frac{[\mathbf{P}]\,[\mathbf{L}]}{[\mathbf{C}]}\,, \tag{2}$$

where [**P**], [**L**] and [**C**] represent the concentrations of the protein, the ligand, and the complex, respectively. The dissociation constant has molar units (M). The smaller the dissociation constant, the more tightly bound the ligand is, or the higher the affinity between ligand and protein. Sub-nanomolar dissociation constants as a result of non-covalent binding interactions between two molecules are rare. Nevertheless, Biotin and avidin bind with a dissociation constant of roughly 10^{-15} M = 1 fM [80].

the selective reflow of the edge of SiO_2 microdisks. Unlike a simple optical waveguide sensor, in which the input light has only one opportunity to interact with the target molecule, in such a toroid microcavity with a Q factor of 10^8 the molecule is sampled more than 100,000 times. This increased sampling manifests itself both as a shift of the resonant wavelength and a decrease in the Q factor as the target molecules directly change the optical path length and/or the cavity loss of the sensor. Nevertheless, the toroid sensor extended these ideas even further by adding a new mechanism through which molecules can induce a resonant wavelength shift when the high circulating intensities within the resonator locally heat molecules attached to the whispering gallery. This temperature increase results in a red shift of the resonant wavelength through the thermo-optic effect, when the whispering-gallery material itself (in this case, silica) is heated by the molecule.

Concentrations ranging from 1^{-19} M to 1^{-6} M were controllably flowed past the microtoroid resonator using a syringe pump and the highest sensitivity occurred in the lower concentration range. The dose-response curve is sigmoidal, as would be expected from antibody-antigen binding if there were a finite number of binding sites. An easily detectable response was obtained at 5×10^{-19} M with greater than 10:1 signal-to-noise ratio. This working range is a 12-decade concentration range (10^{12}) which can be compared to that other label-free, room-temperature detection techniques (e.g., nanowire sensors (10^3) [84, 85], and microcantilevers (10^3) [86]).

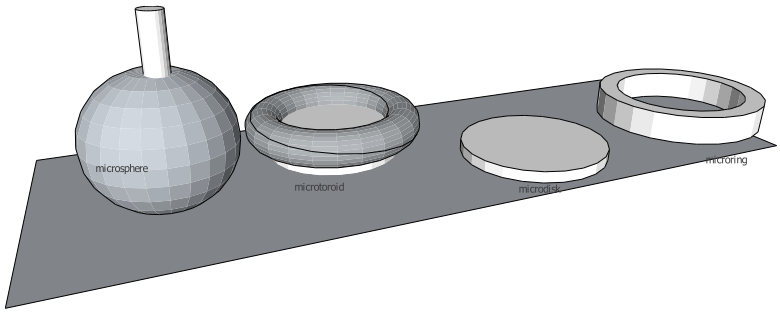

Figure 3: Microresonators

For the lowest concentrations where shifts are observed, small numbers of molecules would be expected to interact with the toroid, which suggests that the sensor might accomplish label free single-molecule detection. The time domain monitoring of the resonance frequency showed and stepwise gradual red shift in the resonance which showed the sensitivity of the toroid to single molecule attachments.

Toroid resonators, despite their superior sensitivity and accuracy, lack the integrated coupling scheme. Because of selective reflowing of the oxide edges, and also wet chemical undercutting necessary because of the low index of the resonator, no integrated optical wire can be monolithically fabricated in the vicinity of the resonator. Thus, a complicated fiber-taper alignment setup with nanometer-scale accuracy is needed to couple light into/out of the toroid. This complicates the integration of the toroid resonator with micro/nano scale fluidic channels, which are necessary for practical biological sensor applications. Moreover, as the fiber can be coupled to one resonator at a time, parallel processing with different biological markers is very difficult.

1.3.1 Slot Based Sensors

Conventional strip and rib waveguides are commonly used in biochemical sensors based on integrated optics. In these waveguides, the guiding mechanism is based on total internal reflection (TWR) in a high-index material (core) surrounded by a low-index material (cladding). A novel guided-wave configuration—known as a slot-waveguide—was introduced by Almeida et al. in 2004 [87]. This structure is able to guide and strongly confine light in a nanoscale, low-refractive index material by using TIR at levels that cannot be achieved with conventional waveguides. Figure 4(a) shows a schematic picture of a slot-waveguide. It consists of two strips of high refractive index (n_H) separated by a low-index (n_S) region (slot) of width W_{slot}. The principle of operation of this structure is based on the discontinuity of the

electric (E) field at the boundary between the two materials. For an electromagnetic wave propagating along the waveguide, the major E-field component of the quasi-TE eigenmode (which is aligned horizontally) undergoes a discontinuity at the perpendicular strips/slot interfaces. The discontinuity, according to Maxwell's equations, is determined by the relation $E_S/E_H = (n_H/n_S)^2$, where S and H denote slot region and high-index region, respectively. Thus if n_H is much larger than n_S, this discontinuity is such that the E-field is much more intense in the low-index slot region than in the high-index rails. Given that the width of the slot is comparable to the decay length of the field, the E-field remains high across the slot, resulting in a power density in the slot that is much higher than that in the high-index regions. This unique characteristic makes the slot-waveguide very attractive for numerous applications, including biochemical sensing. Using the slot as the sensing region, larger light-analyte interaction and higher sensitivity can be obtained as compared to a conventional waveguide. In addition, since TIR mechanism is employed, there is no interference effect involved, and the slot-structure exhibits very low wavelength-sensitivity.

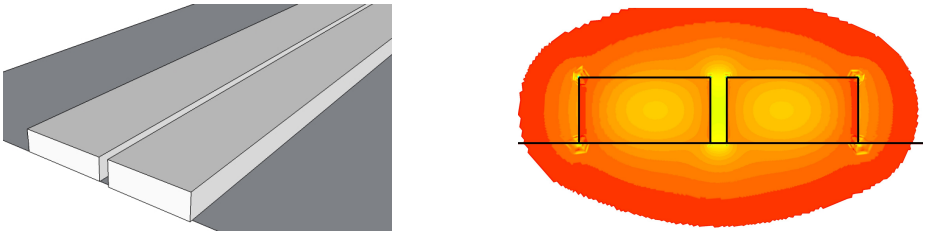

Figure 4: (a) The structure of a slot waveguide. A narrow slot of air (or a low index cladding material) sandwiched between two higher index waveguides. (b) The intensity of the electric field in a slot waveguide for a TE-like mode. The intensity of the field is maximum in the low index slot.

In particular, refractive index (RI) sensors based on slot-waveguide microring resonators [88] and directional couplers have been recently demonstrated. The former were fabricated in two different material systems, Si_3N_4/SiO_2 [88, 89] and Si/SiO_2 [90]. In 2007, Borrios et al. reported an experimental demonstration of an integrated

biochemical sensor based on a slot-waveguide microring resonator. The microresonator was fabricated on a Si_3N_4-SiO_2 platform and operated at a wavelength of 1.3 μm. The sensor detected minimal refractive index variation of 2×10^{-4} refractive index unit (RIU). The resonator showed a linear shift of the resonance wavelength of 212.13 nm/RIU. This value is more than twice as large as that of conventional strip waveguide ring resonator biochemical sensors. In 2008 they expanded this structures to sensors sensitive to Bovine serum albumin (BSA) protein and anti-BSA antibodies [89, 91].

The sensitivity of biomolecule detection is given by

$$S_B = \frac{\delta\lambda}{\sigma_p}, \tag{3}$$

where $\delta\lambda$ is the spectral shift at saturation and σ_p is the surface density of a monolayer of biomolecules. For the reported structure, $S_{antiBSA} = 1.8$ nm/(ng/mm^2). The biomolecule detection limit is given by $\mathrm{DL}_B = R/S_B$, where R is the sensor resolution. Assuming the sensor resolution as the spectral resolution ($R = 50$ pm), the authors reported a detection limit of $\mathrm{DL}_{antiBSA} = 28$ pg/mm^2.

In 2008, Lipson et al. reported a gas sensor based on a slot microring resonator [90]. The shifts in the resonance wavelength due to the presence and pressure of acetylene gas was measured and differences in its refractive index as small as 10^{-4} in infrared was resolved. The observed sensitivity of this device (enhanced due to the slot-waveguide geometry) agreed with the expected value of 490 nm/RIU. By measuring changes in the resonant wavelength of the microring ($\delta\lambda$) it was possible to detect small changes in the refractive index of the gas (Δn_{gas}). For changes in n_{gas} small compared to the core-cladding index difference, it is possible to assume that the mode shape does not change. This is equivalent to taking the first-order correction to the resonant wavelength, which can be expressed mathematically as

$$\delta\lambda = \lambda_o \frac{\Gamma}{n_{eff}} \Delta n_{gas}\,, \tag{4}$$

where λ_o is the unperturbed resonance wavelength, n_{eff} is the unperturbed value of the effective index in the ring, and Γ is the proportionality constant satisfying the relationship $\Delta n_{eff} = \Gamma \Delta n_{gas}$. This proportionality constant is defined as the interaction factor of the guided mode

$$\Gamma \equiv \frac{n_{gas} \int_{gas} |\mathbf{E}|^2 \, d\mathrm{A}}{Z_o \int_{\infty} (\mathbf{E} \times \mathbf{H}^*) \cdot \hat{\mathbf{z}} \, d\mathrm{A}} \tag{5}$$

where Z_o is the impedance of free space, $\hat{\mathbf{z}}$ is the propagation direction, and the integrals are evaluated over the cross-sectional area of the waveguide[2]. One should note that the shift in resonant wavelength is dependent only on the ratio λ/n_{eff} and independent of the cavity quality factor (Q). The ability to accurately quantify very small changes in the resonance wavelength can be aided by an increase in Q since this results in a narrowing of the resonance linewidth ($\Delta\lambda$). Due to the large value of λ/n_{eff} this experiment was possible with a resonator with a relatively low Q factor of about 5000. Much larger Q factors in the order of 10^6could greatly improve this technique by allowing more accurate readout of the wavelength shift.

Recently researchers at Gent University demonstrated a slot-waveguide-based ring resonator in silicon on insulator (SOI) with a footprint of only 13 μm $\times$ 10 μm. Experiments showed that it has 298 nm/RIU sensitivity and a detection limit of 4.2×10^{-5} RIU for changes in the refractive index of the top cladding. It was demonstrated that surface activation for selective label-free sensing of proteins can be applied inside a 100 nm-wide slot region, and showed that the application of a slot waveguide instead of a normal waveguide increases the sensitivity of an SOI ring resonator with a factor 3.5 for detection of proteins [91].

In addition to microring resonators, interferometric configurations, such as Mach-Zenhder interferometers, directional couplers, and Fabry-Perot cavities, could also

[2]Since the polarizability of matter (and thus its refractive index) is determined by the material response to the electric field, it is the concentration of the electric field in the sensing region which is important not the concentration of power.

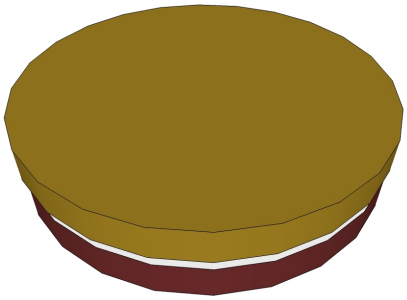

Figure 5: A double disk, horizontal slot sensor. The top surface is Si_3N_4 and the bottom disk is a Si resonator. The surface of the Si_3N_4 disk is functionalized to adsorb specific biomolecules. Upon an attachment event, the Si_3N_4 bends and reduces the effective distance of the two disks, leading to a change in the resonance frequency of the structure.

work as highly sensitive transducers for RI label-free sensing. Slot-based passive directional couplers[92] and Fabry-Perot cavities [93] have both been demonstrated in Si/SiO_2 and Si_3N_4/SiO_2, respectively. They could be used for RI sensing by defining a proper sensing window on them. Passaro et al. [94] reported a theoretical analysis of a compact directional coupler formed by SOI slot waveguides for chemical sensing. The minimum detectable refractive index change was calculated to be 10^{-5}. Sensor design and optimization allowed a good trade-off between device length (L) and sensitivity. The estimated sensor limit-of-detection for glucose concentration in an aqueous solution was in the order of 0.1 g/L.

In the optical configurations described so far, vertical slot-waveguides with a single slot-sensing region have been used. However, the slot-waveguide principle can be extended to other geometries such as vertical multi-slot [95, 96] and horizontal (multi-)slot waveguides [97]. Both types of structures have been demonstrated to operate properly as passive optical elements in Si/SiO_2, $Si/Si_3N_4/SiO_2$ and Si_3N_4/SiO_2 material systems. The effective index variation of the guided mode for a Si_3N_4/SiO_2 triple-slot structure as a function of the cladding refractive index variation has been estimated to be improved by 20% as compared to that of a single-slot waveguide [96]. This is a consequence of a larger localization of the E-field of the optical mode in

the sensing region. However, multi-slot structures possess more high-index interfaces, which may increase optical scattering losses due to interface roughness. Additionally, horizontal slot-waveguide configurations can be implemented by using conventional deposition techniques (CVD) which results in lower rail/slot interface roughness.

Utilizing the horizontal slot idea, Borris proposed a very sensitive double microdisk sensor in 2006 [98]. As shown in Fig. 5, the structure consisted of a Si_3N_4 disk fabricated on top of a high index Si resonator with a narrow slot of fluid separating the two disks. The surface of the Si_3N_4 disk is functionalized to adsorb specific biomolecules. Upon an attachment event, the Si_3N_4 bends and reduces the effective distance of the two disks leading to a change in the resonance frequency of the structure. A deflection sensitivity of 33 nm^{-1} was predicted, showing an enhancement of four orders of magnitude as compared to the state-of-the-art microcantilever sensors at the time.

1.3.2 Labeling-Based Optical Slot-Waveguide Sensors

The evanescent field in planar waveguides can be employed in both optical absorption based sensors and fluorescence sensors. In the former, the presence of an absorbing label (e.g. a gold nanoparticle) within the penetration depth of the evanescent field induces an increase in the propagation loss of the guided mode. Such an increase can then be related to the concentration of the target analyte. In fluorescence-based sensors, the evanescent field can be used to excite the fluorescent labels residing in the immediate region near the waveguide interface, and also to collect the fluorescence via resonant back tunneling into the waveguide [99].

Bernini et al. [100] investigated both fluorophore excitation and fluorescence collection efficiencies of two-dimensional slot-waveguides. They considered excitation and collection wavelengths of 633 nm and 690 nm, respectively, and refractive indexes

of 2 and 1.33 for the high-index rails and low-index slot region. Their analysis indicated that the use of a slot-waveguide can improve both the excitation and collection efficiencies compared to a single slab waveguide due to the enhanced E-field intensity at the rail/slot interfaces. In particular, numerical calculations revealed maximum excitation efficiency of 36% by using the slot geometry (slot thickness = 160 nm) as compared to 26% of a conventional slab waveguide. The extension of this study to three dimensional guiding configurations would provide useful information and design guidelines for an actual implementation of labeling-based detection configurations based on slot-waveguides.

CHAPTER II

THEORETICAL BACKGROUND

In this chapter the theoretical background of the research is presented. The mode structure of the microdisks is investigated (section 2.1), and the coupled mode theory (CMT) is used to calculate the coupling between the resonators and the waveguides.

2.1 Electromagnetic Treatment of Microresonators

In the linear regime, by assuming a harmonic time dependence, $\exp(j\omega t)$, for the electromagnetic field components, Maxwell's curl equations in the frequency domain (for linear dielectric and nonmagnetic materials) are expressed as

$$\nabla \times \mathbf{H} = \quad j\omega\epsilon_o n^2 \mathbf{E}, \tag{6}$$

$$\nabla \times \mathbf{E} = -j\omega\mu_o \mathbf{H}, \tag{7}$$

where μ_o and ϵ_o are the permeability and permittivity of the vacuum, respectively, and n is the refractive index, which can be a complex number to include loss. Equations 6 and 7, can be combined to leads to the Helmholtz equations

$$\nabla \times (\frac{1}{n^2}\nabla \times \mathbf{H}) = \left(\frac{\omega}{c}\right)^2 \mathbf{H}, \tag{8}$$

$$\nabla \times \nabla \times \mathbf{E} = \left(\frac{\omega}{c}\right)^2 n^2 \mathbf{E}, \tag{9}$$

in which $c = (\epsilon_o\mu_o)^{-\frac{1}{2}}$ is the speed of light in vacuum. By solving the above equation for a resonator structure, the resonance frequency and mode profile of the resonator can be obtained. Because of the intrinsic leakage of photons out of a circular resonator and also material and fabrication imperfections, the lifetime of the photons in the cavity is limited (denoted by τ_o). Therefore the eigen-frequency $\omega_{resonance}$

has an imaginary part ($\omega_{resonance} = \omega_o - j/\tau_o$). Thus the solutions to the Helmholtz equations assume solutions in the form

$$\mathbf{E} = \mathbf{E}(r)\exp(j\omega_o - t/\tau_o), \tag{10}$$

$$\mathbf{H} = \mathbf{H}(r)\exp(j\omega_o - t/\tau_o), \tag{11}$$

in which τ_o is the photon lifetime, and $\mathbf{E}(r)$ and $\mathbf{H}(r)$ are spatial variation of the electric and magnetic field of the resonator. τ_o also represents the broadening of the resonator energy spectrum. An important figure of merit in the whispering gallery modes is their optical quality factor (Q_o). The definition of the quality factor extends well beyond that of microphotonics and is generally defined for all resonant elements as

$$Q_o \equiv \omega_o \frac{U(t)}{P_{loss}(t)} \tag{12}$$

in which $U(t)$ is the energy stored in the cavity and $P_{loss}(t)$ is the power dissipated by the resonator. Assuming an initial stored energy $U_o = U(t=0)$, the time dependence of U can be obtained as

$$U(t) = \int_\infty \left[\frac{1}{4}\epsilon_o n^2 |\mathbf{E}(t)|^2 + \frac{1}{4}\mu_o |\mathbf{H}(t)|^2\right] d\mathrm{V} \tag{13}$$

$$= \int_\infty \left[\frac{1}{4}\epsilon_o n^2 |\mathbf{E}|^2 e^{-2t/\tau} + \frac{1}{4}\mu_o |\mathbf{H}|^2 e^{-2t/\tau}\right] d\mathrm{V} \tag{14}$$

$$= U_o e^{-2t/\tau}. \tag{15}$$

Combining Eqs. (12) and (15):

$$Q_o \equiv \omega_o \frac{U(t)}{P_{loss}(t)} \tag{16}$$

$$= \omega_o \frac{U_o \exp(-2t/\tau_o)}{-\frac{\partial}{\partial t}(U_o \exp(-2t/\tau_o))} \tag{17}$$

$$= \omega_o \frac{U_o \exp(-2t/\tau_o)}{2/\tau_o U_o \exp(-2t/\tau_o)} \tag{18}$$

$$= \omega_o \tau_o / 2. \tag{19}$$

From Eq. 19 it is obvious that higher Q leads to a longer photon lifetime and vice versa. The quality factor can be related to standard absorption coefficients (α) via

the group velocity of the optical energy as $\alpha = \omega/(Q_o v_g)$. Also $\delta\omega$ and τ_o are related as

$$\tau_o = \frac{2Q_o}{\omega_o} = \frac{2}{\delta\omega}. \tag{20}$$

Another useful quantity defined for an optical microcavity is the *mode volume* (V). V is commonly defined based on two quantities: (1) the total energy stored in the electric field of the cavity (U_E); (2) the maximum of the electric field energy density. V can be written as

$$V \equiv \frac{U_E}{\max(\frac{1}{2}\epsilon_o n^2 |\mathbf{E}|^2)} \tag{21}$$

$$= \frac{\int_\infty \frac{1}{2}\epsilon_o n^2 |\mathbf{E}|^2 \, d\mathrm{V}}{\max(\frac{1}{2}\epsilon_o n^2 |\mathbf{E}|^2)} \tag{22}$$

$$= \frac{\int_\infty |n\mathbf{E}|^2 \, d\mathrm{V}}{\max(|n\mathbf{E}|^2)}. \tag{23}$$

It is clear from Eq. (21) that for a certain amount of stored energy in the cavity, smaller mode volumes lead to larger densities of the electric field, which are beneficial in a broad range of applications, especially in nonlinear optics.

2.1.1 Free Spectral Range

Noticing the radial symmetry of the resonators, one can expect the modes to display a radial symmetry and also a periodic behavior as a function of azimuthal angle (ϕ). Knowing that the traveling mode experiences a multiple of π phase shift in a round trip around the circular structure, the field distribution can be written as

$$\mathbf{E} = E_z(r,z) E_r(r,z) E_\phi(r,z) \, \exp(j\omega t - jm\phi) \tag{24}$$

$$\mathbf{H} = H_z(r,z) H_r(r,z) H_\phi(r,z) \, \exp(j\omega t - jm\phi + \psi) \tag{25}$$

in which ϕ is the axial coordinate (shown in Fig. 6). ψ is the phase difference between the electric and magnetic fields. The integer m denotes the axial order of the mode.

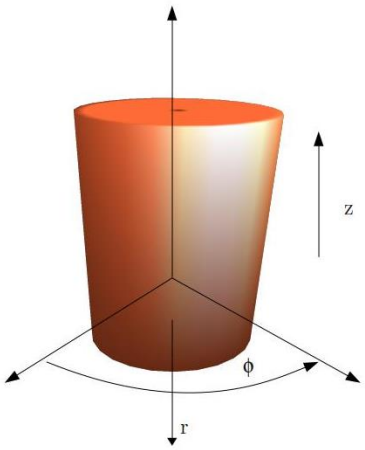

Figure 6: The z, ϕ and r axes as used in the electromagnetic (EM) description of cylindrically symmetric resonators.

Three examples of typical field distributions in a microdisk cavity are depicted in Fig. 7. In each case the m and N numbers specify the azimuthal and radial mode orders, respectively. Figures (a) and (b) depict first rank radial ($N = 1$) modes. A mode with $N = 1$ is often called the *"fundamental"* mode. For Fig. (a), as seen from the six null lines—a three-fold odd symmetry—the traveling wave experiences a $3 \times 2\pi$ phase shift in a round trip around the disk. Hence the m order of the mode is three. On the other hand, for Fig. (c), a 2^{nd} radial and 8^{th} azimuthal order mode, the null ring in the radial direction shows the higher radial rank of the mode[1] .

The free-spectral range (FSR) is defined as the frequency spacing between the modes of an optical cavity (given that the modes have the same rank, i.e. the same N).

[1]Here a 2D finite difference time domain (FDTD) solver is used to obtain the mode profiles. In section 2.1.2 the mode profiles will be achieved with a full vectorial, 3D analysis based on the axial symmetry of the resonators. On the other hand, the effective index 2D analysis can provide a quick insight into the profile shape and the resonance frequency of the modes. Moreover, in a 2D effective index method, one can use the analytical solutions available for optical fibers (assuming no out-of-plane propagation, i.e., $\beta_{perpendicular} = 0$) [101]. The solutions to such simplified model have the form:

$$\mathrm{E}_z = \cos(m\phi) \begin{cases} A\, J_m\left(r\sqrt{n^2 k_o^2 - \beta^2}\right) & r \le R \\ B\, K_m\left(r\sqrt{\beta^2 - k_o^2}\right) & r \ge R \end{cases}, \tag{26}$$

in which J_m and K_m are Bessel and Hankel functions of first and second kind, respectively.

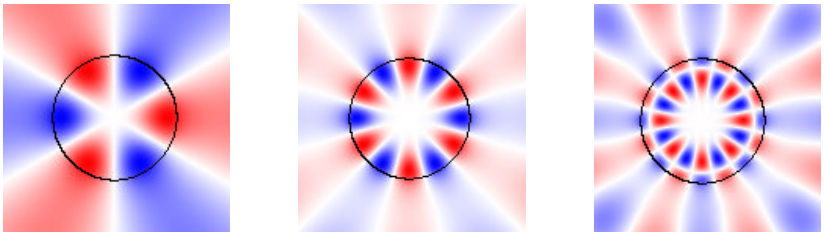

(a) $N=1 \quad m=3$ (b) $N=1 \quad m=6$ (c) $N=2 \quad m=8$

Figure 7: The field distribution (E_z) of different modes of a microdisk simulated with 2D finite difference time domain (FDTD) method. The modes are identified with their radial rank (N) and azimuthal order (m). (a) A first rank ($N=1$) mode. The mode with $N=1$ is often called the *"fundamental"* mode. As seen from the six null lines—a three-fold odd symmetry—the traveling wave experiences a $3\times 2\pi$ phase shift in a round trip around the disk. Hence the m order of the mode is three. (b) A 1^{st} radial rank and 6^{th} azimuthal order mode. (c) The null ring in the radial direction shows the higher radial rank of the mode. A 2^{nd} radial rank and 8^{th} azimuthal order mode.

Typically the FSR increases as the physical size of the resonator is shrunk (similar to a Fabry-Perot). In the cylindrical resonators investigated here, the resonance condition is met when the phase change in a round trip is a multiple of 2π. For a certain mode with azimuthal order m,

$$L\,\beta = 2\pi\, m\,, \tag{27}$$

in which L is the effective travel distance around the resonator for the specified mode and

$$\beta \equiv n_{eff}\, k_o \tag{28}$$

$$= n_{eff}\, 2\pi/\lambda_o \tag{29}$$

$$= n_{eff}\, \omega_o/c \tag{30}$$

is the propagation constant (k_o is the vacuum wavenumber and n_{eff} is the effective refractive index of the traveling mode.) Therefore from Eq. (30) and (27):

$$n_{eff}\, \omega L/c = 2\pi\, m\,. \tag{31}$$

Taking the derivative of the above equations in respect to m, we have

$$\frac{\partial\beta}{\partial\omega}\frac{d\omega}{dm}L = 2\pi. \tag{32}$$

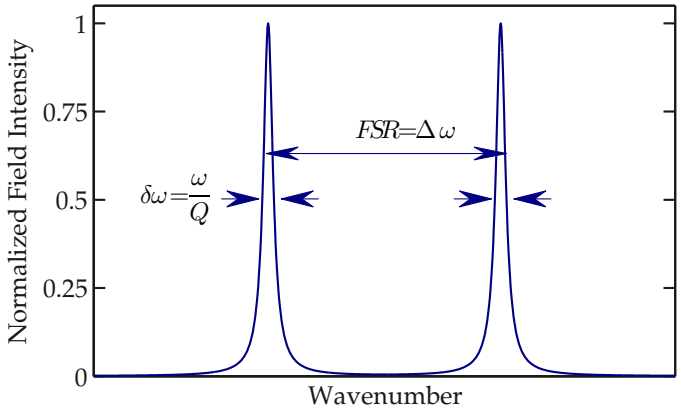

Figure 8: The field intensity as a function of wavenumber. The FSR and $\delta\omega$ are shown.

The FSR(ω) is the spectral distance of two similar modes satisfying Eq. (27) for m and $m+1$. For m large enough (usually $m > 100$ for practical cases) one can replace dw with FSR(ω)=$\omega_{m+1} - \omega_m = \Delta\omega$ and dm with 1 to have

$$\frac{\partial\beta}{\partial\omega}\Delta\omega\, L = 2\pi. \tag{33}$$

The group velocity v_g, which is a measure of the speed of propagating packets of light inside the resonator, is defined as $v_g \equiv \partial\omega/\partial\beta$. Therefore, Eq. (33) can be written as

$$\frac{1}{v_g}\Delta\omega\, L = 2\pi. \tag{34}$$

Also taking a derivative from $\beta = n_{eff}\omega/c$ in regard to ω, one can derive

$$\frac{\partial\beta}{\partial\omega} = \frac{1}{c}\left(\frac{\partial n_{eff}}{\partial\omega}\omega + n_{eff}\right), \tag{35}$$

which leads to

$$\frac{c}{v_g} = \left(\frac{\partial n_{eff}}{\partial\omega}\omega + n_{eff}\right). \tag{36}$$

This enables us to write the FSR in terms of the dispersion of n_{eff} and the group index n_g as

$$\text{FSR} = \frac{2\pi\, c}{L\left(\frac{\partial n_{eff}}{\partial \omega}\omega + n_{eff}\right)} = \frac{2\pi\, c}{L n_g} \qquad \text{where} \quad n_g = c/v_g = \frac{\partial n_{eff}}{\partial \omega}\omega + n_{eff}\,. \tag{37}$$

Knowing that the time it takes a packet of energy a time to travel around the circular resonator is $T = L/v_g = Ln_g/c$, Eq. (34) can be simplified as

$$\text{FSR} = \Delta\omega = 2\pi\frac{v_g}{L} = 2\pi\frac{c}{Ln_g} = \frac{2\pi}{T}\,. \tag{38}$$

Because of the energy leakage of the resonator (which corresponds to finite photon lifetime τ_o), the total number of round trips is finite and approximately equal to $2\tau_o/T$, where $2\tau_o$ is the energy leakage time constant. As a result, the resonator circulating power (which is proportional to $|E_{resonator}|^2$) is enhanced compared to the electric field of the light coupled into the structure ($|E_{external}|^2$).

$$|E_{resonator}|^2 = \frac{2\tau_o}{T}|E_{external}|^2\,. \tag{39}$$

The enhancement factor $\mathcal{E} \equiv (|E_{resonator}|/|E_{external}|)^2$ can then be written as

$$\mathcal{E} = \frac{2\tau_o}{T} = \frac{4/\,\delta\omega}{2\pi\,/\,\Delta\omega} = \frac{2}{\pi}\frac{\Delta\omega}{\delta\omega}. \tag{40}$$

Then, defining the finesse for the resonator as $\mathcal{F} \equiv \Delta\omega/\delta\omega$, the field enhancement is

$$\mathcal{E} = \frac{2}{\pi}\mathcal{F}. \tag{41}$$

2.1.2 3D Solutions of Helmholtz Equation with Axial Symmetry

From the two Helmholtz equations (Eq. 8 and 9) the magnetic field equation is easier to be handled as the medium is magnetically homogeneous. The magnetic field can be separated into the transverse (i.e., r and z directions) and perpendicular (i.e., ϕ) components. Therefore, $\mathbf{H}$ can be rewritten as

$$\mathbf{H} = \mathbf{H}_t + \mathrm{H}_\phi\,\widehat{\phi} \qquad (\mathbf{H}_t = \mathrm{H}_r\,\widehat{r} + \mathrm{H}_z\,\widehat{z})\,. \tag{42}$$

Knowing that $\nabla \cdot \mathbf{H} = 0$, we can apply the divergence in the cylindrical coordinates on $\mathbf{H}$:

$$0 = \frac{\mathrm{H}_r}{r} + \frac{\partial \mathrm{H}_r}{\partial r} + \frac{1}{r}\frac{\partial \mathrm{H}_\phi}{\partial \phi} + \frac{\partial \mathrm{H}_z}{\partial z} \qquad \left(\text{axial symmetry} \Rightarrow \tfrac{\partial}{\partial \phi} = -jm\right) \tag{43}$$

$$= \frac{1}{r}\frac{\partial}{\partial r}(r\mathrm{H}_r) + \frac{-jm}{r}\mathrm{H}_\phi + \frac{\partial \mathrm{H}_z}{\partial z} \qquad \left(\text{we write } \tfrac{\partial \mathrm{H}_z}{\partial z} \text{ as } \tfrac{\partial (r\mathrm{H}_z)}{r\,\partial z}\right) \tag{44}$$

$$= \frac{1}{r}\frac{\partial}{\partial r}(r\mathrm{H}_r) + \frac{-jm}{r}\mathrm{H}_\phi + \frac{\partial (r\mathrm{H}_z)}{r\,\partial z} \tag{45}$$

Equation 45 can be rewritten in a more compact form

$$\nabla_t \cdot \mathbf{H}_t = jm\mathrm{H}_\phi\,, \tag{46}$$

in which $\mathbf{H}_t = \mathrm{H}_r\,\hat{r} + \mathrm{H}_z\,\hat{z}$ and the transverse divergence (∇_t) is defined as $\nabla_t \cdot \mathbf{a} = \partial a_r/\partial r + \partial a_z/\partial z$.

Using the above equation, H_ϕ can be replaced by its equivalent $-j\nabla_t \cdot \mathbf{H}_t/m$. Therefore, in the Helmholtz equation (Eq. (8)), only H_t and its derivatives are remaining. In other words, having found a solution to Eq. (8), one can find all of the six field components from H_r, H_z, and their derivatives. Rewriting the Helmholtz equation and with some simplifications we have

$$\nabla_t \times \left[\frac{1}{n^2}\left(\nabla_t \times (r\mathbf{H}_t) - \frac{\hat{r}}{r} \times (r\mathbf{H}_t)\right)\right] - \frac{1}{n^2 r}\nabla_t\left[r\nabla_t \cdot (r\mathbf{H}_t)\right] + (\frac{m}{nr})^2 r\mathbf{H}_t = {k_o}^2 r\mathbf{H}_t, \tag{47}$$

in which $r\mathbf{H}_t$ can be replaced by a newly defined variable $\mathcal{H} \equiv r\mathbf{H}_t$. Thus we have

$$\nabla_t \times \left[\frac{1}{n^2}\left(\nabla_t \times \mathcal{H} - \frac{\hat{r}}{r} \times \mathcal{H}\right)\right] - \frac{1}{n^2 r}\nabla_t\left[r\nabla_t \cdot \mathcal{H}\right] + (\frac{m}{nr})^2 \mathcal{H} = {k_o}^2 \mathcal{H}. \tag{48}$$

Either Eq. (47) or (48) can be used in an EM solver to obtain the mode profiles and the resonant frequencies of the resonator. Here we concentrate on Eq. (47). As a result, the differential equation takes the following form

$$[A][\mathbf{H}_t] = {k_o}^2[B][\mathbf{H}_t].$$

In this formulation, $[\mathbf{H}_t]$ is a column vector and $[A]$ and $[B]$ are the global finite element method (FEM) matrices. The COMSOL™ commercial multi-physics mode solver was then used to analyze the resonators.

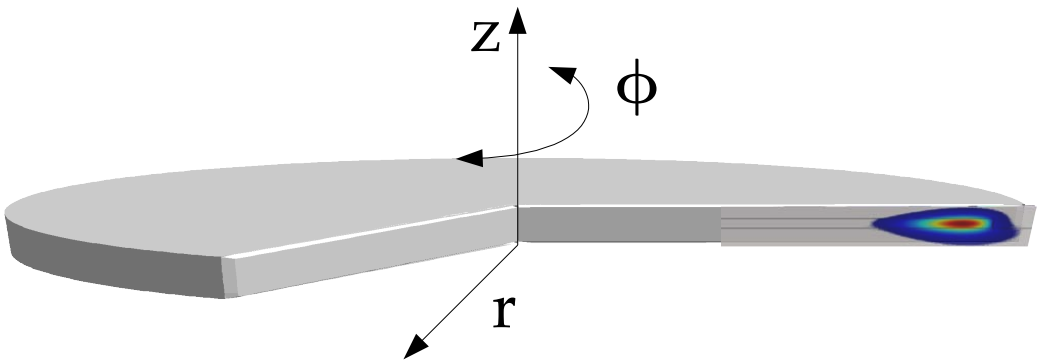

Figure 9: The field is calculated on a radial cross section of the microdisk cavity.

Figure 9 depicts a typical structure simulated with COMSOL. The figure shows a radial cross section of the disk with the magnetic field of the TE mode superimposed on the cross section. Figures 10(a) and 10(b) show, respectively, the cross sections of the structure and the FEM grid used for the COMSOL simulations. Figures 10(c)-(h) depict the magnetic (H_z, H_r, and H_ϕ) and electric (E_z, E_r, and E_ϕ) field components of of the fundamental mode of the microdisk. This mode is quasi-TE (or TE-like), as the electric field is predominantly projected into the in-plane components (E_r and E_ϕ), and the out-of-plane component (E_z), as shown in Figure 10(f), is very small. This mode is a 1st order radial mode, as the energy densities have one lobe in the radial direction inside the microdisk. Figure 10(i) compares the radial distribution of the field components of the two first radial modes (TE_1 and TE_2) of a 20 μm microdisk along a line passing through the middle of the microdisk and along the radial direction.

Another important property of the resonator is the value of the effective index, defined as

$$n_{eff} \equiv \frac{\beta}{k_o} \approx \frac{m}{k_o R},$$

for different physical dimensions of the disk and also resonant wavelengths. For instance, as the radius of the disk is reduced, the electric field energy is gradually pushed into the lower index substrate and cladding, and the effective index of the

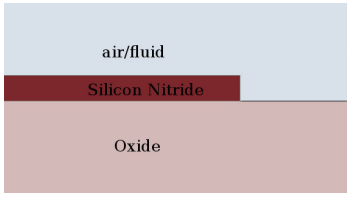

(a) The analyzed structure.

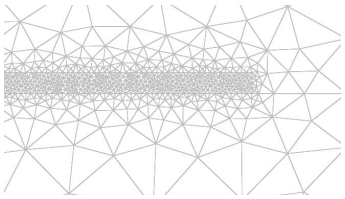

(b) A typical grid for FEM analysis.

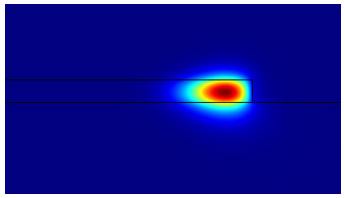

(c) H_z of the fundamental TE mode.

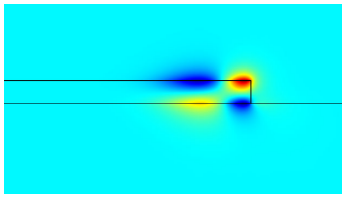

(d) H_r

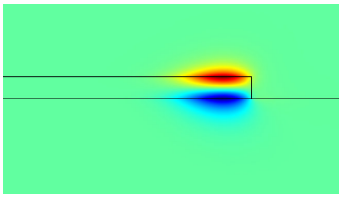

(e) H_ϕ

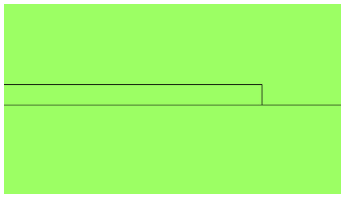

(f) E_z

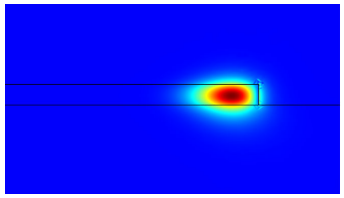

(g) E_r

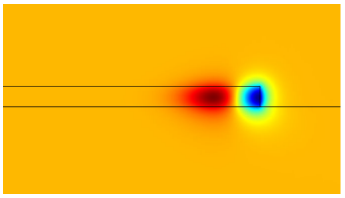

(h) E_ϕ

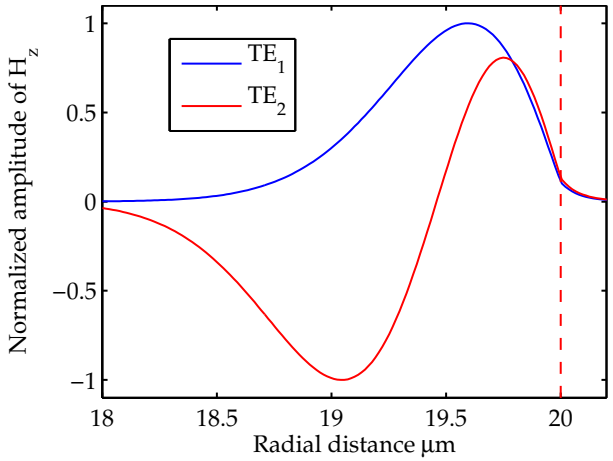

(i) Amplitude of H_z for TE_1 and TE_2 as a function of radial distance from the center.

Figure 10: COMSOL simulation of the field distribution of the first order mode. (a) The analyzed structure. A 5 μm radius microdisk fabricated in a layer of 200 nm of Si_3N4 on top of an oxide substrate. (b) The FEM grid. (c)–(g) The field components of the TE mode. (i) The normalized amplitude of H_z for the first two radial modes (TE_1 and TE_2).

resonant mode is reduced (Fig. 11).

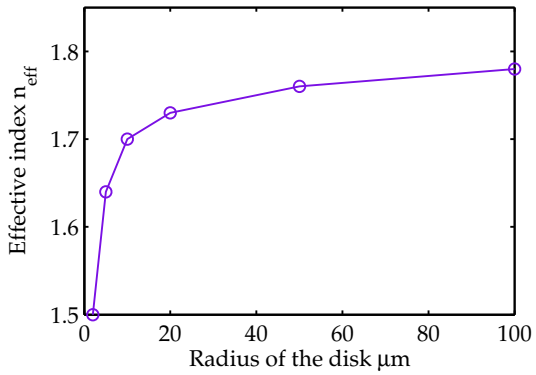

Figure 11: The effective index (n_{eff}) of the fundamental resonant mode vs. the radius of the disk. As the radius is increased, the effective index of the resonant mode approaches n_{eff} of the slab mode.

On the other hand, one can find several different modes of the microdisk simultaneously using the FEM method. Changing the azimuthal mode order (m), the solver finds the k_o eigenvalue for various modes of the disk. This leads to the dispersion diagram shown in Fig. 13.

As the azimuthal mode order (m) is increased a larger number of wavelengths should be fitted in the $2\pi R$ circumference of the disk, which leads to a smaller wavelength and higher frequency resonances. Knowing the m and k_o values for different dispersion bands, the effective index and also the group index of different modes are found.

As shown in Fig. 14, as m increases the effective index of the modes increase toward the bulk index of the Si_3N_4 layer. The circular markers indicate the rang of m for which each mode falls in the operation range of the tunable laser (652–660 nm). The effective indices of the lower order modes are higher as their electric field is more concentrated inside the high-index layer.

By finding the spectral distance of consecutive modes of the same branch, the FSR_λ of each mode can be found. It is clear from Fig. 15 that the TE_1 mode has the smallest FSR among the TE modes, and as the mode order increases, the

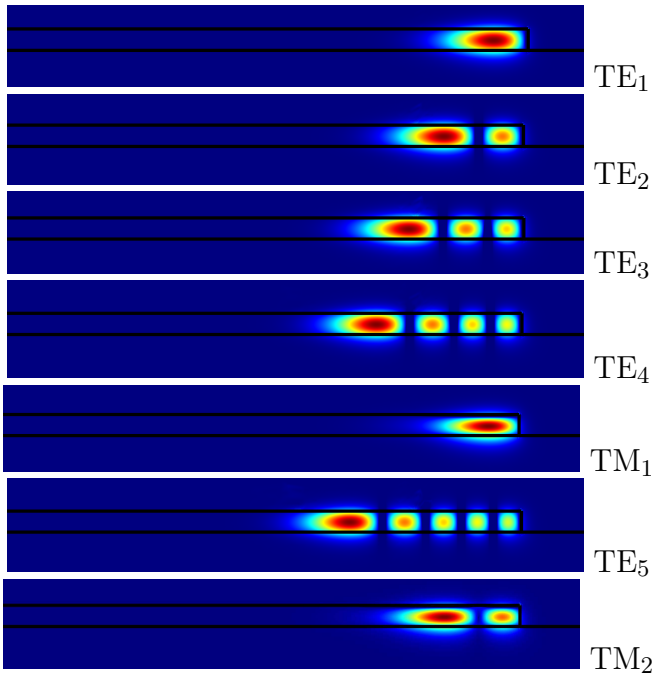

Figure 12: The intensity of the electric field $\sqrt{E_r^2 + E_\phi^2 + E_z^2}$ for the modes with higher effective indices. For higher order modes the electric field is less confined in the high-index layer, and the effective index is smaller.

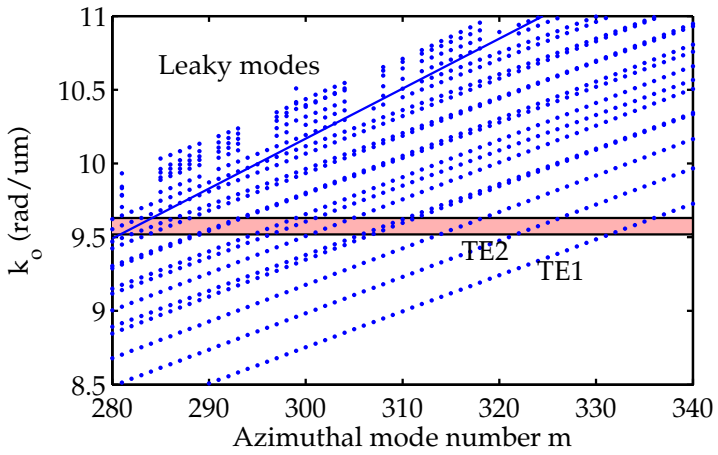

Figure 13: The wavenumber of the resonant modes of a microdisk cavity vs. the azimuthal mode number (m). The radius (R) of the microdisk is 20 μm and the thickness of the high-index guiding layer (Si_3N_4) is 200 nm. The lowest frequency branch is the fundamental ($N = 1$) TE mode. TE_4 and TM_1 modes are accidentally degenerate at some frequencies. The area above the blue line shows the range in which the solutions of the Helmholtz equation lie above the substrate light-line and can leak into the substrate. The horizontal band is the operation range of the tunable visible laser.

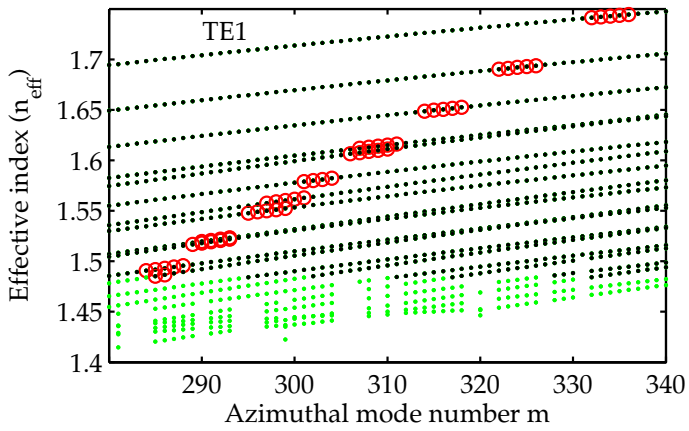

Figure 14: The effective index of the resonant modes of a 20-μm-radius microdisk cavity vs. the azimuthal mode number (m). The green parts each band is the range in which the solutions of the Helmholtz equation lie above the substrate light-line and can leak into the substrate. The round markers show the modes that fall in the operation range of the tunable laser.

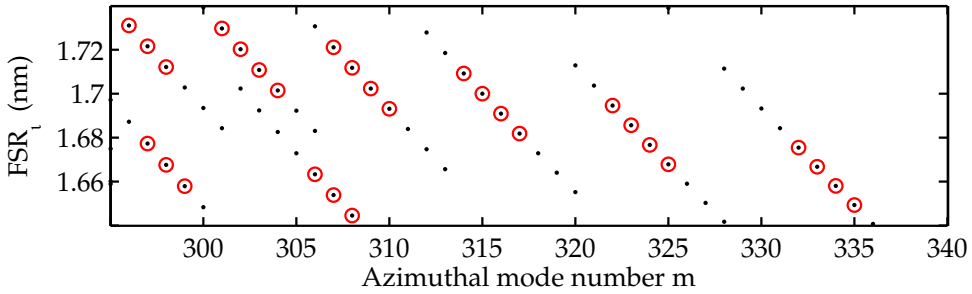

Figure 15: The FSR of the resonant modes of a 20-μm-radius microdisk cavity vs. the azimuthal mode number (m). The round markers show the modes which fall in the operation range of the tunable laser.

FSR becomes larger. Interestingly, TM_1 has the smallest FSR. Remembering that FSR$\propto 1/n_g$ and $n_g = \frac{\partial n_{eff}}{\partial \omega}\omega + n_{eff}$, it is clear that although the TM_1 mode has a smaller n_{eff} compared to the fist three TE modes, its larger dispersion $n_g = \partial n_{eff}/\partial\omega$ leads to a larger group index and a smaller FSR.

2.2 Analysis of Waveguide-Resonator Coupling

In this section the coupling of passive resonators to the light sources is investigated. In the integrated scheme, light is generated in a laser either on chip (often by iii-v chips bonded on top of the passive Si-based optics) or off chip (coupled to the chip by end-coupling, grating coupling or tapered fibers). The light traveling in the optical waveguide is then coupled into the traveling wave resonators (TWRs) such as microrings, microdisks or racetracks.

In a WG–TWR coupling, the waveguide is either vertically seated on top of the resonator, or it is laterally side coupled to the resonator. In the vertical coupling approach, there is minimal lithography challenge to define the spacing between the resonator and the waveguide. Whereas,challenges such as complicated fabrication with multiple steps and planarization requirements exist. On the other hand, the laterally side-coupled approach has the advantage of fewer fabrication steps while suffering from the lithography challenges associated with the fine-line spacing between the resonator and the waveguide. However, recent advances in nano-lithography, especially electron-beam lithography, have alleviated this problem.

In a WG–TWR coupling architecture, the strength of the coupling is determined predominantly by three conditions: 1) the modal field overlap of the resonator and the waveguide in the waveguide core, which acts as a perturbation to the resonator, 2) the interaction length between the resonator and the waveguide, and 3) the level of phase matching between the resonator mode and the waveguide mode.

2.2.1 Time-Domain Analysis of Waveguide-Resonator Coupling

The temporal response of an isolated resonator with a lifetime τ_o can be written as

$$\frac{\partial a}{\partial t} = (j\omega_o - 1/\tau_o)a, \tag{49}$$

where a is normalized such that its squared magnitude corresponds to the resonator energy. The $j\omega_o$ term shows the harmonic oscillation of the resonator mode and the

$1/\tau_o$ represents the loss of energy. From Eq. (49) it can be shown that the resonator energy varies as

$$\frac{\mathrm{d}|a|^2}{\mathrm{d}t} = \frac{-2}{\tau_o}|a|^2. \tag{50}$$

Figure 16 shows the structure of a TWR side coupled to a straight waveguide. A waveguide source mode with an amplitude S_{in} is traveling in the forward direction (from the left to the right). S_{in} is normalized such that its squared magnitude corresponds to the power of this mode. The resonator supports two degenerate clockwise (CW) and counterclockwise (CCW) traveling modes at the resonance frequency ω_o. The forward mode of the waveguide can couple to the CW mode of the resonator. The degenerate CW and CCW modes of the resonator are orthogonal to each other and do not interchange energy unless there is considerable perturbation in the resonator (such as roughness at the sidewall of the resonator). Assuming no CW-CCW coupling and no reflected power ($S_{ref} = 0$), the time-domain coupling of the forward mode of the waveguide and the CW mode of the resonator can be presented (in the 1st order approximation [102]) as

$$\begin{cases} \partial/\partial t(a_{cw}) = (j\omega_o - 1/\tau_o - 1/\tau_c)a_{cw} + \kappa S_{in}, \\ S_{out} = S_{in} - \kappa^* a_{sw}, \\ |\kappa| = \sqrt{2/\tau_c}. \end{cases} \tag{51}$$

In Eq. (51), a_{cw} is the amplitude of the CW mode of the resonator, κ is the coupling coefficient between the forward mode of the waveguide and the CW mode of the resonator, S_{out} is the waveguide-mode amplitude in the forward direction after the interaction with the resonator, and τ_c is the time constant of the rate of the energy coupling from the cavity CW mode to the waveguide mode.

By solving Eq. (51) in the frequency domain, the resonator CW amplitude and the waveguide transmission (which is $T = S_{out}/S_{in}$) can be obtained as

$$a_{cw}(\omega) = \frac{\kappa}{j(\omega - \omega_o) + 1/\tau_o + 1/\tau_c} S_{in}(\omega), \tag{52}$$

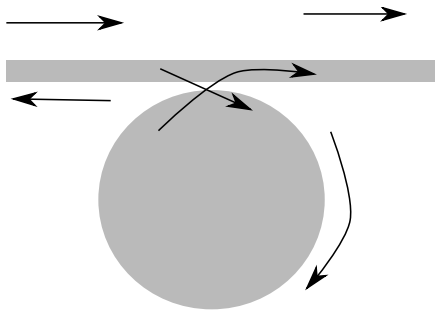

Figure 16: The configuration of the side-coupling scheme. S_{in} is the input power which couples into the clockwise (CW) mode of the cavity (a_{cw}). Interaction of S_{in} and a_{cw} results in the output waveguide amplitude S_{out}. If there is considerable perturbation in the resonator, the counterclockwise (CCW) mode of the resonator can be excited as a result of coupling to the CW mode. The generated CCW mode can couple to the backward waveguide mode and generate a reflection in the waveguide, as shown by S_{ref}. When there is no CW-CCW coupling, S_{ref} is almost zero.

$$T(\omega) = \frac{S_{out}}{S_{in}} = \frac{j(\omega-\omega_o) + 1/\tau_o - 1/\tau_c}{j(\omega-\omega_o) + 1/\tau_o + 1/\tau_c}. \tag{53}$$

Similar to the intrinsic quality factor of the resonator, which is $Q_o \equiv \omega_o \tau_o/2$, a quality factor for the waveguide-resonator coupling can be defined as

$$Q_c = \frac{\text{Resonator Energy}}{\text{Power Coupled to the Waveguide}} \tag{54}$$

$$= \omega_o \tau_c/2. \tag{55}$$

Therefore, the transmission function can be rewritten as

$$T(\omega) = \frac{j(\omega-\omega_o)/\omega_o + 1/Q_o - 1/Q_c}{j(\omega-\omega_o)/\omega_o + 1/Q_o + 1/Q_c}. \tag{56}$$

The full-width half-maximum (FWHM) of the transmission (i.e., Eq. (56)) can be simply obtained as $\delta\omega_{\text{loaded}} = \omega_o/Q_{\text{loaded}}$ in which the loaded quality factor (Q_{loaded}) can be defined as

$$\frac{1}{Q_{\text{loaded}}} \equiv \frac{1}{Q_o} + \frac{1}{Q_c}. \tag{57}$$

Therefore, the amplitude of transmission at resonance ($\omega = \omega_o$) can be obtained from Eq. (56) as

$$T(\omega_o)^2 = \left| \frac{1/Q_o - 1/Q_c}{1/Q_o + 1/Q_c} \right|^2 = \left| 1 - 2\frac{Q_{\text{loaded}}}{Q_o} \right|^2. \tag{58}$$

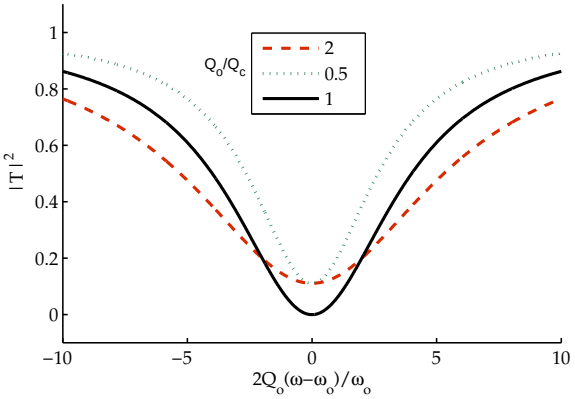

(a) Amplitude of power transmission $|T|^2$

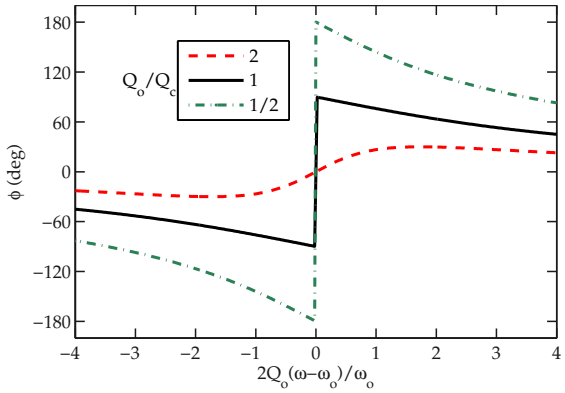

(b) Phase of transmission $\phi = \text{phase}(T)$

Figure 17: (a) The amplitude of the transmission function ($T(\omega)$) for three different ratios of Q_o/Q_c. If $Q_c = Q_o$ (i.e., critical coupling), $T(\omega_o)$ reaches zero. In the case of over-coupling ($Q_o > Q_c$) the linewidth is broadened. (b) The phase of the transmission function.

There are three regimes in which the WG-cavity coupled structure operates: (1) critical coupling, in which the coupling quality factor (Q_c) matches the intrinsic cavity quality factor (Q_o); (2) over-coupling, for which the coupling is stronger than critical coupling $Q_c < Q_o$; (3) under-coupling, in which the coupling is weak. The amplitude and phase of these case are depicted in Fig. 17. In the critical coupling case, all of the power is transferred from the cavity to the resonator. In the over-coupling situation, the power is coupled back to the resonator. In the extreme case (i.e., $Q_c \ll Q_o$), the transmission is almost constant and equal to unity while the phase of transmission changes linearly with ω. Such a structure is then an all-pass filter.

For many nonlinear and sensing applications the intensity of light inside the cavity is of utmost importance. The highest intensity is achieved when all of the power is transferred from the waveguide to the cavity and the photon life-time inside the cavity is long. Therefore, for high intensity, critical coupling to a high finesse cavity is desirable. As seen in Eq. (39) the enhancement factor depends on the travel time of a wave packet (T) compared to the photon leakage lifetime ($1/\tau = 1/\tau_o + 1/\tau_c$). Knowing that the power circulating the cavity can be written as $P_{cir} = |a_{cw}|^2/T$, and using Eq. (52):

$$\text{(at resonance)} \qquad \frac{P_{cir}}{|S_{in}|^2} = \frac{a_{cw}^2/T}{|S_{in}|^2} \tag{59}$$

$$= \frac{\kappa^2}{(1/\tau_c + 1/\tau_o)^2}\, 1/T \tag{60}$$

$$= \kappa^2 \tau^2 / T \tag{61}$$

$$= \frac{2\tau}{\tau_c}\, \tau/T \tag{62}$$

$$= 2\frac{Q_{\text{loaded}}}{Q_c} \tau/T \tag{63}$$

$$= 2/\pi\, \frac{Q_{\text{loaded}}}{Q_c}\, \mathcal{F} \tag{64}$$

$$= \frac{1/Q_c}{1/Q_c + 1/Q_o}\, (2/\pi)\mathcal{F}\,. \tag{65}$$

The first term in Eq. (65) represents the percentage of power initially dropped to the cavity, and the second term shows the enhancement inside the cavity. At critical coupling:

$$\frac{P_{cir}}{|S_{in}|^2} = (1/\pi)\mathcal{F}, \tag{66}$$

which can be written as

$$\frac{P_{cir}}{|S_{in}|^2} = (1/\pi)\frac{\Delta\omega}{\delta\omega}. \tag{67}$$

Therefore, in a typical microdisk with $\text{FSR}_\lambda = 2$ nm and a *loaded* linewidth of $\delta\omega =$ 1 pm, the circulating power inside the cavity can be 637 times stronger than the waveguide power.

2.2.2 Calculation of the Coupling factor

As shown above, the operation of the WG-cavity structure depends on the ratio of the coupling quality factor (Q_c) to the intrinsic microdisk quality factor (Q_o). Therefore, knowledge of Q_c is important in the device design and fabrication. Using the first order perturbation theory [102] the coupling coefficient κ can be written as

$$\kappa = \frac{j\omega\epsilon_o}{4}\int_{wg}(\Delta n)^2\tilde{\mathbf{E}}^*_{disk}\cdot\tilde{\mathbf{E}}_{wg}\,\mathrm{d}V, \tag{68}$$

in which the resonator field is normalized to $\sqrt{Energy_{disk}}$ and the waveguide field is normalized to $\sqrt{Power_{wg}}$. The integration is performed over the waveguide volume where $\Delta n = n_{wg} - n_{background}$ is nonzero. Assuming that the disk has a azimuthal order m, and the waveguide has a propagation constant β, the above integral can be rewritten as

$$\kappa = \frac{j\omega\epsilon_o}{4}\int_{wg}(\Delta n)^2\mathbf{E}_{disk}e^{jm\phi}\cdot\mathbf{E}_{wg}e^{-j\beta l}\,\mathrm{d}V, \tag{69}$$

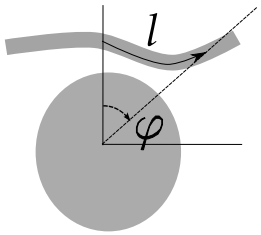

Figure 18: The parameters l and ϕ as used in the calculation of κ.

This integration can be performed in a coordinate system appropriate for the shape of the waveguide. In the sections 4 and 5, the coupling for two cases of a straight waveguide and a circular waveguide are investigated.

2.3 Analysis of the Material Dispersion

To have a good estimate about the behavior of the device in different wavelengths, it is necessary to start with the general trend of the material index and loss. The general relation between the displacement vector (D) and the electric field (E) for

any material (with intrinsic delay in response) is

$$\mathbf{D} = \int_0^{+\infty} \mathrm{d}\tau\, \epsilon(\tau)\, \mathbf{E}, \tag{70}$$

in which τ is a response delay and $\epsilon(\tau < 0) = 0$. The Fourier transform of $\epsilon(t)$ is generally complex and is customary written as $\epsilon(\omega) = \epsilon_o[\epsilon_1(\omega) + j\epsilon_2(\omega)]$ in which ϵ_1 and ϵ_2 are real and $\epsilon(-\omega) = \epsilon^*(-\omega)$. Therefore, $\epsilon_2(\omega)$ is an odd function of the frequency while $\epsilon_1(\omega)$ is even. The causality of $\epsilon(\tau)$ requires the analyticity of $\epsilon(\omega)$ in the upper half side of the complex ω plane [103]. This in turn leads to the Kramers-Kronig relations between the real and imaginary parts of the dielectric function $\epsilon(\omega)$ [104]:

$$\epsilon_1(\omega) = \frac{2}{\pi}\mathscr{P}\int_0^{\infty} \frac{\Omega\epsilon_2(\Omega)}{\Omega^2-\omega^2}\,\mathrm{d}\Omega + 1 \tag{71}$$

$$\epsilon_2(\omega) = \frac{2}{\pi}\mathscr{P}\int_0^{\infty} \frac{\omega[\epsilon_1(\Omega)-1]}{\Omega^2-\omega^2}\,\mathrm{d}\Omega\,, \tag{72}$$

in which the integrals are Cauchy principle values [105]. As the integral in Eq. (72) is generally nonzero, any material with a dielectric function larger than one is essentially lossy in nature. Suppose the frequency ω lies in the linear vicinity of a sharp absorption line centered at frequency ω_o. We assume this line is well separated from other absorption lines as illustrated in Fig. 19. The material may have low-frequency absorption features which lie below ω_m and high frequency structures which lie above ω_M. Provided that ω lies outside the narrow absorption bad around ω_o, to very good approximation, $\epsilon_1(\omega)$ is given by

$$\epsilon_1(\omega) = 1 + \frac{2}{\pi}\left[\int_{\omega_M}^{\infty} \frac{\Omega\epsilon_2(\Omega)}{\Omega^2-\omega^2}\,\mathrm{d}\Omega + \frac{1}{\omega_o^2-\omega^2}\int_{\omega_o} \Omega\epsilon_2(\Omega)\,\mathrm{d}\Omega + \int_0^{\omega_m} \frac{\Omega\epsilon_2(\Omega)}{\Omega^2-\omega^2}\,\mathrm{d}\Omega\right], \tag{73}$$

in which the second integral ranges over only the absorption line at ω_o. If ω lies near ω_o, and $\omega_o \ll \omega_M$, thebn ω may be set to zero in the first term of (73). furthermore, if $\omega_m \ll \omega_o$, the last term can be set to zero for a nonconducting material. We then define

$$\epsilon_\infty = 1 + \frac{2}{\pi}\int_{\omega_M}^{\infty} \frac{\epsilon_2(\Omega)}{\Omega}\,\mathrm{d}\Omega, \tag{74}$$

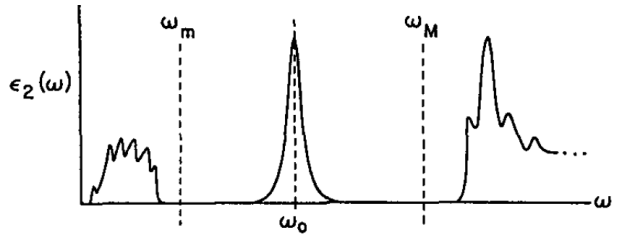

Figure 19: Absorption spectrum of a material with a sharp absorption line at frequency ω_o, separated from low frequency absorptions which lie below ω_m, and also well separated from high frequency absorption bands which lie above ω_M [106].

and

$$\Omega_p^2 = \frac{2}{\pi}\int_{\omega_o} \Omega\epsilon_2(\Omega)\,\mathrm{d}\Omega, \tag{75}$$

to find

$$\epsilon_1(\omega) = \epsilon_\infty + \frac{\Omega_p^2}{\omega_o^2 - \omega^2}\,. \tag{76}$$

The presence of an absorption line in any physical medium thus introduces dramatic structure in the frequency variation of the dielectric constant. The high frequency transitions, well above ω_o, give a frequency independent "background dielectric" constant ϵ_∞, and the presence of the line itself leads to the resonant term.

The expression in (76) applies for frequencies ω which lie close to a sharp absorption line, but still outside the absorption profile of the line. To find the behavior of $\epsilon_2(\omega)$ as one tunes the frequency ω through the line, we need the explicit form of $\epsilon_2(\omega)$. Many theories produce Lorentzian profiles for the line shape. With the assumption the line profile is Lorentzian, the Kramers–Kronig integral may be evaluated in closed form, and a complete (but now model dependent) expression for $\epsilon_1(\omega)$ follows: For example, suppose in the vicinity of the absorption line centered at ω_o, $\epsilon_2(\omega)$ is given by

$$\epsilon_2(\omega) = \frac{\Omega_p^2}{2\omega_o}\left(\frac{\gamma/2}{(\omega-\omega_o)^2 + (\gamma/2)^2} - \frac{\gamma/2}{(\omega+\omega_o)^2 + (\gamma/2)^2}\right) \tag{77}$$

where γ is the full width of the absorption line at half maximum, and Ω_p^2 serves s a measure of its integrated strength. We recall, in writing down (77) , that $\epsilon_2(\omega)$ is an

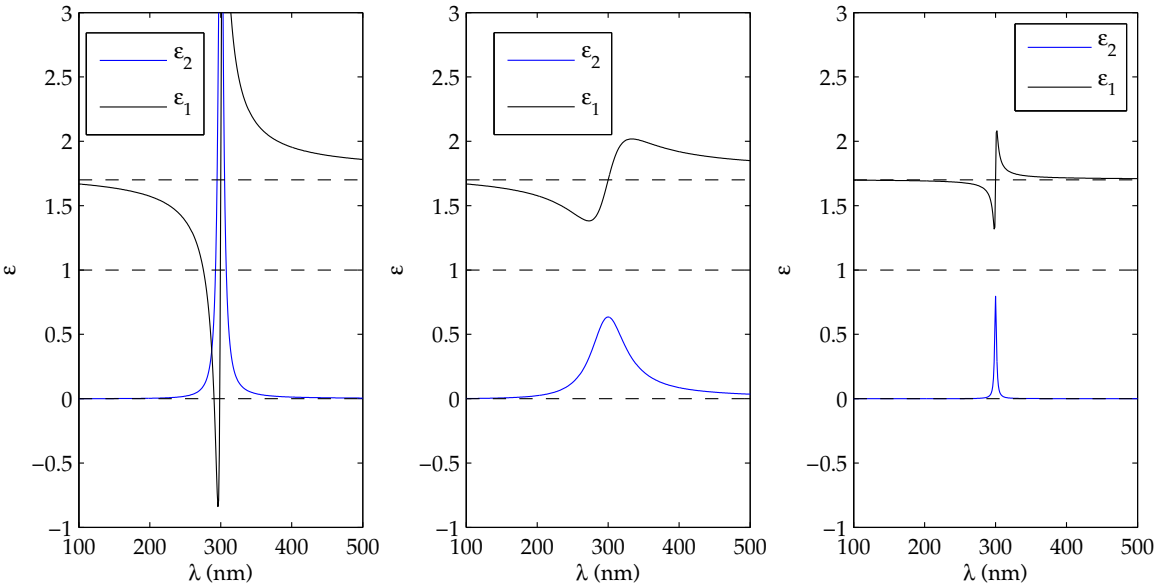

Figure 20: The real and imaginary parts of the dielectric function for a typical dielectric near one resonant absorption feature. If the line width of the absorption is narrow, $\epsilon_1(\omega)$ can become negative at wavelengths slightly shorter than the transition wavelength. **(left)** A material with a strong narrow band absorption. ϵ_1 goes becomes negative at frequencies above the absorption band and also becomes larger than ϵ_∞ for a large wavelength range in the visible range of the spectrum. **(center)** A material with a wide band strong absorption. **(right)** A material with a narrow but weak absorption band. ϵ_1 goes back to ϵ_∞ quickly.

odd function of frequency. If we absorb the influence of high frequency transitions in a "background" dielectric constant ϵ_∞, then the combination of (77) with (71) gives

$$\epsilon_1(\omega) = \frac{\Omega_p^2}{2\omega_o}\left(\frac{\omega_o^2-\omega^2-(\gamma/2)^2}{[(\omega-\omega_o)^2+(\gamma/2)^2]\,[(\omega+\omega_o)^2+(\gamma/2)^2]}\right) \tag{78}$$

which agrees in form with (75), if $|\omega-\omega_o|$ is large compared to the linewidth γ. If the line is very narrow, then for frequencies near ω_o, ϵ_1 is well approximated by

$$\epsilon_1(\omega) \approx \epsilon_\infty + \frac{\Omega_p^2}{2\omega_o}\frac{\omega_o-\omega}{(\omega_o-\omega)^2+(\gamma/2)^2} \tag{79}$$

In Fig. 20, we give a sketch of the behavior of ϵ, near the resonance. Notice that above ω_o, ϵ_1 can become negative, if Ω_p^2, is sufficiently large, or the linewidth γ sufficiently small.

For a plane wave satisfying the wave equation $(\nabla^2+\mu\epsilon\omega^2)\mathbf{E}=0$ and traveling in a dispersive media, a possible solution (traveling in the x direction) is $e^{i\omega t-ikx}$. In

this solution, the wave number k and the angular frequency ω are related by

$$k = \sqrt{\mu\epsilon}\,\omega. \tag{80}$$

Considering the the frequency dependence of the dielectric function as in Eq. (79), the dispersion equation of the material can be written as

$$\frac{c^2k^2}{\omega^2} = \epsilon_\infty + \frac{\Omega_p^2}{\omega_o^2 - \omega^2}\,. \tag{81}$$

and The *phase velocity* of the wave is

$$v_p = \frac{\omega}{k} = \frac{1}{\sqrt{\mu\epsilon}} = \frac{c}{n}\,, \qquad n = \sqrt{\frac{\mu}{\mu_o}\frac{\epsilon}{\epsilon_o}}\,, \tag{82}$$

in which the n is a function of frequency.

The phase velocity, $v_p(\omega) = \omega/k(\omega)$ now depends on frequency. Thus, the wave packet will spread as it propagates through the material and the "center of mas" of the wave packet propagates at the group velocity $v_g(\omega) = \partial\omega/\partial k$, which can differ greatly from the phase velocity. From (81), it is straightforward to find an explicit expression for ω as a function of k; this functional relationship is called often the dispersion relation of the wave in the medium. For each choice of wave vector, there are two frequencies allowed. There is thus an upper branch, and a lower branch to the dispersion relation:

$$\omega_\pm = \sqrt{\frac{1}{2}\left(\frac{c^2k^2}{\epsilon_\infty} + \omega_o^2 + \frac{\Omega_p^2}{\epsilon_\infty}\right) \pm \left[\left(\frac{c^2k^2}{\epsilon_\infty} + \omega_o^2 + \frac{\Omega_p^2}{\epsilon_\infty}\right)^2 - 4\omega_o^2\frac{c^2k^2}{\epsilon_\infty}.\right]^{1/2}} \tag{83}$$

The dispersion relations are plotted in Fig. 21; here $\epsilon_s = \epsilon_\infty + \Omega_p^2/\omega_o^2$ is the static dielectric constant of the model. In the frequency band between ω_o and $\omega_o\sqrt{\epsilon_s/\epsilon_\infty}$, ϵ_1 is negative, and electromagnetic waves cannot propagate in the medium and the wave vector is purely imaginary. On the lower branch, described by ω_-, the phase velocity is always less than $c/\sqrt{\epsilon_s}$ while on the upper branch described by ω, it is always greater than $c/\sqrt{\epsilon_\infty}$. Most particularly, as $k \to 0$, the phase velocity becomes

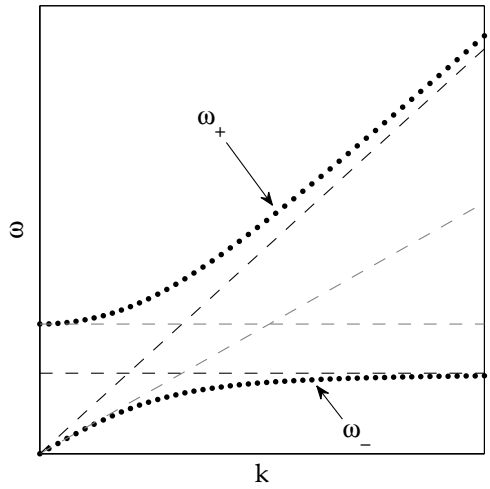

Figure 21: The dispersion relation for electromagnetic waves which propagate in a medium with a dispersion relation shown in (83).

infinite; there is a finite region of wave vector near $k = 0$ where $v_p(\omega)$ is greater than the vacuum velocity of light. The group velocity, $v_g(\omega)$, is always less than the velocity of light. Thus, an electromagnetic pulse, which transports energy

This information about the material dispersion will be useful in the next section when the dispersion of the guiding structures is investigated. The materials used the most throughout this thesis are Si_3N_4, SiO_2, Su-8 and TiO_2, all of which are transparent in the visible range of the spectrum.

The optical parameters of a material can be extrapolated from the experimental data achieved by ellipsometry. Upon the analysis of the change of polarization of light, which is reflected off a sample, ellipsometry can yield information about layers that are thinner than the wavelength of the probing light itself. Ellipsometry can probe the complex refractive index or dielectric function tensor. After the experimental data points are extracted (range of which depend mainly on the spectral range of the source and detector in the ellipsometer) some empirical formulae can be used to extend the range of dielectric function beyond the measurement points. The most famous forms of this extrapolation are Cauchy and Sellmeier equations.

Cauchy's equation is an empirical relationship between the refractive index and wavelength of light for a particular transparent material. It is named for the mathematician Augustin Louis Cauchy, who defined it in 1836. The most general form of Cauchy's equation is

$$n(\lambda) = A + \frac{B}{\lambda^2} + \frac{C}{\lambda^4} + \cdots, \tag{84}$$

where n is the refractive index, λ is the wavelength, A, B, C, etc., are coefficients that can be determined for a material by fitting the equation to measured refractive indices at known wavelengths. The coefficients are usually quoted for *lambda* as the vacuum wavelength in micrometers. The theory of light-matter interaction on which Cauchy based this equation was later found to be incorrect. In particular, the equation is only valid for regions of normal dispersion in the visible wavelength region. In the infrared, the equation becomes inaccurate, and it cannot represent regions of anomalous dispersion. Despite this, its mathematical simplicity makes it useful in some applications [107]. The Sellmeier equation—first proposed in 1871 by W. Sellmeier—is a later development of Cauchy's work that handles anomalously dispersive regions, and more accurately models a material's refractive index across the ultraviolet, visible, and infrared spectrum. The usual form of the equation for glasses is

$$n^2(\lambda) = 1 + \frac{B_1\lambda^2}{\lambda^2 - C_1} + \frac{B_2\lambda^2}{\lambda^2 - C_2} + \frac{B_3\lambda^2}{\lambda^2 - C_3}, \tag{85}$$

which is obtainable from (81) by substituting ω for $2\pi c/\lambda$ and assuming several resonant absorptions for the material. For silicon nitride The Sellmeier model predicts two main absorption lines at 132 and 273 nm wavelengths.

2.3.1 Significance of Visible Wavelengths for Water Ambient Sensors

The attenuation of the plane wave is expressed in terms of the real and imaginary parts of the wave number k. if the wave number is written as

$$k = \beta + i\frac{\alpha}{2} \tag{86}$$

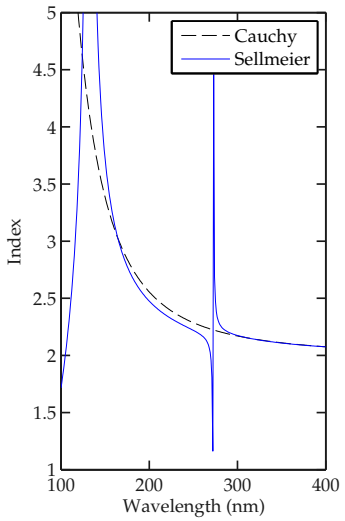

(a) Comparison of Cauchy and Sellmeier fits to the index of the silicon nitride. The Sellmeier model predicts two main absorption lines at 132 and 273 nm wavelengths.

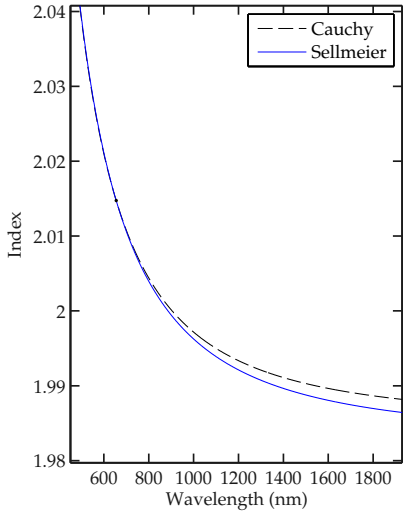

(b) Comparison of Cauchy and Sellmeier fits to the index of the silicon nitride. The Cauchy model is a good model for the visible range but becomes inaccurate at longer wavelengths.

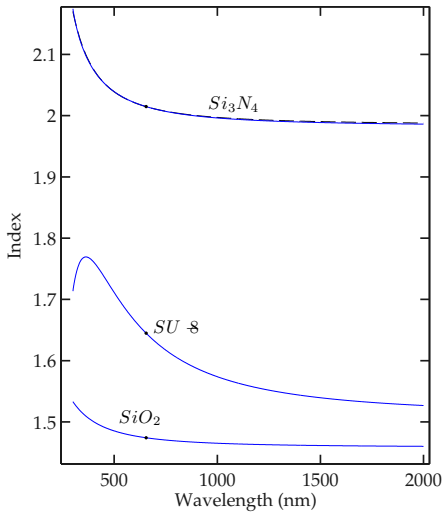

(c) The optical refractive index of materials used in this work for the visible and near infrared (NIR) range.

Figure 22:

Table 1: The index and Cauchy parameters for materials used in this thesis

Material	n@ 655 nm	A	B	C
SiN	2.0147	1.985	7.615e-3	1.872e-4
SiO2	1.4742	1.4585	4.3633e-3	0
Su-8	1.6449	1.51	0.0444	-0.00190
TiO2	2.2			

then the parameter α is known as the attenuation constant or absorption coefficient [108]. The *intensity* of the wave falls off as $e^{-\alpha x}$. Equation 80 yields the connection between (α, β) and (ϵ_1, ϵ_2):

$$\beta^2 - \frac{\alpha^2}{4} = \frac{\omega^2}{c^2}\epsilon_1 \tag{87}$$

$$\beta\alpha = \frac{\omega^2}{c^2}\epsilon_2. \tag{88}$$

If $\alpha \ll \beta$, as occurs unless the absorption is very strong or ϵ_1 is negative, the attenuation constant α can be written approximately as

$$\alpha = \frac{\epsilon_2(\omega)}{\epsilon_1(\omega)}\beta \tag{89}$$

where $\beta = \sqrt{\epsilon_1}\omega/c$. The fractional decrease in intensity per wavelength divided by 2π is thus given by the ration ϵ_2/ϵ_1 (Fig. 23).

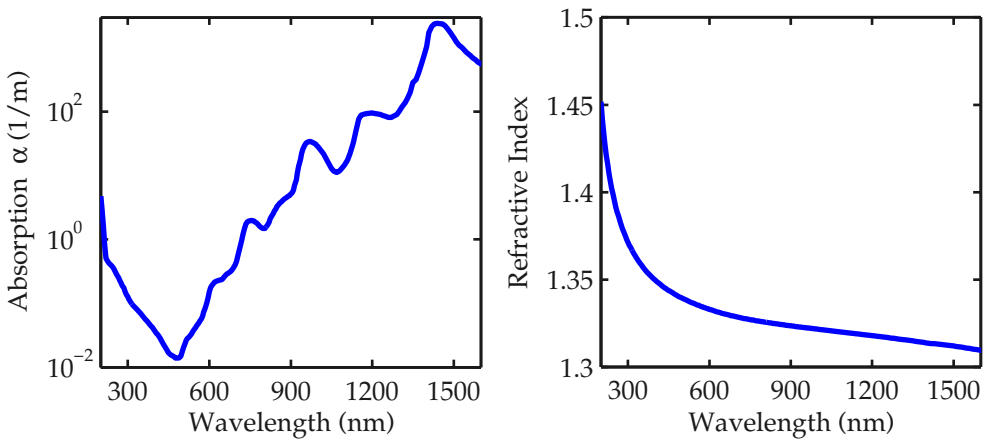

Figure 23: (left) The absorption spectrum of liquid water in the visible and infrared regions of the spectrum. The absorption coefficient in 1550 is $\alpha = 834$, and at 650 is 0.256 [109]. Therefore, water is more than 3000 times more absorptive in the communication wavelength than in the visible. (right) The refractive index of water in the visible and IR [109].

2.4 Analysis of the Waveguide

Now that the dispersion of the refractive bulk materials is obtained for a wide range of frequencies, we can obtain the effective index and group velocity of light inside channel waveguides. For this purpose, the Maxwell equations are solved with finite element method using Comsol$^{\text{ő}}$ to obtain the effective index of the waveguide

$$n_{eff} = \beta c/\omega.$$

Also, taking a derivative from $\beta = n_{eff}\omega/c$ in regard to ω, one can derive

$$\frac{\partial \beta}{\partial \omega} = \frac{1}{c}\left(\frac{\partial n_{eff}}{\partial \omega}\omega + n_{eff}\right), \tag{90}$$

which leads to

$$\frac{c}{v_g} = \left(\frac{\partial n_{eff}}{\partial \omega}\omega + n_{eff}\right), \tag{91}$$

which shows the group index can easily be obtained this way. As the width of the waveguide is increased, higher order mode are supported by the waveguide. For example Fig. 2.4 shows a waveguide that can support 3 transverse electric (TE) modes when the width of the waveguide is 800 nm.

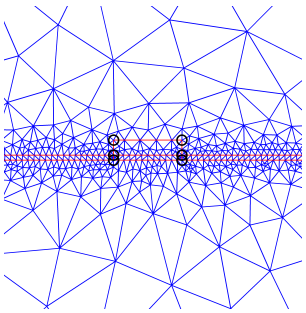

(a) The mesh used for the FEM analysis

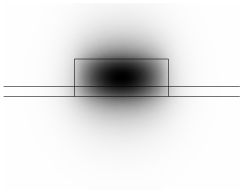

(b) H_z of TE_1

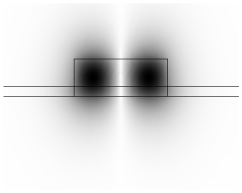

(c) H_z of TE_2

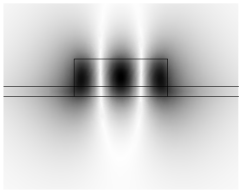

(d) H_z of TE_3

Figure 24: The mesh (a) and the magnetics fields (b-c) of TE waveguide modes with the waveguide withs set to 800 nm and the height of the silicon nitride layer is 200 nm. The index of the pedestal layer in this simulation is set two one, i.e. the silicon nitride layer is etched all the way.

In order to find the single mode operation region of the waveguide, the wavelength of the simulation can be set to 656 nm (middle of the sweeping range of the laser introduced in later chapters) and the width of the waveguide can be swept across a wide range. This simulation is done with the cladding set to air (25(c)), cladding set to oxide (25(b)), and with a 50 nm rib-waveguide pedestal (25(c)). As seen from the Fig. 25(a) the air-clad waveguide becomes multi-mode around W=580nm. Thus in the design of waveguide based structures in the next chapters, the widths of the single mode waveguides is kept less than 580 nm. This information will be particularly useful in section 5 where the phase matching of traveling wave modes depends on the effective index, hence the width of the waveguide.

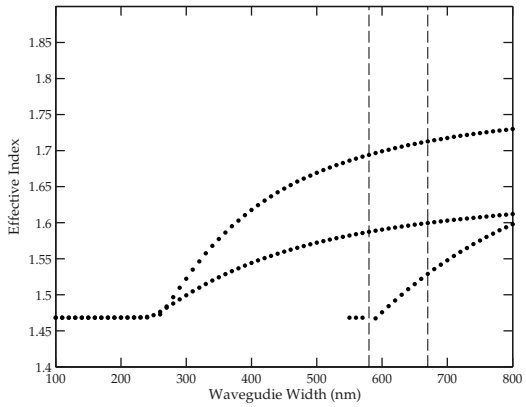

(a) Air cladding, no pedestal

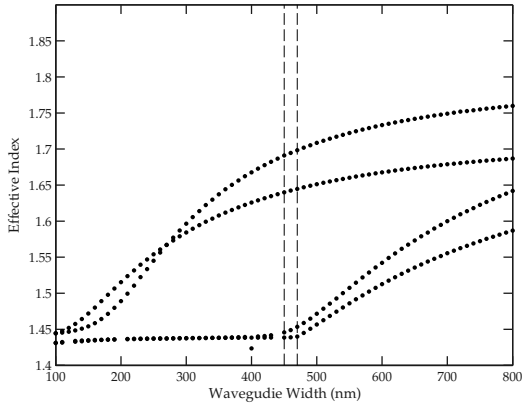

(b) Oxide cladding, no pedestal

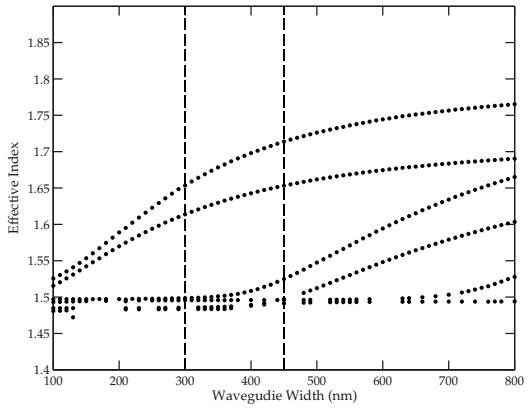

(c) Air cladding, 50 nm pedestal

Figure 25: Effective index of the waveguide with (a) the cladding set to air, (b) cladding set to oxide, and (c) with a 50 nm rib-waveguide pedestal. As seen from the (a) the air-clad waveguide becomes multi-mode around W=580nm.

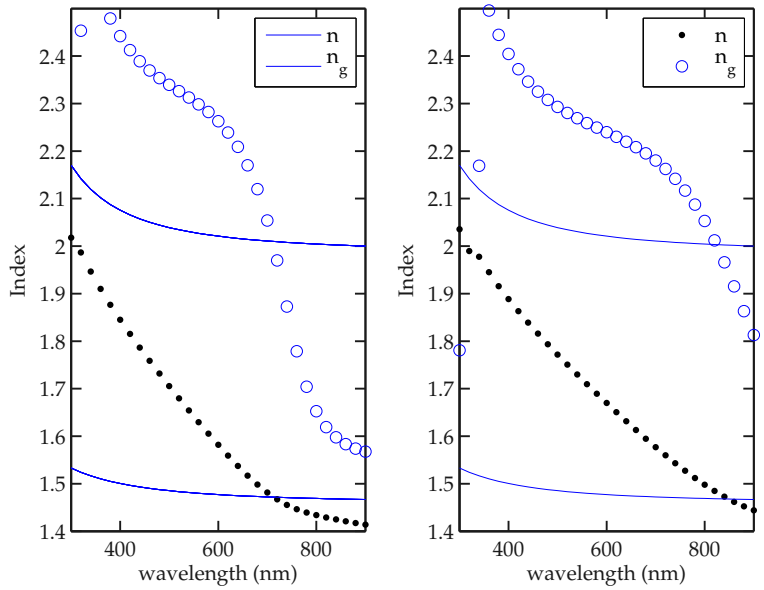

(a) W=300 nm (b) W=400 nm

(c) W=500 nm (d) W=600 nm

Figure 26: The effective index (n) and group index (n_g) of the first TE modes of different waveguides. The material dispersion (which is more dominant in shorter wavelengths) is taken into the account and effects the (n_g) significantly.

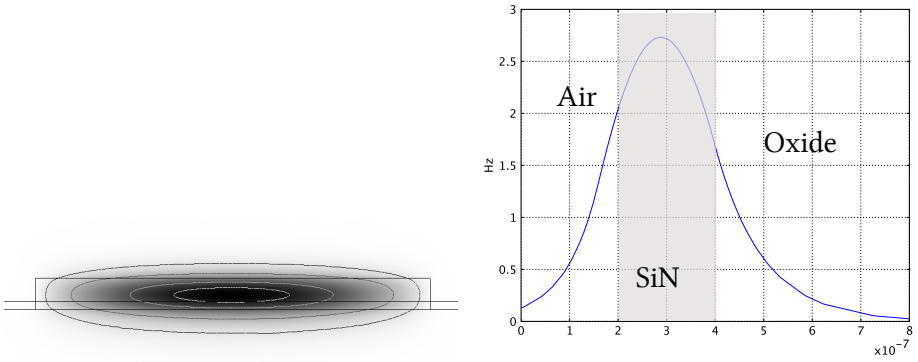

(a) (b)

Figure 27: (a) A wide waveguide simulated with Comsol. The effective index of the waveguide is close to the effective index of a slab of silicon nitride on top of an oxide substrate. ($n_{slab} = 1.8186$). (b) The distribution of the H_z component in the vertical direction

In the simulations in Fig. 2.4 the wavelength is kept constant at 656 nm. in order to find the dispersion of the waveguide mode, we can set the widths of the waveguide and observe the change in its effective index and group index. The group index shows its importance in 8.

We might also need to use the effective index of the waveguide for fast 2D simulations. For this end, a wide, multimode waveguide can be simulated and the effective index of the fundamental mode is close to the effective index of the slab. The effective index of the wide waveguide depicted in

CHAPTER III

FABRICATION

One of the major reasons of interest in integrated photonics with microdisks/microrings and one and two dimensional (1D,2D) photonic crystal based devices, is the ease of fabrication using mature semiconductor fabrication techniques.

In this chapter the fabrication process for SiN, Si, and iii-v based structures is describes. Nevertheless, the main focus has been on silicon nitride structures for visible applications.

All the fabrication in this research was performed at Nanotechnology Research Center (NRC) Georgia Institute of Technology.

3.1 Silicon Nitride Fabrication

In this section the procedure for fabrication of SiN structures is detailed.

3.1.1 Wafer specifications and Preparation

The first step of fabrication is to grow thick isolating oxides on prime silicon wafers. As the dry oxidation rate is very low, the majority of the oxidation process is done in a hydrogen rich environment (wet oxidation). The temperature during the oxidation is limited to 1100°C. Using an online oxidation calculator the required time for the production of 3μm oxide is 32 hours. During this process 1.76μm of the silicon is consumed.

The light guiding SiN layer can be deposited by either plasma enhanced chemical vapor deposition (PECVD) or low pressure chemical vapor deposition (LPCVD). The films deposited by LPCVD are of higher quality than the PECVD films [110, 111]. While PECVD SiN is etched approximately twice as fast by the inductively

coupled plasma (ICP) reactive ion etching (RIE) dry etch as the LPCVD material, somewhat reducing the difficulty of the fabrication, the much higher impurity density (primarily hydrogen) and higher optical absorption makes it inappropriate for high quality devices [111]. Nevertheless, the first devices fabricated were made in a PECVD chamber at the MiRC and demonstrated a moderate quality factor ($Q < 10^5$).

The first LPCVD grown films were deposited in a Tystar nitride furnace at MiRC. The gases used in this process are dichlorosilane (DCS) and ammonia and the process is run at 700-850°C.

$$3\,SiH_2Cl_2 + 4\,NH_3 \rightarrow Si_3N_4 + 6\,HCl + 6\,H_2$$

Unfortunately, this specific tube is also used to deposit high temperature (900°C) oxide (HTO) films: At higher temperatures (900 °C), oxide can be created in the so called HTO process (high temperature oxide), but also by a combination of dichlorosilane (SiH_2Cl_2) and N_2O:

$$SiH_2Cl_2 + 2\,N2O \rightarrow SiO2 + \mathrm{decompositionproducts}$$

. The use of the same tube for these processes, while reducing cleanroom expenses, leads to significant cross contaminations and renders the MiRC LPCVD tube unusable for photonic applications (Fig. 28).

Therefor the deposition of the SiN layer is done at LioniX Inc. To have a qualitative assessment of the transparency of the film, a 633 nm laser beam is prism coupled to the wafer and the propagation across the wafer is monitored (Fig. 29).

Having obtained the wafers, the fabrication process can be roughly broken down into following steps.

1. CAD file preparation.
2. Lithography and patterning definition.
3. Etching.

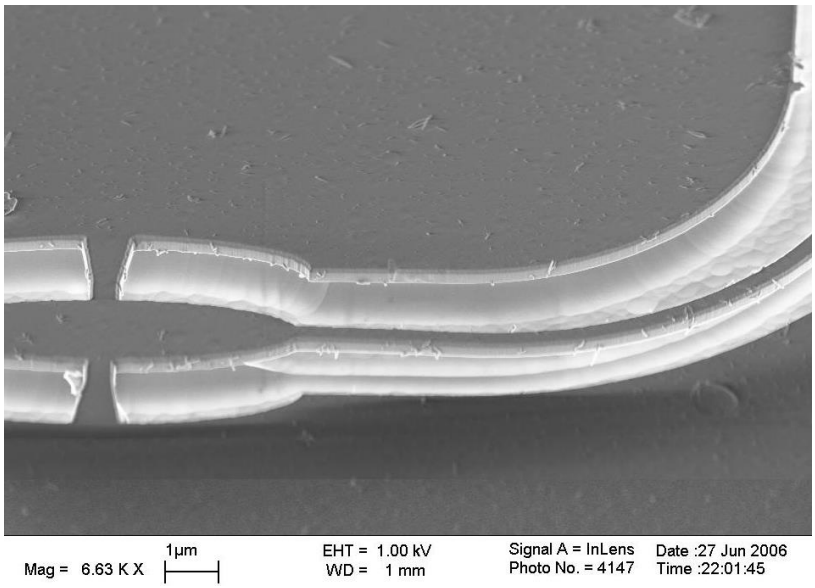

Figure 28: Cross contamination resulting HTO and SiN deposited in the same LPCVD chamber.

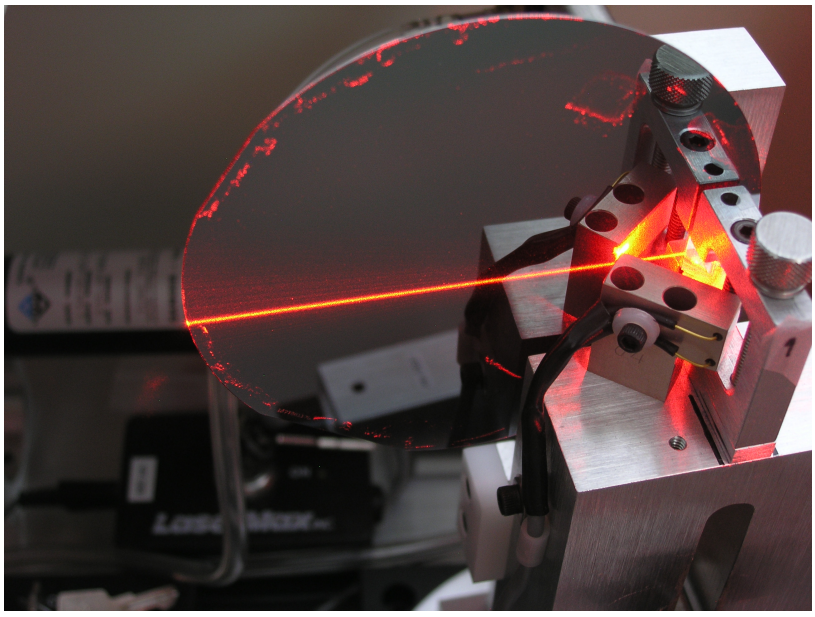

Figure 29: Prism coupling of the visible light across the LPCVD deposited wafer.

4. optional Undercutting.

5. Imaging.

3.1.2 CAD File Preparation

The first step in fabricating any device is computer-aided design (CAD) file preparation. CAD stands for computer aided drawing. Different softwares can be used for this purpose. The most widely used software is AutoCAD provided by Autodesk Inc. This software is available from Georgia Tech and is also installed on various machines in NRC. The disadvantage of the Autocad is that is is only installable on Microsoft windows computers. An alternative, which works with UNIX machines (although slower in some aspects) is Bricscad. Another shortcoming of Autocad is it's inability to do boolean operations on different layers. A software initially used for this purpose was Cadence. Moreover Cadance, unlike Autocad, is capable of producing GDSII file outputs. With AutoCad you have to use another software (LinkCad, provided by Bay Technology) to convert it to gds format.

The CAD drawing of photonic elements, especially when complicated structures like AWGs, arbitrary shaped waveguides, and multiple series-parallel elements are involved, is almost impossible. Therefore, we finally opted for scripting the layouts with Matlab, feeding the Matlab text output into Autocad/Bricscad, and converting the .dxf file by GenISys' Layout Beamer. This particular software is capable of "healing" the layout if there is any overlap between the solids generated by Matlab and also partially correcting the proximity effects in electron beam lithography (see 3.1.3).

3.1.3 Lithography and Pattern Definition

The second step in fabrication is to use the CAD file to write pattern into a resist layer (see Fig. 30 (b) and (c)). Photolithography is the most widely used lithography method, which allows wafer scale patterning. The smallest feature sizes writable using

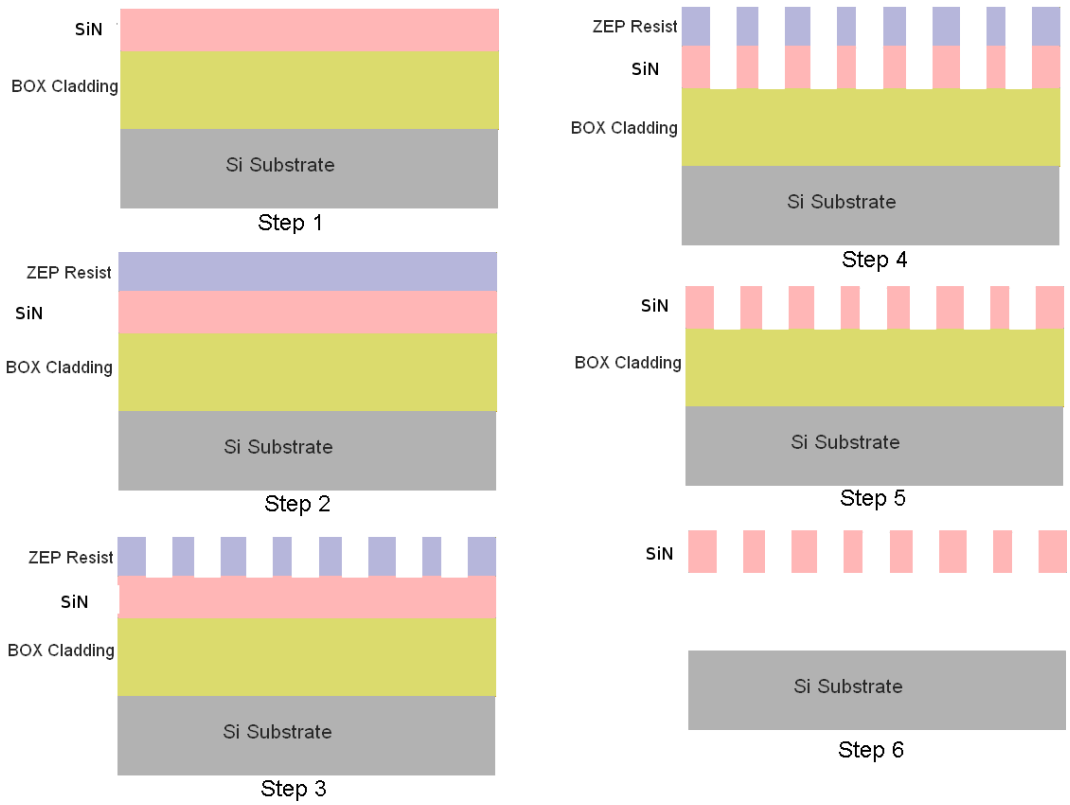

Figure 30: Fabrication process: (a). Start off with an SiN-on-BOX wafer. (b) Spin on e-beam resist. (c) Pattern the resist. (d) Etch into the guiding layer. (e) Remove the remaining resist after etching. (f) Optionally undercut the BOX layer underneath the guiding layer.

photolithography depends on the wavelength of light used to expose the pattern and the accuracy of the mask provided. However, since the critical dimensions used in this project are small ($\sim$100 nm), which are not resolvable by photolithography equipment available at NRC, we have used electron beam lithography (EBL).

An important issue in electron beam lithography (also sometimes encountered in photolithography with thick resists) is the proximity effect. The proximity effect in electron beam lithography (EBL) is the phenomenon that the exposure dose distribution, and hence the developed pattern, is wider than the scanned pattern, due to the interactions of the primary beam electrons with the resist and substrate. These cause the resist outside the scanned pattern to receive a non-zero dose. Important contributions to weak resist polymer chain scission (for positive resists) or cross-linking (for negative resists) come from electron forward scattering and backscattering. The forward scattering process is due to electron-electron interactions which deflect the primary electrons by a typically small angle, thus statistically broadening the beam in the resist (and further in the substrate). The majority of the electrons do not stop in the resist but penetrate the substrate. These electrons can still contribute to resist exposure by scattering back into the resist and causing subsequent exposing processes. This backscattering process originates from a collision with a heavy particle (i.e. substrate nucleus) and leads to wide angle scattering of the light electron from a range of depths ($\sim$ 30micrometres) in the substrate. The above effects can be approximated by a simple two-Gaussian model where a perfect point-like electron beam is broadened to a superposition of a Gaussian with a width α of a few nanometers to order 10's of nanometers—depending on the acceleration voltage—due to forward scattering and a Gaussian with a width β of the order of a few micrometers to order 10's due to backscattering, again depending on the acceleration voltage but also on the materials involved:

$$PSF(r) = \frac{1}{\pi(1+\eta)}\left[\frac{1}{\alpha^2}e^{-\frac{r^2}{\alpha^2}} + \frac{\eta}{\beta^2}e^{-\frac{r^2}{\beta^2}}\right]$$

Table 2: Proximity effect parameters for electron beam lithography

	Si	SOI	SiO2	GaAs	Ge	Au
α	0.0118	0.0118	0.0118	0.0118	0.0118	0.0118
β	33.3003	33.5357	31.7935	13.078	12.9845	2.3217
η	0.6137	0.6748	0.5248	1.0942	1.0621	1.159

, in which η is of order 1 so the contribution of backscattered electrons to the exposure is of the same order as the contribution of 'direct' forward scattered electrons. The above parameters are determined by the resist and substrate materials and the primary beam energy. The two-Gaussian model parameters, including the development process, can be determined experimentally or by a Monte Carlo simulation. A light substrate (light nuclei) will reduce backscattering. When electron beam lithography is performed on substrates with 'heavy' films, such as gold coatings, the backscatter effect will (depending on thickness) significantly increase. Increasing beam energy will reduce the forward scattering width, but since the beam penetrates the substrate more deeply, the backscatter width will increase. In our experiments the parameters α, β, and η are chosen to be 0.05, $\sim$30 and 0.08.

The EBL machine at NRC is a JBX-9300FS manufactured by Jeol ltd. The NRC nanolithography website provides process details for various e-beam resists. The choice of the resist depends on the shape of the patterns, accuracy needed, the time allocated to the pattern writing, and the selectivity. The thickness of the resist required is primarily determined by the dry etch selectivity the resist offer over the material you are trying to etch. The etch selectivity is defined as:

$$Selectivity = \frac{Etch\ rate\ of\ material\ to\ etch}{Etch\ rate\ of\ the\ resist\ (mask)} \tag{92}$$

Two types of positive resists; namely ZEP-520, manufactured by ZEON corporation, and different dilutions of PMMA (polymethyl methacrylate), provided by MicroChem; and two types of negative tone resists—to wit, MaN 2304 from Micro Resist Technology, and XR-1541 (icphydrogen silsequioxane, HSQ) provided by Dow

Corning—are most often used in this thesis. Each of the aforementioned has its own advantages.

3.1.3.1 ZEP resist

ZEP requires the lowest dosage and offers an acceptable selectivity (1/2) over SiN. On the other hand, achieving thick ZEP layers in a single spinning is not possible and is selectivity to Si in a chlorine plasma etching is very low. The spin speed curve for ZEP-520A is shown in Fig. 31. These resist thickness shown in the figure are for a 4" wafer. Since usually small pieces of SiN are used, typically 3 cm x 3 cm, the thickness obtained is around 1.2 times more than the values shown in the figure. After spin coating the sample is baked at 180°C for two minutes to allow the solvent to evaporate. A typical a dosage of $\sim 280 \mu C/cm^2$ is used. After e-beam writing, the samples are developed in Amyl acetate (pentyl acetate, $CH_3COO[CH_2]_4CH_3$) for 2 min and rinsing it with Isopropyl alcohol (IPA) after the development.

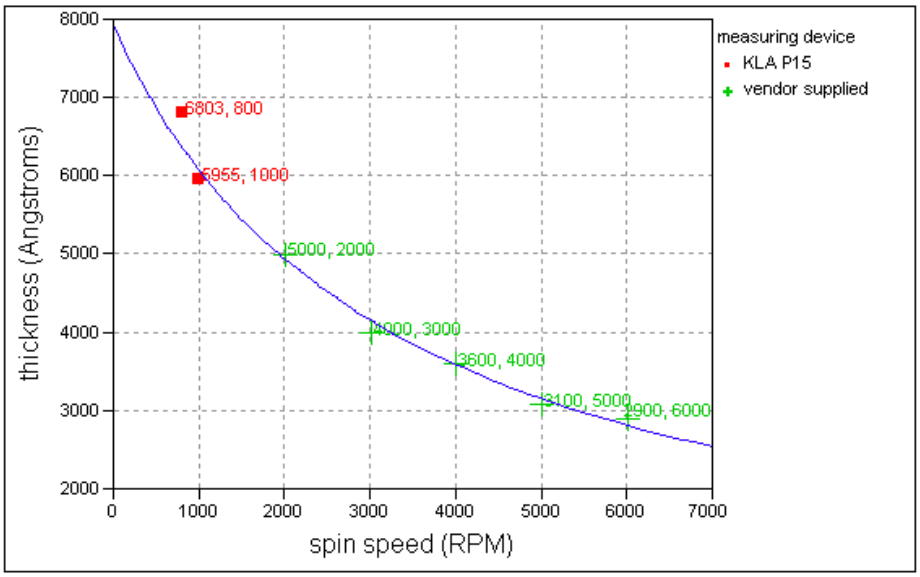

Figure 31: Spin speed curve for ZEP-520A resist on a 4" wafer. The green values are obtained from vendor and the red values are measured at NRC on KLA-15 profilometer.

3.1.3.2 Negative resists

Using negative resists, nevertheless, makes the pattern preparation significantly easier (shown in Fig. 32). On the other hand, if one chooses to use inverse tapers and 3D integration the writing time with the negative resist is much shorter (even considering the usually higher dosages required).

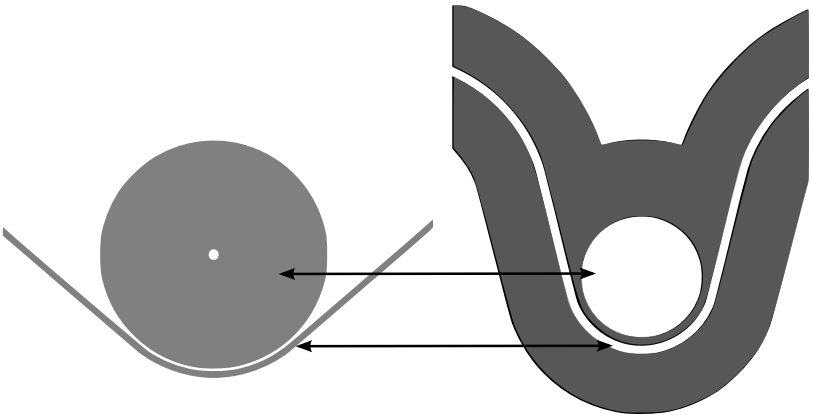

(a) Two microdisks written with negative tone resists (left) and positive tone resists (right). The Matlab algorithm for the production of the negative tone pattern is significantly more complicated. If there are several disks coupled in a coupled-resonator optical waveguide (CROW) configuration, the pattern becomes unmanageably complicated.

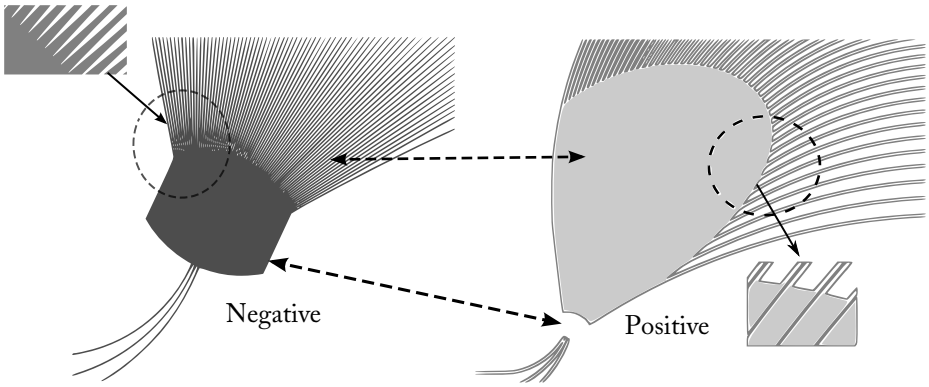

(b) Two arrayed waveguide grating (AWG) structures drawn on a negative (left) and positive (right) resists. While the free propagation region is easier to achieve in a positive resist, the fan shaped array of waveguide is complicated in such structure. Moreover, the proximity effect from such a large written area (due to the the fact that the trenches and not the waveguides are written) can lead to narrowing of the central waveguides and phase aberrations.

Figure 32: The advantage of the negative tone resists in pattern preparation.

For the patterns requiring high dimension accuracy and also high selectivity to Si,

HSQ is a good candidate (despite the very high dosage required). HSQ is a negative tone resist and is very similar to SiO_2 that allows to get very good selectivity between the resist and the Si, and it allows etching directly into Si using a pure Cl_2 recipe. The large selectivity also allows getting vertical side walls during the etching. However, HSQ requires a much larger base dose, and hence the writing time on an e-beam machine is more when compared to ZEP, which implies that its costlier to write patterns in HSQ than ZEP. Also, HSQ requires accurate optimization of the dosage and careful proximity adjustments (see Fig. 33). After careful optimization, we concluded that the best dosage for HSQ on top of SiN films (for 500 nm waveguides) is 3200 $\mu C/cm^2$. This is the dosage an isolated feature should receive and if it is places close to a large disk or a free propagation region of a star coupler (Fig. 32(b)) the dosage should be significantly reduced to compensate the proximity effect.

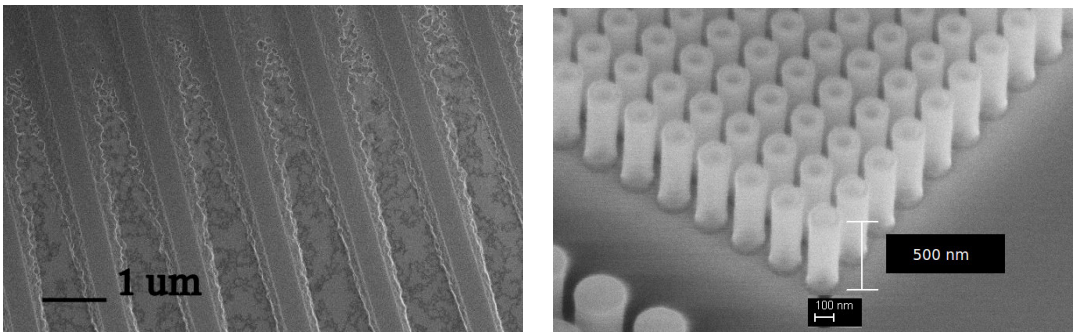

(a) The proximity effect can cause severe residue and roughness in dosage-sensitive HSQ.

(b) Proper adjustment of the dosage on HSQ

Figure 33: Comparison of patterns (a) affected by high dosage (due to the proximity effect) and (b) with well adjusted dosage.

Having optimized the required dosage, the HSQ is spun on the pieces at 1000 rpm with 500 rpm/min acceleration. Note that we do not spin the resist on whole wafers as HSQ as the properties of the film changes in a few hours and he results might not be repeatable on the remainder of the wafer. Afterwards the samples are baked at 80°C on a hotplate for 4 minutes. To avoid any charge up due to the electron accumulation during the pattern writing, a conductive layer should be introduced. This layer (which

is not necessary on semiconductor SOI wafers) is crucial when the sample consists of insulating SiN and oxide layers. A conventional method has involved evaporating a thin gold layer on top or beneath the wafer. As all metals are optically absorptive in the visible range, we have tried to eliminate any potentially contaminating step involving metals. Instead, we opted for a conducting polymer called ESPACER. ESPACER, developed by Denko, is a water soluble low viscosity polymer, which can be easily spun on top of the e-beam resists and remove the charge-up positional error on the electron-beam (EB) lithography process. There are two series of ESPACER ; one is ESPACER-100 series (used here) is an acidic solution and is appropriate for non-chemically-amplified resists. ESPACER 300 series, on the other hand, is a weak acidic solution and more suitable for chemically-amplified resists. After the exposure, the ESPACER layer is washed off under running water and the sample is ready for development. HSQ is typically developed in an Alkaline base developer [112]. Here we used tetramethyl ammonium hydroxide (TMAH) developer (MF-322 from Rohm and Haas) but KOH aqueous solution is also a possible developer. It has been shown that adding NaCl to the developer solution leads to superior contrasts (which is a possible subject of further optimization for photonic structures). There are typically two development conditions for HSQ. The first, called the "normal" method, involves a high temperature pre-bake (at 250°C) for 24 minutes, a lower dosage (almost half of the dosages used here, and a 70 seconds room temperature development in low concentration developer (2.3% TMAH (MF-319)). The second method, called the "high contrast" conditions and used here, requires a hot plate bake at 80°C for 4 minutes, a higher dosage (base dose $\sim 2000\mu C/cm^2$), and a shorter (30 sec) development in a concentrated (25%) TMAH at high temperature (80°C).

An alternative negative tone resist to HSQ is MaN 2400 series resist (here 2403 is used). MaN requires significantly lower dosage than HSQ, therefore the writing time almost a quarter of that of the HSQ. The over exposure residues are less troublesome

as a longer development in MF-319 or a short oxygen descum (11.9 Å/sec in 140 mTorr, 18 sscm, and 50 W RIE) can eliminate the scum (Fig. 34).

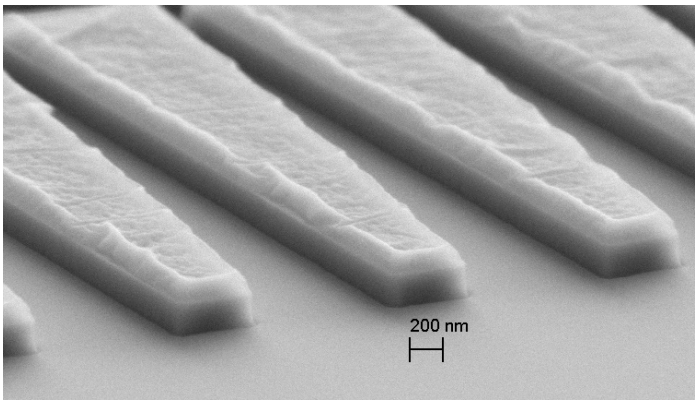

Figure 34: A structure written with MaN resist with a dosage of $600\mu C/cm^2$. Note the smooth sidewalls and absence of any residues.

A major issue with the MaN resists, nevertheless, is its weak adhesion to the substrate. The delamination failure, often happening in aqueous developers (like the MF-319 used in MaN's case) is usually alleviated by hexamethyldisilazane (HMDS) priming. The wafer is initially heated to a temperature sufficient to drive off any moisture that may be present on the wafer surface. A liquid or gaseous "adhesion promoter", such as Bis(trimethylsilyl)amine ("hexamethyldisilazane", HMDS), is applied to promote adhesion of the photoresist to the wafer. The phrase "adhesion promoter" is a misnomer, as the surface layer of silicon dioxide on the wafer reacts with the agent to form Methylated Silicon-hydroxide, a highly water repellent layer. This water repellent layer prevents the aqueous developer from penetrating between the photoresist layer and the wafer's surface, thus preventing so-called lifting of small photoresist structures in the (developing) pattern. Nevertheless, our different attempts with HMDS priming did not lead to repeatable results. Instead, a chemical named SurPass 3000 (provided by DisChem Inc.) is used [113]. The best curing steps are yet to be optimized, but in short the wafers need to be submerged in SurPass 3000 for 30 seconds, rinsed with deionized (DI) water and covered with MaN

immediately. After the development of the exposed patterns an optional re-flow of the resist at 145°C for 3 minutes can lower the sidewall roughnesses significantly. This step, although very beneficial for ultra-high quality photonics, can lead to feature size changes or sticking of patterns if the MaN resist is not perfectly adhering to the substrate.

A major point to consider in all of the above methods is the stitching error. Large-area electron beam lithography tools pattern substrates as a series of writing fields (500 μm in our case) that are stitched together. Pattern defects, termed stitching errors, can arise at field boundaries and these can have detrimental effects on device performance. Electron beam lithography tools often correct for gain and rotation errors that arise from variations in the distance between the substrate and the final lens. Corrections commonly assume that substrates are perfectly flat and this can be true for rigid substrates such as mask plates. Less rigid substrates such as wafers are often bowed due to process induced stress and, when loaded into lithography tools, wafer surfaces can be tilted. Contamination on the back of thinned substrates can also cause such problems, resulting in variations of wafer height across a writing field, and is not usually corrected for (Fig. 35). I corrected this problem by always putting a circular, thick quarts wafer behind the device sample when the sample is being loaded into the EBL cassette.

Alternative to the aforementioned masking layers, metals can be used specially if a high selectivity is required (either due to a deep etch or close to vertical sidewalls). As an example a structure made with a chromium mask can be seen in Fig. 36. The metal masks can be either obtained by a lift-off process or be etched in the first step. For this type of structures aluminum has proven to be a superior mask. Firstly, unlike nickel, gold or copper, it does not an adhesion layer. Secondly, in the presence of a slight fraction of oxygen in the plasma chemistry it oxidizes to Al_2O_3 give a $sim100$ mask-to-etch selectivity [114].

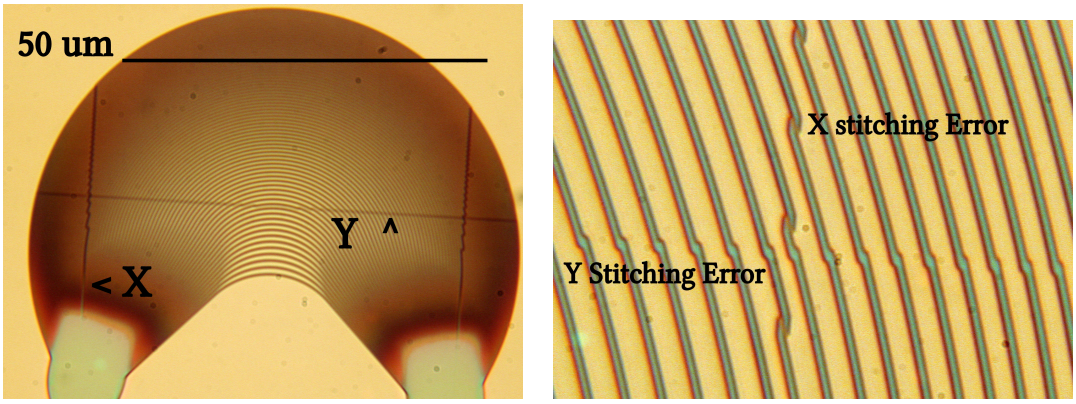

(a) Stitching error degrading an AWG.

(b) close up of the stitching error shows an error close to 0.5 μm

Figure 35: Stitching error

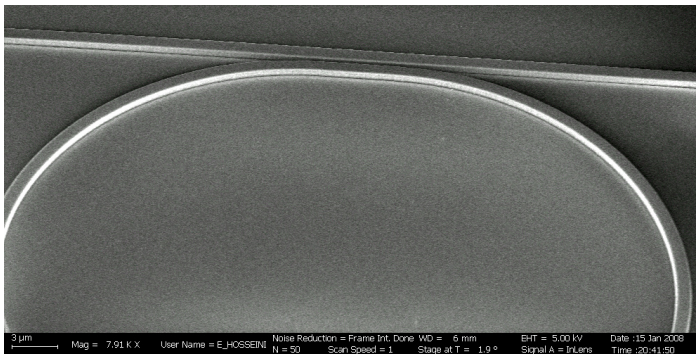

Figure 36: A racetrack structure etched with a chromium mask obtained with a lift-off process. Note the near vertical sidewalls and the high aspect ratio.

3.1.4 Etching

The next step in fabricating our devices is plasma etching (Fig. 30(d)). Plasma etching is used to transfer the pattern from the resist layer into the SiN device layer of our wafer. The etching is most often done the STS SOE inductively couple plasma (ICP) reactive ion etching (RIE) machine in the NRC. The plasma parameters are initially optimized for the least sidewall roughness (visible with an electron scanning microscope (SEM)). The parameters of the optimized plasma etch is as follows: Pressure=5 mTorr, P_{coil}=800 W, P_{platen}=20W, and the CH_4 flow=30 sccm. Afterwards some microring resonators are fabricated with different combinations of power/pressure and the quality factor of the rings is measured. No significant change in the quality factor was noticeable as long as the plasma parameters did not deviate too much from the above values. For example the pressure can be chosen between 3 to 20 mTorr, the coil power can be 400–1000 W, and the platen power can be varied between 10 and 50 W. The only major difference is more vertical sidewalls when the pressure is reduced and the DC bias point is increased (via increasing the platen power). A detailed investigation of the effect of different plasma parameters can be seen in [115]. It should be mentioned that as the conditions of the chamber change on a daily basis (due to possible faulty mass flow meters, air leakage into the chamber, polymer build-up on the sidewalls, etc.) the etch rate and quality should be monitored regularly. A good practice is to record the reflected powers for both the RF sources (coil and platen), He flow rates, and the color of plasma for each run. These parameters are a good indication of the state of the chamber. If any of the values change by more than a few percent the etch results may be different. Also before performing an actual etch, we always perform an etch rate measurement step with dummy sample to measure the actual etch rate, as the etch rate changes from run to run. Nevertheless the following approximate etch rates show the typical selectivities for different resists.

Table 3: Typical plasma conditions and approximate corresponding etch rates in nm/min. Pressure is 5 mTorr.

coil	platen	CF_4	LPCVD SiN	PECVD SiN	SiO_2	HSQ	ZEP	MaN
800 W	20 W	30 sccm	130	200	90	120	180	130

3.1.5 Imaging

Although imaging is not a part of fabrication, but is usually performed after the fabrication to make sure the fabrication quality is acceptable. I have used Zeiss Ultra 60 Scanning Electron Microscope (SEM) manufactured by Oxford Instruments to take SEM images of the fabricated devices. Zeiss SEM is a very high resolution SEM with a field emission source. As the SiN/SiO_2 samples are not conductive, the electron build up (specially if the resist is left on the structure for imaging) makes the imaging very challenging. Therefore, most of the time a thin (~ 5 nm) layer of Au or Cr is evaporated on the samples before imaging. With this method and also using the In-lens detector it is relatively easy to obtain clear images down to 30 nm resolution.

3.2 Silicon Fabrication

The fabrication of Si devices are very similar to the procedures mentioned in Section 3.1. The only major difference is the plasma etching is done mainly in a halogens gas plasma. The three gas combinations usually used for Si etching are Cl_2, HBr, and SF_6+C_4F_8. The former, being a very clean, low roughness and straightforward etch, has very low selectivity to polymer based resists. The remedy is either using HSQ as a e-beam resist, or using SiN or SiO_2 as a hard mask. The hard mask material is etched with a fluorine based gas first, the resist is stripped away and Si is etched with Cl_2 while the hard mask protects the device areas. HBr and SF_6+C_4F_8, while contaminating to the chamber, can be used with ZEP/MaN resists. Fig 37(b) shows such a structure etched with a Cl_2+HBr+Ar combination, which has a selectivity high enough to use a 600 nm ZEP as the only mask.

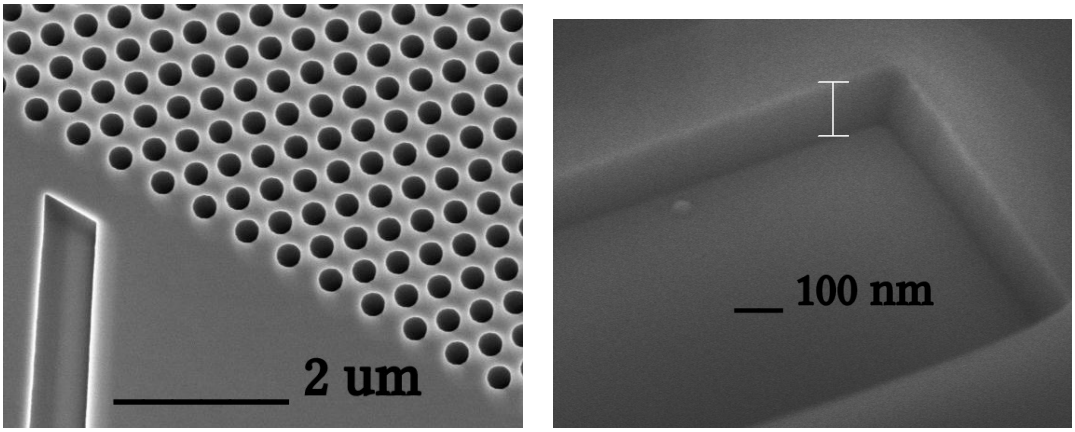

(a) An SOI wafer etched with pure Cl_2 using an oxide hard mask.

(b) A Si wafer etched with Cl_2+HBr+Ar combination using a ZEP mask.

Figure 37: Silicon etching.

3.2.1 Undercutting

The term undercutting refers to the removal of oxide layer underneath the device region. In photonic crystals cavities and waveguides this leads to larger Q and wider bandwidth. In microdisk devices the undercutting can lead to increased interaction of the field mode with the surrounding and lower power required for thermal tuning and modulation. Usually the BOX layer underneath the device is removed by using the buffered oxide etchant (BOE) solution, Figure 30 (f). Photolithography is required to mask off the regions where we do not want to remove the underlying oxide layer such as the input and output ridge waveguides. For photo-lithography I use the Shiply 1813 positive tone resist. after HMDS treatment, the resist is spun using one of the spin coaters available in NRC at a spin speed of 4000 rpm for 30 seconds. Soft bake is performed for 3 minute on a hotplate set at 100°C. The resist is exposed to 405 nm UV radiation on a Karl Suss MA-6 Mask Aligner. The required dose to fully develop the pattern is $400mJ/cm^2$. Since the intensity of the light source can fluctuate over time, it is required to check the lamp intensity at the exposure wavelength by using the light meter. The patterns are developed in MF-319 developer for 30 sec. The sample is then hard baked at 120^oC on a hotplate for 10 min. The sample is then

dipped in a BOE solution for a few minutes depending on the desired lateral wet etch. The etch rate of oxide in a BOE solution at room temperature is ~100 nm/min. The photoresist is then stripped in an O_2 plasma. It is important not to use wet etching to remove the resist, as wet etching can break the suspended structures unless a critical drying machine (rather than a nitrogen gun) is used after the acid dip. The critical dryer machine in NRC is used for different samples and leads to contamination on photonic devices. Therefore the resist removal is performed in an asher machine. It is noteworthy that the BOE etch usually leads to rough oxide surfaces (Fig. 38(c)). Nonetheless, Most often this roughness does not degrade the optical performance as the light is confined in the Si region (Fig. 38(a)) or the oxide is etched all the way reaching the underlying Si wafer (Fig. 38(b)). Otherwise, if the etched oxide surface is in the vicinity of the optical field, a combination of BOE:HCl:Water 20:37:340 can lead to a very smooth surface [116].

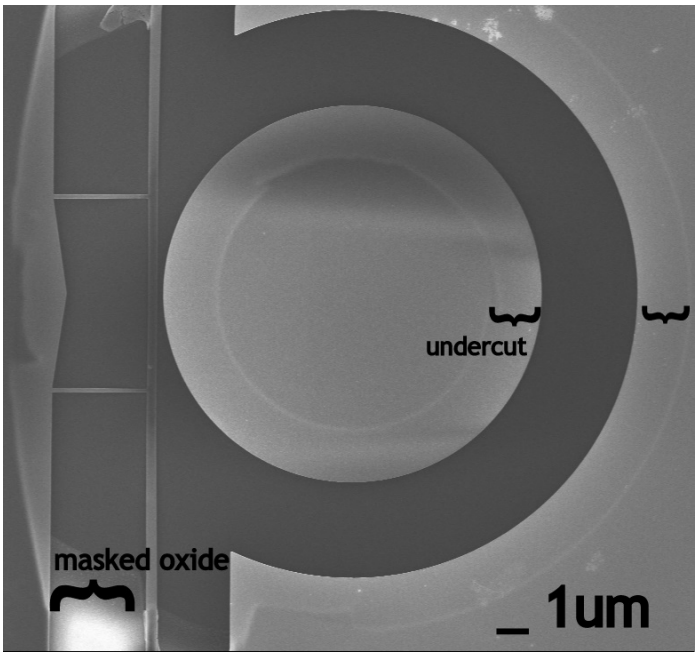

(a)

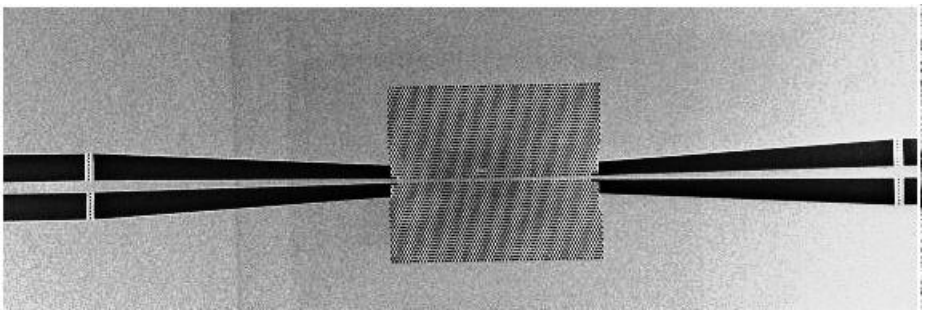

(b)

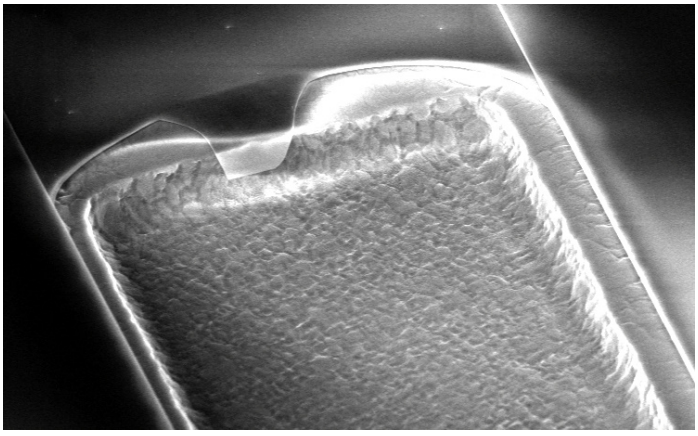

(c)

Figure 38: (a) An undercut silicon microdisk with two beams supporting the free-standing waveguide. (b) An undercut photonic crystal waveguide. (c) Roughness on the oxide substrate resulting from the BOE etching.

3.3 iii-v Fabrication

As silicon nitride is transparent in a wide spectral range ($\lambda = 300$nm–$6\mu m$) it can be integrated with different active materials in this range. In the following sections fabrication of different types of iii-v materials is investigated.

3.3.1 InAlGaAs QW Lasers

Several active materials for laser diodes and light emitting diodes have been investigated. Among them GaN (for blue/green); GaP (for red); and (Al,In)GaAs/GaAs, InGaAs/InP and (In,Ga)AlAs/InGaAs for infrared (IR) region have drawn a lot of attention.

As seen in Fig. 39(b) the semiconductors discussed here are composed of Al/Ga/In from group iii and P/As from group iv. When a ternary material $A_xB_{1-x}C$ is generated (usually with metalorganic vapor phase epitaxy (MOVPE)), some of the properties of the ternary can be linearly deduced from its binary components:

$$Ter_{ABC}(x) = xBin_{AC} + (1-x)Bin_{BC}$$

. For example, as seen in Table. 4, the lattice constant a behaves in this manner. Some of the other parameters (for example the bandgap) usually follow a quadratic curve:

$$Ter_{ABC}(x) = xBin_{AC} + (1-x)Bin_{BC} + \alpha_{AB}x(1-x)$$

. The parameter α is called the "bowing" parameter [117, 118].

As an example of a ternary material, the alloy system AlGaAS/GaAs is potentially of great importance for many high speed electronic and optoelectronic devices, because the lattice parameter difference between GaAs and $AlGa_xAs_{1-x}$ is very small, less than 0.15%. Moreover a high Al compound can be oxidized and wet etched with HF (an advantage not found in other discussed materials).

Constructing a quaternary material can be done in two ways. The first type (which I call type "2+2") is composed of two group iii and two group iv materials

($A_xB_{1-x}C_yD_{1-y}$). The type "3+1" quaternaries discussed here are made of three elements from group iii and one group iv element ($A_vB_wC_{1-v-w}D$). The properties of first type can be deduced from a quadratic mixing of properties of their four basic binaries (AC, AD, BC, BD) and for type 3+1 the properties of their three basic binaries are needed (Table 4).

As an example of type "2+2" alloy, the $Ga_xIn_{1-x}P_yAs_{1-y}$ can be grown lattice-matched to GaAs and InP. The quaternary system is used to produce lasers operating in the wavelength range between 1.3 and 1.6 μm (As seen in Table. 4 and Fig. 39(a)). Lasers emitting at this spectral range are of great technological interest because of their application in an optical fiber communication system. The $Ga_xIn_{1-x}P_yAs_{1-y}$ laser structures are grown lattice-matched to InP substrates. The $Ga_{0.47}In_{0.53}PAs_{y=0}$/InP heterostructure system has also broader interest since it is used for various optoelectronic and transport device applications [117]. Thus, this material has been the most common combination used for hybrid (iii-v)–Si applications [119].

The $Al_xGa_yIn_{1-x-y}As$ is an example of the "3+1" quaternary system, which can be grown lattice-matched to InP [with the composition $(Al_xGa_{1-x})_{0.48}In_{0.52}As/InP$]. The alloy system is an ideal candidate for the implementation of several electronic and optoelectronic devices, since its band gap can be continuously varied from 0.75 eV (x=0) to 1.47 eV (x=1). In this thesis we focus on this material. The MOCVD growth is done in Prof. Dupuis' group at GaTech ([120]).

As the AlGaInAs material is grown on InP substrates, the first basic step is to achieve a smooth and vertical dry etching for InP. The following section discusses this issue in detail.

Table 4: Bandgap and lattice of iii-v materials.

material	Bandgap (eV)	lattice (Å)
$Al_wGa_{1-w}As$	$1.4+1.6w+$ $w(1-w)(0.13-1.3w)$	$5.6533+0.0078w$
$In_xAl_{1-x}As$	$3-3.4x+0.7x^2$	$5.6611+0.3972x$
$In_wGa_{1-w}As_vP_{1-v}$ âĂć	$1.4-1.12v+0.67(1-w)+...$ âĂć	$5.7(1-w)v+6.1wv+$ $5.5(1-w)(1-v)+5.9w(1-v)$
$In_wAl_vGa_{1-w-v}As$ âĂć âĂć	$0.354w+3.017v+$ $1.423(1-w-v)+...$ âĂć	âĂć $5.653325+0.404975w+0.007775v$ âĂć

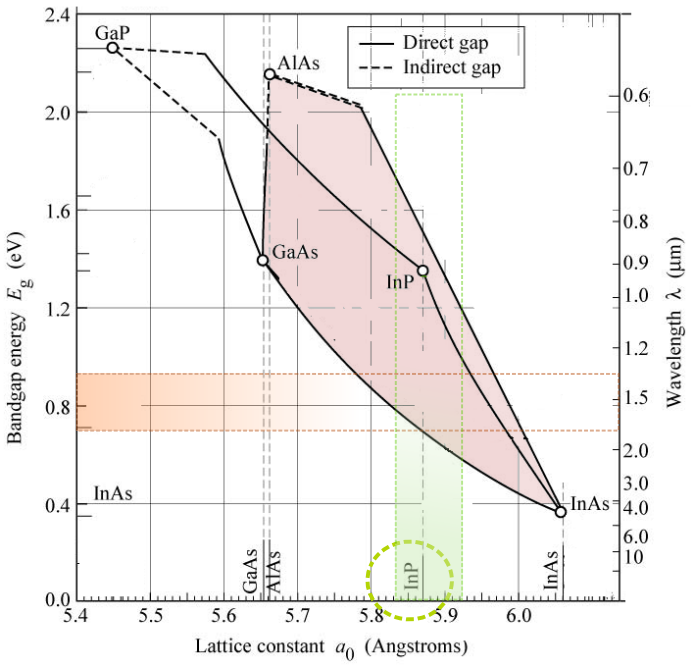

(a)

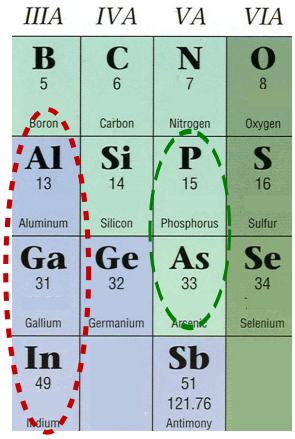

(b)

Figure 39: Bandgap and lattice constant of iii-v materials; the elements are Al, Ga, and In from group iii; P and As from group iv.

3.3.2 Dry etching of InP

In general, smooth dry etching of any compound material requires the almost equal removal of the alloy materials (In and P here). In the case of InP, the difference between the atomic weights of In and P can lead to slower removal of In which can lead to extremely rough surfaces [121] and this can be seen in Fig. 40. For example when chlorine is used as the etching gas indium chlorides are not removed efficiently at temperatures below 150°C in a reactive ion etching [122]. Therefore there are three common chemistries developed for InP etching:

- CH_4+H_2
- Cl_2/BCl_3 at temperatures above 150°C
- HBr/HI

The chlorine process requires an elevated temperature of the sample holder during the plasma process. The third type requires expensive, highly corrosive and contaminating gas/liquids. At the time of the InP optimization, none of these where available. So we used a combination of methane, hydrogen and argon (also known as MHA mixture) as the etching chemistry.

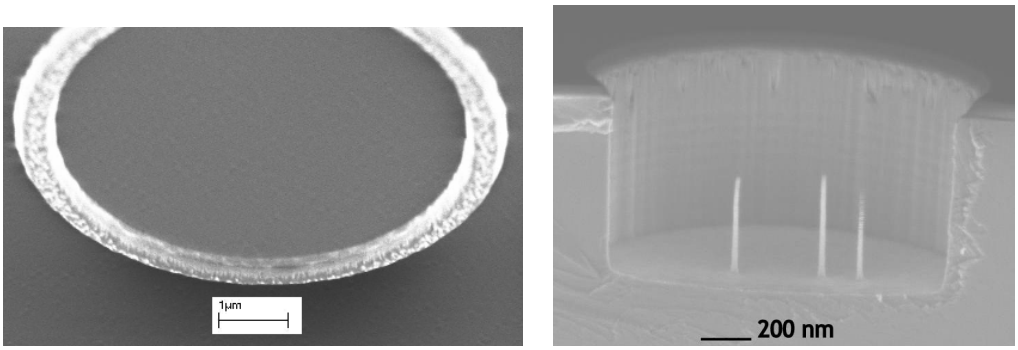

(a) (b)

Figure 40: (a) An InP wafer etched in a chlorine plasma at room temperature. (b) InP etched in a MHA gas mixture with periodic oxygen clean steps.

This gas combination is very sensitive to the percentage of the methane present in the chamber. Saturation with methane can lead to high polymerization, inefficient removal of phosphorus, and tilted sidewalls. Lack of enough methane can leave In particles behind (as can be seen in Fig. 41(a)). Also as the process is highley directional (because of the passivation of the sidewalls during the etch), any particles on the surface prior to the etch can lead to pillar shaped residues. Figure 40(b) shows a structure with proper cleaning prior to etching, and Fig. 41(b) shows a structure without a pre-clean. The final optimized process had a MHA ratio of 8/40/20, a pressure of 50 mTorr in the RIE chamber, an RF power of 300 W, and repetitive oxygen clean cycles every minute. The oxygen clean cycles were 30 seconds long and were performed with an oxygen flow of 50 sccm, pressure of 125 mTorr and power of 75 W.

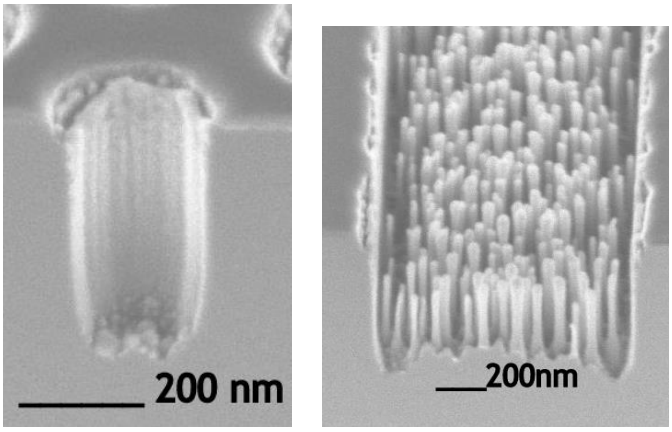

(a) (b)

Figure 41: (a) Too little methane causes left-over In particles. (b) The lack of a proper pre-clean leads to pillar shaped residues.

3.3.3 Dry etching of InAlGaAs

For 1.55μm applications, InP-based material system is a choice of materials and they are $Ga_xIn_{1-x}P_yAs_{1-y}$ and $In_{0.52–0.53}(Al_xGa_{1-x})_{0.48–0.47}As$ lattice-matched or nearly-lattice-matched to the InP substrates. In this study, we investigated InAlGaAs material system. InAlGaAs is expected to have better etching selectivity over InP than InGaAsP over InP due to different group V elements. Also, conduction band offset (CBO) of InAlGaAs/InP is generally larger than that of InGaAsP/InP heterostructure interface, which will be beneficial in transverse carrier confinement.

The InAlGaAs structure was grown by metalorganic chemical vapor deposition (MOCVD) in a Thomas-Swan reactor system equipped with a close-coupled showerhead growth chamber. The epitaxial layers were grown at low pressure of 100 Torr using H_2 carrier gas. The precursors employed include EpiPureTM trimethylindium (TMIn), trimethylgallium (TMGa), and trimethylaluminum (TMAl) for Column III elements, and phosphine (PH_3) and arsine (AsH_3) for Column V elements.

The growth was carried out at 650°C by initially growing an unintentionally InP buffer layer, followed by InAlGaAs etch-stop layer and active region. The active region consists of compressively strained $In_{0.58}Ga_{0.42}As$ quantum well (QW) and lattice-matched $In_{0.53}(Al_{0.4}Ga_{0.6})_{0.47}$ As QW barrier (QWB). A layout of the structure can be seen in Fig. 42.

Any etching gas combination and plasma condition should etch the active layer with smooth surfaces and be smooth enough in the capping and underlying InP layers. There are two possible plasma chemistries: based on HBr and BCl_3 and with addition of methane for efficient In removal. As any oxygen in the plasma leads to the oxidation of Al (which functions as a hard-to-remove mask) the percentage of methane should be precisely adjusted so that no oxygen clean cycle is necessary. The first plasma condition leading to acceptable results was: P=10 mTorr, $BCl_3/Ar/CH_4$ 16:10:5, P_{platen}=300 W, P_{coil}=700 W. A structure etched through the InP cap into

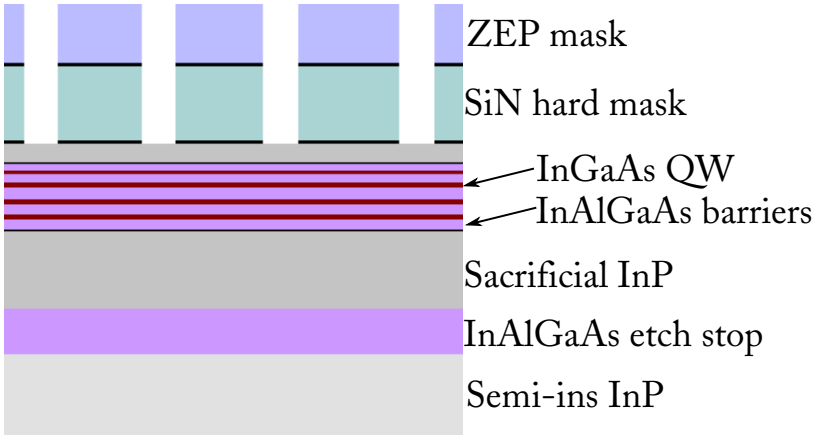

Figure 42: Layout of the MQW structure. Two sacrificial InP claddings surround the $In_{0.53}(Al_{0.4}Ga_{0.6})_{0.47}$ barriers. Several $In_{0.58}Ga_{0.42}As$ are stacked up in the active region.

the underlying InAlGaAs is presented in Fig. 43(a). The other chemistry capable of smooth etching of both InP and InAlGaAs is $Ar/HBr/CH_4$ 20:10:5, P=5 mTorr, P_{platen}=200 W, P_{coil}=600 W (Fig. 43(b)). In both of these processes (performed in the STS-SOE RIE-ICP at NRC), the temperature of the chiller is set at 180°C, which leads to a temperature of almost 160°C on the sample. It is necessary to bond the sample to the substrate to ensure the high temperature is transferred properly from the carrier wafer to the pieces.

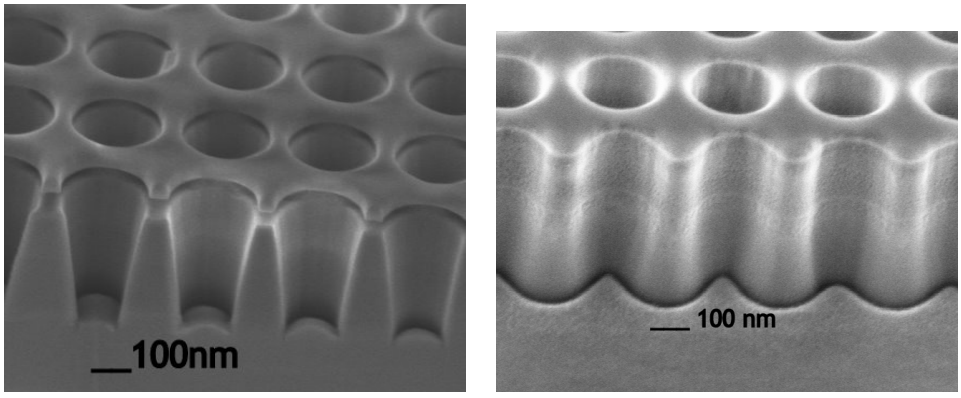

(a) (b)

Figure 43: (a) Too little methane causes left-over In particles. (b) The lack of a proper pre-clean leads to pillar shaped residues.

After the dry etching the SiN and the sacrificial InP are removed. The SiN can

be easily removed with hot phosphoric acid while the removal of the InP is more challenging. An acidic combination which removes the InP but does not touch the InAlGaAs is required. This can be done in a dilute (10%) HCl at 10°C. A MQW undercut microdisk and a photonic crystal are demonstrated in Figs. 44(a) and 44(b).

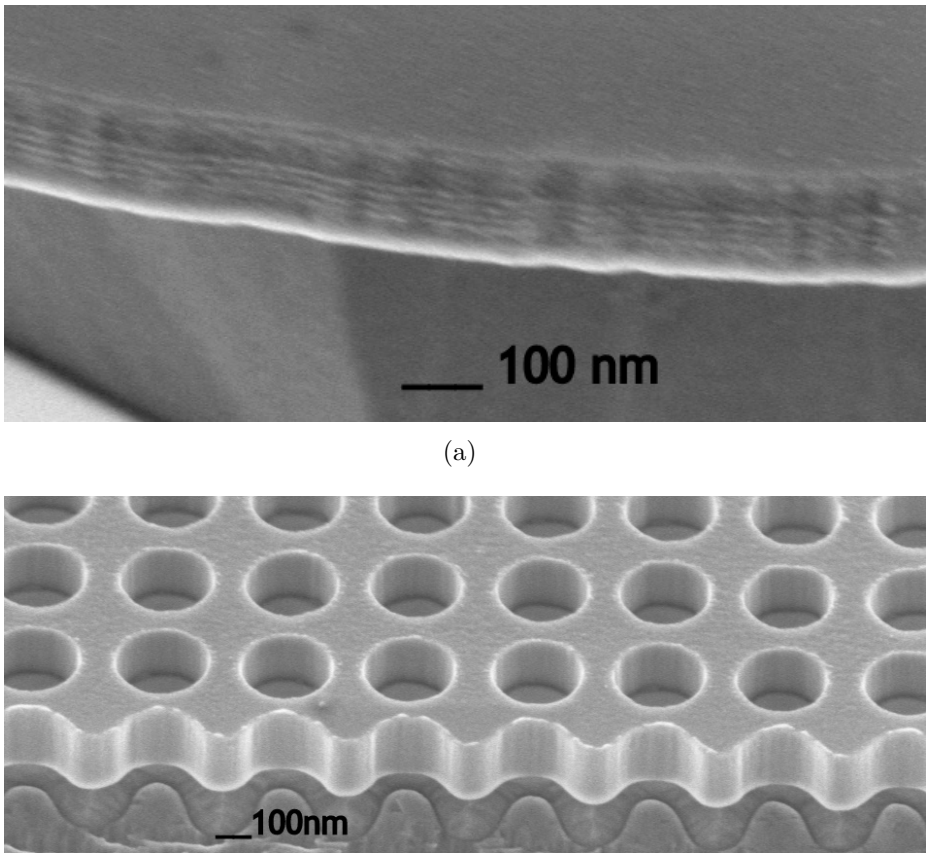

(a)

(b)

Figure 44: (a) A MQW undercut microdisk and a (b) photonic crystal etched in InAlGaAs and undercut with dilute HCl.

3.3.4 GaN diodes

GaN based materials are widely used today for green/blue LEDs. Despite the challenges in their growth and doping [123], their dry etching is straightforward and can be easily done in pure Cl plasma (Fig. reffabpic:gan). On the other hand demonstration of nanophotonic lasers in these structures is challenging as GaN does

not have a high index contrast with the underlying AlGaN and there is no simple wet etching removing the sacrificial layer without effecting the gain layers. Recently, a sophisticated photoelectrochemical wet etching is suggested by Nakamura [124], but this procedure remains very complicated.

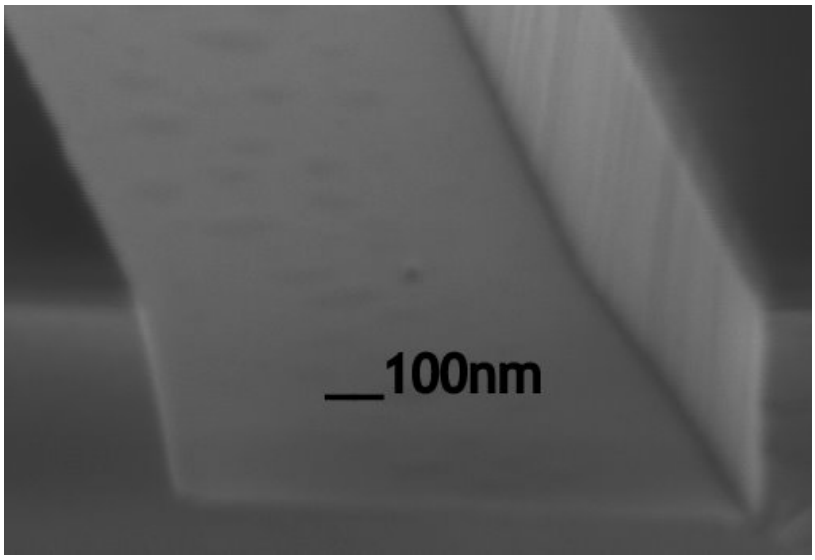

Figure 45: A GaN film etched with pure Cl plasma.

CHAPTER IV

DEMONSTRATION OF ULTRA HIGH Q MICRODISK RESONATORS IN THE VISIBLE RANGE

In this section, monolithic, high Q, compact Si_3N_4/SiO_2 resonators are demonstrated in the visible range, and critical coupling of the resonators to in-plane waveguides is demonstrated (at λ=652–660 nm). Details of fabrication of the devices are explained in section 4.1. The characterization setup and the experimental results are discussed in section 4.2. Coupling of high Q resonators to adjacent waveguides and its optimization are covered in section 4.3.

4.1 Fabrication of Si_3N_4 *Structures*

Fabrication of these structures is done on top of a thermally grown, 6-micron-thick oxide layer, which isolates the guiding Si_3N_4 layer from the lossy Si substrate (as shown in Fig. 46). A 200 ± 3 nm-thick layer of low loss, stoichiometric Si_3N_4 is then deposited on top of the oxide using low pressure chemical vapor deposition (LPCVD). The LPCVD deposition was done at the LioniX foundry. The resulting films were slightly higher in Si content and the refractive index of the silicon nitride layer, without any subsequent annealing, was almost %1 higher than the nitride films reported elsewhere [125]. For fabrication of the microresonators, 500 nm of ZEP-520 electron beam resist is used as the etching mask. In order to inhibit the surface charge-up during the electron beam writing, a thin layer of Espacer 300 is spun on top of the resist. The waveguides and microdisks with the desired coupling gap between them are patterned using a JEOL JBX-9300FS 100kV electron beam lithography system. The pattern addressing grid size is 1 nm, the beam scanning

frequency is f=50 MHz, and the beam current is set to I=2 nA (using a 60 μm aperture). Choosing a dosage of D=250 μC/cm^2 for the ZEP, the smallest possible shot pitch (SP) is 4 nm (SP$\geq [I/(f \cdot D)]^{1/2}$). Moreover, the beam spot size for the 2 nA current is approximately 6 nm. It is expected that with such shot pitch and beam spot size, the roughness introduced to the structure during the electron beam lithography is smaller than 10 nm (Fig. 48). The etching is then performed using CF_4 gas in an STS inductively coupled plasma (ICP) etcher, in which a detailed optimization of the etching process is performed to minimize the sidewall roughness and thus to maximize the Q. The optimized pressure, coil power, and platen power are P=5 mTorr, P_c=600 W, and P_p=20 W, respectively. The sidewall roughness is inspected with scanning electron microscopy (SEM), and the sidewall tilt angle is measured to be 85°. A scanning electron microscopy (SEM) image of a microdisk resonator coupled to a waveguide is shown in Fig. 47 and the smoothness of the etched sidewalls is apparent from Fig. 48.

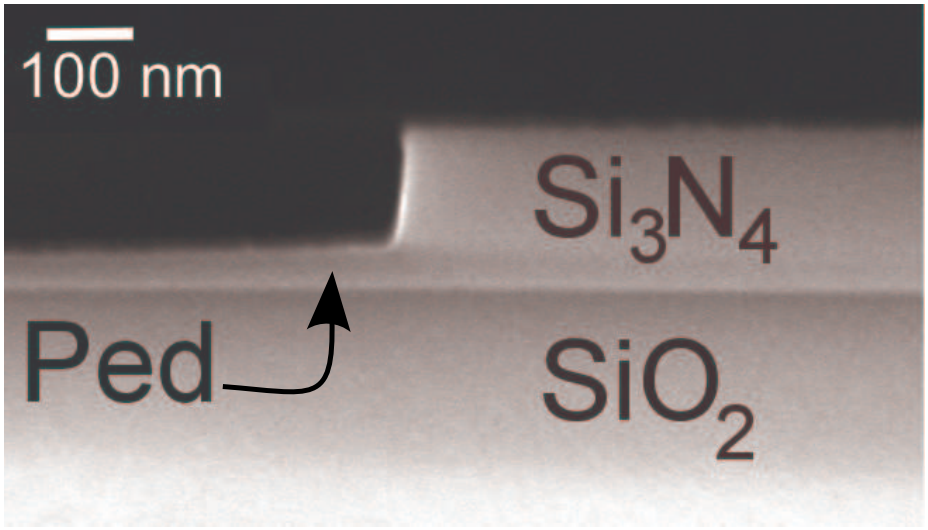

Figure 46: SEM image of a waveguide etched on a 203 nm layer of Si_3N_4 on top of 6 μm of isolating SiO_2 on a Si substrate. A Si_3N_4 pedestal layer is created to enhance the in-plane coupling strength of the resonators to the waveguides to achieve critical coupling. This layer is accurately defined during the etching by controlling the etch time of the ICP plasma process.

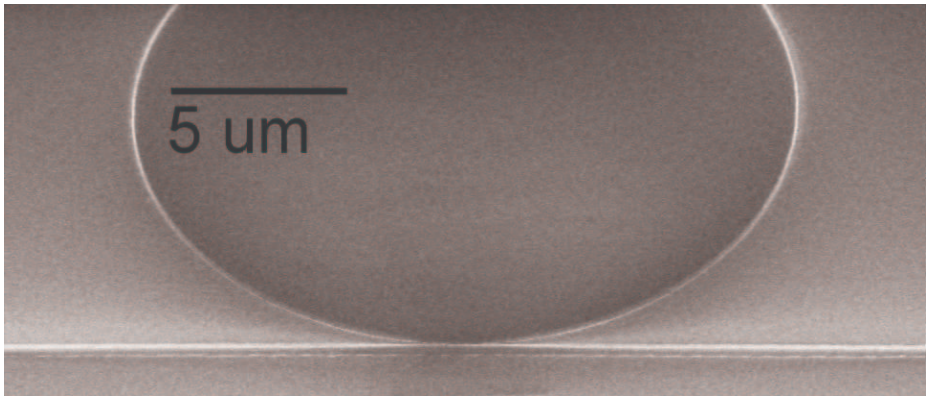

Figure 47: Tilted SEM image of a microdisk resonator side-coupled to an in-plane single mode waveguide with a 190 nm coupling gap. The radius of the disk is 20 μm.

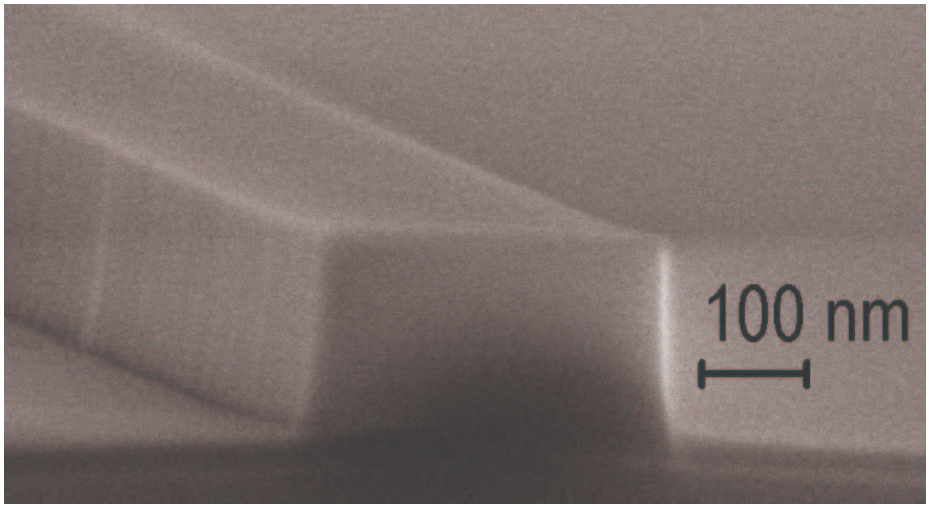

Figure 48: The cleaved facet of a low roughness waveguide etched using the optimized plasma etching parameters.

4.2 Characterizations

To characterize the fabricated structures, the output light of a tunable laser diode source (New Focus™TLB-6305) is coupled to the cleaved facet of the waveguide using a microscope objective lens. The wavelength of the laser is swept across the 652–660 nm wavelength range in 0.25 pm steps, and the transmission is measured as a function of wavelength by a Si detector at the waveguide output. The data is then transfered to the computer through a data acquisition (DAQ) card. The polarization of interest in this work is TE (transverse electric i.e., electric field in the plane of the resonator). Figure 49 shows the transmission spectrum for the structure shown in Fig. 46. Each dip in Fig. 49 corresponds to a TE cavity mode.

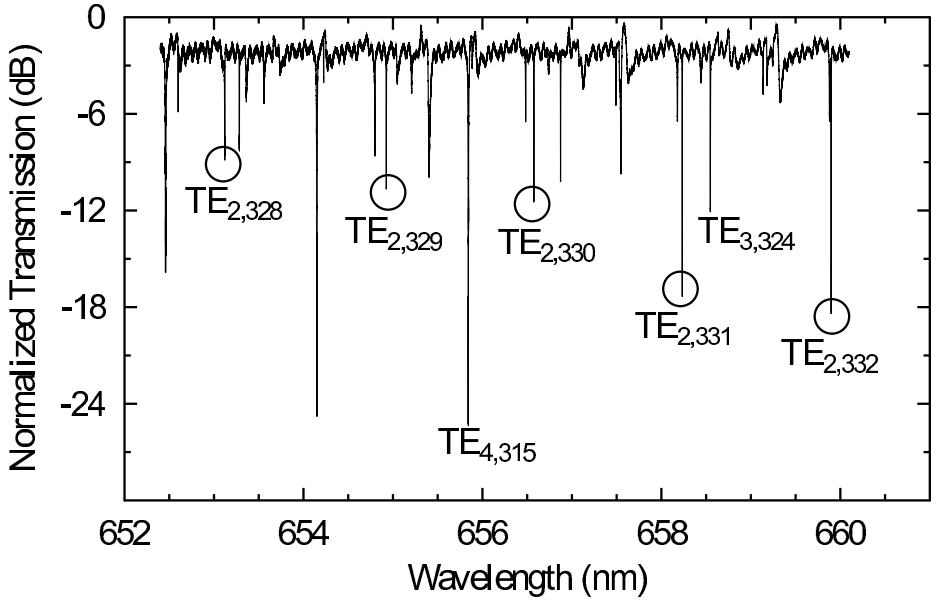

Figure 49: The normalized transmission of the waveguide coupled to the microdisk shown in Fig. 47. Each dip in the spectrum represents a specific $TE_{p,m}$ resonance. The dips denoted by the circles are due to $TE_{2,m}$ family of modes, which have the highest quality factor among all the radial families (for a 20 μm radius disk). The mode identification is based on the free spectral range (FSR) of the modes, matched with the FEM simulation data in Table 5.

While the resonator has several modes, the characterization bandwidth is limited to the range of 652–660 nm that is available from the characterization laser. Each $TE_{p,m}$ is characterized by its radial order (p) and azimuthal order (m). The dips in the

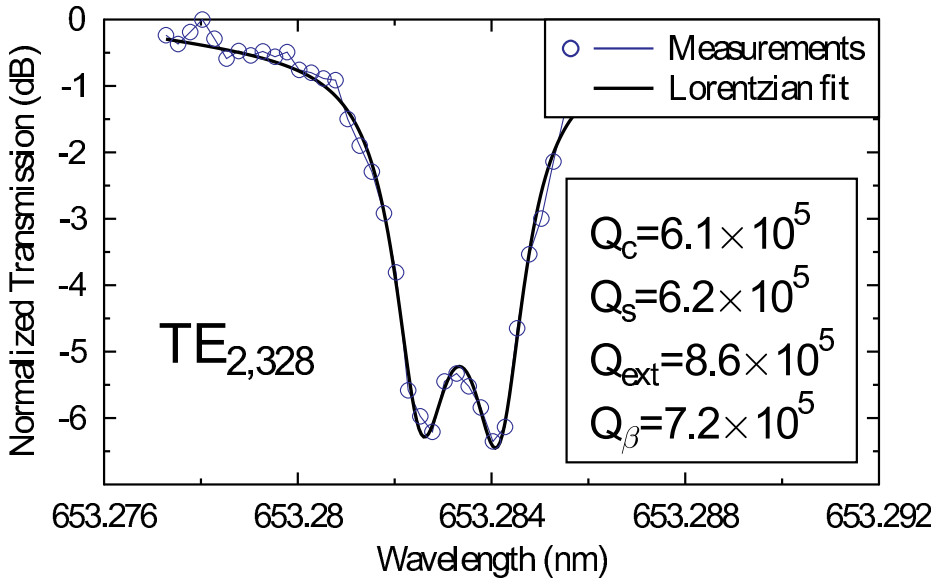

Figure 50: Transmission spectrum zoomed around $TE_{2,328}$. By fitting a double-Lorentzian lineshape to the experimental data, the intrinsic Q of $TE_{2,328}$ is found to be about 6.1×10^5.

transmission spectrum in Fig. 49 are attributed to different modes using the detailed theoretical analysis of the resonator mode structure using the finite element method (FEM) implemented in the COMSOL® environment. Variant transmission levels at different radial modes are due to unequal coupling levels to the adjacent waveguide. The full width at half maximum (FWHM) of each dip ($\Delta\lambda$) can be used to measure the loaded Q of that mode using $Q = \lambda_o/\Delta\lambda$, with λ_o being the central resonance wavelength of the mode in air. Figure 50 shows the zoomed version of the $TE_{2,328}$ resonance mode in Fig. 49, for which an intrinsic $Q_o = 6.1 \times 10^5$ is measured. As seen in Fig. 50, the back-scattering from the sidewall roughness results in coupling of the clockwise (CW) and counterclockwise (CCW) modes, leading to a doublet mode splitting [126]. Thus, the extraction of the Q from the experimental results is done by fitting a double-Lorentzian line shape with Q_c, Q_s, Q_{ext}, and Q_β as the fit parameters [2]. Q_c and Q_s represent the intrinsic quality factors of the two microdisk standing wave modes, while Q_{ext} and Q_β show the loading and back-scattering coupling Qs, respectively. The important properties of the first four radial order modes of the

microdisk resonator in Fig. 47 (with 20 μm radius and a pedestal thickness of 50 nm) are summarized in Table 5. The results in Table 5 are calculated using the FEM simulations.

Table 5: *Measured* intrinsic quality factor (Q_o), *simulated* normalized mode volume ($V(n/\lambda_o)^3$), *simulated* effective index of the disk defined as $n_{disk} \equiv m/(k_o R)$, and the free spectral range (FSR) of the first four radial TE modes of the Si_3N_4 microdisk with $R = 20$ μm, thickness of $d = 203$ nm and a pedestal layer of $ped = 50$ nm (k_o is the free–space wavenumber $k_o \equiv 2\pi/\lambda_o$). TE_2 mode has the highest quality, and TE_1 has the smallest mode volume.

	Q	$V^\dagger$	$(Q/V)^\ddagger$	n_{disk}	FSR
TE_1	5.10×10^5	352	1449	1.78	1.64 nm
TE_2	6.10×10^5	470	1297	1.73	1.66 nm
TE_3	2.00×10^5	515	388	1.68	1.68 nm
TE_4	1.10×10^5	670	178	1.65	1.69 nm

†,‡ The mode volume is normalized to $(\lambda/n)^3$.

The main source of loss in the demonstrated microdisk resonators is coupling to the radiation modes because of sidewall roughness. When the radius of the disk is increased, the scattering of the resonance mode to the radiation modes is reduced. Therefore, higher values of Q can be obtained. To verify this, microdisks with radii of 100 μm (the height of the Si_3N_4 layer, the pedestal height, the coupling gap, and the waveguide width are the same as those of the structure in Fig. 47) were fabricated and characterized. Figure 51(a) shows the transmission spectrum of the larger disk. The comparatively large size of the disk leads to larger number of nonleaky modes and also to a smaller FSR for each radial order mode. Therefore, the spectrum in Fig. 51(a) is much more condensed with the resonant dips in transmission than that in Fig. 49. Figure 51(b) shows the spectrum zoomed around one the resonant modes of the 100 μm radius microdisk for which a $Q_o \approx 3.4 \times 10^6$ was measured.

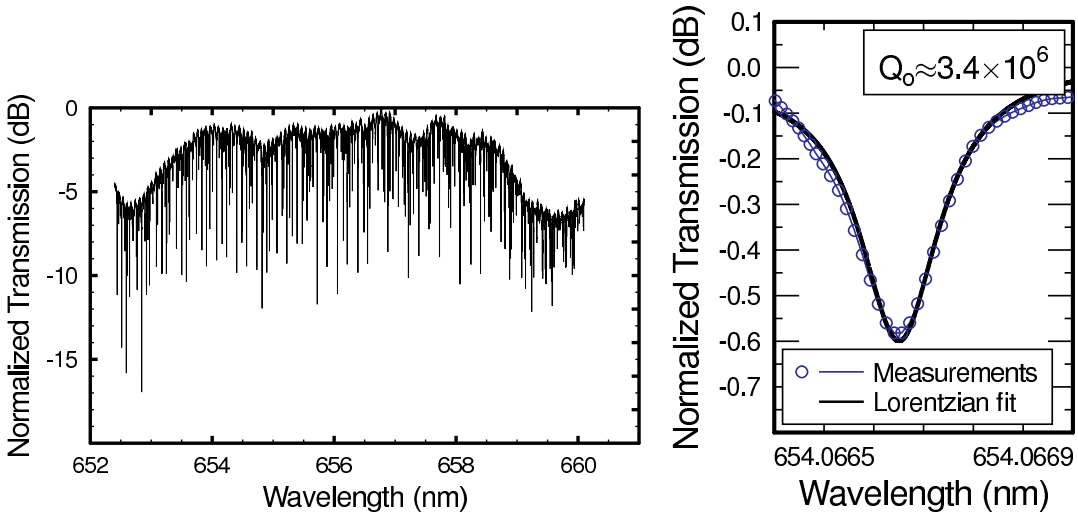

Figure 51: (a) The normalized transmission of a waveguide coupled to a large microdisk with radius $R=100$ μm (other properties of the structure are the same as those in the caption of Fig. 50. (b) Transmission spectrum zoomed around one of the high Q resonant modes of the $R=100$ μm microdisk resonator in (a). The intrinsic quality factor of the higher Q mode is $Q_o = 3.4 \times 10^6$.

4.3 Coupling

Most applications of high Q resonators (e.g., sensing, nonlinear optics, and quantum optics) require high field intensity inside the resonator. This requires very good coupling between the resonator and the adjacent waveguide or fiber. The maximum coupling between a waveguide and a cavity can be close to 100% when the rate of energy coupling from the waveguide to the cavity is equal to the rate of energy loss in the cavity [127]. Here, just the first few radial mode orders of the disk are of concern, as the less confined higher-order modes have lower effective mode indices and eventually become leaky. For example, in a 20 μm radius disk, only the first eight TE and the first four transverse magnetic (TM) modes are well-confined inside the resonator. Here the TE case is concentrated on; the results from the TM modes are comparable, nonetheless. As an example, Fig. 53 shows the magnetic field pattern for the first TE mode of the Si_3N_4 pedestal resonator with radius $R=20$ μm and the adjacent waveguide with 380 nm width at a distance (gap) of g=190 nm. The

thickness of the Si_3N_4 pedestal layer is 50 nm. The coupling strength between the waveguide and the cavity depends on the field overlap as well as the phase mismatch between the two structures.

FEM coupling calculations show that for a 20 μm radius disk with $Q < 1 \times 10^6$, the coupling gap should be narrower than 100 nm for critical coupling to the first few modes, which renders the fabrication of such structures challenging and non-repeatable with current electron beam lithography and ICP etching tools. The is gap is narrow primarily due to the insufficient overlap of the waveguide field with the first few more confined (and hence higher Q_o) TE modes at large gaps. To solve this issue, a thin (50 nm) pedestal Si_3N_4 layer—fabricated by proper selection of the etching time of the pedestal region—around the microdisk is added (as shown in Fig. 53). The addition of the pedestal layer results in stronger field overlap between the waveguide and the resonator, thereby enabling critical coupling to the low-order higher Q modes at gap distances larger than 200 nm. In addition to facilitating the critical coupling to the high Q mode, the added pedestal layer improves the thermal and mechanical properties of the microdisk cavity [128].

The coupling coefficient between a waveguide and an adjacent cavity is given by the first order perturbation theory [129, 130], and can be written as

$$\kappa = \frac{i\omega\epsilon_o}{4} \int_{-\infty}^{\infty} \int_{0}^{W} \int_{ped}^{d} (n_{SiN}^2 - 1)\, \mathbf{E}_{\text{disk}} \cdot \mathbf{E}_{\text{wg}} e^{j\phi}\, \mathrm{d}y\, \mathrm{d}x\, \mathrm{d}z \tag{93}$$

in which $\mathbf{E}_{\text{disk}}$ and $\mathbf{E}_{\text{wg}}$ correspond to the amplitude of the electric fields of the disk and the waveguide, respectively; n_{SiN} is the bulk index of the Si_3N_4. The phase factor ϕ is the difference between the propagation phases of the waveguide and the

cavity mode, and it can be approximated as

$$\begin{aligned}
\phi = \phi_{disk} - \phi_{wg} &= -m\theta + \beta_{wg} z \qquad \text{(z is the direction of waveguide propagation)} \\
&\approx -m(z/(R+g+W/2)) + \beta_{wg} z \quad \text{(for small z, } \theta \approx z/(R+g+W/2)\text{)} \\
&= -n_{disk} k_o z R/(R+g+W/2) + n_{wg} k_o z \\
&\qquad\qquad \text{(at resonance, } 2\pi R n_{disk} k_o = 2\pi m\text{)} \\
&= k_o z (n_{wg} - n_{disk}\xi). \qquad\qquad \text{(define } \xi \equiv \tfrac{R}{R+g+W/2}\text{)}
\end{aligned} \tag{94}$$

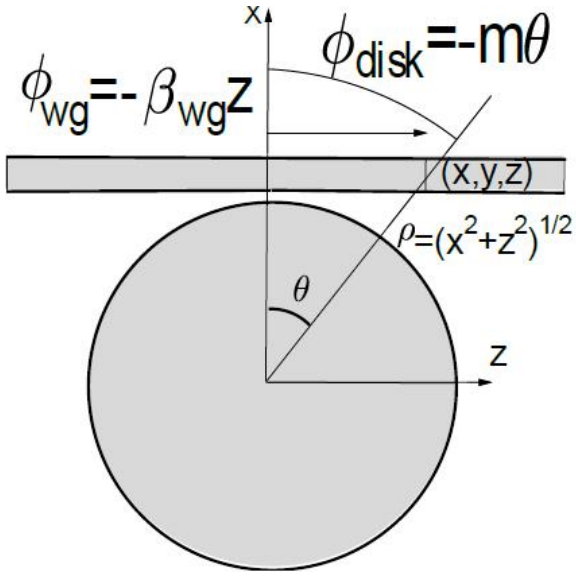

Figure 52: Digram of a disk side-coupled to a waveguide. The phase of $\mathbf{E}_{\text{disk}}$ at any point can be evaluated as $\phi_{disk} = -m\theta$ in which θ is calculated in reference to the $z = 0$ plane. The waveguide field ($\mathbf{E}_{\text{wg}}$), on the other hand, experiences a linear phase change along the waveguide $\phi_{wg} = -\beta_{wg} z$.

In this formulation, $k_o = 2\pi/\lambda_o$ is the wavenumber in free space, β_{wg} is the propagation constant of the waveguide mode, m is the azimuthal mode order of the resonator, g is the gap between the microdisk and waveguide, W is the waveguide width, R is the resonator radius and $\xi \equiv R/(R+g+W/2)$ is defined for brevity (more detail can be found in [131]). The effective index of the disk and the waveguide is defined as $n_{disk} \equiv m/k_o R$ and $n_{wg} \equiv \beta_{wg}/k_o$, respectively. It is clear form Eq. (93)

that the phase mismatch $k_o z(n_{wg} - n_{disk}\xi)$ between the two structures can reduce the coupling coefficient considerably. Since the operation is in the regime of small overlap between the resonator and waveguide fields, it is essential to achieve close to complete phase matching to allow for critical coupling with a reasonably large gap between waveguide and the cavity. This happens approximately when n_{wg}/ξ and n_{disk} are equal.

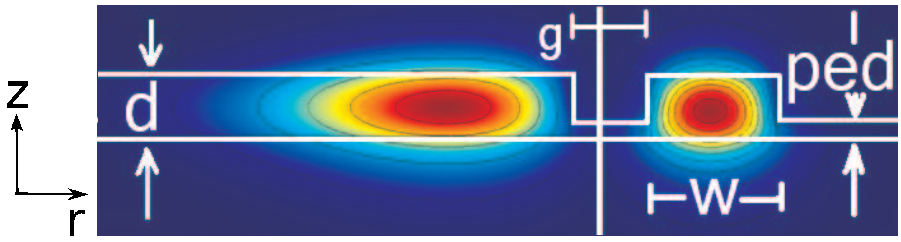

Figure 53: (left) H_z field pattern of the $TE_{2,328}$ microdisk mode simulated with COMSOL® using a cylindrical symmetry. (right) The vertical magnetic field (H_z) of the first-order WG mode is demonstrated. A pedestal layer, which is achieved with partial etching of the silicon nitride layer, is used to increase the coupling coefficient. W, d, ped, and g denote the waveguide width, Si_3N_4 layer thickness, the pedestal height, and the gap between the waveguide and the cavity, respectively. In the field simulated, d=200 nm, W=380 nm, and ped=50 nm.

The simulated effective index of the TE mode of the waveguide, multiplied by $1/\xi$ is plotted in Fig. 54(a) as a function of W in the range that the waveguide supports only one mode in the TE polarization (W =150–550 nm) while the other dimensions of the waveguide are kept at $h = 200$ nm and $ped = 50$. The horizontal lines in 54(a) depict the effective indices (n_{disk}) of the first four TE modes (with the lower order modes having higher effective indices). The approximate optimal waveguide width for coupling to each resonator mode can be deduced from the crossing points. Nevertheless, it is noteworthy that—as the distance between the waveguide and the resonators increases rapidly with propagation along the z direction—the above argument provides just an *approximation* for waveguide width for maximum coupling. Therefore, for a better determination of the optimal waveguide width (W), a rigorous calculation of Eq. (93) is required.

This calculation is performed using $TE_{2,m}$–$TE_{4,m}$ to obtain the field distribution of the microdisk and waveguide modes. Then, the coupling quality factor (Q_c) is calculated as a function of the waveguide width. The minimum of each curve in Fig. 54(b) corresponds to the highest level of coupling between the waveguide and each cavity mode. The waveguide width (W) for each minimum in Fig. 54(b) is approximately equal to the corresponding crossing points in Fig. 54(a). This shows the reasonable accuracy of the approximate index model used in the derivation of the results in Fig. 54(a). Note that the critical coupling is achieved when $Q_c = Q_o$ and this does not necessarily correspond to the minimum of the Q_c–W curve and can even be satisfied at two different waveguide widths.

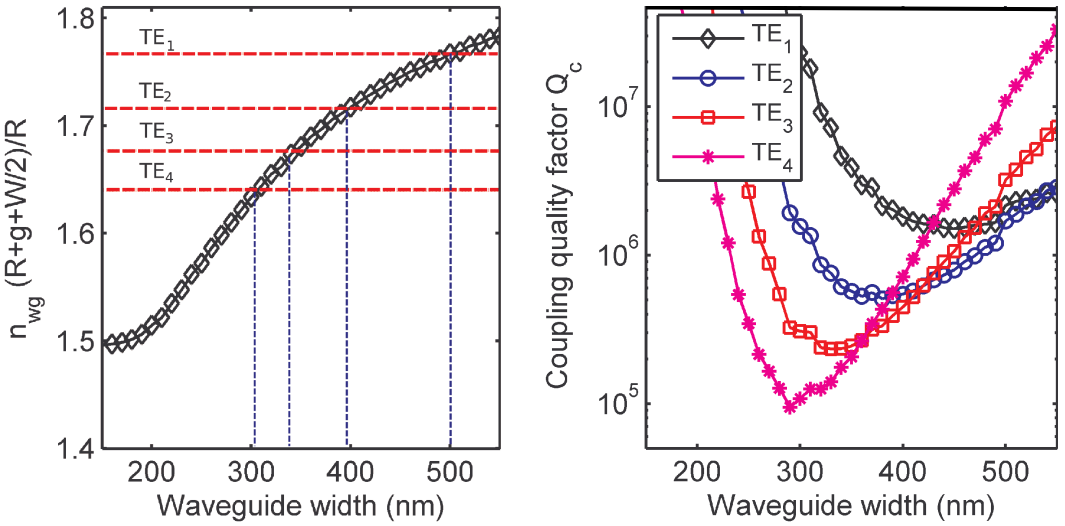

Figure 54: (a) The effective index of the TE mode of the waveguide multiplied by $1/\xi = (R+g+W/2)/R$ as a function of the waveguide thickness (W) with $h = 200$ nm and $ped = 50$ nm . The horizontal lines depict the effective indices of the different TE radial mode orders. The first mode (TE_1) has the highest effective index. (b) The coupling quality factor (Q_c) as the function of the waveguide width with a constant gap of 190 nm and the other parameters as mentioned in the caption of Fig. 53.

As the width of the fabricated waveguide is 380 nm, the expected coupling Q to $TE_{1,m}$ from Fig. 54(b) is much larger than the other three higher order modes ($TE_{2,m}$–$TE_{4,m}$)(see 54(b)). Comparing the intrinsic quality factors listed in Table

5 with the calculated coupling Q from Fig. 54(b), it is expected not to observe significant coupling to the $TE_{1,m}$ compared with the coupling to $TE_{2,m}$–$TE_{4,m}$ modes. This agrees with the measurement results (shown in Fig. 49). Also, identification of the dips in Fig. 49 is consistent with this, as the larger dips in transmission are due to $TE_{2,m}$–$TE_{4,m}$ modes.

Note that in the analysis here a few parameters were fixed in the coupled structure to investigate the effect of a specific design parameter. In general, the thickness of the pedestal layer, the gap between the waveguide and the resonator, and the widths of the waveguide are the parameters to be optimized for coupling to the desired high Q modes of a microdisk resonator with the specific radius.

4.4 Conclusion

In this chapter, the first ever high quality factor resonators in the visible range were introduced. The fabrication of the devices reviewed and the coupling with straight waveguides was analyzed. In the next chapter, a more general form of the coupling (i.e. curved waveguides) is investigated.

CHAPTER V

SINGLE-MODE PULLEY-COUPLED PLANAR SILICON NITRIDE MICRODISK RESONATORS

In chapter 4, high Q, planar Si_3N_4 microdisk resonators in the visible range were demonstrated. In the mentioned structures, coupling to the resonator is achieved by an optical waveguide (WG) side-coupled to the resonator [132]. When the waveguide is side-coupled to the resonator at a single point, the critical coupling condition [127] requires a very narrow coupling gap (gap < 100 nm) between the waveguide and the resonator. To ease the fabrication, a rib-like configuration with a thin pedestal was introduced increases the field overlap between the coupled elements thus increasing the coupling coefficient [132]. Nevertheless, such rib-type structures require an accurate control over the etch depth to achieve the targeted pedestal height. In addition, single-mode operation is hard to achieve in such rib-type structures. Another effective, yet seldom investigated, approach to increase the gap size and thus ease the fabrication is increasing the effective coupling length rather than the field overlap. In this approach—termed "pulley" coupling—the waveguide wraps around the resonator (e.g., a microdisk), effectively increasing the coupling length several times compared to the single point coupling with a straight waveguide. This approach was initially modeled with conformal transformation method [133] and recently utilized in a chalcogenide glass sensor. [134]. However, a thorough investigation of this technique is needed to develop a systematic design approach for high Q resonators with whispering gallery modes.

By wrapping the waveguide around the disk we can increase the effective interaction length from a few microns to ultimately 120 μm for 20 μm-radius disks (Fig.

55). Nevertheless, such a configuration requires a strict phase matching condition as, unless the two traveling waves have the same phase velocity, the phase walk-off between them makes the coupling coefficient practically negligible.

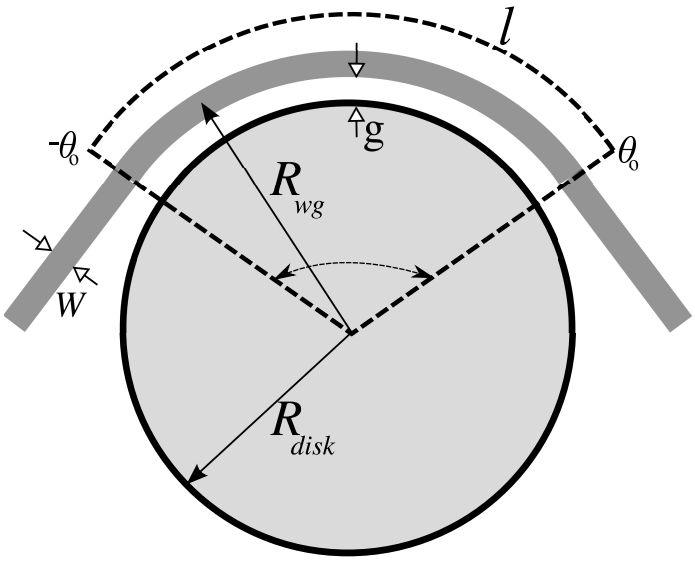

Figure 55: The pulley coupling configuration in which the waveguide effectively interacts with the microdisk in the radial region between $-\theta_o$ and θ_o. R_{disk} is the radius of the disk (20 μm in this case), g is the coupling gap between the microdisk and the waveguide, W is the width of the waveguide, and $R_{wg} = R_{disk} + g + W/2$ is the effective radius of the curved waveguide.

To model this numerically, the coupling coefficient between a waveguide and an adjacent cavity is given by the first order perturbation theory [129, 130, 115] as

$$\kappa = \int_{-\theta_o}^{\theta_o} \left[\frac{i\omega}{4} \int_0^W \int_0^d \Big(\epsilon(r,z) - \epsilon_o \Big) \mathbf{E}_{\text{disk}} \cdot \mathbf{E}_{\text{wg}} \; r \, \mathrm{d}r \, \mathrm{d}z \right] e^{j\phi} \mathrm{d}\theta, \tag{95}$$

in which $\mathbf{E}_{\text{disk}}$ and $\mathbf{E}_{\text{wg}}$ correspond to the normalized amplitudes of the electric fields of the disk and the waveguide, respectively, θ_o is the angular range of the wrap-around coupling, d is the thickness of the guiding layer (i.e., Si_3N_4), and W is the width of the waveguide. $\epsilon(r,z) - \epsilon_o$ is the perturbation introduced to the microdisk mode by the waveguide and depends on the shape of the waveguide. Figure 55 shows the geometry of the coupled structures and the parameters used in our modeling. The phase factor ϕ in Eq. (95) is the difference between the propagation phases of the waveguide and

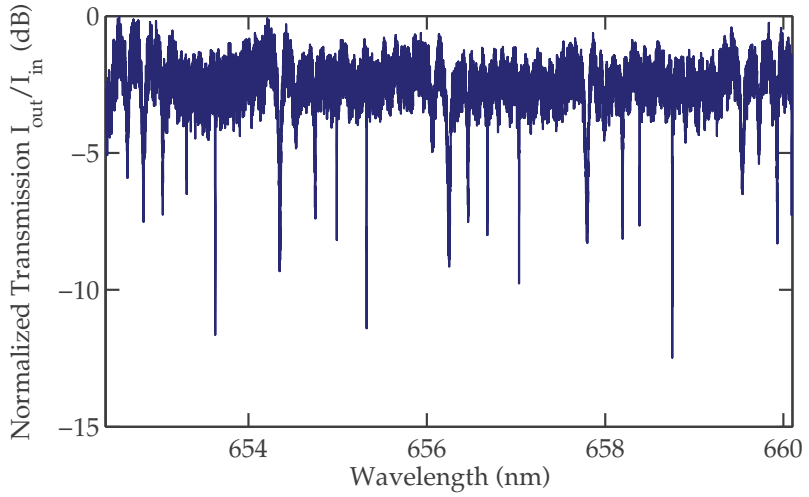

(a)

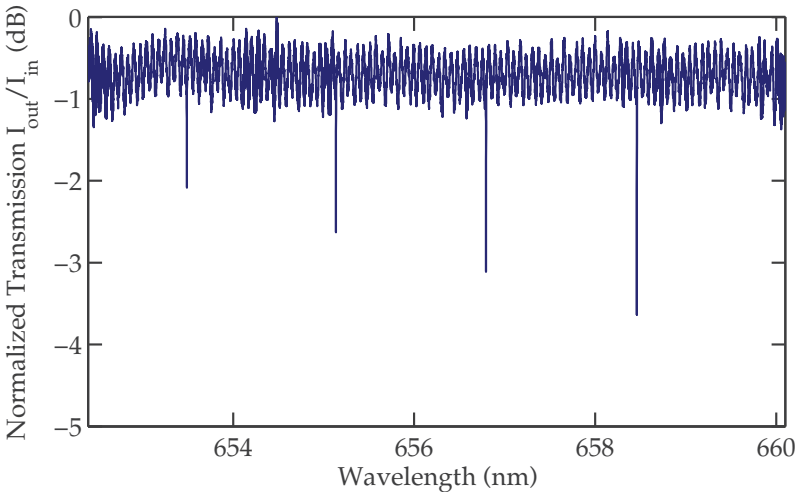

(b)

Figure 56: (a) The normalized transmission spectrum of a 20-micron-radius Si_3N_4 microdisk side coupled to a waveguide with a single point coupling scheme (see Fig. 56(a)). The coupling gap is 100 nm and several radial TE modes of the microdisk are excited. The waveguide width is 400 nm. The effective coupling length is about 4 μm. The polarization of the input waveguide is TE. (b) The normalized transmission of the waveguides coupled to the same microdisk as in (a) in the pulley configuration shown in Fig. 59(a). The coupling length is 30 μm and the coupling gap is 400 nm. The waveguide width is 390 nm and only the second radial order mode of the disk is excited. The strict phase matching condition does not allow the other radial modes of the microdisk to have significant coupling to the waveguide. The inset figure shows a Lorentzian fit to the transmission spectrum zoomed around one of the resonances showing a Q of 6×10^5.

the cavity modes and can be written as

$$\phi = -m\theta + \beta_{wg} R_{wg} \theta = -m\theta + k_o n_{wg} R_{wg} \theta, \tag{96}$$

in which $k_o = 2\pi/\lambda_o$ is the wavenumber in free space, β_{wg} is the propagation constant of the waveguide mode, and m is the azimuthal mode order of the resonator. Apparently, the effective radius of the curved waveguide (R_{wg}) is larger than the radius of the disk ($R_{wg}=R_{disk}+g+W/2$). Assuming that the width of the waveguide (W) and the coupling gap (g) remain constant throughout the coupling length, the term inside the brackets in Eq. (95) is independent of θ and can be written as S. Therefore, κ from Eq. (95) can be simplified as

$$\kappa = S \int_{-\theta_o}^{\theta_o} e^{j\theta(k_o n_{wg} R_{wg} - m)} \mathrm{d}\theta = 2\theta_o S \,\mathrm{sinc}\left[(k_o n_{wg} R_{wg} - m)\frac{\theta_o}{\pi}\right], \tag{97}$$

where $\mathrm{sinc}(u) = \sin(\pi u)/(\pi u)$.

It is clear form Eq. (97) that the phase mismatch ($\theta_o (k_o n_{wg} R_{wg} - m)$) between the two structures can reduce the coupling coefficient considerably. If the phase matching condition is met (i.e., $k_o n_{wg} R_{wg} = m$), the coupling coefficient is a linear function of the coupling length (which is proportional to θ_o). Conversely, if the phase mismatch builds up to a multiple of π, the coupling vanishes no matter how strong the field overlap is. It is also noteworthy that—similar to the results from the conformal transformation method for modeling waveguide-microring coupling [133]—the phase matching condition depends on the effective radius of the waveguide (R_{wg} in Fig. 55).

Since the phase velocity of different WGMs of the resonator in Fig. 55 vary across different radial modes, one can expect the phase matching condition to be mode-dependent. If the effective index of each radial mode is defined as ($n_{disk} \equiv m/k_o R_{disk}$), it is clear that the phase matching is achieved when $n_{wg} R_{wg} = n_{disk} R_{disk}$. The effective index of the waveguide is controllable by changing the waveguide width (W) within the range 150 nm $< W <$ 550 nm to ensure single mode guiding [132]. Increasing W results in larger effective indices for all waveguide modes. On the

other hand, the effective indices of of different radial mode orders of the microdisk resonator depend on the geometrical properties of the microdisk. Noting that the lower order modes of the microdisk have higher effective indices, the required W for phase matching is the largest for the fundamental microdisk mode.

FEM simulations are performed to obtain the field distribution of the first three radial microdisk TE modes (TE_1–TE_3) and the fundamental TE waveguide mode. These field distributions (obtained from the COMSOL FEM simulations) are then used in Eq. (95) to calculate the coupling coefficient (κ) between the cavity and the waveguide in the structure shown in Fig. 55. The calculated Q_c for the first three radial TE modes (TE_1–TE_3) as a function of W for waveguide-cavity gaps of $g = 400$ nm and $g = 200$ nm is shown in Figs. 57(a) and 57(b), respectively. The coupling length for both cases is 30 μm The calculated κ is then used to find the coupling quality factor ($Q_c = \omega_o/\kappa^2$) as a function of the waveguide width for the waveguide-cavity coupled structure shown in Fig. 55. The minimum of each Q_c curve in Fig. 57 corresponds to the highest level of coupling between the waveguide and each corresponding cavity mode. As expected from Eq. (97), the optimal waveguide width for coupling to each cavity mode is slightly smaller at a larger gap size. Moreover, increasing the coupling length (l), while increasing the coupling coefficient (i.e. $\kappa \propto l$), reduces the reproducibly of the design as the tolerance to fabrication errors in the width of the fabricated waveguide is reduced almost linearly with l. It is important to note that with our current results for the intrinsic Q (e.g., $Q_o(TE_2) = 6 \times 10^5$) it is possible to achieve close to critical coupling (i.e., $Q_c = Q_o$) with gaps larger than 400 nm by using appropriate coupling length l. Figure 57(a) shows that with gaps as large as $g = 400$ nm, it is possible to achieve coupling Qs close to 10^6 for some modes ($Q_c = 1.37 \times 10^6$ for TE_3 and $Q_c = 3.0 \times 10^6$ for TE_2). We can further reduce Q_c (i.e., stronger coupling or larger κ) for the same gap size by increasing the coupling length. This considerably facilitates the fabrication process as explained earlier. It is

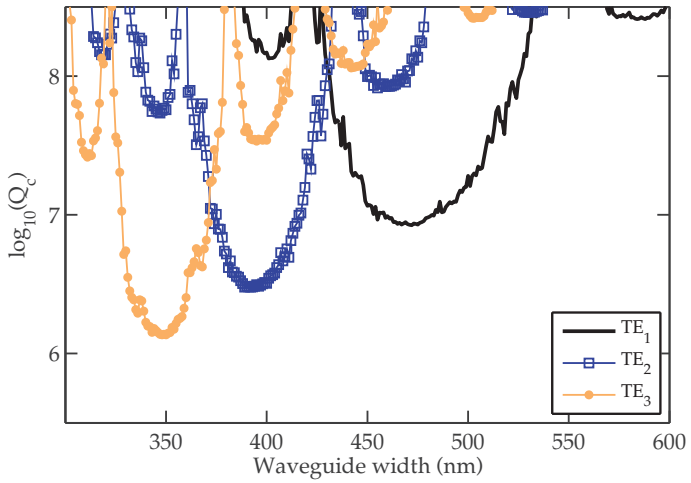

(a) $g = 400$ nm

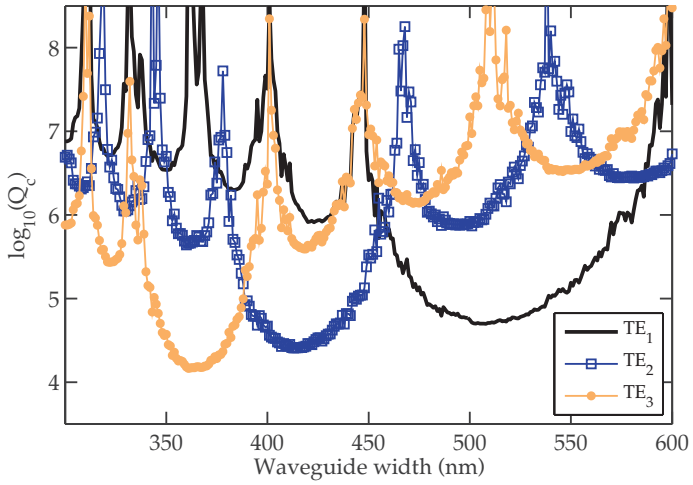

(b) $g = 200$ nm

Figure 57: (a) The simulated coupling quality factor (Q_c) of a 20 μm radius disk at $\lambda = 650$ nm when the waveguide wraps around the disk and the coupling length is 30 μm. As the width of the waveguide is changed, the phase matching condition is met for three different radial order TE modes of the disk. (a) The coupling gap size is $g = 400$ nm and the phase matching condition is met for the first three orders of the disk when the waveguide width is 470, 390 and 340 nm respectively. (b) The gap size is reduced to $g = 200$ nm, without changing any other parameter compared to part (a). The coupling is enhanced almost two orders of magnitude for all three modes. As the phase matching condition depends on the radius of the curved waveguide, all microdisk modes are coupled to slightly wider waveguides.

also clear from Fig. 57(a) that at the optimal coupling width (W) for each TE mode, coupling to the other modes is negligible due to the phase mismatch. This facilitates the highly desired single mode operation of the high Q resonators.

Another interesting feature is the width of each curve in Fig. 57 around its optimal point, which is an indicator of the tolerance of the optimal structure to the fabrication imperfection in the waveguide width W. It is clear from Fig. 57 that coupling to the lowest order resonance TE mode (i.e., TE_1) has better tolerance than that to the higher order modes. The tolerance of Q_c to fabrication imperfections is shown in Fig. 58. In Fig. 58, the normalized Q_c^{-1} is plotted in the dB scale for the three lower radial order TE modes. Depending on the tolerance required for Q_c, the width of each curve identifies the acceptable error in the width of the fabricated waveguides (δW) when $g = 400$ nm. Based on Fig. 58, the acceptable fabrication error for the first three radial order modes (assuming only 3 dB tolerance in Q_c) is $\delta W = \pm 26$ nm for TE_1, ± 16 nm for TE_2, and ± 14 nm for TE_3. These values, consideraing the high accuracy of the electron beam machine used, and also possibility of pre-fabrication corrections in the designs, is well within the achievable accuracy in our current fabrication facility.

5.1 Fabrication

It has been shown that reflowing the resist after development leads to smoother sidewalls resulting in higher Q's [3]. Therefore, the developed patterns on ZEP are reflowed on a hot plate at 160°C for 3–5 minutes depending on the desired sidewall smoothness and sidewall angle. Longer reflow times results in smoother sidewalls (as can be seen in Fig. 59(c) for a 5 minute reflow) but requires wider gap sizes as the waveguide and resonator with narrow coupling gaps stick to each other during the reflow process (the rest of the paper is based on the 3 minute reflow). With the 3 minute reflow process performed within 24 hours from the resist spinning, the

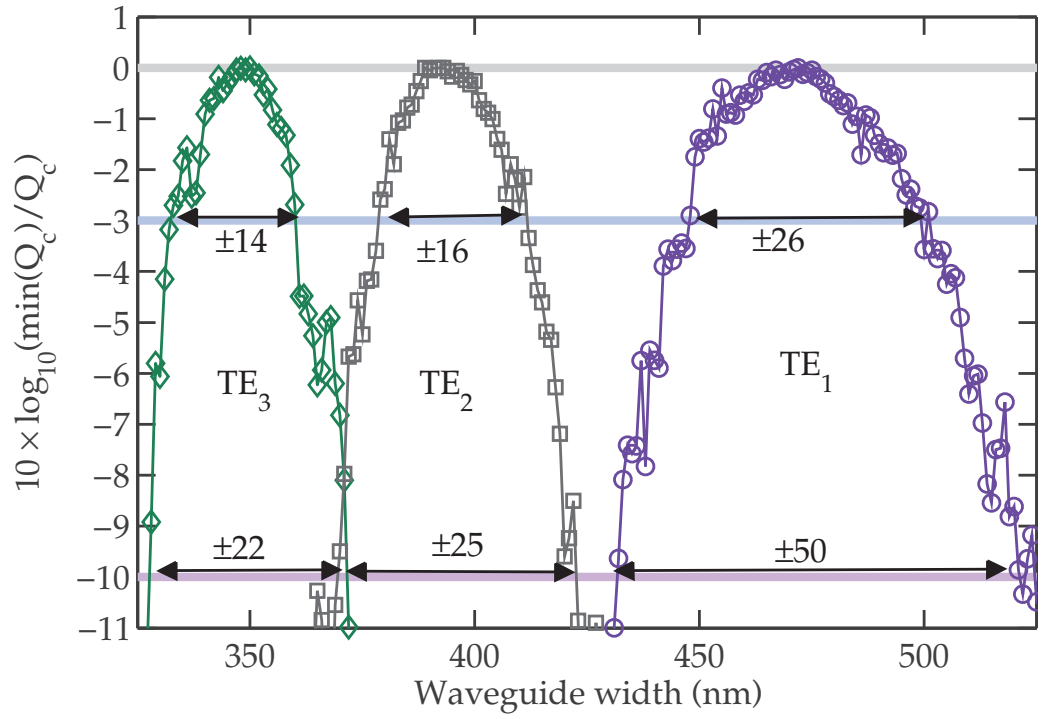

Figure 58: The normalized $1/Q_c$ of the waveguide-cavity coupling in the pulley configuration as shown in Fig. 55. The three curves depict the coupling of the waveguides to each of the three lower radial order TE modes. Each curve is normalized to the best coupling for each mode (occurring at the perfect phase matching condition for each mode). The vertical axis is in dB scale. The requiring tolerance in Q_c imposes a certain accuracy requirement on the width of the fabricated waveguides; the required accuracy depends on the length of coupling (l), and the radial order chosen (TE_1, TE_2, or TE_3). When the coupling length is 30 μm and the coupling gap is 400 nm, the 3dB fabrication tolerance of the waveguide width (δW) is ± 26, ± 16 and ± 14 for the three first TE modes (TE_1-TE_3), respectively.

waveguides become 90 ± 10 nm narrower than the e-beam written patterns. Etching is then performed using CF_4 gas in an inductively coupled plasma (ICP) etcher. The sidewall roughness is inspected with scanning electron microscopy which shows very high quality of the sidewalls.

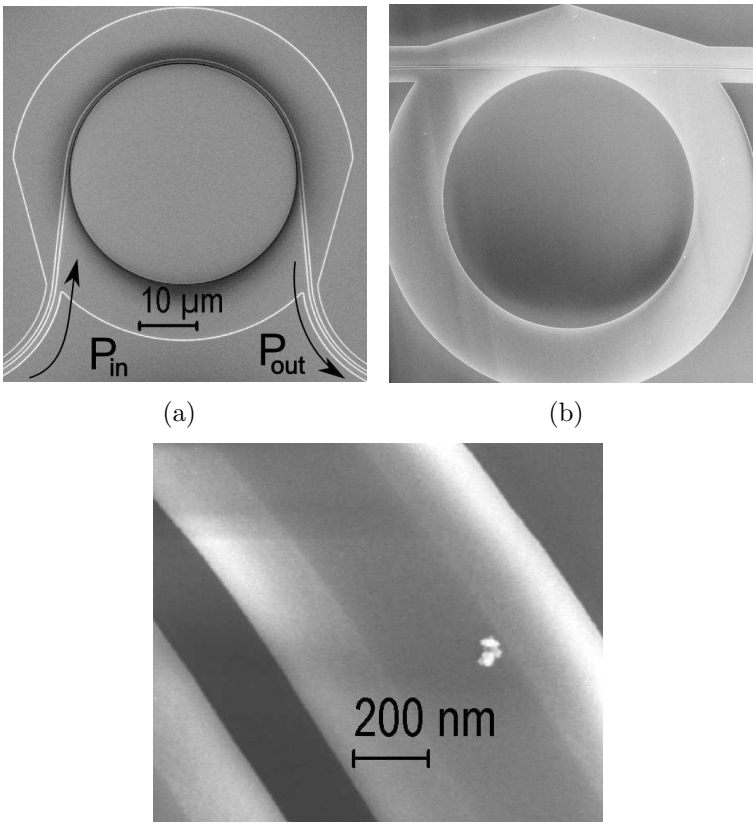

(a) (b)

(c)

Figure 59: (a) The pulley coupling configuration in which the waveguide wraps around the microdisk resonator to increase the effective coupling length. The phase matching to different radial modes of the microdisk is achieved by the choice of the waveguide width. (b) The conventional straight coupling configuration in which the waveguide couples to the microdisk only at a single point. In this configuration the effective interaction length is significantly shorter than the pulley scheme depicted in (a), making the coupling much less sensitive to the phase matching condition. (c) Top view of an SEM image of a waveguide etched on a 200 nm layer of Si_3N_4 on top of an isolating SiO_2 layer on a Si substrate with a 5 minute reflow of the resist. The reflow process leads to smooth but tilted sidewalls.

5.2 Characterization

To demonstrates the practicality of the optimal design criteria shown in Fig. 57, structures with three different waveguides widths (W=470, 390, and 340 nm) were fabricated in both single waveguide and add-drop configurations. The waveguides are all single mode for the desired range of wavelengths (652–660 nm). Figures 60(a) and 60(b) depict the normalized transmission for the single waveguides coupled to TE_1 and TE_2 with W of 470 nm and 390 nm, respectively. The coupling gap is 400 nm for all the fabricated structures. To identify the radial mode order in each case in Fig. 60, we compared the measured free spectral range (FSR) with the theoretically calculated FSRs of different radial mode orders. The resonant mode in the structure with $W = 470$ nm (Fig. 60(a)) has the largest FSR=1.632 nm, and it corresponds to the TE_1 mode. Similarly the resonant dips in the transmission spectrum of the structure with W=390 nm (shown in Fig. 60(b)) correspond to an FSR of 1.658 nm and are attributed to the TE_2 mode.

Finally, Fig. 60(c) depicts the output of the drop waveguide when the through and the drop waveguides are both chosen to be 340 nm wide. In such structures, power is transferred to the drop port only when the third order mode of the microdisk is in resonance. Thus, such an add-drop filter is practically single mode even though the microdisk—unlike a microring—is multimode.

Comparison of Fig. 60 and Fig. 57 shows that for each waveguide width design, the waveguide mode couples better to the resonator mode for which stronger coupling (or smaller Q_c) exists. Fig 57(a) clearly shows that at $W = 470$ nm, 390 nm, and 340 nm, Q_c is the smallest for TE_1, TE_2, and TE_3, respectively. Thusn the results shown in Fig. 60 confirm the finding in Fig. 57(a) about the optimal waveguide width (W) for each resonator mode.

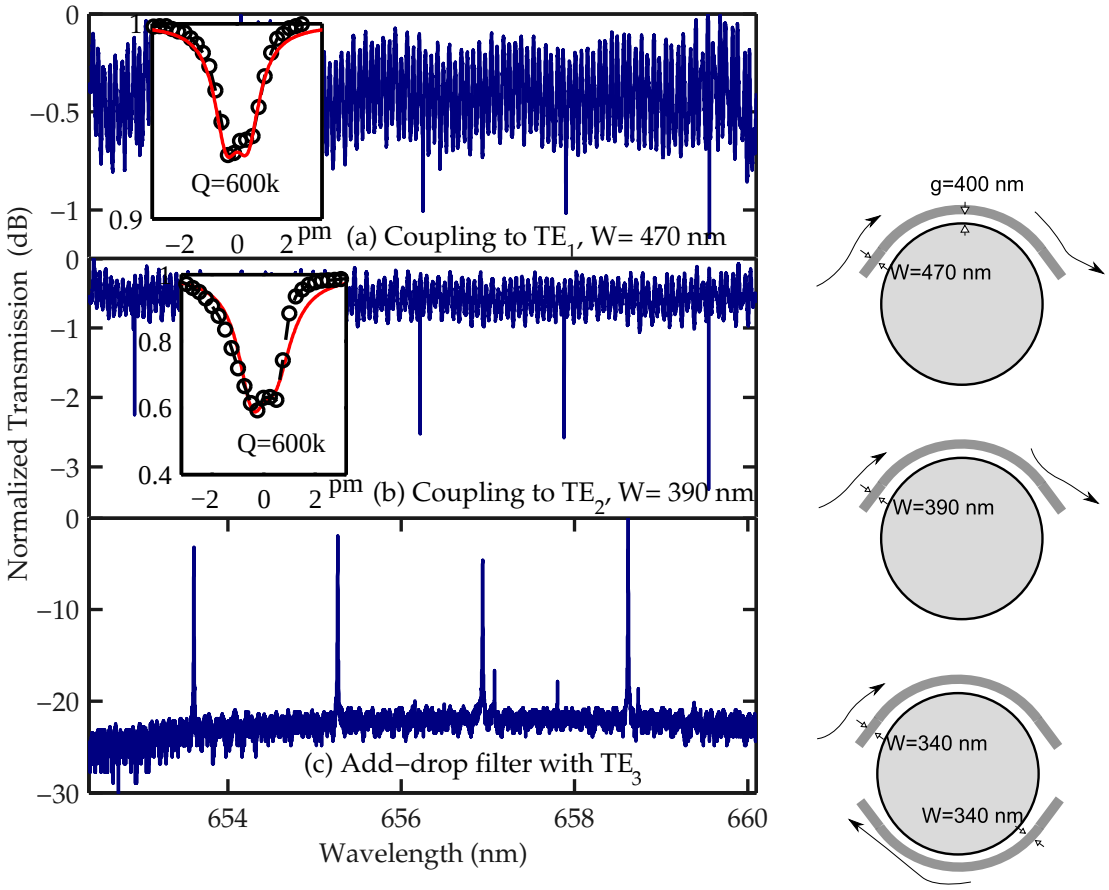

Figure 60: The normalized transmission of a single-mode, curved waveguide coupled to a microdisk with radius $R = 20\,\mu$m in the pulley configuration as shown in Fig. 59(a). The coupling length is $l = 30\ \mu$m, and the coupling gap is 400 nm: (a) coupling to the first order microdisk TE mode with $W = 470$ nm; and (b) coupling to the second order microdisk TE mode with $W = 390$ nm. As the waveguide width is reduced, the effective index of the guided mode is reduced, thus higher order resonator modes are phase-matched to the waveguide. (c) The transmission spectrum of the drop port in an add-drop filter with both waveguides being 340 nm wide. Power is transferred to the drop port only when the third radial order TE mode of the microdisk is resonant.

5.3 conclusion

In summary, we presented here a detailed investigation of the properties of pulley coupled Si_3N_4 microdisk resonators on substrate at visible wavelengths. We showed that it is possible to fabricate these structures with larger coupling gaps taking advantage of the increased interaction length when the waveguide wraps around the resonator. Larger gaps make the reflow process possible to reduce the sidewall roughness of the microdisks and increase the quality factor of resonances. Moreover, the coupling along a pulley-shaped coupler is phase dependent and by choosing the proper width for the waveguide, single mode operation of the microdisk based devices (e.g. filters) is possible.

CHAPTER VI

MICROFLUIDIC INTEGRATION

The microfluidic integration of optical chips with the usually aqueous solutions can be done by three major methods.

- SU-8 photolithography with glass/PDMS capping.
- PDMS stamps.
- Decomposable polymers.

In the following sections each of the three methods are briefly introduced and our approach (with a decomposable polymer) is discussed in detail.

The first method uses Su-8 as the channel material. SU-8 is a high contrast, epoxy[1] based photoresist designed for micro-machining and other microelectronic applications, where a thick chemically and thermally stable image is desired. The exposed and subsequently cross-linked portions of the film are rendered insoluble to liquid developers. SU-8 has very high optical transparency above 360 nm, which makes it ideally suited for imaging near vertical sidewalls in very thick films. SU-8 is best suited for permanent applications where it is imaged, cured and left in place. After the channels are defined using photolithography (with a dark-field mask) the liquid can be dropped on top of the reaction area or flown into the channels. If pressure driven flow (PDF) is required, channels can be covered either by a Polydimethylsiloxane (PDMS) layer or a glass cover. In the later case, access holes need to be etched through the glass cover.

[1]Epoxy or polyepoxide is a thermosetting polymer formed from reaction of an epoxide "resin" with polyamine "hardener".

In the second method, a clear field mask is used to define the channel molds in SU-8, the SU-8 mold is made hydrophobic with a layer of Au evaporated and PDMS (Polydimethylsiloxane) is poured over the mold. After curing for 2 hours at 80°C (during which the reservoirs can be incorporated in the film, as shown in 61(a)), the PDMS can be peeled off the mold. Then the PDMS piece should be made hydrophilic if a permanent and watertight structure is needed. To achieve this the sample is exposed to an oxygen plasma in an RIE machine. It is shown [135] that there is an optimum time for the exposure. If the RIE treatment is longer than 25 seconds the bond strength is degraded. Thus the PDMS is treated at following RIE conditions: time=25 sec, pressure=200 mTorr, RIE power=70 W. If the sample remains exposed to air for a long time, a treatment in diluted (1:5) HCl is necessary before the oxygen plasma. After the oxygen treatment the PDMS surface retains its hydrophilic property for 15 minutes, which is enough for a proper alignment with the optical devices.

To flow the liquids into the channels there are two common methods. The first method (Pressure driven flow or PDF) utilizes a pressure build up between the two reservoirs 61. The other major method is the electroosmotic flow (EOF).

The generally required parameters of microfluidics, namely small size, small velocity and large viscosity, combine in devices to result in generally small values of an important dimensionless parameter, the Reynolds number [136]:

$$Rey = wb/\nu, \tag{98}$$

where w[m/s] is the characteristic flow velocity, b[m] is the characteristic dimension and ν[m^2/m] is kinematic viscosity of the fluid. The ν parameter for water is 1.01. b is typically the smallest dimension along the channel. Due to the small dimensions of micro-channels, the Rey is usually much less than 100, often less than 1.0. In this Reynolds number regime, flow is completely laminar and no turbulence occurs. The transition to turbulent flow generally occurs in the range of Reynolds number 2000.

Laminar flow provides a means by which molecules can be transported in a relatively predictable manner through micro-channels. One of the basic laws of fluid mechanics for pressure driven laminar flow, the so-called no-slip boundary condition, states that the fluid velocity at the walls must be zero. This produces a parabolic velocity profile within the channel. despite the simplicity of the pressure driven approach—which only needs a syringe pump or a vacuum line—the drawback is non-scalability of the devices. As for a rectangular channel with a characteristic dimension d and for a circular shaped tube with a radius r, the pressure needed for a certain velocity scales with:

$$\Delta P \propto 1/wd^3$$

and

$$\Delta P \propto 1/r^4.$$

This, imposes a limit on the size of the channels and makes nanofluicid with manageable pressures impossible. Therefore, if the channel sizes are smaller than roughly 10 microns the electroosmotic flow is the preferred method.

Electroosmotic flow (often abbreviated as EOF and synonymous with electroosmosis or electroendosmosis) is the motion of liquid induced by an applied potential across a porous material, capillary tube, membrane, micro-channel, or any other fluid conduit. Because electroosmotic velocities are independent of conduit size, as long as the double layer is much smaller than the characteristic length scale of the channel, electroosmotic flow is most significant when in small channels. Therefore, in the smalled channels described in the following sections the flow is achieved by applying a high voltage (200 V) through a pair of platinum electrodes across the LB conductive medium obtained from “Faster Better Media LLC”.

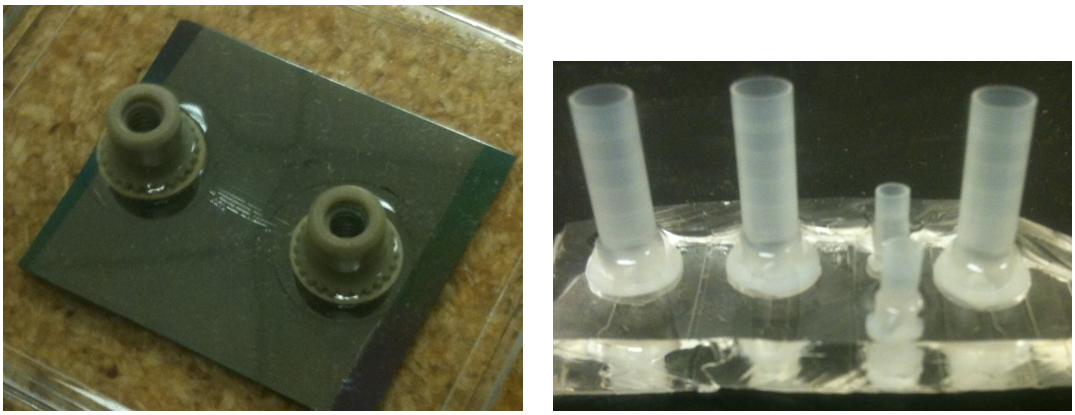

(a) SU-8 microchannels

(b) PDMS microchannels

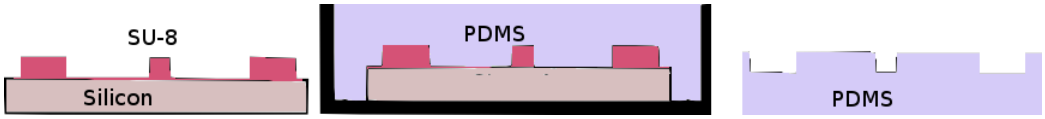

(c) PDMS molding

Figure 61: (a) A fluidic structure made with SU-8, capped with PDMS and interfaced with nanoport reservoirs. (b) PDMS stamps with the reservoirs incorporated into them during the curing. (c) The process of molding of PDMS channels.

6.1 Microfluidic integration with sacrificial polymers

This research investigates a heat de-polymerizable polycarbonate (HDP) for use as a sacrificial layer in fabricating nanofluidic devices by electron beam or photolithography. The material used is a photosensitive polynorbornene (PNB)-based polymers (Fig. 62) When solid HDP films are heated to 400°C, the monomer units separate into a nontoxic vapor. This property suggests that a patterned HDP film may be used as a temporary support for another film which is stable at the de-polymerization temperature. Heating the structure removes the HDP, leaving a single channel or a network of micro/nanofluidic tubes without the use of solvents or other chemicals as required in most other sacrificial layer processes. The HDP films can be patterned either by photo-lithography [137] or directly by electron beam lithography [138]. The patterned polycarbonate structures could be coated with an overcoat layer and thermally decomposed. Since polynorbornene-based Unity can permeate through overcoat dielectrics, venting ports are not required.

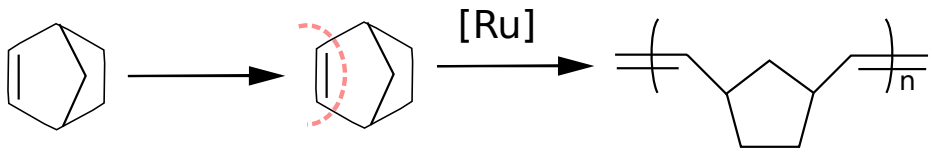

Figure 62: Polynorbornene.

In this project we mainly used two polymers (from the same family but with different viscosities). The first was Unity (for thin films) and the second was Avatrel both provided by Promerus.

The Unity 4671E process is as follows:

1. spun coated at 1000 rpm for 60 s for expected thickness of 620 nm
2. soft baked at 100°C for 5 min to evaporate the solvent
3. exposed by EBL at 100 kV acceleration voltage and 2 nA beam current with a 5 C/cm^2 dosage
4. post-exposure baked at 90°C for 30 s to cross link the polymer
5. developed in toluene for 45 s to remove the unexposed areas
6. 1 min rinse in isopropanol by an squeeze bottle to remove the residues and also the developer
7. descum in an RIE oxygen plasma to make sure there is no residual polymer left on the wafer
8. covered with a 1-micron-thick PECVD oxide at 250°C
9. heated to 450°C in a nitrogen-filled furnace for several hours to decompose the Unity

The final structure can be seen in Fig. 63

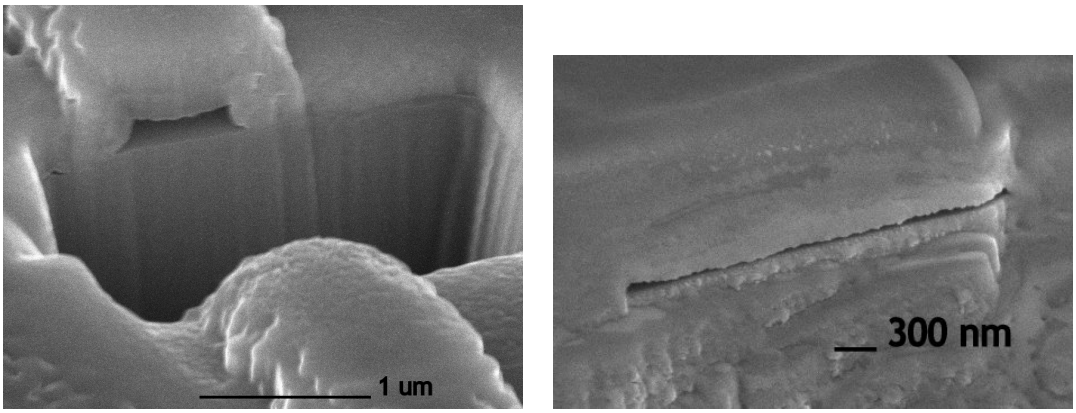

(a) Unity nanochannel (b) Sub 100nm thin channels with Unity

Figure 63: Channels fabricated with Unity.

For thicker films, which can facilitate pressure driven flow, the Avatrel polymer is used as follows:

1. remove the polymer mixture from the freezer and let it stand at room temperature for two hours
2. spun coated at 500 rpm for 10 seconds followed by 900 rpm for 30 seconds to get almost 7.5 μm thick films
3. soft baked at 110°C for 5 min to evaporate the solvent
4. exposed by EBL at 100 kV acceleration voltage and 2 nA beam current with a 10 C/cm^2 base dosage or photolithography with 400 mJ
5. post-exposure baked at 90°C for 4 minutes followed by 4 minute cooling time
6. developed in cyclopentanone for several minutes till no residue is visible
7. 1 min rinse in isopropanol by an squeeze bottle and descum in for one minute
8. covered with a 10-micron-thick PECVD oxide at 250°C
9. heated to 450°C in a nitrogen-filled furnace for several hours

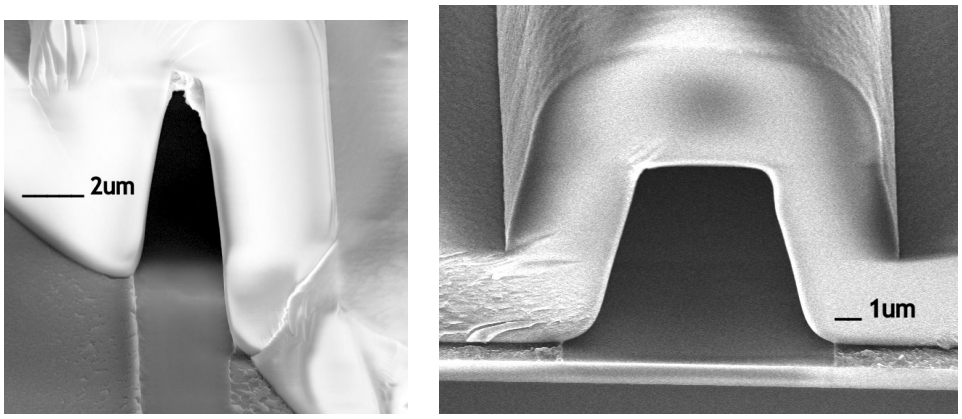

(a) High aspect ratio channel fabricated with Avatrel.

(b) Wider channel.

Figure 64: Channels fabricated with Avatrel using electron beam lithography.

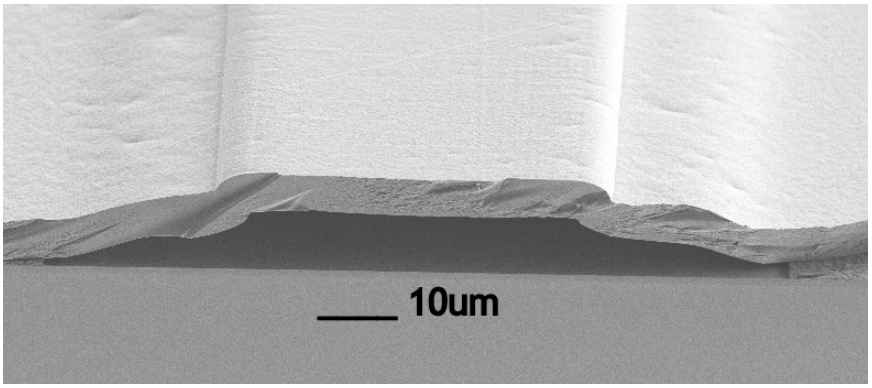

(a) Residues from proximity effects for wider channels lift the sides of the channel.

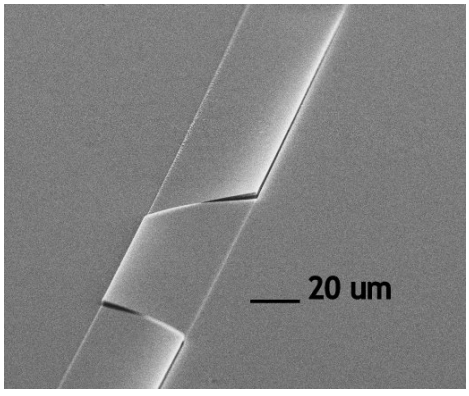

(b) If the thickness of the oxide cap is not large enough, thermal stress breaks the channels.

Figure 65: Channels fabricated with Avatrel using electron beam lithography. (a) the effect of the residues before oxide capping, and (b) the effect of small height/width for oxide capping.

The resulting structures can be seen in Fig. 64. As it can be seen in this figure, there is no residue inside the channels, which is promising for optofluidic integration, as otherwise the performance of the optical devices would be highly degraded.

After the channel fabrication is optimized, integration with optical devices is the logical next step. We needed to overcome several challenges for this process. The first challenge was that the very first devices would not pass the fluid. Further investigation showed that the decomposition process leaves the inside surfaces of the channels hydrophobic. It is virtually impossible to flow a liquid through a narrow hydrophobic channel. A high temperature oxygen plasma in an asher makes the channels hydrophilic and the fluid flows inside the channels (as can be seen in Fig. 66).

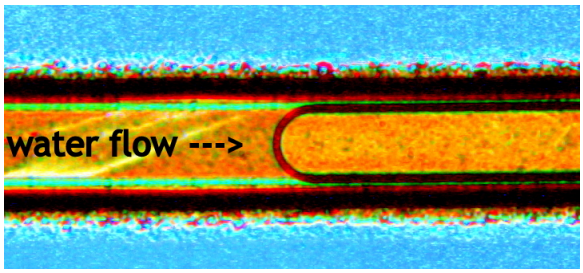

Figure 66: Flow of water inside the channel.

The next challenge was to make sure no residue is left inside the channels (otherwise the performance of the optical devices would be degraded). Usually for conventional photonic devices a piranha clean removes the residues effectively. Piranha solution, also known as piranha etch, is a mixture of sulfuric acid and hydrogen peroxide, used to clean organic residues off substrates. Because the mixture is a strong oxidizer, it will remove most organic matter, and it will also hydroxylate most surfaces (add OH groups), making them extremely hydrophilic (water compatible). But because of the bubbles generated during the piranha etch this process is not compatible with these channels. Instead a solution of chromic acid is used. Chromic acid is a mixture made by adding concentrated sulfuric acid to a dichromate, which

may contain a variety of compounds, including solid chromium trioxide. Another

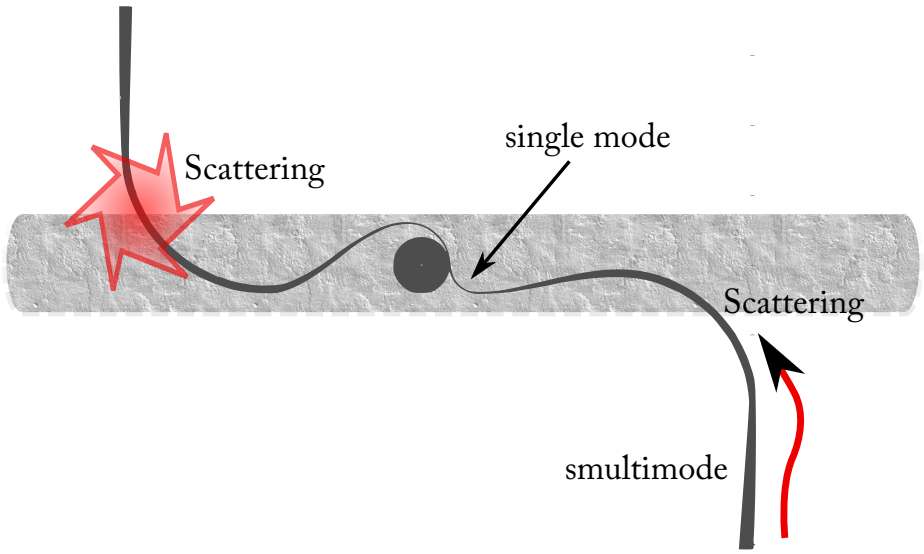

Figure 67: The size of the disk puts an upper limit on the width of the channel. Scattering from the waveguide-channel interface can be reduced by using a multimode waveguide at the interface.

issue to be considered is the scattering of light from the waveguide-channel interface. As the index mismatch between the oxide covered sections and the channel is large (specially if no fluid is flowing inside the channel), a large portion of the optical guided wave is scattered at the boundary (Fig. 67). To alleviate this problem we used large multi-mode waveguides at the intersection and tapered the waveguide to a single mode profile inside the channels. Considering this issue, it is undesirable to cover a ring resonator with the channels only partially, as this would lead to very low quality factors due to the scattering.

As we need to cover the resonators with the channels, the width of the channels should be larger than the diameter of the resonators used (20-40 microns). This leads to fragile overcoats (Fig. (b)) unless a thick oxide layer is used, which in turn leads to longer and higher temperature decomposition conditions.

6.2 Characterization

The characterization setup used for index change and florescence measurements is depicted in Fig. 68. As can be seen in the figure, red light laser beam (652–660 nm) enters the setup from the left. A quarter wave plate and a polarizer ensure the light energy is in the TE mode. A Mitutoyo 20x long distance objective is used to couple the light into the structures. One long distant lens and one regular objective are used to collect light from the top and the output respectively.

A custom-built microscope in the Z direction is used for most of the analysis. As shown in Fig. 68, using 50/50 polarizing beam splitters, a spectrometer, a detector and a camera are integrated in the microscope. For all the setup structures Thorlabs 30 mm cage system where used. The cage system is very versatile and stable and allowed fast and easy reconfigurations in the setup without requiring an extensive alignment readjustment. The only necessary part lacking to this day is a cage-mountable flip mirror (which would increase the measured power by eliminating some of the beam splitters.)

As a test of the capabilities of our system to measure fluorescence, the output of a waveguide covered with 60 mg/lit Oxazine dye (Abs/Em at 646/670 nm) is measured with an Ocean Optics spectrometer. A sharp edge filter (with an optical density (OD) of over 70 is used to filter out the pump). The unfiltered and filtered spectra are shown in Fig. 69.

6.3 Outlook

In this chapter we showed that it is possible to integrate micro/nano channels with optical devices. The channels made with low-temperature decomposability are the most promising for future applications. Considering possible size reduction of the photonic devices (specially through photonic crystal cavities discussed in this thesis), it is possible to shrink the size of the channels even further and achieve ultra-small

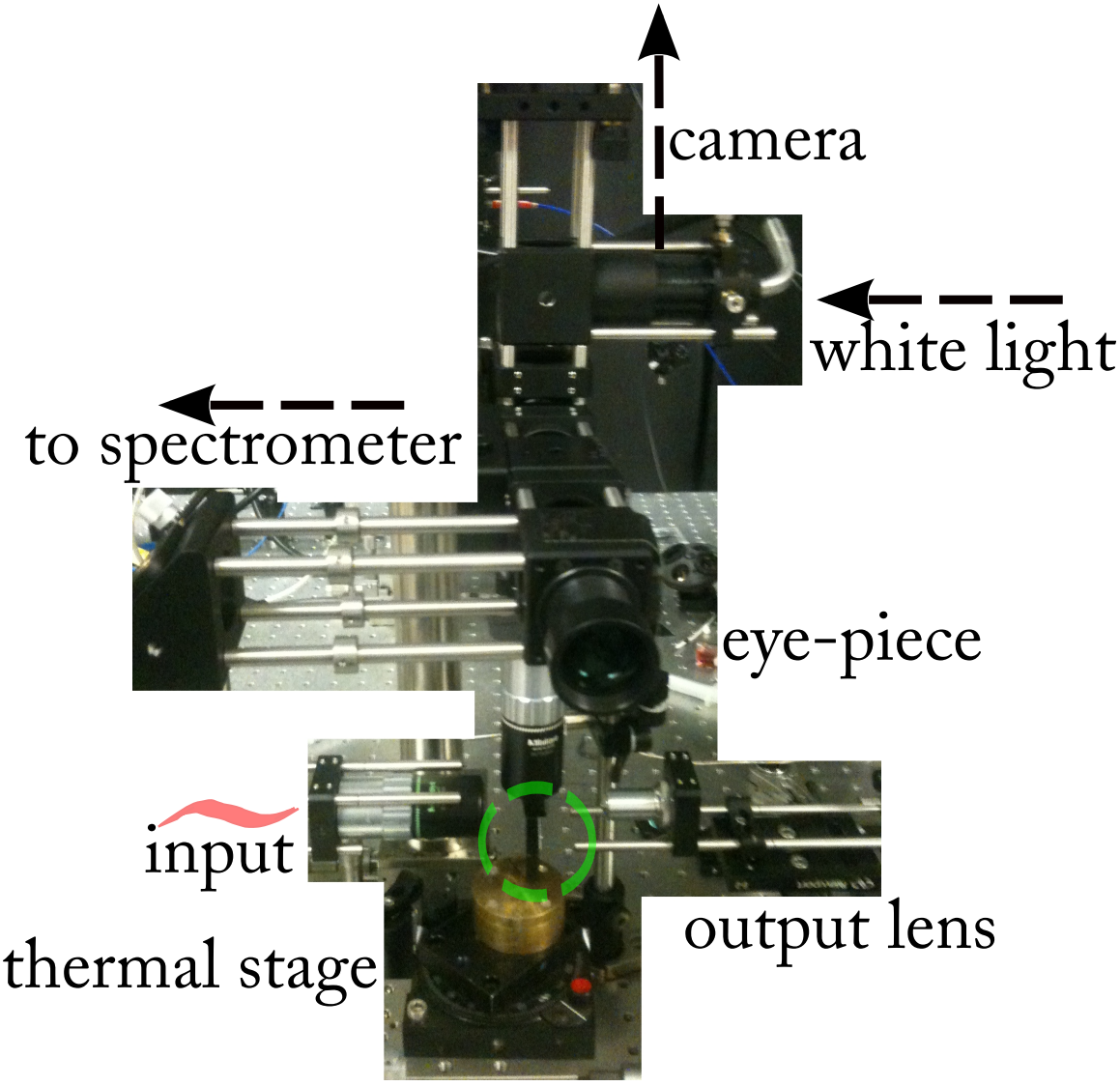

Figure 68: The size of the disk puts an upper limit on the width of the channel. Scattering from the waveguide-channel interface can be reduced by using a multimode waveguide at the interface.

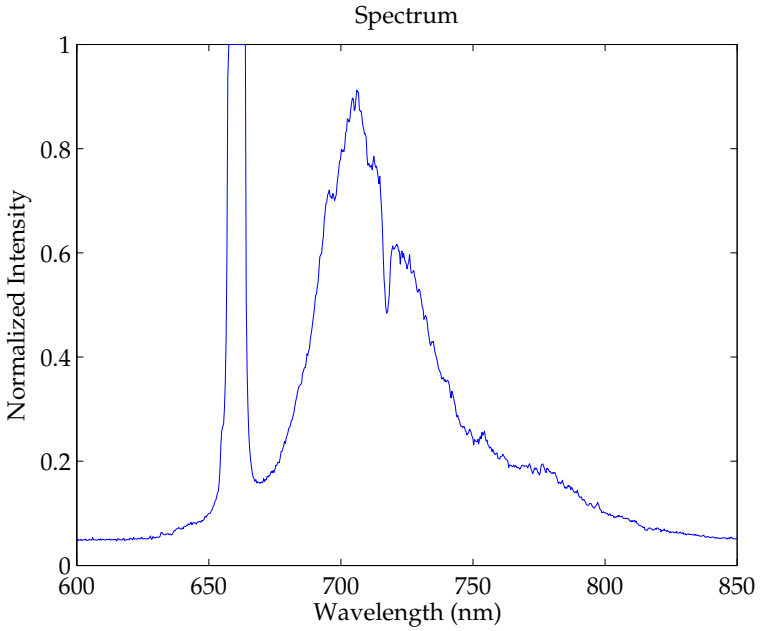

(a)

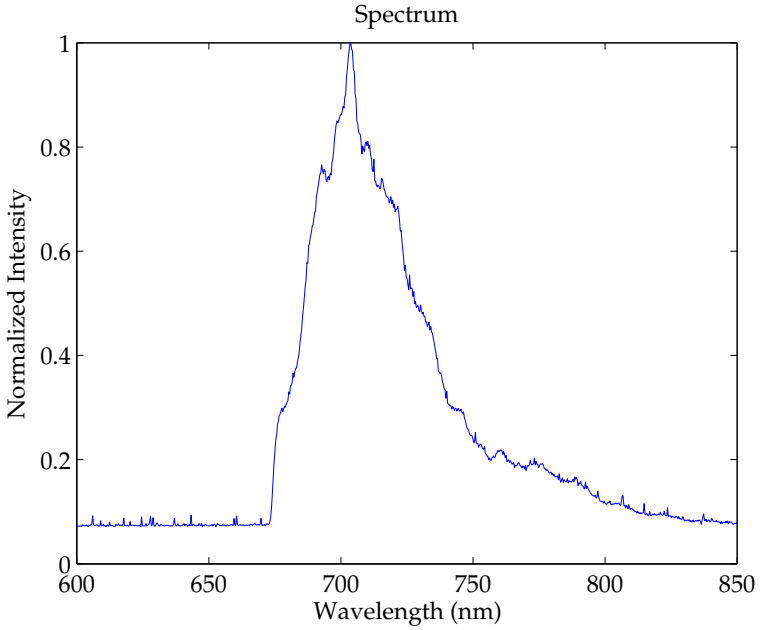

(b)

Figure 69: (a) Fluorescence from Oxazine pumped and collected with SiN waveguides. (b) The pump signal is filtered out.

sample sizes and multi-mode sensing functionalities through florescence and Raman signals. The Raman signal can be excited and collected through metallic nanoparticles fabricated on top of the photonic devices and integrated with nanofluidic channels for single molecule sensing. The SEM of such devices, which are under development in our group, is depicted in Fig.

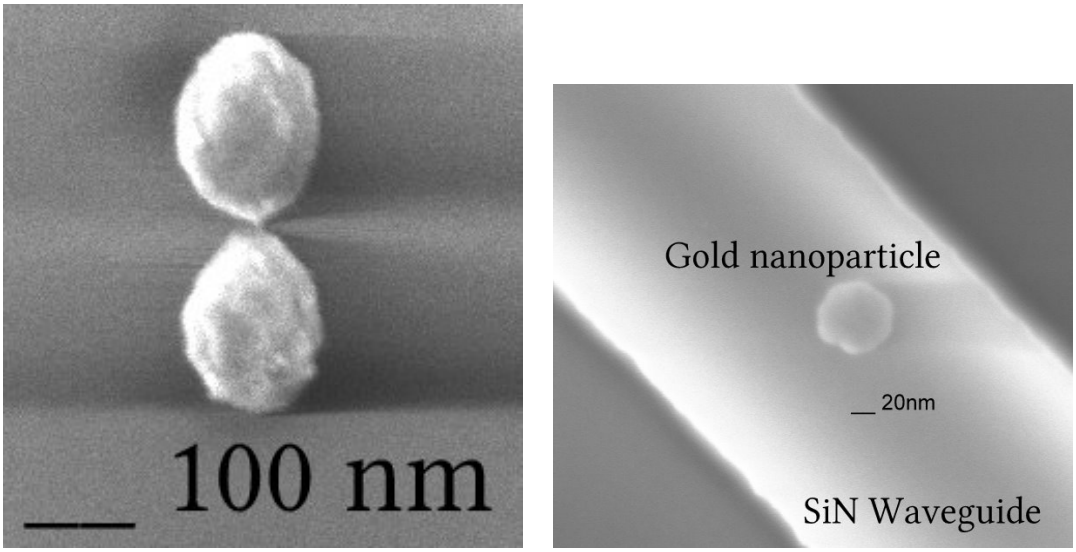

(a) (b)

Figure 70: (a) Gold dimer nanoparticle fabricated with the lift-off process. (b) Integration of nanoparticles on top of SiN waveguides.

CHAPTER VII

SUPERPRISM SPECTROMETER

7.1 abstract

We demonstrate the feasibility of forming a compact integrated photonic spectrometer for operation in the visible wavelength range using the dispersive properties of a planar photonic crystal structure fabricated in silicon nitride. High wavelength resolution and compact device sizes in these spectrometers are enabled by combining superprism effect, negative diffraction effect, and negative refraction effect in a 45°-rotated square lattice photonic crystal. Our experimental demonstration shows 1.2 nm wavelength resolution in a 70μm by 130μm photonic crystal structure with better performance than alternative structures for on-chip spectroscopy, confirming the unique capability of the proposed approach to realize *compact* integrated spectrometers.

7.2 Introduction

The potential of integrated photonic platforms to realize strong light-matter interaction and efficient sensing functionalities in a compact structure has been the driving force for the emerging field of integrated photonic sensors. Different integrated sensing platforms and devices have been proposed to implement a variety of mechanisms for biological and chemical sensing [76, 77, 139, 140, 141, 142]. Many such sensing mechanisms of interest (e.g., fluorescence and surface-enhanced Raman effects) rely on optical phenomena that occur in the visible wavelength range, which require the development of functional integrated photonic structures in the visible range.

Development of the required components in SiN to form a complete sensing system is the next step in the path to capacitate these systems to address major demands

of different sensing applications. Spectrometers, which enable spectral analysis and detection of spectral emission and absorption features, are one of the essential building blocks required to implement the systems needed for many sensing applications. While conventional sensing approaches rely on using bulky off-chip spectrometers, the need for compact mobile or handheld structures has motivated extensive recent progress in the development of integrated onchip microspectrometers [143].

Several approaches to realize compact spectrometers in the visible range have been proposed previously, including off-chip separation of wavelengths [144], grating spectrometers in low index contrast material [145], frequency-selective detection of light [146], polymer-based implementation [147], and integrated optical spectrometers [148]. However, all these approaches require large structures and offer limited spectral resolution. The focus of this section is to use the relatively large index contrast in Si_3N_4 on SiO_2 (through fabricating strongly dispersive photonic crystals) to demonstrate the potential for realizing high-resolution, integrated photonic spectrometers with a very small footprint in the visible wavelength range (around 656 nm). The availability of compact spectrometers enables new sensing mechanisms (e.g., monitoring fluorescence and Raman spectra) and new sensing architectures (e.g., multiplexing several resonators for parallel sensing) [142] in the visible integrated photonic systems. The potential integration of silicon detectors and electronic processing units in a compatible platform with Si_3N_4 sensing components offers a unique prospective for the future of such modules for low-cost, compact, sensitive, and portable sensing applications.

In the following sections, the demonstration of a photonic crystal spectrometer in SiN is described. In Section 7.3, the operation principle and theoretical background of these spectrometers are explained. In Section 7.4, the process of fabricating these spectrometer devices and the experimental characterization results are presented. The implementation issues are discussed and future steps to further improve the

spectrometer performance are laid out in Section 7.5. Finally, in Section 7.6, the results are summarized and conclusions are made.

7.3 Operation principle

Implementation of compact on-chip spectrometers naturally require a mechanism to differentiate between the wavelengths of the input light. This differentiation may occur in a lumped element (e.g., at an interface) as in grating spectrometers [149], using the dispersion of a set of waveguides as in arrayed waveguide gratings [150], or through propagation in a dispersive material as in superprism-based devices [151]. It is clear that employing stronger dispersion in all these cases results in more compact high-resolution devices. Here, we use the superprism effect in photonic crystals as the main mechanism to achieve spatial spectral mapping in the spectrometer. We follow the basic principle used in silicon-based focusing superprism wavelength demultiplexers [152] to realize compact devices in SiN. The operation concept is based on combining the superprism effect, the negative diffraction effect, and the negative refraction effect inside a photonic crystal structure. The overall configuration is schematically visualized in Fig. 71(a), in which different wavelengths are separated inside the photonic crystal region.

In this approach, the angular dispersion inside the photonic crystal is used to steer different wavelengths in different directions inside the structure. At the same time, the negative diffraction property is used to focus the (initially broadened) beam into small spots at the output to make the overall device compact, and the negative refraction is employed to separate the signal of interest from unwanted stray light [152]. It can be observed that the in-plane band structure of the first TE-like mode (i.e., electric field inside the plane of periodicity of the photonic crystal) of a 45°-rotated square lattice photonic crystal, as shown in Fig. 71(b), satisfies all the requirements for achieving superprism, negative diffraction, and negative refraction simultaneously.

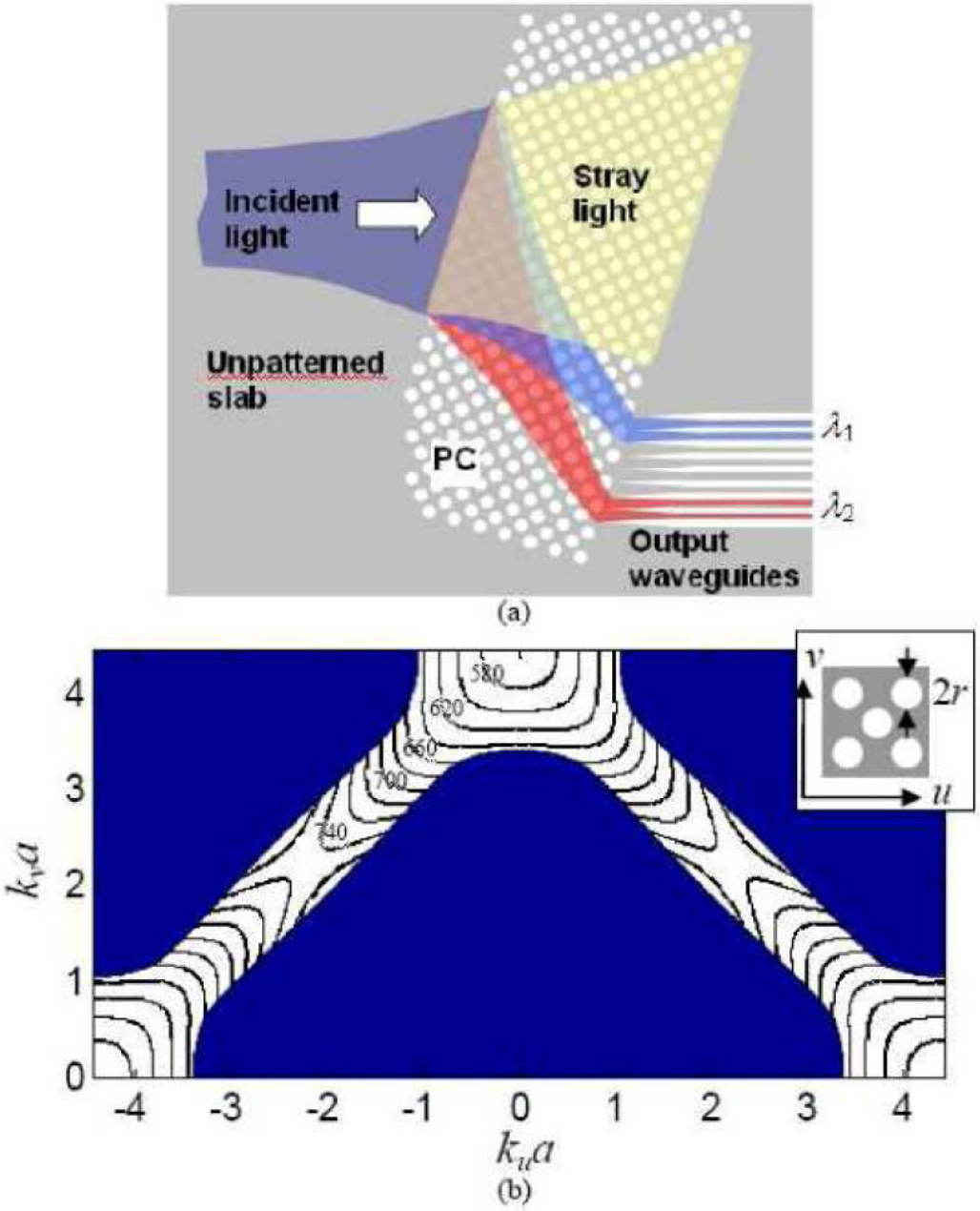

Figure 71: (a) Schematic visualization of the wavelength separation in a focusing superprism photonic crystal spectrometer is shown. (b) Band structure of a 45°–rotated square lattice planar photonic crystal in SiN on oxide, with holes of 85 nm radius and a lattice constant of 240 nm is shown. Numbers on each contour are the corresponding wavelength for that contour. The shaded regions exclude the modes that leak to the substrate and are not confined to the SiN layer slab. The inset shows the relative direction of the lattice with respect to the principal lattice directions.

This band structure is calculated using a three dimensional plane wave expansion method (based on a supercell) considering the finite thickness of the SiN slab (205 nm). The diameter of holes in this simulation is 170 nm, and the lattice constant is 240 nm. As it can be seen from Fig. 71(b), in this structure there is an operation range below the light line that shows strong dispersion effects while demonstrating simultaneous negative diffraction and negative refraction. To explore the extent of strong dispersion in this structure, we can also consider higher photonic bands of the planar photonic crystal [153]; however, because of the limited contrast between the SiN layer and the underneath SiO_2 layer, higher photonic bands of this planar structure are not confined to the slab anymore.

To find the optimal device parameters, we use the envelope transfer function [154] to approximately model the beam propagation inside the photonic crystal region. The configuration of the structure used in this modeling is shown in Fig. 72(a). The input beam is incident on the photonic crystal interface from an unpatterned slab region (to simulate the operation of the actual device) at an incident angle of 13°in this case. The beam undergoes some diffractive broadening prior to entering the photonic crystal region, such that the overall second-order diffraction is canceled at the output of the device at the center wavelength of 656 nm. The width of the photonic crystal region is L = 70 μm, and it has a 45°-rotated square lattice with lattice constant a = 240 nm and hole diameter 2r = 170 nm. Figure 72(b) shows the simulated intensity of the beam at the output of the photonic crystal region at three different wavelengths. The separation of adjacent wavelength channels with wavelength difference $\lambda = 2.4$ nm is evident from Fig. 72(b). For this structure, two non-idealities determine the crosstalk between these wavelength channels: (1) relatively strong side-lobes in the intensity profile introduced by the third-order diffraction effect in these structures [155], and (2) second-order broadening at wavelengths away from the center wavelength of operation. These effects degrade the cross-talk isolation level from potentially higher

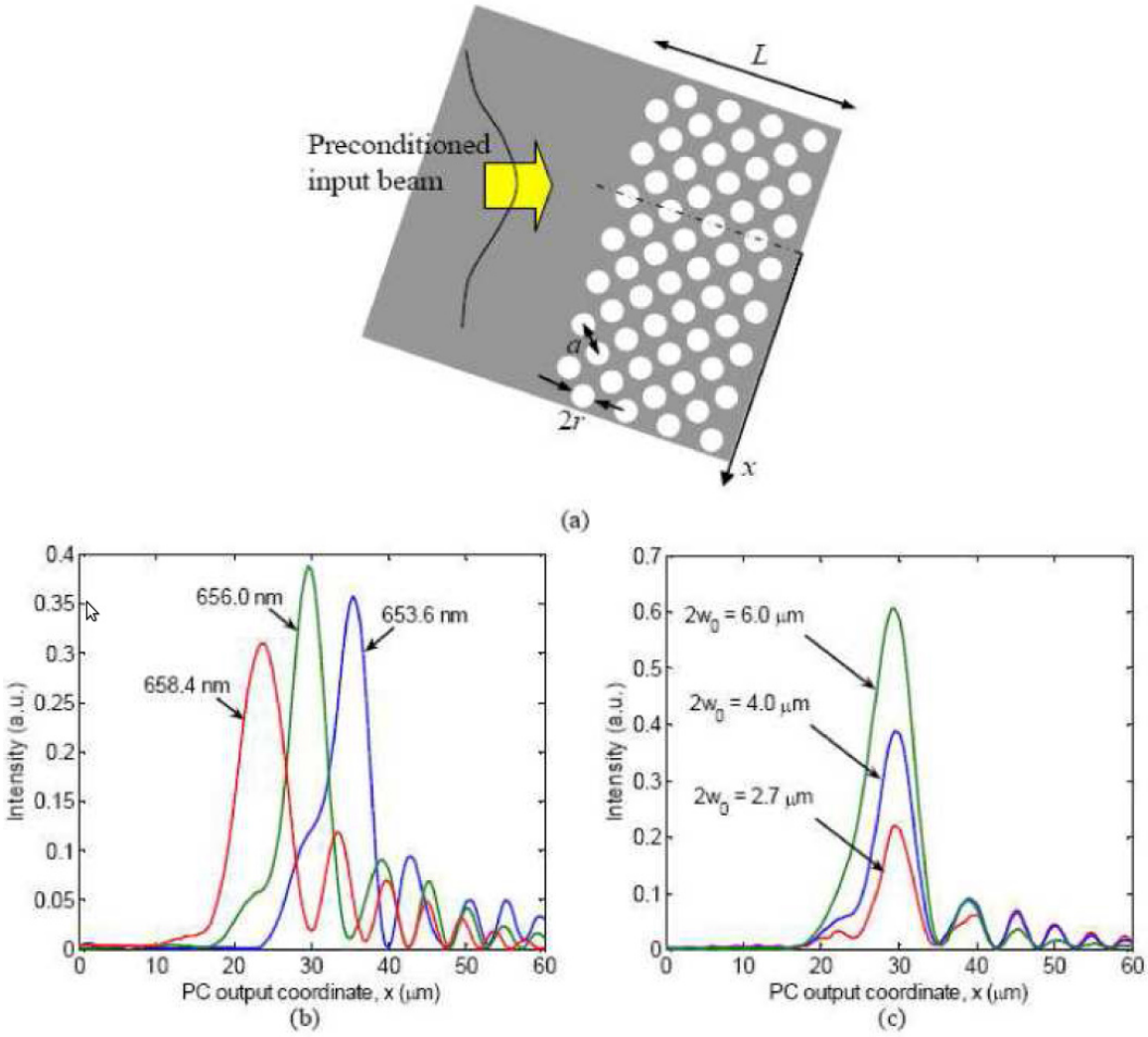

Figure 72: (a) The configuration used for the simulation of optical beam propagation in a Si_3N_4 PC is shown. A 45°-rotated square lattice photonics crystal with L = 70 μm, 2r = 170 nm, a = 240 nm is assumed. The thickness of the SiN slab is 205 nm, the incident angle is 13°, and the light has TE-like polarization. (b) Output beam profiles at different wavelengths (653.6 nm, 656.0 nm, and 658.4 nm) for input beam waist of $2w_o = 4$ μm are plotted. The input beam is preconditioned to compensate the effect of second-order diffraction at 656 nm. (c) For the same structure as in part (b), output beam profiles at different input beam waists of $2w_o = 2.7$, 4.0, and 6.0 μm are shown.

than 12 dB (for non-distorted Gaussian beams with 2.4 nm spacing in the same structure) to around 6 dB. Figure 72(c) shows the effect of changing the width of the incoming optical beam in the same structure. Increasing the input beamwidth has two direct effects. On one hand, it directly increases the spatial extent of the beam at the output (even when the beam is not affected by diffractive broadening); on the other hand, it reduces the effect of both second-order and third-order distortions [155], by reducing the spatial frequency content of the beam. Figure 72(c) clearly shows both of these effects. The intensity of each plot in Fig. 72(c) is compared to its nondistorted Gaussian case; therefore, lower peak intensity for smaller beamwidths in this figure is an indication of more diffractive broadening. The optimal beamwidth, $2w_o$, can be determined by considering the trade-off between the original extent of the beam and its diffractive broadening inside the structure. In this particular design, we have chosen $2w_o = 4$ μm as the waist of the input beam.

7.4 Implementation and experimental results

To experimentally demonstrate the operation of these SiN spectrometer devices, we have used standard microelectronic fabrication facilities to pattern the planar SiN slab [132]. The process consists of electron-beam lithography (EBL) followed by CF_4-based inductively coupled plasma (ICP) etching to transfer the desired pattern into the wafer. The stoichiometric SiN wafer used in our fabrication has a 205 nm ($\pm$5 nm) thick SiN device layer deposited on 6 μm of thermally grown silicon dioxide (SiO_2). The SiO_2 layer completely isolates the light in the device layer from the lossy silicon substrate. Figure 73(a) shows the scanning electron microscope (SEM) image of the fabricated structure consisting of a photonic crystal region, similar to the configuration in Fig. 72(a), and an array of waveguides at the output to spatially sample the beam profile and carry it to the output edge of the sample. Figure 73(b) shows the details of the photonic crystal structure fabricated in SiN.

To characterize the performance of the device, we have used a tunable laser (New Focus Velocity TLB-6305) covering the 652-660nm wavelength range. The output beam from the laser source is collimated and focused using a 40× objective lens to the input facet of the sample to couple the light into the planar input waveguide. The input waveguide has an initial width of 2.5 μm at the input interface and is gradually tapered down to 500 nm to suppress higher-order modes in the input beam. The input waveguide is then tapered up to 4 μm, and is then terminated to an unpatterned SiN slab to launch the incident beam to the photonic crystal region. To precondition the beam, the input beam propagates and diffracts in the unpatterned SiN slab region before reaching the photonic crystal region [152]. The length of the preconditioning region in this structure is 1.1 mm; however, note that this length does not impose an intrinsic limit on the compactness of the structure, since, for example, it can be replaced by a curved mirror [156]. After passing through the photonic crystal, the output light from the photonic crystal region is coupled into an array of output waveguides with 3 μm spacing. The signal in these output waveguides is measured by imaging the output facet onto a single detector (using a 20× objective lens at the output). The signal from individual output waveguides is isolated using an iris and measured while the tunable laser scans the wavelength. Figure 74(a) shows the measured power in seven of the output waveguides that fall within the range of the available tunable laser.

From the measurement results in Fig. 74(a), we mark the wavelength of the peak of the beam intensity at each output and deduce the angular dispersion of the photonic crystal structure. Figure 74(b) shows the angle of refraction found from the measurement (solid line) and compares it with the estimated angle of refraction from the theoretical model (dotted line, based on the band structure calculations in Fig. 71). It can be seen that the measured dispersion matches the theoretical expectations closely. From Fig. 74(b) it can be observed that the device is operating

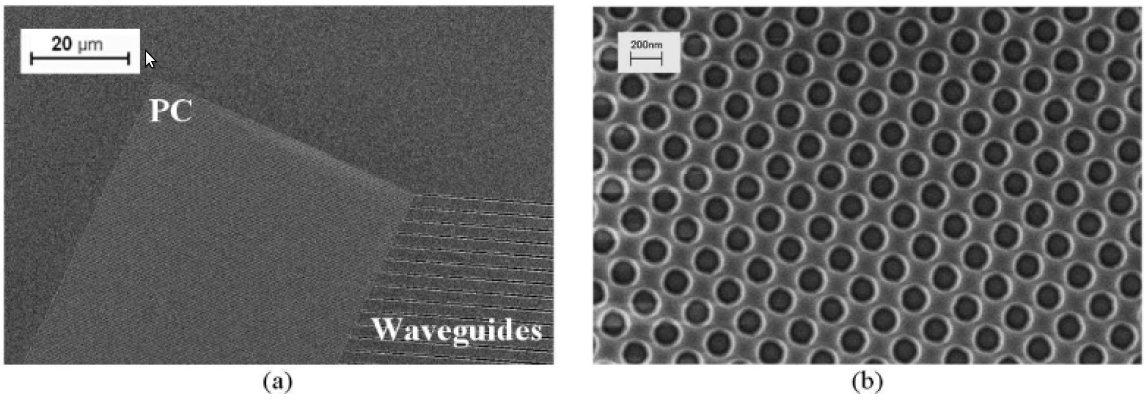

Figure 73: (a) SEM image of the fabricated structure is shown with a rotated PC region and an array of waveguides at the output. The incident beam is directed from a tapered waveguide from the left side of the device at an incident angle of 13°with respect to the interface of the photonic crystal region. (b) SEM image of the details of the photonic crystal region is shown. From SEM images, the lattice constant in the fabricated device is a = 240 nm, and the diameter of holes is 168 nm (compared to the 170 nm designed value).

in the negative refraction regime (as designed), and the angle of refraction changes rapidly with wavelength (strong superprism effect). Considering the 3 μm spacing between the adjacent output waveguides, the extent of the output beam intensity at each wavelength can be estimated from Fig. 74(a) to be around 5 μm. By comparing this beam extent with the initial beam waist (4 μm) and the beamwidth at the input plane of the photonic crystal region (80 μm), we can readily see that the device is working in the negative diffraction regime. These observations confirm the operation of the fabricated device in the desired operation regime. This fabricated device shows spatial separation of different wavelength channels with around 1.2 nm wavelength resolution in a 70 μm$\times$130 μm photonic crystal structure.

To further validate the operation of the device, we have simulated the propagation of optical beams at different wavelengths in a photonic crystal structure with the parameters similar to our fabricated device. Note that the actual parameters of the fabricated device are slightly different from the design values because of the limited accuracy of the fabrication process. We have employed the in-plane band

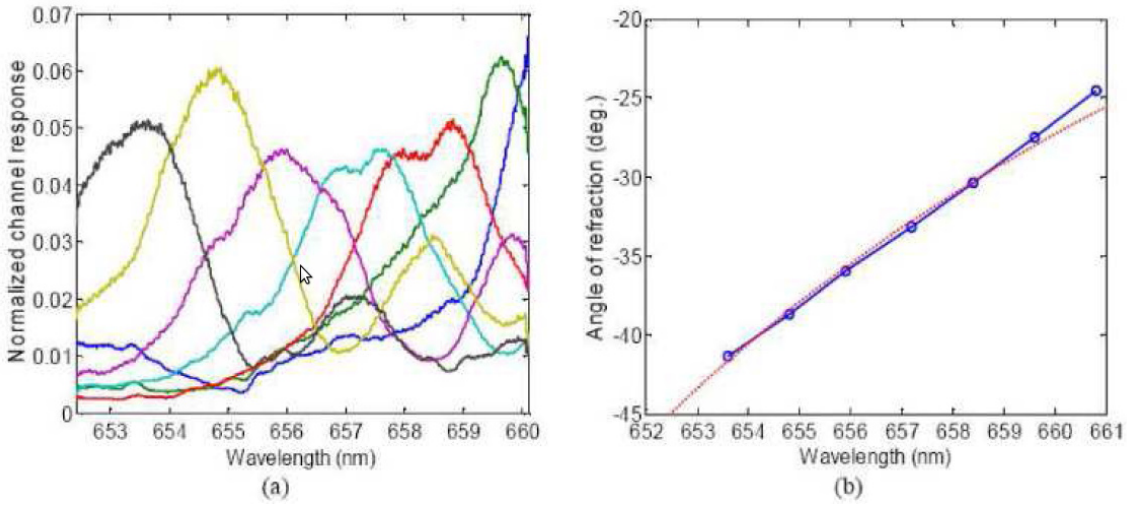

Figure 74: (a) Measured normalized transmission responses in adjacent channels are shown for seven output waveguides, showing a 3-dB wavelength resolution less than 1.2 nm. (b) The experimentally measured angle of refraction (solid curve) is shown and compared with theoretical prediction (dotted line). Theoretical results are corrected by a wavelength shift of 1.1% that accounts for the deviations of the thickness of the SiN slab and the size of holes from the designed values.

structure of the planar photonic crystal (calculated using a three-dimensional plane wave expansion method) and the envelope transfer function [154] to calculate the output beam intensity at different wavelengths (similar to what we did to obtain the results shown in Fig. 72). By integrating the beam power over 3 μm intervals (i.e., the acceptance range of each output waveguide) at the output plane of the photonic crystal region, the channel responses (at output waveguides) is found. Figure 75 shows the calculated channel responses calculated with the same waveguide positions and spacing as the fabricated structure. By comparing Fig. 75 with Fig. 74(a), we can observe that the theoretical estimates and experimental results of the spatial extent of the beam and the level of side-lobes are in good agreement. Thus, we expect this theoretical model to accurately represent the performance of such spectrometers in future designs and perform as a reliable tool for estimating the spectral resolution and the isolation level.

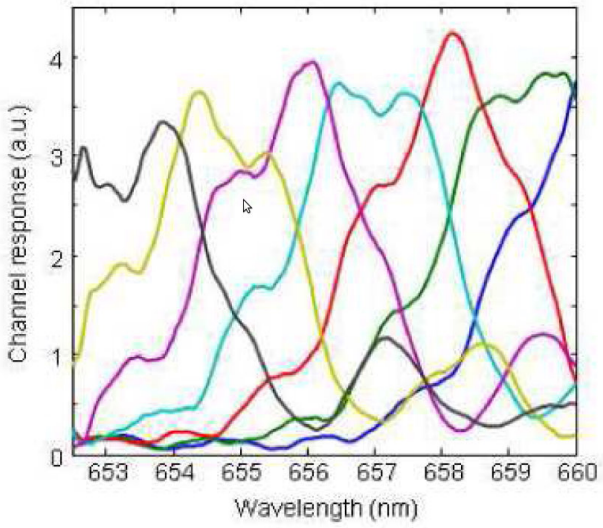

Figure 75: Simulated channel responses of optical beams at different wavelengths (calculated at 50 pm wavelength steps) in a planar photonic crystal spectrometer are shown. All the parameters of the simulated structure are similar to the fabricated structure in Fig. 72. Similar to Fig. 74(b), the theoretical results are corrected by a wavelength shift of 1.1% to account for the deviations of the fabricated structure from the designed values. The simulated channel response for each output waveguide in these results is in good agreement with the experimental measurements in Fig. 74(a).

7.5 Discussion

There are three major criteria for evaluating the performance of spectrometer devices and configurations: compactness, spectral resolution, and insertion loss. These parameters determine how well the spectrometer can perform in different applications, e.g., as a spectral analysis unit in a sensing platform or as a wavelength demultiplexer in an optical information processing system. The use of strong dispersion in photonic crystals provides the potential to implement a high resolution device in a small footprint. From Fig. 74(b), an angular dispersion factor (i.e., change in angle as a function of wavelength) of 2.3°/nm is observed, which is much larger than 0.17°/nm achievable in a conventional grating spectrometer realized in the same platform. This large angular dispersion factor further confirms the size advantage of the superprism-based photonic crystal spectrometers over alternative implementations. The angular dispersion in this device is almost twice as high as previous demonstration of the superprism effect in silicon nitride [18]. Furthermore, combining the superprism effect with the diffraction compensation scheme significantly improves the spatial separation (in a similar size) compared to the brute-force angular separation scheme (with diverging optical beams) in previous works [18]. Note that the structures shown in this work, which are optimized for compactness and high spectral resolution, are not necessarily the optimal designs in terms of insertion loss. We have observed less than 8 dB insertion loss (defined as total output power divided by total input power) in the device shown in Fig. 74. This insertion loss value is estimated by comparing the output power from all the output channels of the spectrometer with the power in a ridge waveguide fabricated on the same substrate and is accurate within Âś1 dB (due to the limitations of our characterization setup). A considerable portion of the loss ($>$ 4 dB) in the demonstrated photonic crystal spectrometer is caused by the choice of excitation of the structure using a terminated waveguide in the far-field. This loss can be significantly reduced by using a mirror with proper curvature

as the preconditioning region at the input of the structure [156]. Further reduction of loss can be achieved by modifying the interface of the structure and by including matching stages [157, 158] to reduce the scattering and reflection losses when coupling the light into and out of the photonic crystal region. Furthermore, more elaborate fabrication processes, such as deep anisotropic etching the SiO_2 layer underneath the Si_3N_4 layer or undercutting the structure by wet etching can be used to further reduce the loss in the structure. We expect to considerably reduce this insertion loss by considering all these factors in the design and fabrication of these planar photonic crystal spectrometers. To compare the performance of the demonstrated spectrometer with the alternative implementations, we have fabricated spectrometers based on different operation principles on the same substrate. The structures being compared here are (1) the photonic crystal spectrometer studied earlier in this paper; (2) an arrayed waveguide grating (AWG) made by following the standard design in [159]; (3) the same AWG as in (2) after a resist reflow process [3] to reduce the sidewall roughness and reduce the waveguide propagation loss; and (4) a folded grating spectrometer operating in the first-order reflection grating mode [156]. All these devices are designed to have small footprints, and are fabricated in our group with the same fabrication recipe. The SEM images of these fabricated structures are shown in Fig. 76. To characterize the performance of each device, we have used the same measurement setup explained in Section 7.4. The resolution of each spectrometer is measured by scanning the wavelength of the input laser and measuring the power at each output waveguide. The insertion loss is also measured by comparing the total output power of the device with that of a straight waveguide fabricated on the same substrate. The performance of the devices, shown in Table 7.5, are compared using two main metrics: (1) compactness factor, $C_\lambda = [l_p(\Delta\lambda)_{3dB}]^{-1}$ where l_p is the length scale of the device and $\Delta\lambda_{3dB}$ is the spectrometer full-width half maximum wavelength resolution, and (2) insertion loss of the spectrometer. The compactness

factor provides a measure that for a given wavelength resolution how compact each device is, and the insertion loss is the drop in the signal level while passing through the spectrometer. Note that in some practical situations, e.g., in a sensing platform [142], higher signal-to-noise ratio at the output can be traded in favor of an effectively higher detectable wavelength resolution. Therefore, we can use the power-normalized compactness factor, C_λ/IL (listed in the last column of Table 7.5), as the main spectrometer comparison criteria. It can be observed that among these compact implementations, the photonic crystal spectrometer shows favorable performance even without employing further loss-reduction solutions. Note that this comparison between different device implementations cannot be viewed as an absolute measure for performance of such structures. All the different spectrometers demonstrated here have been designed with compactness as one of the major factors, and can be further optimized for better resolution and lower insertion loss. Nevertheless, the preliminary comparison of the performance of these structures under similar fabrication quality as presented in Table 7.5 provides a point of reference for future optimization of these devices. In our view, the compactness and insertion loss of the spectrometers as mentioned in Table 7.5, should be directly included in the performance measure of the device for future integrated spectrometer optimizations. Note that the operation range in the devices used in this paper is located at the crossing of the zeroth order and the first-order bands of the photonic crystal [160]. The modes in this operation region are hybrid modes mainly consisting of the zeroth order and first-order Bloch components. The transition of the dominant component from the zeroth order component to the first-order component is the main factor in the rapid change in the direction of propagation of the hybrid mode (and therefore, a strong superprism effect). In low-contrast Si_3N_4 photonic crystal structures, compared to high contrast platforms such as silicon-on-insulator (SOI), the coupling between the zeroth order and the first-order components is weaker. This weaker coupling manifests itself in

Table 6: The performances of Si_3N_4 spectrometers based on different operation principles are compared.

	Compactness factor, C_λ (nm.mm)$^{\hat{a}\acute{L}\check{S}1}$	Insertion loss, IL (dB)	C_λ/IL (nm.mm)$^{\hat{a}\acute{L}\check{S}1}$
Photonic crystal	7.0	8.0	1.1
AWG-reflow	2.8	6.5	0.63
AWG	2.8	11	0.22
Grating-based	1.1	8.0	0.17

smaller available bandwidth and more higher-order diffractive distortion (and thus, lower cross-talk isolation) in spectrometer devices made in the low-contrast Si_3N_4 photonic crystals. The higher-order diffraction effects distort the optical beam shape at the output of the device and causes relatively large channel-to- channel cross-talk in these spectrometers. In principle, a multistage photonic crystal structure can be used to provide more degrees of freedom to control the beam shape and reduce the cross-talk. Currently, the applicability of this multistage scheme is, however, limited by the required fabrication accuracy in different regions of such multistage structure. The limited available operation bandwidth (around 10 nm) of the demonstrated Si_3N_4 photonic crystal spectrometer (for example, compared to AWGs in which the operation bandwidth is easily scalable) is one of the shortcomings of the proposed scheme. However, the useful bandwidth of the photonic crystal spectrometer can be extended by using a cascaded scheme with a coarse wavelength demultiplexer in the first stage followed by compact high-resolution photonic crystal spectrometers to cover different bands (dicussed in Chapter 8).

7.6 Conclusions

In summary, we have shown the potentials of planar photonic crystal devices as on-chip spectrometers in Si_3N_4. The demonstrated structures offer exceptional compactness and high spectral resolution performance as integrated components. A 3-dB spectral resolution of 1.2 nm and less than 8 dB insertion loss are experimentally

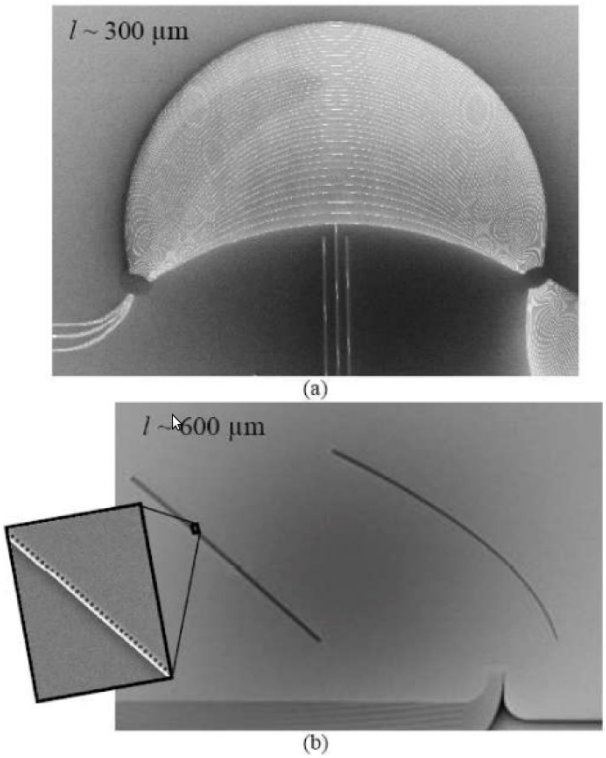

Figure 76: SEM images of alternative on-chip spectrometers implemented in Si_3N_4 for comparison of spectroscopy performance are shown. (a) An AWG spectrometer with a size-scale of l = 300 μm and wavelength resolution of 1.2 nm. (b) A folded grating spectrometer with a size-scale of l = 600 μm and wavelength resolution of 1.5 nm. The inset magnifies a portion of the grating reflector that consists of a periodic pattern of air holes next to a wide trench [156].

observed in the 70 μm by 130 μm photonic crystal structure investigated in this work. It is shown that the demonstrated superprism-based photonic crystal spectrometers even without further optimization are advantageous over other compact implementations of spectrometers in Si_3N_4. Future steps to reduce the insertion loss in these devices are expected to further improve their performance.

CHAPTER VIII

ARRAYED WAVEGUIDE GRATINGS

In this chapter arrayed waveguide gratings (AWGs) in the visible range are demonstrated for the first time. The resolution of these spectrometers can be as small as 100 pm while keeping a 10 nm bandwidth (using a cascaded design). In the first section a historical overview is presented, in section 8.2 the design strategy is laid out, and in 8.3 the experimental results are presented and compared with competing technologies.

8.1 Introduction

Arrayed waveguide gratings (AWG) were first conceived by Smit et al. in 1988 [161]. At the time the advantage of these structures over the conventional curved gratings was ease of fabrication with conventional photolithography of the 80s. Two years later, encouraged by the emergence of laser arrays of 20 wavelengths with a wavelength spacing of 1 nm (suitable for wavelength division multiplexing), Takahashi et al. introduced AWGs with sub-nanometer resolution fabricated on glass substrates [162]. N×N demultiplexers were subsequently demonstrated on silicon [163]. In 2004 compact AWG demultiplexer were demonstrated at Gent University using SOI technology with deep UV lithography [164]. AWGs are currently the most popular integrated devices for multiplexing and demultiplexing multiple wavelength channels. Photonic wires with short bend radii and high group index can dramatically reduce the dimensions of the devices. Recently a fully integrated, multi-channel, iii-v/Si AWG-based laser was demonstrated at UCSB [165].

We believe SiN with its relatively high index compared with the underlying oxide and its ease of fabrication is good candidate for AWG spectrometers in the visible

range, specially for spectral detection and sensing of biological samples in the visible range. The first demonstration of such devices is laid out in the next sections.

8.2 Theoretical Background and Design Strategy

Figure 77(a) shows the schematic layout of a phased-array (PHASAR) demultiplexer. PHASARs is also called Arrayed waveguide gratings (AWG) in the literature. The operation is understood as follows. When the beam propagating through the transmitter waveguide enters the free propagation region (FPR) it is no longer laterally confined and becomes divergent. On arriving at the input aperture the beam is coupled into the waveguide array and propagates through the individual array waveguides to the output aperture.

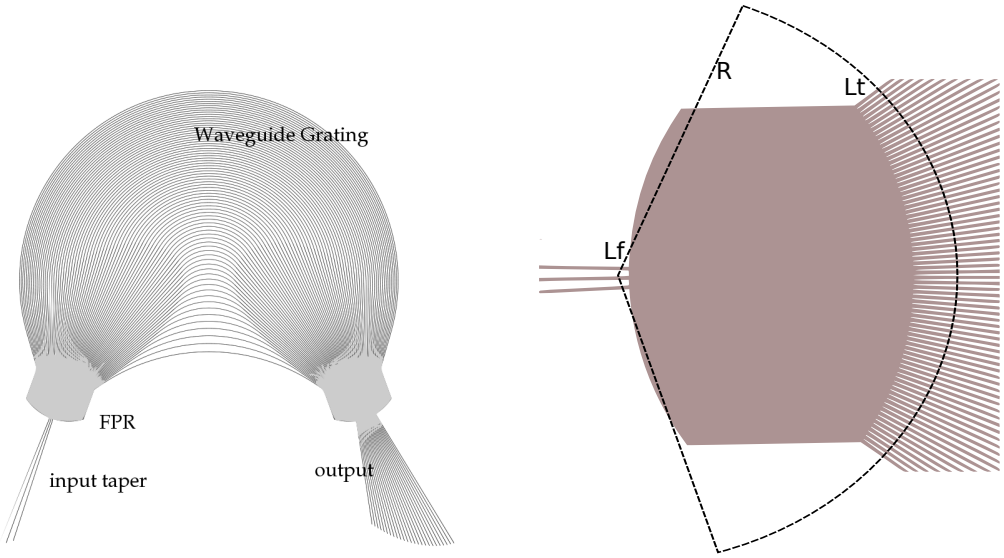

Figure 77: (a) the layout of a typical AWG. (b) The star coupler.

The length of the array waveguides is chosen such that the optical path length difference between adjacent waveguides equals an integer multiple of the central wavelength of the demultiplexer. For this wavelength the fields in the individual waveguides will arrive at the output aperture with equal phase (apart from an integer multiple of 2), and the field distribution at the input aperture will be reproduced at

the output aperture. The divergent beam at the input aperture is thus transformed into a convergent one with equal amplitude and phase distribution, and an image of the input field at the object plane will be formed at the center of the image plane. The dispersion of the PHASAR is due to the linearly increasing length of the array waveguides, which will cause the phase change induced by a change in the wavelength to vary linearly along the output aperture. As a consequence, the outgoing beam will be tilted and the focal point will shift along the image plane. By placing receiver waveguides at proper positions along the image plane, spatial separation of the different wavelength channels is obtained.

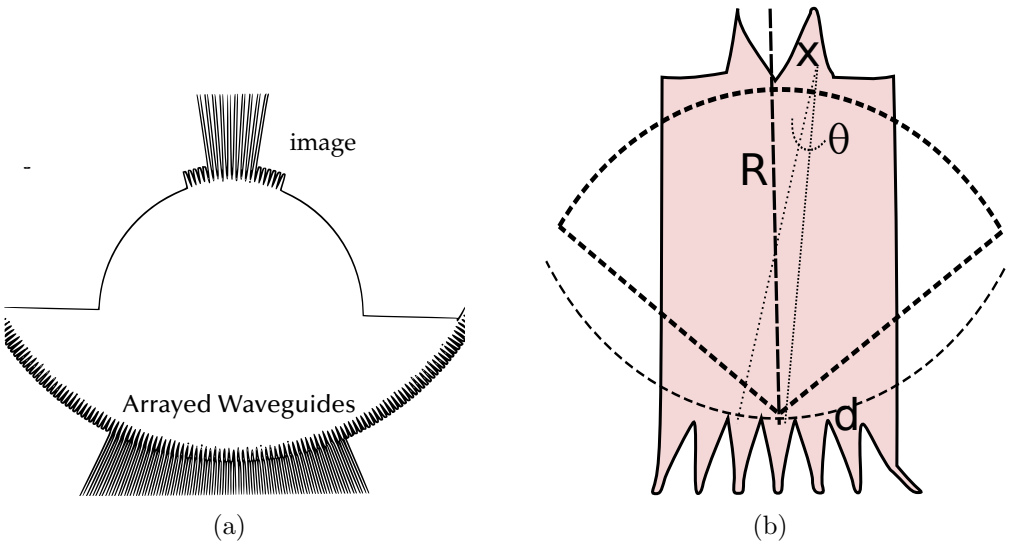

Figure 78: (a) The architecture of the star coupler in Rowland-type mounting in which the curvature of the image plane is half of the distance between the image and the arrayed waveguide (R). (b) The simplified star coupler. x denotes the location of the image point and d is array waveguide separation.

The input and output apertures of the phased array can be positioned in a Rowland-type configuration [166] in which the curvature of the image plane is $R/2$. Here, due to the small number of channels in the output, the aberration caused by a simpler design (curvature of the image plane=R) is not significant and a simpler design is used. Focusing is obtained by choosing the length difference Δl between adjacent array waveguides equal to an integer number of wavelengths, measured inside the

array waveguides

$$\Delta l = m \cdot \frac{\lambda_c}{n_w} \tag{99}$$

in which m is the order of the phased array, λ_c is the free-space central wavelength, and n_w is the effective index of the waveguide mode. With this choice the array acts as a lens with image and object planes at a distance R of the array apertures.

Following the design strategy laid out in [167] and [159], assuming the distance between the center of the array waveguides at the star coupler is d, and the location of input and output points—measured from the central waveguide—are x_{in} and x_{out} we can measure the phase experienced by two rays of lights starting from x_{in} passing through two adjacent central waveguides and received at x_{out}. From simple geometrical calculations we can approximate the distance of two adjacent array waveguides to the image point x_{out} as $R - x_{out}d/2R$ and $R + x_{out}d/2R$. Therefore for constructive interference of the two paths we have

$$\beta_s(R_{in} - \frac{d_{in}x_{in}}{2R_{in}}) + \beta_w(l_c) + \beta_s(R_{out} - \frac{d_{out}x_{out}}{2R_{out}}) = \tag{100}$$

$$\beta_s(R_{in} + \frac{d_{in}x_{in}}{2R_{in}}) + \beta_w(l_c + \Delta l) + \beta_s(R_{out} + \frac{d_{out}x_{out}}{2R_{out}}) - 2m\pi, \tag{101}$$

in which β_s and β_w are propagation constants in the slab and in the waveguide, and l_c is the length of the path in the central waveguide. Subtracting the common terms, we obtain

$$\beta_s(\lambda_c)\frac{d_{in}x_{in}}{R_{in}} + \beta_w(\lambda_c)\Delta l + \beta_s(\lambda_c)\frac{d_{out}x_{out}}{R_{out}} = 2m\pi. \tag{102}$$

When the condition $\beta_w(\lambda_c)\Delta l = 2m\pi$ (i.e. $\lambda_c = n_w\Delta l/m$) is satisfied the light input and output positions x_in and x_out should satisfy the condition

$$\frac{d_{in}x_{in}}{R_{in}} = \frac{d_{out}x_{out}}{R_{out}}. \tag{103}$$

. Assuming the input and output star couplers are similar ($d_{in} = d_{out} = d_{awg}$ and $R_{in} = R_{out} = R_{star}$), the position of x_{in} and x_{out} would be equal for the central

frequency (λ_c). The frequency dependence of the structure can then be established by fixing x_{in} differentiating x_{out} with respect to λ in Eq. (103):

$$\frac{2\pi n_s}{\lambda_c}\frac{d_{awg}}{R_{star}}\frac{\mathrm{d}x_{out}}{\mathrm{d}\lambda} = -\frac{2\pi}{\lambda_c^2}\Delta l(n_w - \lambda\frac{\mathrm{d}n_w}{\mathrm{d}\lambda}). \tag{104}$$

Noting that $n_w - \lambda\frac{\mathrm{d}n_w}{\mathrm{d}\lambda}$ is defined as the group index (n_g) the above equation can be simplified to get the wavelength dispersion as

$$\frac{\delta x}{\delta\lambda} = D_\lambda = -\frac{1}{\lambda_c}\cdot\frac{n_g}{n_s}\cdot\frac{R_{star}\,\Delta l}{d_{awg}}. \tag{105}$$

Knowing that the channel separation in the output is D_{out}, the wavelength separation ($\delta\lambda$) can be written as

$$\delta\lambda = \frac{n_s d_{awg}\lambda_c}{n_g R_{star}\Delta l}D_{out}. \tag{106}$$

On the other hand if x_in is fixed, Eq. 101 can be satisfied for m and $m+1$. Subtracting the equations for m and $m+1$ we get the spatial repetition rate (X_{FSR}):

$$X_{FSR} = x_m - x_{m+1} = \frac{\lambda_c R_{star}}{n_s d_{awg}}. \tag{107}$$

Knowing the dispersion D_λ from 105, the wavelength free spectral range (FSR_λ) can be written as

$$FSR_\lambda = \frac{\lambda_c^2}{n_g\Delta l}, \tag{108}$$

$$FSR_f = \frac{c}{n_g\,\Delta l}. \tag{109}$$

As can be seen from the above equation, the FSR is notably independent of the star coupler parameters.

To know the optimum number of waveguides assigned to the AWG, we need to estimate the beam divergence at the input. For a Gaussian beam the beam width can be written as a function of the beam waist:

$$W = W_o\sqrt{1+(\frac{R_{star}}{r_R})^2} \qquad r_R = \frac{\pi W_o^2}{\lambda} \tag{110}$$

in which W_o is half the input spot size and r_R is the Rayleigh range. For $R_{star} \gg r_R$ (assuming the waist of the beam to be $W_o = D_{in}/4$) the angular divergence of the beam is given by

$$\theta_{max} = \frac{4\lambda_c}{\pi D_{in} n_s}, \tag{111}$$

therefore the number of waveguides is

$$N_{wg} = 2\frac{\theta_{max}}{\theta_{wg}} = \frac{4\lambda_c R_{star}}{\pi D_{in} n_s d_{awg}}. \tag{112}$$

The important design steps and the typical values used in the following section is summarized in table 7.

8.3 Experimental results

As shown in table above, when the FSR and resolution of the AWG is specified, some of the design parameters (e.g. the path length difference and the star coupler radius) are set. Nevertheless, some of the parameters like the taper width, star coupler angle and middle path length are arbitrary. A long AWG leads to significant loss in the waveguides, and a very short WG increases the bending losses. Therefore while adjusting α and L_c, the bending radius of the waveguides should be monitored.

Considering these constraints, there is a degree of freedom and the parameters are based optimized by testing the actual devices. we fabricated several different structures with slightly varying the input and output taper sizes, the middle path, the angle of the mounting and tried to find the finest resolution obtainable with our current fabrication technology.

Considering the difference between the negative and positive tone resists (mentioned in 3.1.3.2) the choice of the resist leads to very different layouts 32(b). With a positive resist (namely ZEP) the free propagation region is not written with the EBL but special care should be taken about the area of arrayed waveguides as the high concentration of trenches close to the star coupler can lead to proximity effects and

Table 7: Design parameters and their value in the order of determination

	notation	Calculation	Typical value
Waveguide width	w	Single mode	550 nm
Slab effective index	n_s	Comsol	1.85
Waveguide group index	n_g	Dispersion	2.185
Input/output WG distance	D_{in}, D_{out}	Low reflection	1.5 μm
WG-WG edge distance	W_f	WG coupling	100 nm
AW separation	d_{awg}	Collection	1.5 μm
Taper length	L_t	Low reflection	5 μm
Waveguide effective index	n_w	Comsol	1.65
Mode order	m	BW and FSR	46
Channel bandwidth	$\delta\lambda$	given	1 nm
Wavelength FSR	FSR_λ	$n_w\lambda/(n_g m)$	12 nm
Star coupler radius	R_{star}	$n_s d_{awg} D_{out} Nch/\lambda_c$	68 μm
Waveguide length difference	Δl	$m\lambda_c/n_w$	16 μm
Beam Divergence angle	θ_{max}	$4\lambda_c/(\pi n_s D_{in})$	24 deg
# of array waveguides	N_{wg}	$2(\theta_{max} R_{star}/d_{awg})$+1	39
Middle WG length	L_c	Loss	150 μm
Stars angle	α	Bending loss	-20 deg

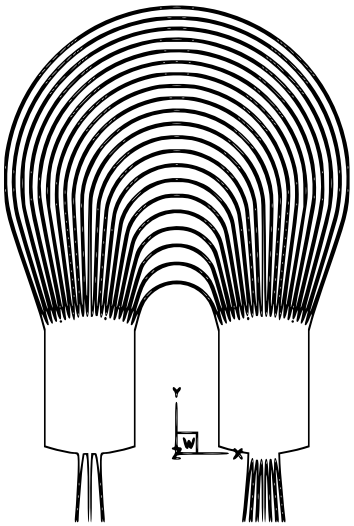

Figure 79: $D = 2$; $N_{ch} = 6$; $\delta\lambda = 2\text{nm}$; $\alpha = 0$; $L_c = 80\mu\text{m}$; $L_t = 10\mu\text{m}$; $W_f = 100\text{nm}$

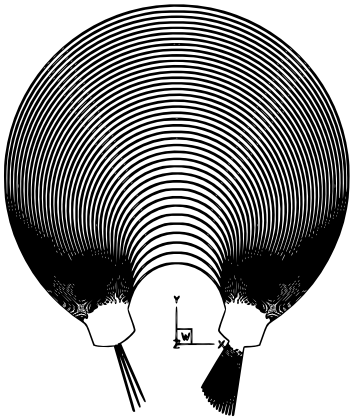

Figure 80: $D = 1$; $N_{ch} = 12$; $\delta\lambda = 1\text{nm}$; $\alpha = -20$; $L_c = 100\mu\text{m}$; $L_t = 5\mu\text{m}$; $W_f = 100\text{nm}$

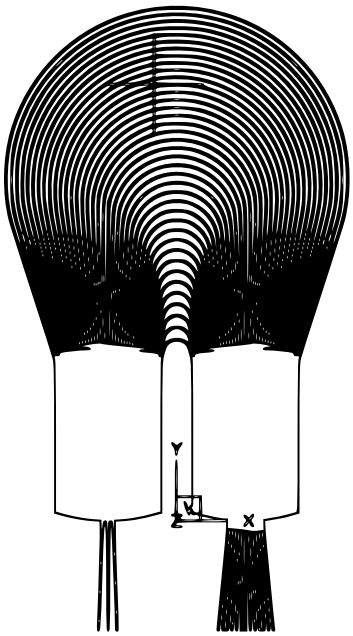

Figure 81: $D = 2$; $N_{ch} = 12$; $\delta\lambda = 1\text{nm}$; $\alpha = 0$; $L_c = 100\mu\text{m}$; $L_t = 5\mu\text{m}$; $W_f = 100\text{nm}$

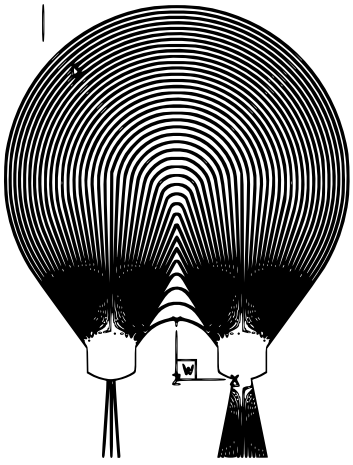

Figure 82: $D = 1$; $N_{ch} = 12$; $\delta\lambda = 1\text{nm}$; $\alpha = 0$; $L_c = 100\mu\text{m}$; $L_t = 5\mu\text{m}$; $W_f = 300\text{nm}$

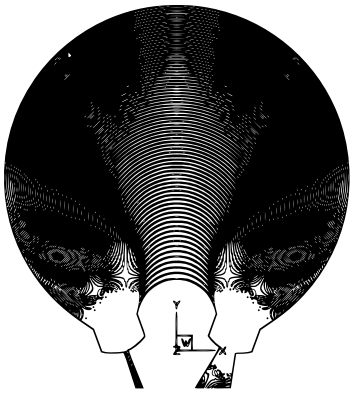

Figure 83: $D = 1$; $N_{ch} = 24$; $\delta\lambda = .5$nm; $\alpha = -20$; $L_c = 80\mu$m; $L_t = 5\mu$m; $W_f = 200$nm

narrowing of the waveguides. On the other hand, for an AWG made with negative tone resists (like HSQ and MaN) the proximity effect due to the free propagation region (FPR) is more significant. Both of these issues can be alleviated but assigning different base doses to different regions using a proximity effect software (Layout Beamer here).

In the following subsections the structures fabricated with ZEP and MaN are demonstrated.

8.3.1 AWGs Fabricated with Positive Tone Resists

When using a positive tone resist the trenches around the devices are written with electron beam lithography. Such a structure can be seen in Fig. 84(a). the structures presented here are all achieved by smoothening of the ZEP resist. This is done through reflowing the resist on a hot plate at 150°C for 5 minutes.

For the structures fabricated in this subsection we focused on two types of designs. For the first structure (seen in Fig. 84(a)) the focus was on the compactness of the structure.This structure (which fits in a $280\mu m \times 300\mu m$ area) is the most compact AWG SiN spectrometer with such resolution. We achieved 8 channels with 1 nm spacing and the insertion loss of the AWG was 8dB. The crosstalk between the channels was as good as 8dB.

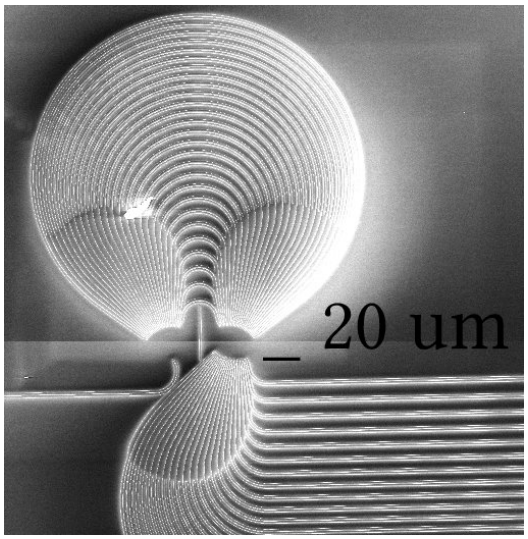

(a)

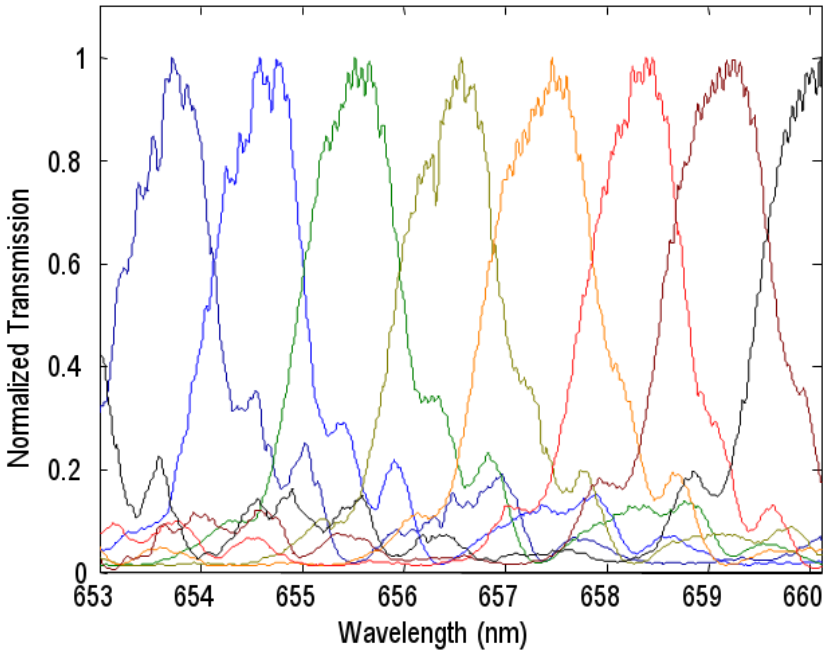

(b)

Figure 84: (a) compact AWG fabricated with ZEP. (b) The output of 8 channels with 1 nm resolution.

The focus for the second fabricated structure was on high resolution. This structure (shown in Fig. 85(a)), fitting in a $1mm \times 1.4mm$ area, demonstrates excellent spectral features as follows: 16 channels of 0.45 nm channel spacing with 10 dB cross-talk isolation. The output of the 16 waveguides can be seen in Fig. 85(b).

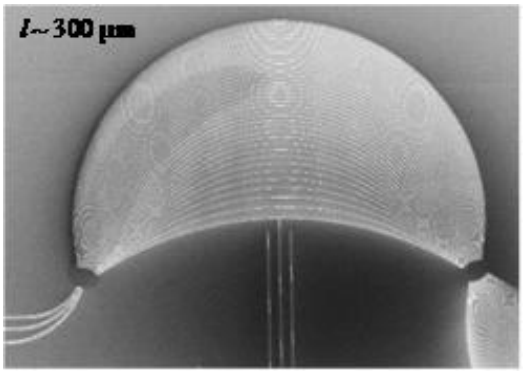

(a)

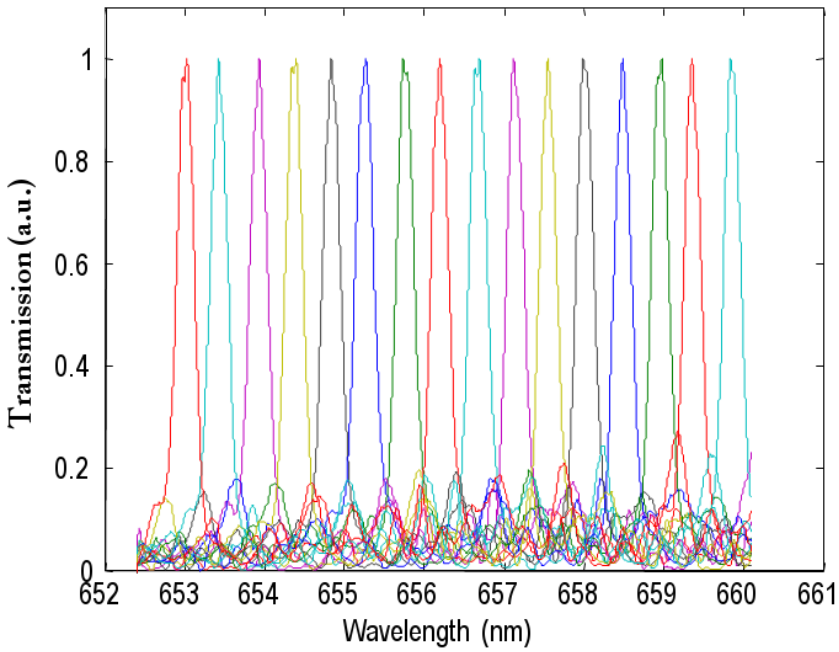

(b)

Figure 85: (a) High resolution AWG fabricated with ZEP. (b) The output of 16 channels with 0.45 nm resolution.

To push the resolution×bandwidth even further we adopted a cascaded design, which is detail in the next subsection.

8.3.1.1 Cascaded AWG and Microring Array

As we saw in this section, the best resolution we achieved with AWGs was 0.45 nm. Although this resolution is the highest of its kind in the visible range, it is orders of magnitude smaller than the resolutions achievable with resonator based structures. As shown in previous chapters, resolutions as small as 0.5 pm (with microdisk) and 5 pm (with microrings) is possible with resonators. On the other hand the FSR of the resonators demonstrated was 1.7 nm. this means a spectral features can be sampled with pm resolution as far as it is limited to a 1.6 nm linewidth. One workaround for this limitation is shrinking the size of the microresonators. Unfortunately, unlike the SOI spectrometers demonstrated in our group [168], the low index of Sin compared with Si leads to very low quality factors for smaller resonators.

To take advantage of relatively large bandwidth of the AWGs and the high resolution of the resonators one can use cascaded structures. If the guiding material has a high thermo-optic coefficient (as that of Si), one can potentially use only one cavity at the input of the AWGs and thermally sweep the cavity resonance across the bandwidth of the each AWG output [169]. As the thermo-optic coefficient (TOC) of SiN is at least an order of magnitude smaller than Si, this task requires a large amount of electrical power dissipated in the heater circuitry.

Alternatively, one can use a series of resonators cascaded in the output, each spectrally separated from the other by a linewidth—by a 6 nm change in the 20 micron radius of the resonator—and the bandwidth of each AWG output smaller than one FSR of the resonators. This way, only one resonance of each microring falls inside an AWG channel and the drop port of each resonator corresponds to only one point in the spectrum rather than several points separated by an FSR.

such a structure is depicted in Fig. 86(a). The AWG has 1 nm channel spacing and 10 resonators in the output of the AWG are separated by 0.1 nm while each has a 1 nm FSR.

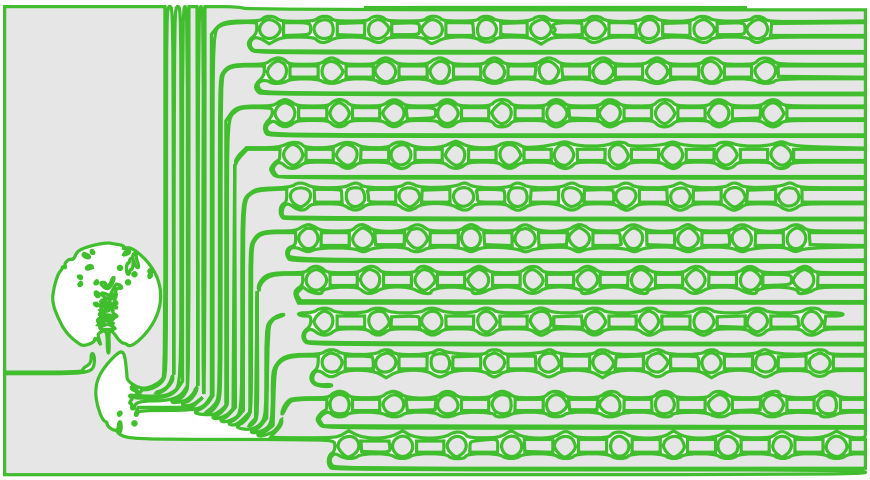

(a)

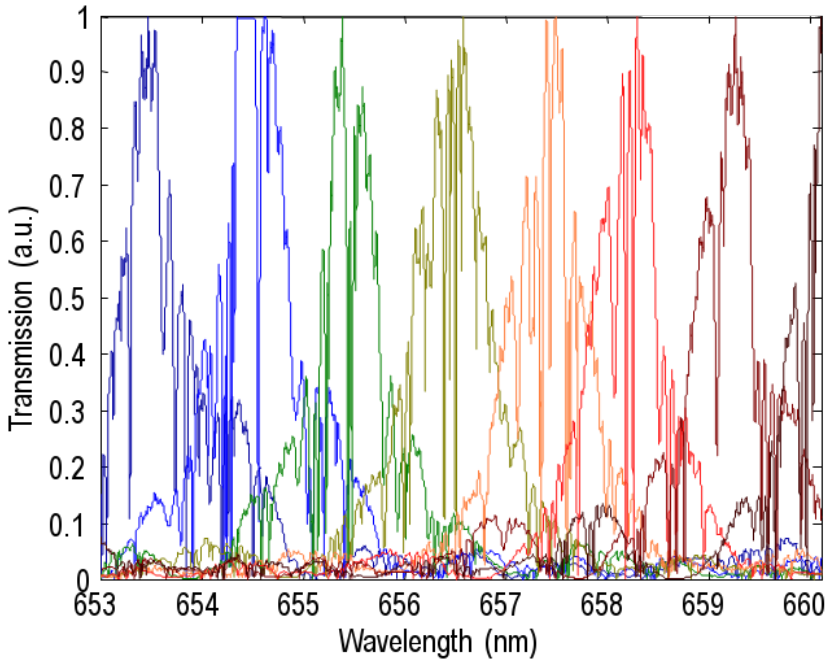

(b)

Figure 86: (a) The layout of an AWG cascaded with an array of microring add-drop filters. (b) The output of the cascaded structure with one waveguide for each row of microrings.

While it is required to use one output drop waveguide for each of the microring add-drop filters, the ZEP electron beam lithography limited us to only one waveguide per series of waveguides. As previously mentioned, while writing patterns with a positive tone resist the trenches around the waveguides are written. A 3 micron wide and few millimeter long trench for each of the required 100 waveguides would take a very long write time. Thus we adopted a negative tone resist to be able to use an short inverse taper with an SU-8 waveguide at the input and output. Such a structure is shown in Fig. 87(a).

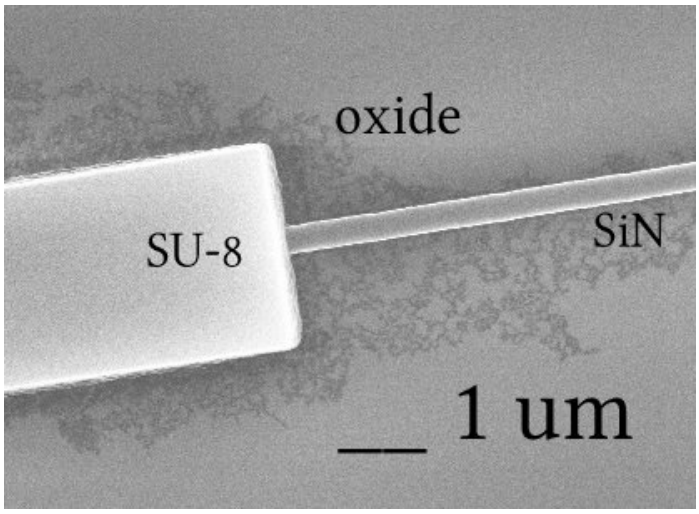

(a) The SU-8 waveguide on top of the tapered SiN waveguide.

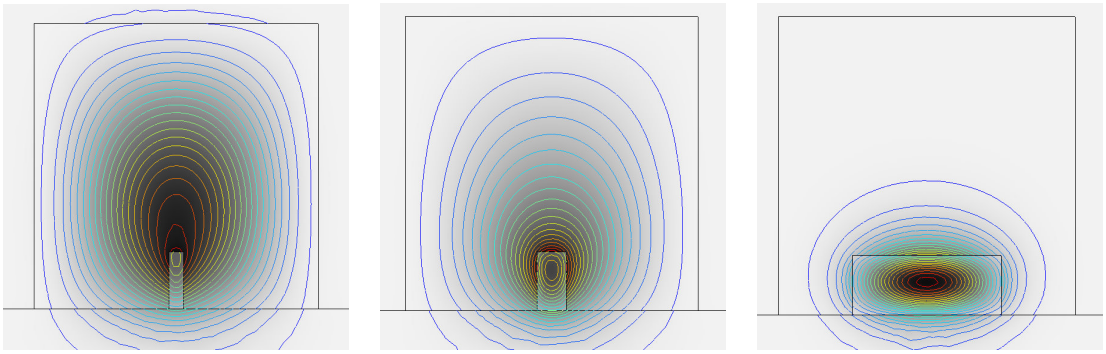

(b) W=50 nm (c) W=100 nm (d) W=500 nm

Figure 87: Inverse taper design and fabrication.

As seen in Fig. 87, as the width of the SiN taper is increased gradually, the mode is more confined in the SiN layer. This is an efficient way of coupling the light to the

structures as the Su-8 waveguide is much larger and the input light from the objective light can couple to the micron scale SU-8 input is much more efficient. As a negative tone resist is preferable with this approach we present some structures fabricated with this approach in the next section.

8.3.2 AWGs Fabricated with Negative Tone Resists

As seen in Figs. 8.3–8.3, the layout of the AWGs written with a negative tone resist is different from the positive counterpart. The star coupler part of the AWG (written with HSQ) is shown in Fig. 8.3.2. If fabrication is done with HSQ, despite the sensitivity to dosage, a better control over the width of the waveguides is possible. Nevertheless, the remaining HSQ on top of the devices after etch—as can be seen in Fig. 8.3.2—is hard to remove as it involves BOE, which undercuts the devices too. Hence we focused on fabrication of the devices with easily removable MaN 2403.

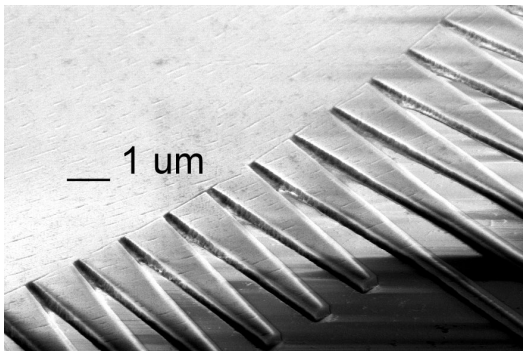

Figure 88: The star coupler of an AWG fabricated with HSQ resist.

Figure 89 shows the output of four different AWgs designed with varying bandwidth and star coupler parameters. As can be seen in the figure, all of these four designs have responses close to the values predicted from the theory. Therefore, the star coupler parameters, e.g. the width D and length L_t of the tapers and the WG-WG separation in the star coupler W_f do not affect the performance of the AWG and significantly the focus of the design and fabrication should be on the length, curvature, and width of the waveguides in the grating array.

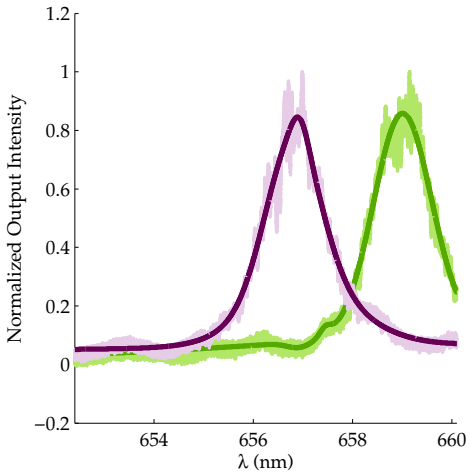

(a) $D = 2$; $\delta\lambda = 2$nm; $L_t = 10\mu$m; $W_f = 100$nm

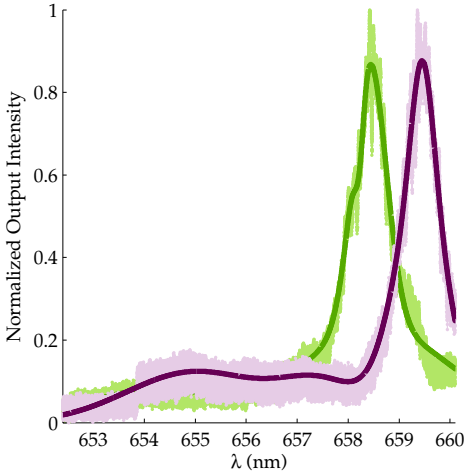

(b) $D = 1$; $\delta\lambda = 1$nm; $L_t = 5\mu$m; $W_f = 100$nm

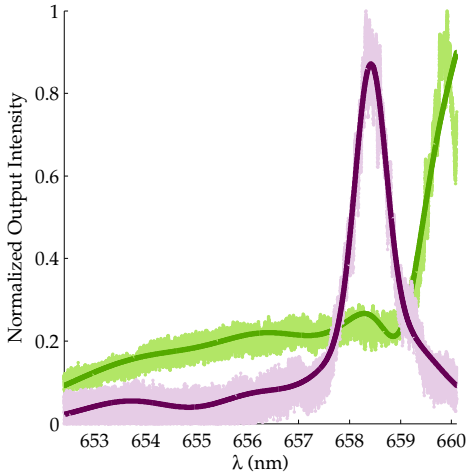

(c) $D = 2$; $\delta\lambda = 1$nm; $L_t = 5\mu$m; $W_f = 100$nm

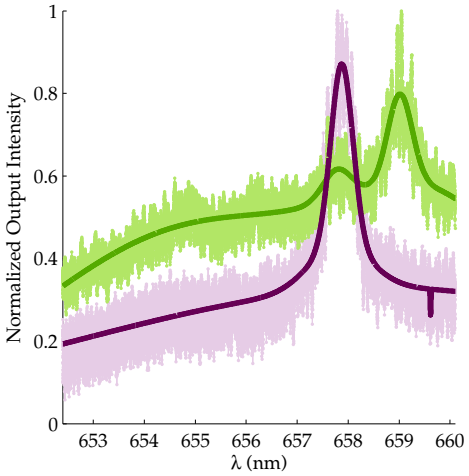

(d) $D = 1$; $\delta\lambda = 1$nm; $L_t = 5\mu$m; $W_f = 300$nm

Figure 89: Output of AWGs fabricated with MaN resist. The FSR of all structures are 12 nm and the length of the central waveguide almost 100 micron.

At each output of the AWG a series of microring based add-drop filters sample the output signal. The radius of the rings is chosen to be 20 microns to give 1.6μm FSR, which is larger than the bandwidth of the AWGs in Figs. 89(b)–89(d). This ensures that only one resonance of each ring is excited (Fig. 90(c)). The linewidth of the add-drop filters is controlled with the coupling rate between the waveguide and resonators. When the coupling gap is chosen to be 150 nm, the bandwidth of the rings is 150 pm, which is equal with the ring-ring resonance distance. Therefore, all of the swept spectrum (10nm) is sampled with microrings without any missing spectral points. This can be improved even more by increasing the number of rings and thus over-sampling the spectrum.

8.4 Conclusion

In this chapter we demonstrated AWG spectrometers operating in the 650-660 nm range. Two fabrication methods using positive/negative tone resists were demonstrated. It is shown that 12 nm of the visible light can be detected with a 150 pm accuracy by using microring resonators at the output of the AWGs. In future flat spectral response from the arrayed-waveguide grating is possible with parabolic waveguide horns [170] In addition, the insertion loss of the devices (currently 10dB) can be significantly improved by using vertically tapered waveguides [171] at the star coupler. Also the input coupling efficiency to the chip can be improved by utilizing Su-8 waveguides on inverse tapers.

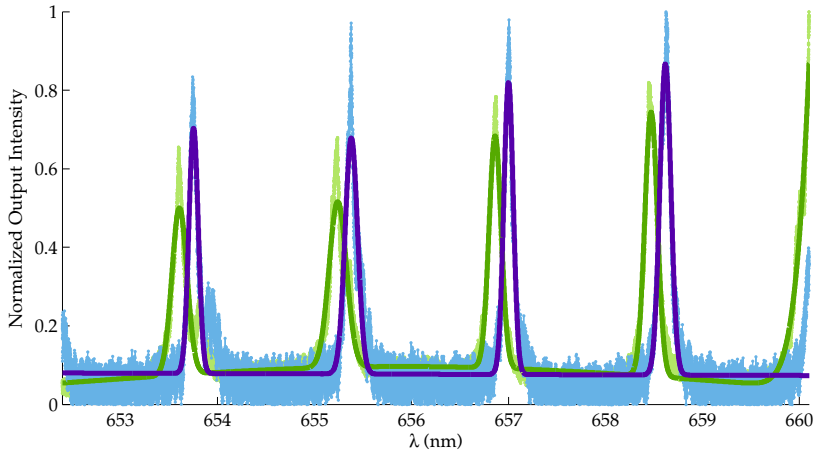

(a) Output of the drop ports of two rings in series.

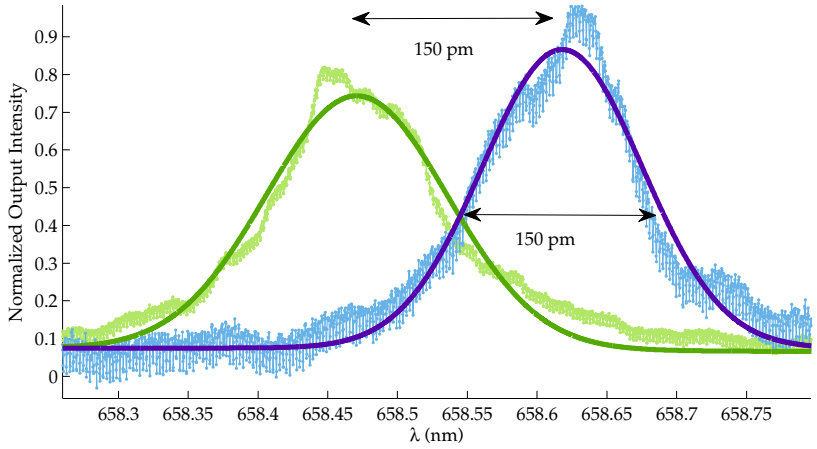

(b) The linewidth and distance of resonances are 150 nm.

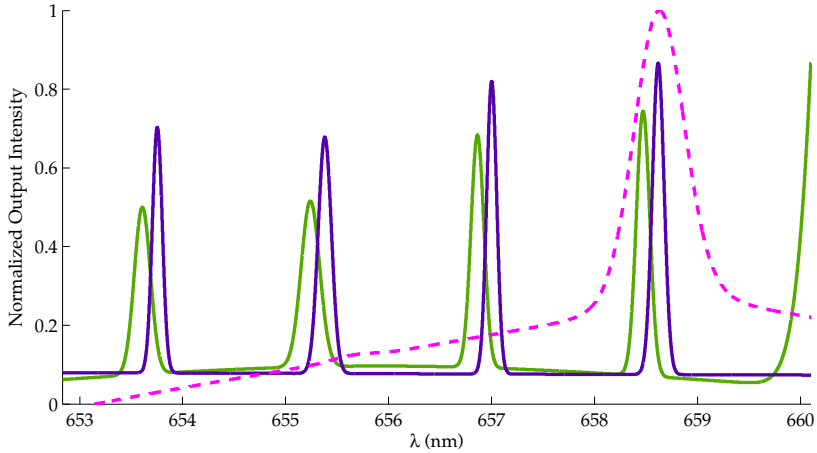

(c) Sampling of an AWG output with microrings in series.

Figure 90: Rings in series. The diameter of the rings is 20 microns and the coupling gap is 150 nm.

CHAPTER IX

PHOTONIC CRYSTALS

In this chapter I propose a photonic crystal structure for sensing applications. Previously, numerous different architectures have been developed for sensing applications including interferometric sensors using Mach Zehnder and Young interferometers [172, 173]; whispering gallery mode sensors using microtorids and microspheres [174, 83, 81]; surface plasma resonance (SPR) sensors [175]; and photonic crystal cavities and waveguides [176, 177, 178, 179]. Of all the different architectures that have been developed, planar photonic crystal sensors are particularly interesting because high quality factor one dimensional (1D) and two dimensional (2D) photonic-bandgap microcavity sensors shrinking the probed volume to the size of the optical cavity, which can be on the order of $(\lambda/n)^3$. Since the mode volume is so small the total amount of mass required to result in a measurable change in the refractive index can also be very small.

The first cavities demonstrated were based on periodic holes in a wire waveguide (1D photonic crystal cavity) [180, 181, 177]. For example the early work by Foresi et.al [177] demonstrated micro-cavity operation with two identical periodic hole mirrors embedded in a suspended photonic wire type waveguide and a quality-factor (Q-factor) value of 500 was obtained. Nevertheless, most of the focus during the next decade was on two dimensional photonic crystal cavities. Two structures proposed by Noda et al. [182] and Notomi et al. [183] attracted the most attention. These structures, fabricated on SOI devices with the oxide sacrificial layers removed, demonstrated Qs as high as a few millions. These structures (as attractive as they are in fundamental studies) suffer from two main disadvantages. (1) The large photonic

bandgap prohibits having multiple sensing sites along the same waveguide. Therefore, the number of targets which can be screened for at once is relatively small. (2) The coupling to/from a photonic wire waveguide is difficult. The coupling from a straight waveguide to a photonic crystal waveguide is not very efficient (unless very careful and detailed optimization is conducted), and the coupling from the photonic crystal waveguide to the cavity is not easily adjustable (Fig. 91(b)).

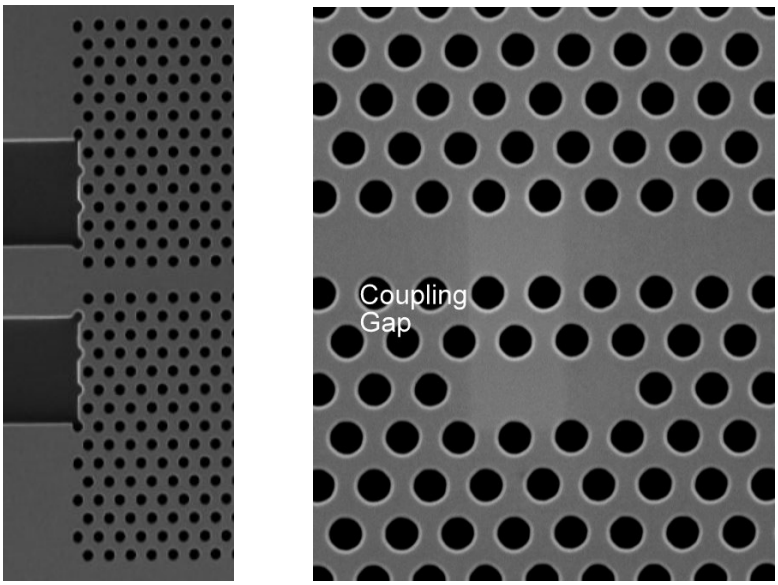

(a) (b)

Figure 91: (a) Coupling from a photonic wire waveguide to a PC waveguide needs careful optimization of the width of the waveguides and cropping surface through the PC. (b) The coupling gap between the PC waveguide and the PC cavity should be a multiple of lattice periodicity hence the coupling is not easily adjustable.

In the past few years several similar approaches have been proposed for 1D periodic waveguide cavities. Recently a large increases in Q-factor have been obtained by adjusting the mirror stack thereby reducing modal mismatch effects at the interfaces between the photonic crystal (PhC) mirrors and the cavity space section (thus reducing the k-components residing inside the light cone) [184, 185]. At the same time, it has been shown that the length of the cavity spacer section must be adjusted precisely to obtain the best results. A growing interest in designing high-Q, photonic crystal and photonic wire embedded photonic crystal micro-cavities has therefore emerged

[186, 187, 188]. In this chapter we focus mainly on adjusting the waveguide width rather than on the hole size or spacing. The waveguide width modulation has recently been investigated [189]. This structure, which is suspended in air, can potentially have Qs as high as 10^7 and lasing action has been demonstrated in this cavity.

The presence of the substrate, specially in low index contrast structures can limit the presence of resonant modes and their quality factor [190]. Barclay et al. have recently shown that increasing the etch depth can potentially reduce the effective index of the substrate, thus increasing the Q/V possible from photonic crystals on substrate. We focus on this approach for SiN on oxide structures in this chapter. Two software packages, namely the free electromagnetic solver developed at MIT called meep [191] and a commercial FDTD solver (Lumerical) are used for the design and optimizations.

In this chapter design and fabrication of photonic crystals is investigated.

9.1 Waveguide Analysis

First, by taking a dielectric waveguide and perforating it with a periodic sequence of holes, we form a kind of photonic crystal: there are still index-guided modes propagating down the periodic waveguide, but there is also a (partial) photonic band gap: a range of frequencies in which no guided modes exist [180]. The bandgap can be calculated with finite difference time domain (FDTD) method.

In particular, we compute the band diagram of the infinite periodic waveguide by itself (with no defects). By analyzing what solutions can propagate in the periodic structure, one gains fundamental insight into the aperiodic structures. In a periodic system of this sort, the eigen-solutions can be expressed in the form of Bloch modes: a periodic Bloch envelope multiplied by a planewave $\exp(j(kx-\omega t))$, where k is the Bloch wave vector. We wish to find the bands $\omega(k)$. In this case, there is only one direction of periodicity, so we only have one wave vector component k_x. Moreover,

the solutions are periodic functions of this wave vector: for a unit-period structure, k_x and $k_x + 2\pi$ are redundant. Also, k_x and $-k_x$ are redundant by time-reversal symmetry, so we only need to look for solutions in the irreducible Brillouin zone from $k_x = 0$ to $k_x = \pi$.

Our computational cell is simply the unit cell of the periodicity. The ϵ function then obeys periodic boundary conditions, but the fields obey Bloch-periodic boundary conditions: the fields at the right side are $\exp(j(k_x))$ times the fields at the left side. For each k_x, we will do a separate computation to get the frequencies at that k_x. this gap (along with the reduced Brillouin zone of a waveguide without holes) is depicted in 9.

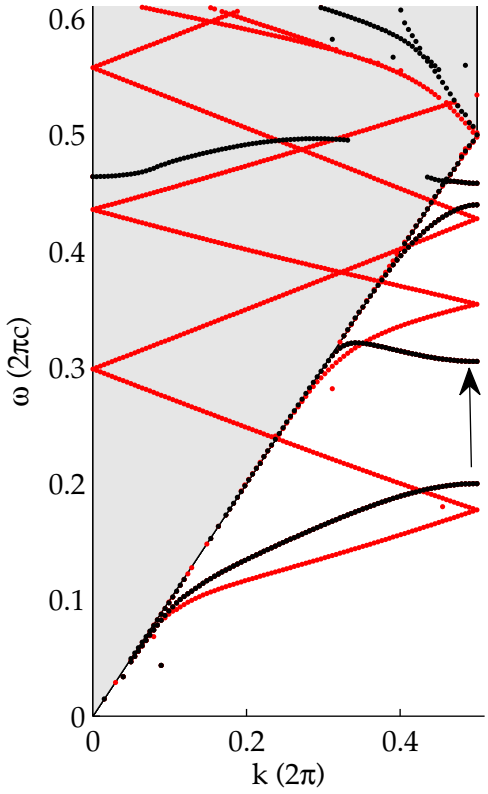

Figure 92: Band digram of a photonic crystal waveguide calculated with FDTD

Here, the gray shaded region is the light cone, $\omega > ck_x$, which is the region corresponding to modes that are extended in the air surrounding the waveguide. Below the light cone, we see several discrete guided bands, which must have field

patterns localized to the vicinity of the waveguide. Note the band gap between the first and second guided mode, from about 0.2 to 0.3.

Inside the light cone, we also see several discrete bands. These are leaky modes, or resonances, which have some intrinsic lifetime/loss because they couple with radiating states inside the light cone, which is reflected in the imaginary parts of their ω. In other words, twice the imaginary part of ω is the energy loss rate per unit time, $Q = \Re(omega)/2\Im(\omega)$. This simulation is done in 2D where the structures assumed to be infinite in the third dimension. All through this chapter simulations are first performed in two dimensions to gain insight about the behavior of the modes. Afterwards the same simulation is repeated with realistic 3D patterns. Note that to have 2D results close to the actual three dimensional (3D) devices the index chosen for the dielectric is lower than the material index (2.07 for SiN). This is due to the fact that—as shown in Fig. 93(a)—the mode extends into the air and oxide claddings and the effective index of the mode is lowered. To get a good estimate of the effective index a wide waveguide of 200 nm height is simulated with Comsol and the eigenvalue is used as the 2D effective index all through this chapter (Fig. 93(b)).

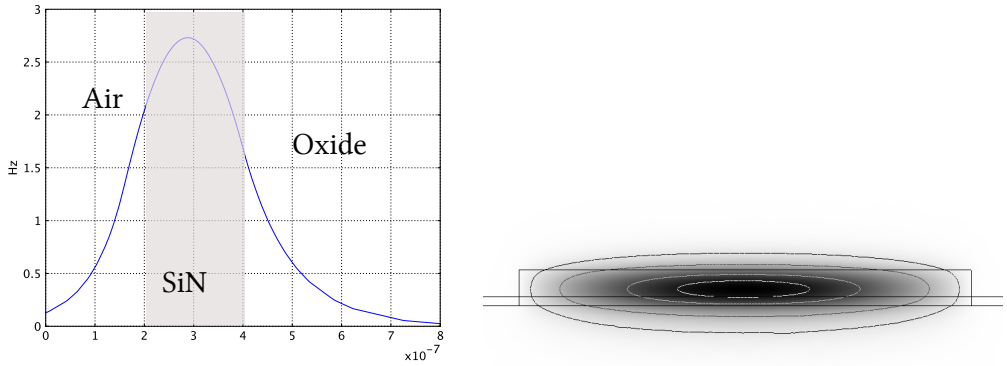

(a) Vertical profile of the field in a slab. (b) Comsol simulation for effective index.

Figure 93: The effective index of a slab.

9.1.1 Bandgap Calculation

The small index contrast of SiN to air makes the width of the two dimensional bandgap very small to nonexistent. This expectation is confirmed by our 3D plane wave expansion (PWE) of a photonic crystal slab. This was a quick simulation with a small number of plane-wave components. Larger holes and more extensive simulation might lead to a narrow (but existent) band gap in all directions, hence the possibility of the reported 2D photonic crystal cavities with large holes and several confining periods reported in [192, 193]. On the other hand, 1D cavities considered here show wide band

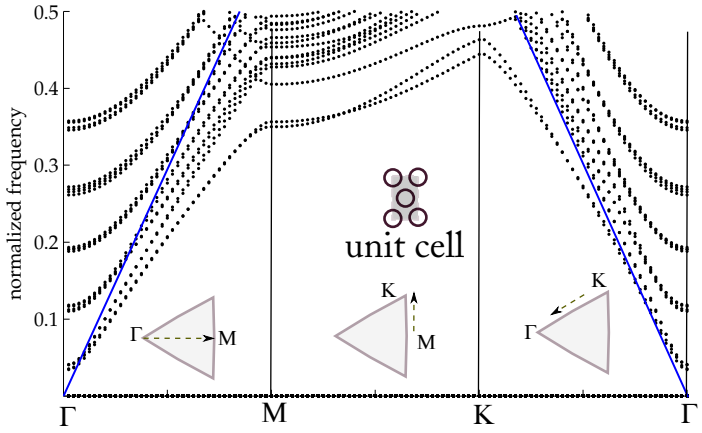

Figure 94: Band digram of a photonic crystal triangular lattice calculated with plane wave expansion method.

gaps, as only the ΓK direction in Fig. 94 is important. In order to design cavities based on 1D photonic crystal structures (also called nanobeam cavities and shown in 97) we need to find the location and width of the bandgap. Most importantly, the center of the bandgap of the waveguide depends on the period of the holes (a). In the following sections the frequencies are reported as the normalized frequency value ($\Omega = a/\lambda_o$) Also, as the width of the waveguide is increased, the electromagnetic mode "sees" more dielectric, and the air and dielectric bands descend in frequency (Fig. 95(a)). On the other hand, increasing the waveguide width reduces the effect of the air holes as the field energy spreads in the horizontal direction, thus reducing the size of the bandgap (Fig. 95(b)). One can also see the effect of the hole sizes

on the band edges by keeping the waveguide width fixed and changing the hole radii (Fig. 96). As the hole size increases the band edges are pushed up in frequency and bandgap becomes wider; and the narrower the waveguide, the more prominent this effect is.

The most straightforward way of constructing a cavity is by breaking the perfect periodic property of the waveguide be introducing a dielectric region in the middle of the hole stack. This is similar to the approach used for building vertical cavity surface emitting lasers (VCSELs) [194]. As can be seen in Fig. 97, as the size of the defect surrounded by two Bragg stacks (d) is increased, higher order modes appear in the cavity. As the size of the defect is increased, more dielectric is introduced into the structure. This causes all the possible modes of the structure to descend in frequency. As the size of the bandgap is limited, different modes enter the bandgap, become more confined in the x direction as they approach the middle of the gap, and then become guided when passing the dielectric band edge. This effect can be clearly seen in Fig. 98. The red and back lines in Fig. 98 represent modes calculated with even/odd symmetry planes introduced in the middle to facilitate faster calculations.

As easy as this approach is, when the confinement in y and z dimensions is considered the limitations are obvious from the not-so-large Q factors seen in 98(b). The mode mismatch between the central defect and the mirror stack results in significant coupling to the radiation modes [184]. This limitation can be alleviated by a gradual transition between the traveling mode in the defect region to the Bloch modes of the mirror stack. In the next section we investigate the design approaches to increase the Q factor by the adiabatic transition between these modes.

9.2 Adiabatic Cavity Design

It is well know in the 2D cavity designs that [182, 183] a Gaussian standing mode envelop is superior to the abrupt rectangular mode intensity confinement. This

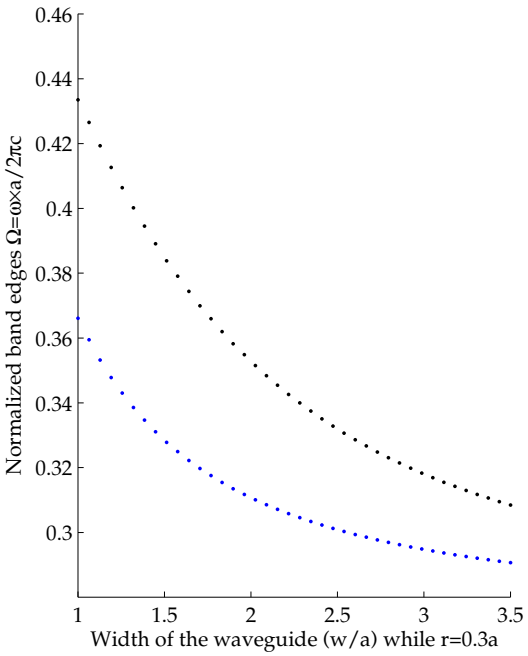

(a) Dielectric and air bands as a function of the waveguide width normalized to lattice constant (W/a).

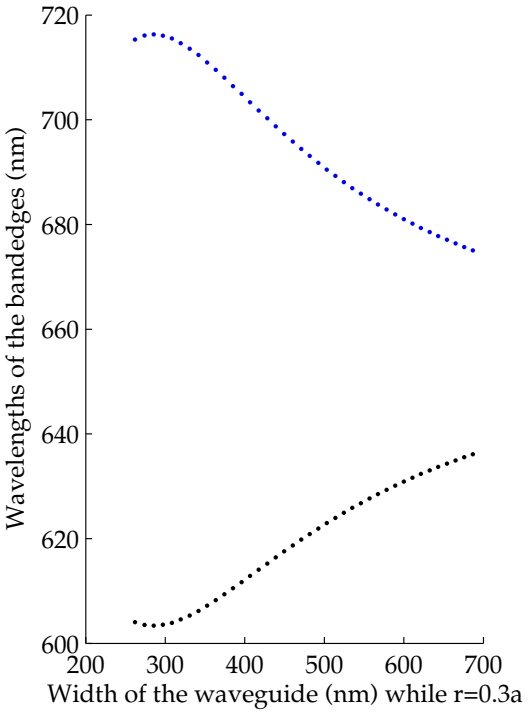

(b) Wavelength of the bandgap as a function of the waveguide width. The lattice constant is adjusted accordingly to keep the center of the gap at 655 nm.

Figure 95: Bandgap vs. the waveguide width calculated with 2D FDTD.

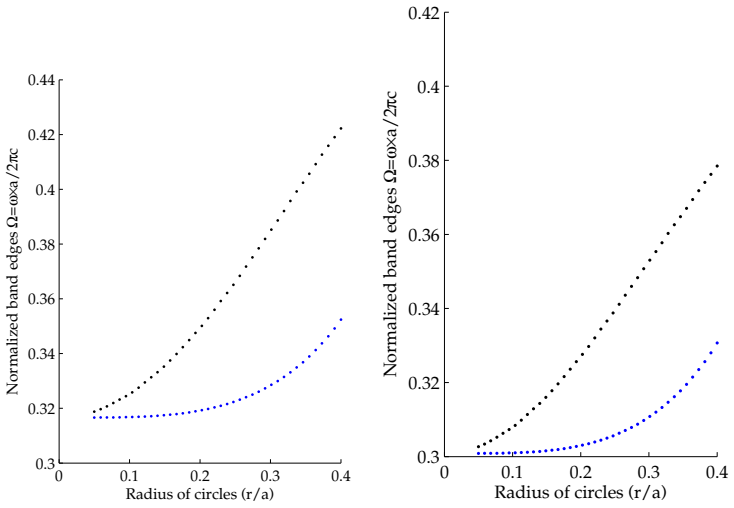

(a) $W = 1.2a$.

(b) $W = 2.0a$.

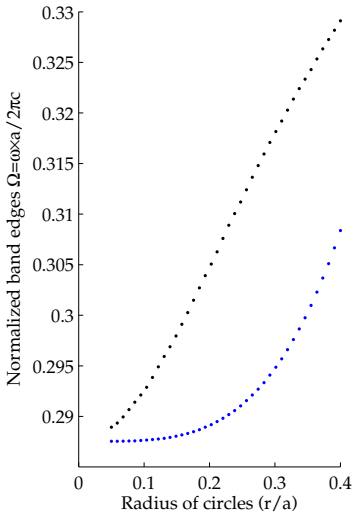

(c) $W = 3.0a$.

Figure 96: Bandgap vs. the hole radii calculated with 2D FDTD. As the hole size increases the band edges are pushed up in frequency and bandgap becomes wider.

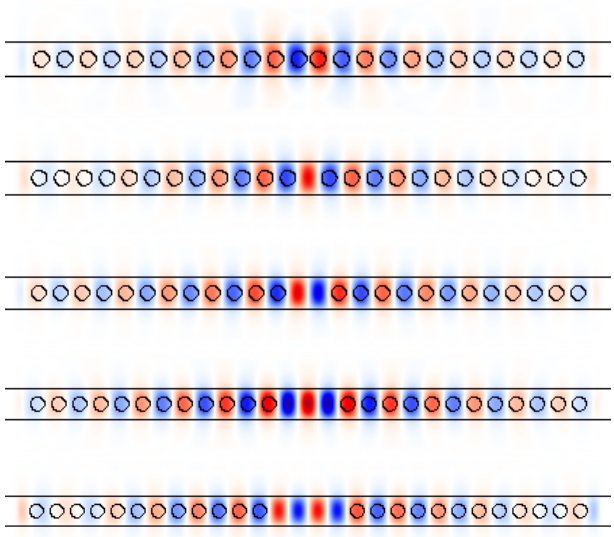

Figure 97: Modes of a Bragg waveguide resonator.

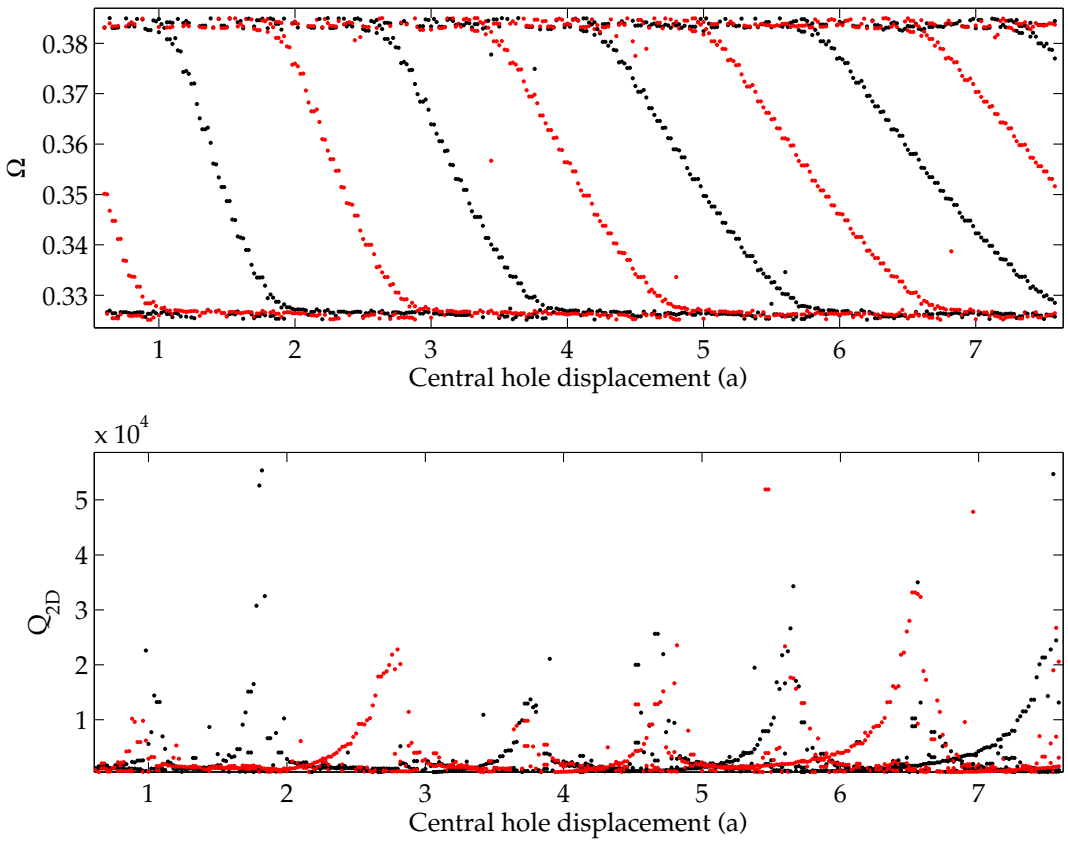

Figure 98: Modes of a Bragg waveguide cavity vs. the defect size.

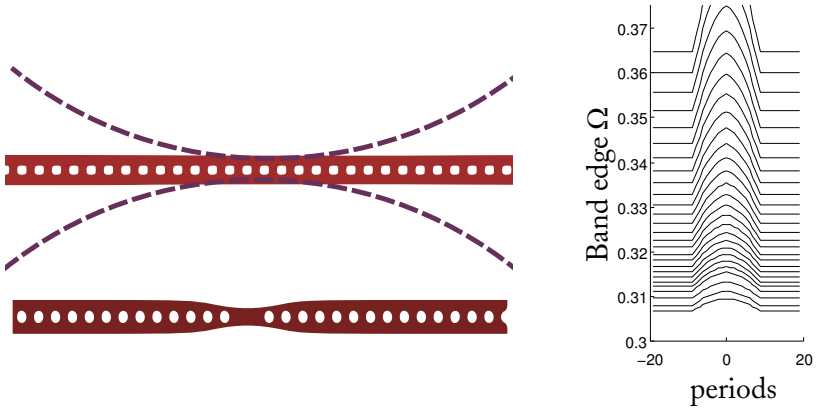

Figure 99: The adiabatic transition between he guided and Bloch modes can be achieved by tuning the waveguide width. The waveguide width can be change by subtracting circular shapes from the waveguide's rectangular shape (top) or introducing a Lorentzian width modulation to the cavity (bottom).

can be both accounted for by the existence of Floquet components inside the light cone or the field/impedance mismatch between the two regions. Recently Lončar et al. demonstrated the possibility of achieving high Qs by adiabatic adjustment of the periodicity of the holes to get an Gaussian mode profile. Here, we adopt a rather simpler (but more flexible) approach by varying the waveguide width rather than the periodicity or hole sizes. I believe this approach—because of constant hole radius and continuity of the adiabatic transition—can lead to more robust and reliable fabrication, while potentially having higher quality factors. The two proposed structures can be seen in Fig. 99. In both of these designs the middle of the structure is narrowed to a waist width (W_o) and the waveguide width gradually approaches a final width (W_f). As previously shown in 95, narrower waveguides have a wider but higher frequency bandgap. Therefore, as can be ween in 99, the band edge modulation introduces a heterostructure similar to that of a electronic quantum well.

A surprisingly high number of similarities has been found between photons, governed by the wave equation, and electrons obeying Schrödinger's equation, due in large part to the similarities between these two equations [195].

$$i\hbar\frac{\partial}{\partial t}\Psi(\mathbf{r},t) = -\frac{\hbar^2}{2m}\nabla^2\Psi(\mathbf{r},t) + V(\mathbf{r})\Psi(\mathbf{r},t) \tag{113}$$

$$\mu\epsilon\frac{\partial^2}{\partial t^2}\mathbf{E} = \nabla^2\mathbf{E} \tag{114}$$

Differences appear, however, as a consequence of the fermionic nature of electrons and bosonic nature of photons, and also because electrons have a scalar wave function compared to vectorial photons. It is interesting to note, however, that the vectorial properties of photons lead to two orthogonal polarizations, analogous with the two spins of electrons. For photonic crystals, the fundamental analogy is between Anderson localization of electrons [196] and localization of light in disordered media. Bloch oscillations have been observed for electrons in semiconductor super-lattices [197]. Semiconductor resonant double barriers are widely assumed to be analogous to the optical Fabry-Perot interferometer.

To design the cavities properly, we need to know the lower band edge of the gap. If one needs the gap map for various waveguide widths and hale radii, 3D simulations over a range of both should be performed. As the 3D simulations take up tremendous calculation resources, we performed the band edge calculations as a function of waveguide width only for three hole radii of $r = 0.25a, 0.3a, 0.35a$ (Fig. 100).

Comparing these results with 2D simulations, we found effective indexes for which the 2D simulation fits the 3D the best (Namely $n \sim 1.8$). The 3D (red curve) and 2D results of the band edges for varying waveguide widths and $r = 0.3a$ can be seen in Fig. 101.

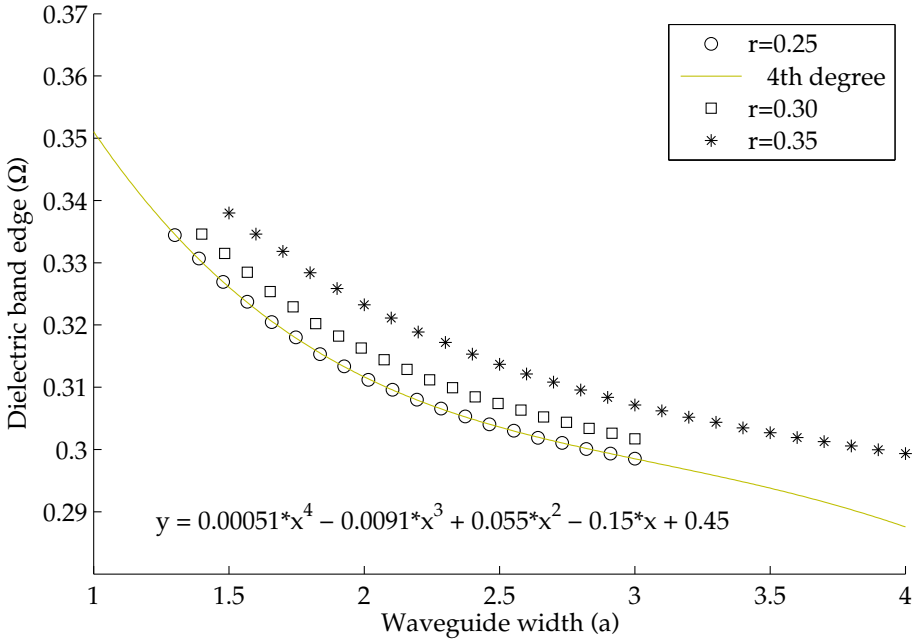

Figure 100: Band edge calculations as a function of waveguide width for three hole radii of $r = 0.25a, 0.3a, 0.35a$

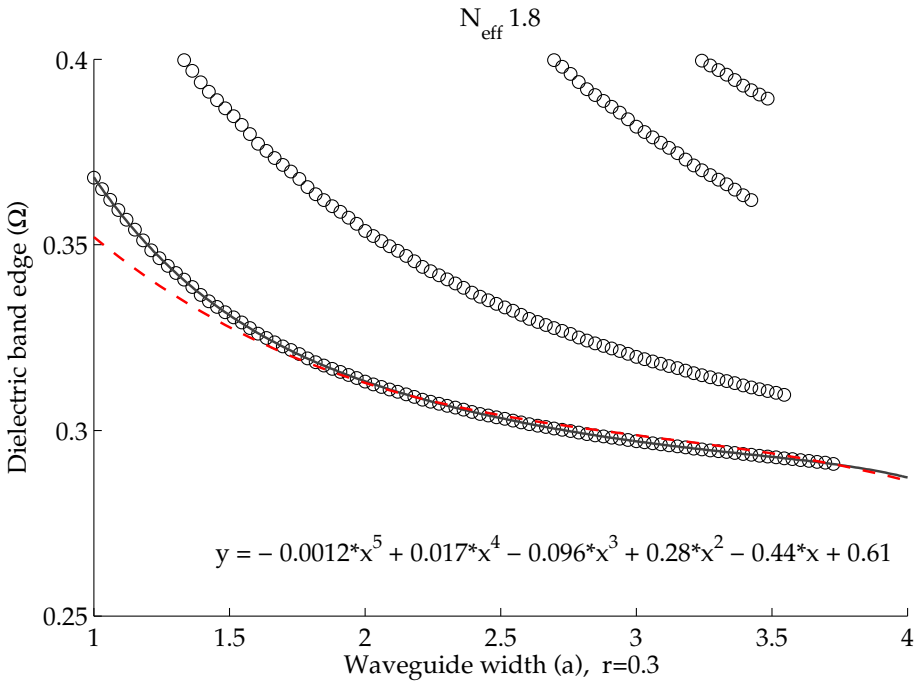

Figure 101: The 3D (red curve) and 2D results of the band edges for varying waveguide widths and $r = 0.3a$.

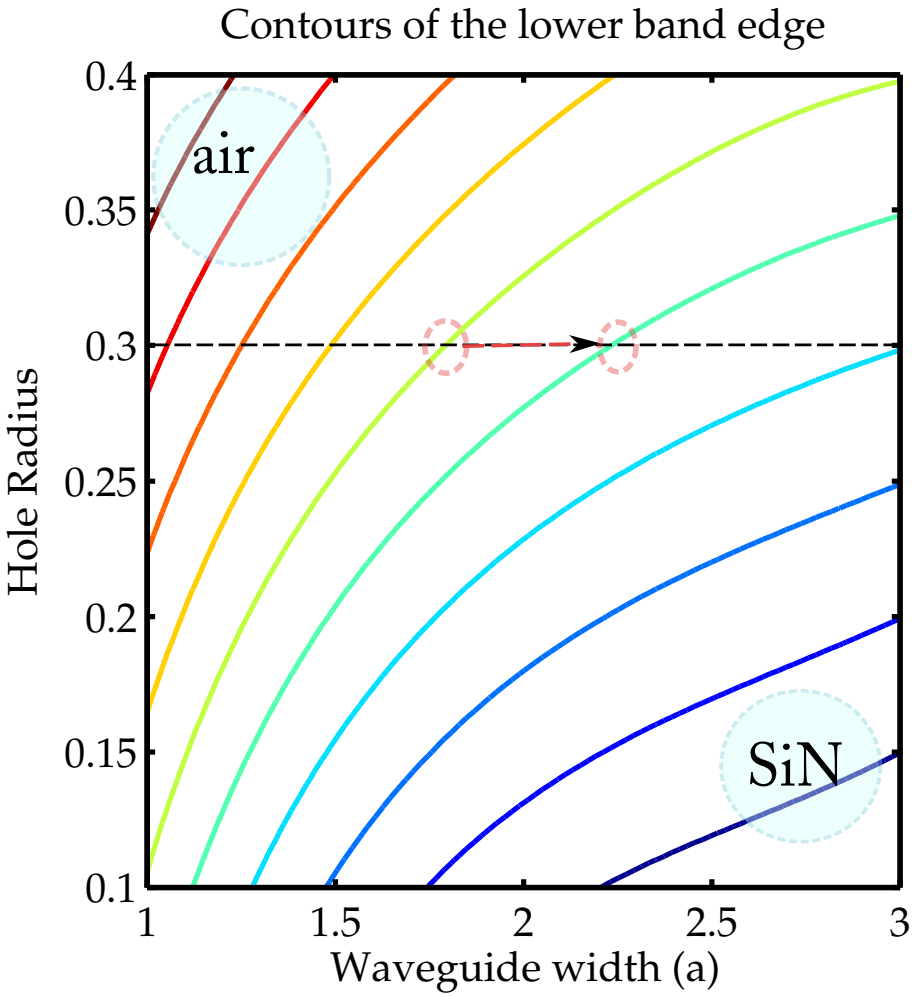

Figure 102: The contours of the dielectric band edge. Moving from lower-right corner toward more air type structures, the band edge is pushed up. A mode which is guided at the left side, will be confined on the right.

Fitting a polynomial surface to the frequency of the dielectric band as a function of W and r, the contours of the band edge can be achieved as shown in Fig. 102. Moving from lower-right corner toward more air type structures, the band edge is pushed up. A mode which is guided at the left side, will be confined on the right.

The gradual change of the dielectric band edge from higher frequencies to lower values can be done three distinct ways. One can gradually reduce the hole sizes (move down on the gap mp in Fig. 102), increase the period, or increase the waveguide width.

Here we choose to focus on the waveguide width. Our 3D simulations showed

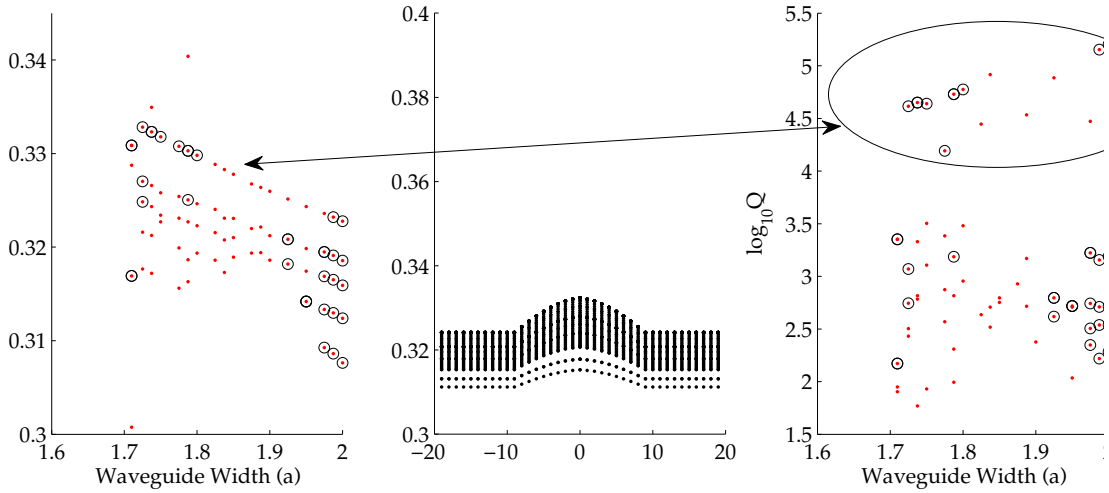

Figure 103: (left) The normalized frequency of the resonant modes as a function of waveguide width while the width modulation is kept constant ($\delta W = 0.2$). (middle) The shape of the band edge as a function of hole number. (Right) The quality factor of the resonant mode.

that the circular waveguide profile modulation (first design), demonstrated higher Q factors. While more optimization (considering the modulation of a, W, and r) on an optimal path is possible, the best results to date were achieved by $W_f = 2$, $W_o = 1.8$, and $r = 0.3$ while the height of the waveguide is $d = 1$ and the etch depth is 3. Apparently, the deeper the etched areas are, the better the confinement in the z direction is. Here we limited the depth of the etch to the values possible with current fabrication capability at NRC.

The anti-symmetric mode (electric field odd in x direction) of the TE mode has been investigated here and shows Q values as high as 10^5 while keeping the substrate under the resonator.

9.3 Conclusion

In this chapter the possibility of fabrication of ultra-high Q factor resonators in SiN is investigated. We showed it is possible to confine the light in an area a few wavelength long while keeping the substrate. Quality factors of 10^5 are observed in the simulations and further optimizations are possible. Deeper etched substrates result in better

confinements and potentially higher Q/V values. In future it is possible to find an optimal path on the gap map which retains the smallest mode volume while the quality factor is optimized (considering the fabrication limitations).

CHAPTER X

THERMAL PROPERTIES

In this chapter, first we investigate the thermal stability of the devices . While characterizing the microdisks, the input power should not be too high. Otherwise the power dissipation due to material absorption and surface particles heats the devices and causes a red shift in the resonance. This effect, which is much more pronounced in Si devices ([198]) leads to a thermal bi-stability in the devices. Silicon, both because of higher thermo-optic coefficient (TOC) and also existence of two photon and free carrier (FC) absorption (FCA) is much more sensitive to higher input powers. Nevertheless, as can be seen in Fig. 104, this effect can be observed in SiN devices too. Higher Q microdisks show this effect more prominently as (1) larger the field enhancement factor leads to higher intensities in the disk, hence more thermal dissipation; (2) The broadening of narrow linewidth of the device is easier to decipher.

If simple SiN designs are used, the only solution to this bistability is keeping the power of the laser under the thermal bi-stability limit. On the other hand, if a material with a large negative TOC is used as a cladding (and covers at least parts of the disk), the thermal sensitivity of the device is reduced or completely compensated. This is much easier to achieve in SiN than silicon devices.

10.1 Thermal Compensation for Si Microdisks

Previously, we tried this compensation method on silicon [199]. The thermo-optic coefficient (dn/dT) (with n and T being the refractive index and the temperature, respectively), is $+1.8 \times 10^{-}4°\text{C}$ for Si. For a typical microdisk resonator with a radius of 10 μ and a thickness of 220 nm, the resulting thermo-optic shift in the resonance

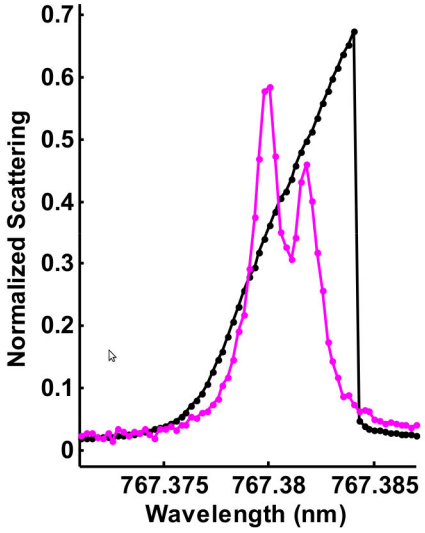

Figure 104: As the laser frequency is swept toward lower frequencies, the resonance of the microdisk red-shifts and follows the laser frequency. If the sweeping direction is reversed, this effect is not observed.

wavelength is about +80 pm/°C at 1550 nm.

The temperature dependence of the resonance wavelength in a traveling wave resonator (TWR) can be expressed as

$$\frac{d\lambda}{dT} = \frac{\lambda}{n_g}\frac{\partial n_{eff}}{\partial T} \tag{115}$$

in which n_g is the group index and n_{eff} is the effective index of the mode. We have neglected the effect of thermal expansion on the optical path length, since for Si it is 2 orders of magnitude smaller than the thermo-optic effect. Equation 115 means that athermal resonance is the result of an athermal effective index. The temperature dependence of n_{eff} can be compensated if the cladding is chosen in a way that:

$$n_{cladd}\Gamma_{cladd}\frac{dn_{cladd}}{dT} = -n_{core}\Gamma_{core}\frac{dn_{core}}{dT}, \tag{116}$$

in which Γ denotes the percentage of the electric field intensity in core/cladding. The material used for Si thermal compensation was aliphatic polyester-based urethane diacrylate polymer (PUA) with a measured TOC of $-4.5 \times 10^{-}4$. which is, to our knowledge, one of the largest TOCs among polymers. The refractive index of PUA is

about 1.45 at 1550 nm. We use the finite-element method to analyze the temperature dependence of the resonance wavelength in PUA-clad Si microdisk resonators. We assume the temperature to be uniform in the entire resonator device. Simulation shows that adding a PUA cladding to a 10 μ radius, 220-nm-thick microdisk reduces its temperature-induced resonance shift (TIRS) by only about 15 percent, which means that using a large-TOC polymer is not adequate by itself in the case of Si microdisks.

One way to improve this result is to enhance the effect of the cladding by reducing the mode confinement , which can be achieved through using a smaller resonator. In Fig. 105, the TIRS is plotted as a function of the Si layer thickness for PUA-clad microdisks with different radii. The results shown here are for the fundamental transverse electric (TE) (i.e., electric field parallel to the substrate surface) mode, for which the cross-sectional profile is shown in the inset. A similar procedure can be used to obtain the TIRS curves for the higher-order modes, which are slightly shifted downward with respect to that of the fundamental TE mode. Figure 105 shows that by reducing the resonator radius and the Si layer thickness, the TIRS is also reduced. It is also clear that changing the Si layer thickness has a stronger effect on the TIRS than changing the resonator radius. Zero TIRS is achieved at thicknesses around 80 and 90 nm, respectively, for resonator radii of 10 and 5 μm, as shown in Fig. 105.

The quality factor Qs of microdisk resonators are typically limited by the surface scattering and the surface absorption losses. As we reduce the size of the resonator, the resulting decrease in confinement leads to an increase in both of these losses. On the other hand, when the Si layer thickness is below 100 nm, the radiation loss becomes increasingly important. These factors lead to a trade-off between the Q and the thermal stability of the resonator. One way to ease this constraint is to undercut the microdisk before adding the polymer cladding. Removing the buried oxide (BOX) layer allows the polymer to fill up the space underneath the microdisk. The BOX

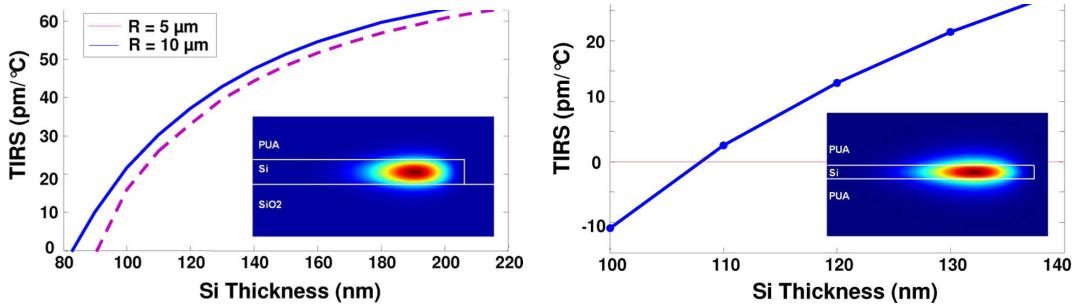

Figure 105: Simulation results for the temperature induced resonance shift (TIRS) (a) at 1550 nm in PUA-clad on-substrate microdisk resonators with various thicknesses and radii and (b) at 1450 nm versus the Si layer thickness, in 10 μm radius PUA-clad undercut microdisk resonators. The results are shown for the fundamental TE mode, for which the cross-sectional profile can be seen in the inset.

layer contains almost half of the optical energy outside the core. Therefore, the new geometry will considerably increase the effect of the polymer and move the athermal condition to larger thicknesses that allow for higher Qs.

Two cases are shown in Figs. 106(b) and 106(c): the first one belongs to a 10 μm radius, 220-nm-thick on substrate microdisk with air cladding, exhibiting a large TIRS (78 pm/°C); the second one is for a PUA-clad 10 μm radius, 110-nm-thick undercut microdisk showing near athermal performance (TIRS 0.2 pm/°C).

10.2 Thermal Compensation for SiN Microdisks

As mentioned before, the TOC of Si is relatively large ($+1.8 \times 10^{-}4$°C) compared to that of for SiN and oxide ($+4 \times 10^{-}5$°C and $+1.5 \times 10^{-}5$°C) respectively [200]. Therefore the thermal compensation of oxide and nitride based structures do not need the considerations discussed in the previous section.

As shown in Fig. 107(b), the 200-nm-thick, 20 micron radius SiN microdisk, when covered by PDMS, is over-compensated and a 15 nm cap layer of oxide is necessary to achieve absolute athermal operation. This calculation is our best estimate as the laser instability (inaccuracy of starting point in each scan), lowers the certainty of the measured resonance frequency in each scan.

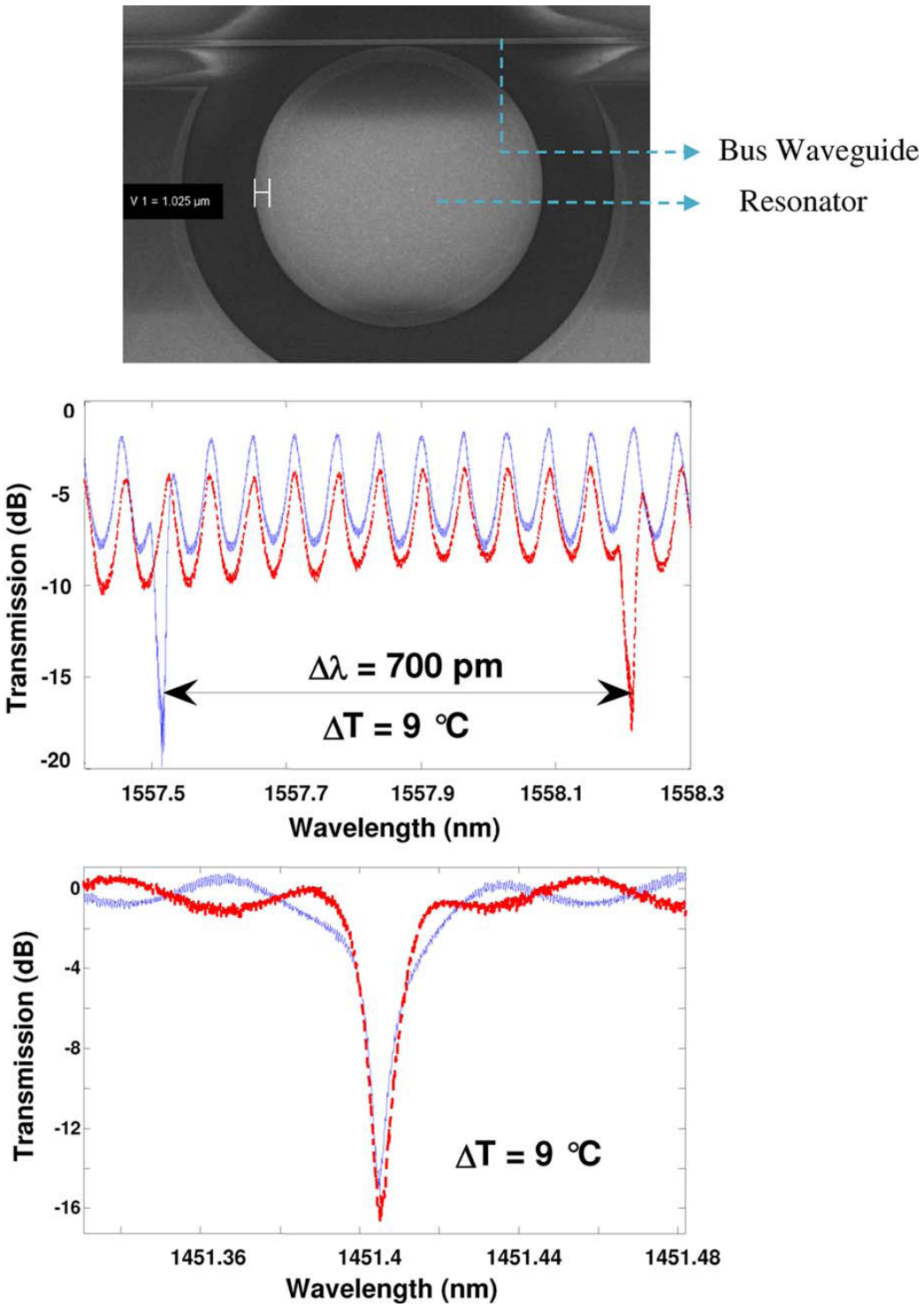

Figure 106: SEM image of an undercut microdisk resonator with a radius of 10 μm. Undercutting depth is 1 μm, and the undercutting boundary beneath the disk is visible from the top and has been marked in the image. (b) Temperature induced resonance shift in a 10 μm radius, 220-nm-thick on-substrate microdisk with air cladding. (c) Athermal resonance in a 10 μm radius, 110-nm-thick PUA-clad undercut microdisk. This disk has an intrinsic Q of 180,000. The solid and dashed curves in (b) and (c) correspond to two measurements with 9 °C temperature difference..

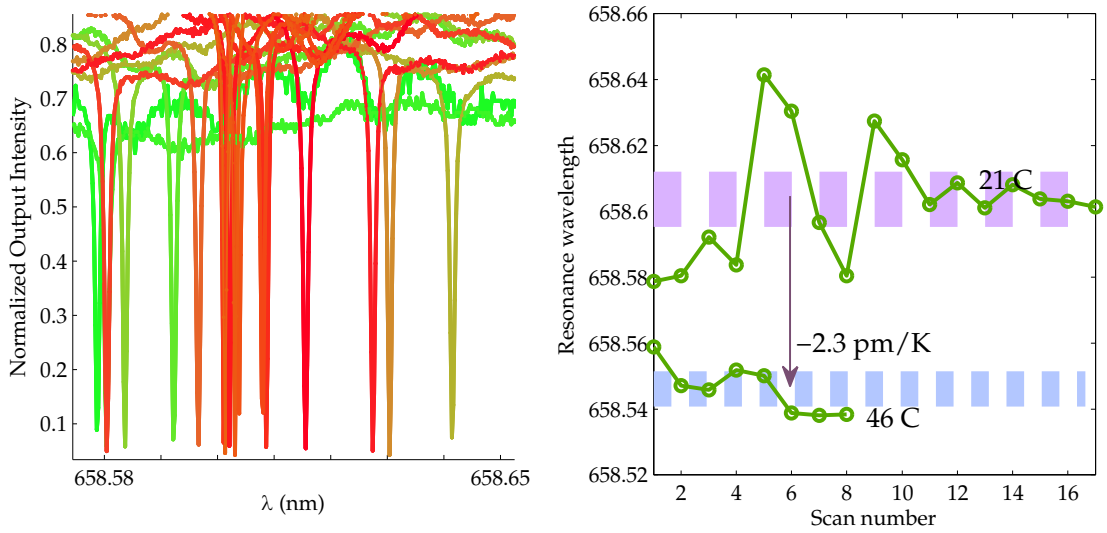

Figure 107: Thermal compensation of SiN; (left) The laser instability causes inaccuracy in calculations. (right) 20 μm SiN microdisk is over-compensated by PDMS.

Nevertheless, with repeated scans over time and averaging the values measured for the resonance wavelength, we can deduce that the microdisk resonance is *blue-shifted* by increasing the temperature. The measured value of temperature sensitivity for the mentioned disk is -2.3 pm/°C.

10.3 Conclusion

In this chapter we showed that both Si and SiN resonators can be stabilized in regards to the temperature variations. We used a high TOC polymer on top of undercut Si resonators to achieve complete athermal operation. For SiN, PDMS was used on top of the disk to over-compensate the thermal variations. In SiN structures no undercutting or thinning was necessary and an absolute athermal operation is possible with a larger disk or with a 15 nm oxide cap separating the microdisk from the covering PDMS.

REFERENCES

[1] D. Armani, T. Kippenberg, S. Spillane, and K. Vahala, "Ultra-high-Q toroid microcavity on a chip," Nature **421**, 925–928 (2003).

[2] M. Borselli, T. Johnson, and O. Painter, "Beyond the Rayleigh scattering limit in high-Q silicon microdisks: theory and experiment," Opt. Express **13**, 1515–1530 (2005).

[3] P. Barclay, K. Srinivasan, O. Painter, B. Lev, and H. Mabuchi, "Integration of fiber-coupled high-Q SiN microdisks with atom chips," Appl. Phys. Lett. **89**, 131108 (2006).

[4] M. Soltani, S. Yegnanarayanan, and A. Adibi, "Ultra-high Q planar silicon microdisk resonators for chip-scale silicon photonics." Opt. Express **15**, 4694 (2007).

[5] D. Jeanmaire and R. Van Duyne, "Surface Raman spectroelectrochemistry. Part I. Heterocyclic, aromatic, and aliphatic amines adsorbed on the anodized silver electrode," J. Electroanal. Chem. **84**, 1–20 (1977).

[6] Z. Lai, Y. Wang, N. Allbritton, G. Li, and M. Bachman, "Label-free biosensor by protein grating coupler on planar optical waveguides," Opt. Lett. **33**, 1735–1737 (2008).

[7] J. Campbell, *Introduction to Remote Sensing* (The Guilford Press, 2006).

[8] L. Pavesi, L. Dal Negro, C. Mazzoleni, G. Franzo, and F. Priolo, "Optical gain in silicon nanocrystals," Nature **408**, 440–444 (2000).

[9] D. Klunder, F. Tan, T. van der Veen, H. Bulthuis, G. Sengo, B. Docter, H. Hoekstra, and A. Driessen, "Experimental and Numerical Study of SiON Microresonators With Air and Polymer Cladding," J. Lightwave Technol. **21**, 1099 (2003).

[10] N. Ma, C. Li, and A. Poon, "Laterally coupled hexagonal micropillar resonator add-drop filters in silicon nitride," IEEE Photonic. Tech. L. **16**, 2487–2489 (2004).

[11] S. Zheng, H. Chen, and A. Poon, "Microring-resonator cross-connect filters in silicon nitride: rib waveguide dimensions dependence," IEEE J. Sel. Top. Quant. **12**, 1380–1387 (2006).

[12] A. Schweinsberg, S. Hocdé, N. Lepeshkin, R. Boyd, C. Chase, and J. Fajardo, "An environmental sensor based on an integrated optical whispering gallery mode disk resonator," Sens. Actuat. B. Chem. **123**, 727–732 (2007).

[13] K. Ikeda, R. Saperstein, N. Alic, and Y. Fainman, "Thermal and Kerr nonlinear properties of plasma-deposited silicon nitride/silicon dioxide waveguides." Opt. Express **16**, 12987 (2008).

[14] A. Gondarenko, J. Levy, and M. Lipson, "High confinement micron-scale silicon nitride high Q ring resonator," Opt. Express **17**, 11366–11370 (2009).

[15] E. Krioukov, D. Klunder, A. Driessen, J. Greve, and C. Otto, "Sensor based on an integrated optical microcavity," Opt. Lett. **27**, 512–514 (2002).

[16] M. Charlton and G. Parker, "Nanofabrication of advanced waveguide structures incorporating a visible photonic band gap," J. Micromech. Microeng. **8**, 172–176 (1998).

[17] M. Netti, M. Charlton, G. Parker, and J. Baumberg, "Visible photonic band gap engineering in silicon nitride waveguides," Appl. Phys. Lett. **76**, 991 (2000).

[18] J. Baumberg, N. Perney, M. Netti, M. Charlton, M. Zoorob, and G. Parker, "Visible-wavelength super-refraction in photonic crystal superprisms," Appl. Phys. Lett. **85**, 354 (2004).

[19] M. Charlton, M. Zoorob, M. Netti, N. Perney, G. Parker, P. Ayliffe, and J. Baumberg, "Realisation of ultra-low loss photonic crystal slab waveguide devices," Microelectron. J. **36**, 277–281 (2005).

[20] K. Crozier, V. Lousse, O. Kilic, S. Kim, S. Fan, and O. Solgaard, "Air-bridged photonic crystal slabs at visible and near-infrared wavelengths," Phys. Rev. B **73**, 115126 (2006).

[21] M. Barth, J. Kouba, J. Stingl, B. L
"ochel, and O. Benson, "Modification of visible spontaneous emission with silicon nitride photonic crystal nanocavities," Opt. Express **15**, 17231–17240 (2007).

[22] E. Krioukov, D. Klunder, A. Driessen, J. Greve, and C. Otto, "Two-photon fluorescence excitation using an integrated optical microcavity: a promising tool for biosensing of natural chromophores," Talanta **65**, 1086–1090 (2005).

[23] Lord Rayleigh, "The problem of the whispering gallery," Phlos. Mag. **xx**, 1001–1004 (1910).

[24] E. Marcatili, "Bends in optical dielectric guides(Light transmission through curved dielectric rectangular rod, studying optical waveguides of various cross sectional dimensions and radii of curvature)," Bell Sys. Technical J. **48**, 2103–2132 (1969).

[25] H. Weber and R. Ulrich, "A Thin-Film Ring Laser," Appl. Phys. Lett. **19**, 38 (1971).

[26] J. Haavisto and G. Pajer, "Resonance effects in low-loss ring waveguides," Opt. Lett. **5**, 510–512 (1980).

[27] R. Walker and C. Wilkinson, "Integrated optical ring resonators made by silver ion-exchange in glass," Appl. Opt. **22**, 1029–1035 (1983).

[28] K. Honda, E. Garmire, and K. Wilson, "Characteristics of an integrated optics ring resonator fabricated in glass," J. Lightwave Technol. **2**, 714–719 (1984).

[29] A. Naumaan and J. Boyd, "Ring resonator fabricated in phosphosilicate glass films deposited by chemical vapor deposition," J. Lightwave Technol. **4**, 1294–1303 (1986).

[30] A. Mahapatra and J. Connors, "High finesse ring resonators-fabrication and analysis," SPIE Integ. Opt. Circ. Eng. III **651**, 272 (1986).

[31] K. Oda, N. Takato, and H. Toba, "A wide-FSR waveguide double-ring resonator for optical FDMtransmission systems," J. Lightwave Technol. **9**, 728–736 (1991).

[32] T. Kominato, Y. Ohmori, N. Takato, H. Okazaki, and M. Yasu, "Ring resonators composed of GeO 2-doped silica waveguides," J. Lightwave Technol. **10**, 1781–1788 (1992).

[33] J. Bismuth, P. Gidon, F. Revol, and S. Valette, "Low-loss ring resonators fabricated from silicon based integrated optics technologies," Electron. Lett. **27**, 722–724 (1991).

[34] S. Suzuki, K. Shuto, and Y. Hibino, "Integrated-optic ring resonators with two stacked layers of silicawaveguide on Si," IEEE Photonic. Tech. L. **4**, 1256–1258 (1992).

[35] D. Lim, B. Little, K. Lee, M. Morse, H. Fujimoto, H. Haus, and L. Kimerling, "Micron-sized channel-dropping filters using silicon waveguide devices," in "Proc. SPIE," , vol. 3847 (1999), vol. 3847, p. 65.

[36] D. Klunder, E. Krioukov, F. Tan, T. Van Der Veen, H. Bulthuis, G. Sengo, C. Otto, H. Hoekstra, and A. Driessen, "Vertically and laterally waveguide-coupled cylindrical microresonators in Si_3N_4 on SiO_2 technology," Appl. Phys. B Laser. O. **73**, 603–608 (2001).

[37] P. RABIEI, W. STEIER, C. ZHANG, and L. DALTON, "Polymer micro-ring filters and modulators," J. Lightwave Technol. **20**, 1968–1975 (2002).

[38] P. Rabiei, W. Steier, C. Zhang, C. Wang, and H. Lee, "Polymer micro-ring modulator with 1 THz FSR," in "Lasers and Electro-Optics, 2002. CLEO'02. Technical Digest. Summaries of Papers Presented at the," (2002).

[39] S. McCall, A. Levi, R. Slusher, S. Pearton, and R. Logan, "Whispering-gallery mode microdisk lasers," Appl. Phys. Lett. **60**, 289 (1992).

[40] D. Chu, M. Chin, N. Sauer, Z. Xu, T. Chang, and S. Ho, "1.5-μm InGaAs/InAlGaAs quantum-well microdisk lasers," IEEE Photonic. Tech. L. **5**, 1353–1355 (1993).

[41] C. Abernathy, S. Pearton, J. MacKenzie, J. Mileham, S. Bharatan, V. Krishnamoorthy, K. Jones, M. Hagerott-Crawford, R. Shul, S. Kilcoyne *et al.*, "Growth and fabrication of GaN-InGaN microdisk laser structures," Solid State Electron. **39**, 311–313 (1996).

[42] T. Baba, M. Fujita, A. Sakai, M. Kihara, and R. Watanabe, "Lasing characteristics of GaInAsP-InP strained quantum-well microdisk injection lasers with diameter of 2-10 μm," IEEE Photonic. Tech. L. **9**, 878–880 (1997).

[43] B. Zhang, R. Mair, K. Zeng, J. Lin, H. Jiang, A. Botchkarev, W. Kim, H. Morkoc, and M. Khan, "Optical properties and resonant modes in GaN/AlGaN and InGaN/GaN multiple quantum well microdisk cavities," in "Proc. SPIE," , vol. 3547 (1998), vol. 3547, p. 158.

[44] R. Mair, K. Zeng, J. Lin, H. Jiang, B. Zhang, L. Dai, A. Botchkarev, W. Kim, H. Morkoc, and M. Khan, "Optical modes within III-nitride multiple quantum well microdisk cavities," Appl. Phys. Lett. **72**, 1530 (1998).

[45] D. Tishinin, P. Dapkus, A. Bond, I. Kim, C. Lin, and J. O'Brien, "Vertical resonant couplers with precise coupling efficiency controlfabricated by wafer bonding," IEEE Photonic. Tech. L. **11**, 1003–1005 (1999).

[46] L. Djaloshinski and M. Orenstein, "Disk and ring microcavity lasers and their concentric coupling," IEEE J. Quantum Elect. **35**, 737–744 (1999).

[47] N. Rex, R. Chang, and L. Guido, "Threshold minimization and directional laser emission from GaN microdisks," in "Proc. SPIE," , vol. 3930 (2000), vol. 3930, p. 163.

[48] D. Rafizadeh, J. Zhang, S. Hagness, A. Taflove, K. Stair, S. Ho, and R. Tiberio, "Waveguide-coupled AlGaAs/GaAs microcavity ring and disk resonators with high f inesse and 21.6-nm f ree spectral range," Opt. lett. **22**, 1244–1246 (1997).

[49] D. Marcuse, "Bend loss of slab and fiber modes computed with diffraction theory," IEEE J. Quantum Elect. **29**, 2957–2961 (1993).

[50] C. Gunn, "CMOS Photonics for High-Speed Interconnects," IEEE Micro **26**, 66 (2006).

[51] A. Liu, R. Jones, L. Liao, D. Samara-Rubio, D. Rubin, O. Cohen, R. Nicolaescu, and M. Paniccia, "A high-speed silicon optical modulator based on a metal–oxide–semiconductor capacitor," Nature **427**, 615–618 (2004).

[52] Q. Xu, B. Schmidt, S. Pradhan, and M. Lipson, "Micrometre-scale silicon electro-optic modulator," Nature **435**, 325–327 (2005).

[53] W. Green, M. Rooks, L. Sekaric, and Y. Vlasov, "Ultra-compact, low RF power, 10 Gb/s silicon Mach-Zehnder modulator," Opt. Express **15**, 17106–17113 (2007).

[54] L. Zhou and A. Poon, "Silicon electro-optic modulators using pin diodes embedded 10-micron-diameter microdisk resonators," Opt. Express **14**, 6851–6857 (2006).

[55] S. Preble, Q. Xu, B. Schmidt, and M. Lipson, "Ultrafast all-optical modulation on a silicon chip," Opt. lett. **30**, 2891–2893 (2005).

[56] V. Almeida, C. Barrios, R. Panepucci, and M. Lipson, "All-optical control of light on a silicon chip," Nature **431**, 1081–1084 (2004).

[57] O. Boyraz and B. Jalali, "Demonstration of a silicon Raman laser." Opt. Express **12**, 5269 (2004).

[58] H. Rong, R. Jones, A. Liu, O. Cohen, D. Hak, A. Fang, and M. Paniccia, "A continuous-wave Raman silicon laser," Nature **433**, 725–728 (2005).

[59] F. Xia, M. Rooks, L. Sekaric, and Y. Vlasov, "Ultra-compact high order ring resonator filters using submicron silicon photonic wires for on-chip optical interconnects," Opt. Express **15**, 19 (2007).

[60] Y. Vlasov, W. Green, and F. Xia, "High-throughput silicon nanophotonic wavelength-insensitive switch for on-chip optical networks," Nat. Photon. **2**, 242–246 (2008).

[61] L. Chen and M. Lipson, "Ultra-low capacitance and high speed germanium photodetectors on silicon," Opt. Express **17**, 7901–7906 (2009).

[62] A. Turner, M. Foster, A. Gaeta, and M. Lipson, "Ultra-low power parametric frequency conversion in a silicon microring resonator," Opt. Express **16**, 4881–4887 (2008).

[63] H. Fukuda, K. Yamada, T. Shoji, M. Takahashi, T. Tsuchizawa, T. Watanabe, J. Takahashi, and S. Itabashi, "Four-wave mixing in silicon wire waveguides," Nature **433**, 725 (2005).

[64] B. Schmidt, V. Almeida, C. Manolatou, S. Preble, and M. Lipson, "Nanocavity in a silicon waveguide for ultrasensitive nanoparticle detection," Appl. Phys. Lett. **85**, 4854 (2004).

[65] A. Nitkowski, L. Chen, and M. Lipson, "Cavity-enhanced on-chip absorption spectroscopy using microring resonators," Opt. Express **16**, 11930–11936 (2008).

[66] A. Yang, S. Moore, B. Schmidt, M. Klug, M. Lipson, and D. Erickson, "Optical manipulation of nanoparticles and biomolecules in sub-wavelength slot waveguides," Nature **457**, 71–75 (2009).

[67] M. Krishnan, J. Park, and D. Erickson, "Optothermorheological flow manipulation," Opt. lett. **34**, 1976–1978 (2009).

[68] M. Li, W. Pernice, C. Xiong, T. Baehr-Jones, M. Hochberg, and H. Tang, "Harnessing optical forces in integrated photonic circuits," Nature **456**, 480–484 (2008).

[69] K. Tiefenthaler and W. Lukosz, "Sensitivity of grating couplers as integrated-optical chemical sensors," J. Opt. Soc. Am. B **6**, 209–220 (1989).

[70] C. Stamm and W. Lukosz, "Integrated optical difference interferometer as refractometer and chemical sensor," Sens. Actuat. B. Chem. **11**, 177–181 (1993).

[71] N. Hartman, D. Campbell, and M. Gross, "Waveguide interferometer configurations," in "Lasers and Electro-Optics Society Annual Meeting, 1988. Conference Proceedings. LEOS'88.", (1988), pp. 298–299.

[72] R. Heideman and P. Lambeck, "Remote opto-chemical sensing with extreme sensitivity: design, fabrication and performance of a pigtailed integrated optical phase-modulated Mach–Zehnder interferometer system," Sens. Actuat. B. Chem. **61**, 100–127 (1999).

[73] A. Brandenburg, "Differential refractometry by an integrated-optical Young interferometer," Sensor. Actuat. B. Chem. **39**, 266–271 (1997).

[74] R. Boyd and J. Heebner, "Sensitive Disk Resonator Photonic Biosensor," Appl. Opt. **40**, 5742–5747 (2001).

[75] S. Blair and Y. Chen, "Resonant-enhanced evanescent-wave fluorescence biosensing with cylindrical optical cavities." Appl. Opt. **40**, 570 (2001).

[76] A. Ksendzov and Y. Lin, "Integrated optics ring-resonator sensors for protein detection," Opt. lett. **30**, 3344–3346 (2005).

[77] A. Yalçın, K. Popat, J. Aldridge, T. Desai, J. Hryniewicz, N. Chbouki, B. Little, O. King, V. Van, S. Chu *et al.*, "Optical sensing of biomolecules using microring resonators," IEEE J. Sel. Top. Quant. **12** (2006).

[78] R. Karlsson and R. Stahlberg, "Surface plasmon resonance detection and multispot sensing for direct monitoring of interactions involving low-molecular-weight analytes and for determination of low affinities," Anal. Biochem. **228**, 274–280 (1995).

[79] R. Eakin, E. Snell, and R. Williams, "A constituent of raw egg white capable of inactivating biotin in vitro," J. Biol. Chem **136**, 157 (1940).

[80] O. Livnah, E. Bayer, M. WiLCHEK, and J. Sussman, "Three-dimensional structures of avidin and the avidin-biotin complex," Proc. Natl. Acad. Sci. USA **90**, 5076–5080 (1993).

[81] F. Vollmer, D. Braun, A. Libchaber, M. Khoshsima, I. Teraoka, and S. Arnold, "Protein detection by optical shift of a resonant microcavity," Appl. Phys. Lett. **80**, 4057 (2002).

[82] S. Arnold, M. Khoshsima, I. Teraoka, S. Holler, and F. Vollmer, "Shift of whispering-gallery modes in microspheres by protein adsorption," Opt. lett. **28**, 272–274 (2003).

[83] A. Armani, R. Kulkarni, S. Fraser, R. Flagan, and K. Vahala, "Label-free, single-molecule detection with optical microcavities," Science **317**, 783 (2007).

[84] G. Zheng, F. Patolsky, Y. Cui, W. Wang, C. Lieber *et al.*, "Multiplexed electrical detection of cancer markers with nanowire sensor arrays," Nat. Biotech. **23**, 1294–1302 (2005).

[85] F. Patolsky, G. Zheng, and C. Lieber, "Nanowire-based biosensors," Anal. Chem. **78**, 4260–4269 (2006).

[86] G. Wu, R. Datar, K. Hansen, T. Thundat, R. Cote, and A. Majumdar, "Bioassay of prostate-specific antigen (PSA) using microcantilevers," Nat. Biotech. **19**, 856–860 (2001).

[87] V. Almeida, Q. Xu, C. Barrios, and M. Lipson, "Guiding and confining light in void nanostructure," Opt. lett. **29**, 1209–1211 (2004).

[88] C. Barrios, K. Gylfason, B. Sánchez, A. Griol, H. Sohlstr
"om, M. Holgado, and R. Casquel, "Slot-waveguide biochemical sensor," Opt. lett. **32**, 3080–3082 (2007).

[89] C. Barrios, M. Bañuls, V. González-Pedro, K. Gylfason, B. Sánchez, A. Griol, A. Maquieira, H. Sohlstr
"om, M. Holgado, and R. Casquel, "Label-free optical biosensing with slot-waveguides," Opt. lett. **33**, 708–710 (2008).

[90] J. Robinson, L. Chen, and M. Lipson, "On-chip gas detection in silicon optical microcavities," Opt. Express **16**, 4296–4301 (2008).

[91] T. Claes, J. G. Molera, K. De Vos, E. Schacht, R. Baets, and P. Bienstman, "Label-free biosensing with a slot-waveguide-based ring resonator in silicon on insulator," IEEE Photon. J. **1**, 197–204 (2009).

[92] V. Passaro, F. DellâĂŹOlio, C. Ciminelli, and M. Armenise, "Efficient Chemical Sensing by Coupled Slot SOI Waveguides," Sensors **9**, 1012–1032 (2009).

[93] C. Barrios, B. Sánchez, K. Gylfason, A. Griol, H. Sohlstr
"om, M. Holgado, and R. Casquel, "Demonstration of slot-waveguide structures on silicon nitride/silicon oxide platform," Opt. Express **15**, 6846–6856 (2007).

[94] V. Passaro, F. DellâĂŹOlio, B. Casamassima, and F. De Leonardis, "Guided-wave optical biosensors," Sensors **7**, 508–536 (2007).

[95] S. Yang, M. Cooper, P. Bandaru, and S. Mookherjea, "Giant birefringence in multi-slotted silicon nanophotonic waveguides," Opt. Express **16**, 8306–8316 (2008).

[96] L. Vivien, D. Marris-Morini, A. Griol, K. Gylfason, D. Hill, J. Álvarez, H. Sohlstr
"om, J. Hurtado, D. Bouville, and E. Cassan, "Vertical multiple-slot waveguide ring resonators in silicon nitride," Opt. Express **16**, 17237–17242 (2008).

[97] C. Barrios, Q. Xu, J. Shakya, C. Manolatou, and M. Lipson, "Compact silicon slot-waveguide disk resonator," in "Conference on Lasers and Electro-Optics/Quantum Electronics and Laser Science Conference and Photonic Applications Systems Technologies," (2006).

[98] C. Barrios, "Ultrasensitive nanomechanical photonic sensor based on horizontal slot-waveguide resonator," IEEE Photonic. Tech. L. **18**, 2419–2421 (2006).

[99] R. Srivastava, C. Bao, and C. Gómez-Reino, "Planar-surface-waveguide evanescent-wave chemical sensors," Sens. Actuat. A. Phys. **51**, 165–171 (1996).

[100] R. Bernini, N. Cennamo, A. Minardo, and L. Zeni, "Planar Waveguides for Fluorescence-Based Biosensing: Optimization and Analysis," IEEE Sens. J. **6**, 1218 (2006).

[101] J. Buck, *Fundamentals of optical fibers* (Wiley-IEEE, 2004).

[102] H. Haus, *Waves and fields in optoelectronics* (Prentice-Hall, 1984).

[103] J. Toll, "Causality and the dispersion relation: logical foundations," Physical Review **104**, 1760–1770 (1956).

[104] L. Landau and E. Lifshitz, *Electrodynamics of continuous media* (Oxford-London-New York-Paris: Pergamon Press, 1960).

[105] J. Brown and R. Churchill, *Complex variables and applications* (McGraw-Hill New York, 1996).

[106] D. Mills, *Nonlinear optics* (Springer Berlin etc., 1991).

[107] F. Jenkins and H. White, "Fundamentals of optics," (1957).

[108] J. Jackson, *Classical Electrodynamics* (Wiley, 1999).

[109] D. Segelstein, "The complex refractive index of water," Master's thesis, Department of Physics. University of Missouri-Kansas City (1981).

[110] P. Barclay, "Fiber-coupled nanophotonic devices for nonlinear optics and cavity QED," Ph.D. thesis (2007).

[111] J. Yota, J. Hander, and A. Saleh, "A comparative study on inductively-coupled plasma high-density plasma, plasma-enhanced, and low pressure chemical vapor deposition silicon nitride films," Journal of Vacuum Science & Technology A: Vacuum, Surfaces, and Films **18**, 372 (2000).

[112] A. Grigorescu, M. van der Krogt, C. Hagen, and P. Kruit, "10 nm lines and spaces written in HSQ, using electron beam lithography," Microelectronic Engineering **84**, 822–824 (2007).

[113] J. Cardenas, M. Foster, N. Sherwood-Droz, C. Poitras, H. Lira, B. Zhang, A. Gaeta, J. Khurgin, P. Morton, and M. Lipson, "Wide-bandwidth continuously tunable optical delay line using silicon microring resonators," Optics Express **18**, 26525–26534 (2010).

[114] W. Li, D. Bulla, and R. Boswell, "Surface oxidation of Al masks for deep dry-etch of silica optical waveguides," Surface and Coatings Technology **201**, 4979–4983 (2007).

[115] M. Soltani, "Novel integrated silicon nanophotonic structures using ultra-high Q resonators," Ph.D. thesis, Georgia Institute of Technology (2009).

[116] M. Bachman, "Glass etch wet process," (2000).

[117] S. Adachi, *properties of group-IV, III-V and II-VI semiconductors* (Wiley, 2005).

[118] E. Li, "Material parameters of InGaAsP and InAlGaAs systems for use in quantum well structures at low and room temperatures," Physica E: Low-dimensional Systems and Nanostructures **5**, 215–273 (2000).

[119] G. Roelkens, L. Liu, D. Liang, R. Jones, A. Fang, B. Koch, and J. Bowers, "III-V/silicon photonics for on-chip and intra-chip optical interconnects," Laser & Photonics Reviews .

[120] Y. Huang, X. Zhang, J. Ryou, R. Dupuis, F. Dixon, N. Holonyak Jr, and M. Feng, "InAlGaAs/ InP light-emitting transistors operating near 1.55 μm," Journal of Applied Physics **103**, 114505 (2008).

[121] J. Shul and P. SL, "Handbook of advanced plasma processing techniques," Plasma Physics and Controlled Fusion **43**, 372 (2001).

[122] I. Maximov, S. Jeppesen, L. Montelius, and L. Samuelson, "Chemical gas etching of InP-based structures," Microelectronic Engineering **35**, 87–89 (1997).

[123] S. Nakamura, S. Pearton, and G. Fasol, *The blue laser diode: the complete story* (Springer Verlag, 2000).

[124] E. Haberer, R. Sharma, C. Meier, A. Stonas, S. Nakamura, S. DenBaars, and E. Hu, "Free-standing, optically pumped, GaN/ InGaN microdisk lasers fabricated by photoelectrochemical etching," Applied Physics Letters **85**, 5179 (2004).

[125] M. Madou, *Fundamentals of microfabrication: the science of miniaturization* (CRC, 2002).

[126] D. Weiss, V. Sandoghdar, J. Hare, V. Lefèvre-Seguin, J. Raimond, and S. Haroche, "Splitting of high-Q Mie modes induced by light backscattering in silica microspheres," Opt. Lett. **20**, 1835–1837 (1995).

[127] A. Yariv, "Universal relations for coupling of optical power between microresonators and dielectric waveguides," Electron. Lett. **36**, 321–322 (2000).

[128] M. Soltani, Q. Li, S. Yegnanarayanan, and A. Adibi, "Improvement of thermal properties of ultra-high Q silicon microdisk resonators," Opt. Express **15**, 17305–17312 (2007).

[129] S. Chuang, "A coupled mode formulation by reciprocity and a variational principle," J. Lightwave Technol. **5**, 5–15 (1987).

[130] C. Manolatou, M. Khan, S. Fan, P. Villeneuve, H. Haus, and J. Joannopoulos, "Coupling of modes analysis of resonant channel add-drop filters," IEEE J. Quantum Electron. **35**, 1322–1331 (1999).

[131] M. Soltani, S. Yegnanarayanan, Q. Li, and A. Adibi, "Systematic engineering of waveguide-resonator coupling for silicon microring/microdisk/racetrack resonators: Theory and experiment," (2009). In preperation.

[132] E. Shah Hosseini, S. Yegnanarayanan, A. H. Atabaki, M. Soltani, and A. Adibi, "High quality planar silicon nitride microdisk resonators for integrated photonics in the visible wavelength range," Opt. Express **17**, 14543–14551 (2009).

[133] M. Chin and S. Ho, "Design and Modeling of Waveguide-Coupled Single-Mode Microring Resonators," J. Lightwave Technol. **16**, 1433 (1998).

[134] J. Hu, N. Carlie, N. Feng, L. Petit, A. Agarwal, K. Richardson, and L. Kimerling, "Planar waveguide-coupled, high-index-contrast, high-Q resonators in chalcogenide glass for sensing," Opt. Lett. **33**, 2500–2502 (2008).

[135] S. Bhattacharya, A. Datta, J. Berg, and S. Gangopadhyay, "Studies on surface wettability of poly (dimethyl) siloxane (PDMS) and glass under oxygen-plasma treatment and correlation with bond strength," Microelectromechanical Systems, Journal of **14**, 590–597 (2005).

[136] V. Tesar, *Pressure Driven Microfluidics* (Artech House: Norwood, MA, 2007).

[137] B. Dang, M. Bakir, and J. Meindl, "Integrated thermal-fluidic I/O interconnects for an on-chip microchannel heat sink," Electron Device Letters, IEEE **27**, 117–119 (2006).

[138] C. Harnett, G. Coates, and H. Craighead, "Heat-depolymerizable polycarbonates as electron beam patternable sacrificial layers for nanofluidics," Journal of Vacuum Science & Technology B: Microelectronics and Nanometer Structures **19**, 2842 (2001).

[139] A. Densmore, D. Xu, P. Waldron, S. Janz, P. Cheben, J. Lapointe, A. Delâge, B. Lamontagne, J. Schmid, and E. Post, "A silicon-on-insulator photonic wire based evanescent field sensor," Photonics Technology Letters, IEEE **18**, 2520–2522 (2006).

[140] J. Xu, D. Suarez, and D. Gottfried, "Detection of avian influenza virus using an interferometric biosensor," Analytical and Bioanalytical Chemistry **389**, 1193–1199 (2007).

[141] Z. Kirill, G. Laura *et al.*, "Silicon Photonic Biosensors for Lab-on-a-Chip Applications," Advances in Optical Technologies **2008** (2008).

[142] B. Momeni, S. Yegnanarayanan, M. Soltani, A. Eftekhar, E. Hosseini, and A. Adibi, "Silicon nanophotonic devices for integrated sensing," J. Nanophoton **3**, 031001 (2009).

[143] R. Wolffenbuttel, "State-of-the-art in integrated optical microspectrometers," Instrumentation and Measurement, IEEE Transactions on **53**, 197–202 (2004).

[144] D. Goldman, P. White, and N. Anheier, "Miniaturized spectrometer employing planar waveguides and grating couplers for chemical analysis," Appl. opt. **29**, 4583–4589 (1990).

[145] D. Sander, M. Duecker, O. Blume, and J. Mueller, "Optical microspectrometer in SiON slab waveguides," in "Proc. SPIE," , vol. 2686 (1996), vol. 2686, p. 100.

[146] Y. Maruyama, K. Sawada, H. Takao, and M. Ishida, "A novel filterless fluorescence detection sensor for DNA analysis," IEEE T. Electron Dev. **53**, 553–558 (2006).

[147] D. Zauner, A. Jorgensen, T. Anhoj, and J. H
"ubner, "Concave reflective SU-8 photoresist gratings for flat-field integrated spectrometers," Appl. opt. **45**, 5877–5880 (2006).

[148] Y. Komai, H. Nagano, K. Okamoto, and K. Kodate, "Compact spectroscopic sensor using a visible arrayed waveguide grating," Jpn. J. Appl. Phys. **45**, 6742–6749 (2006).

[149] S. Janz, A. Balakrishnan, S. Charbonneau, P. Cheben, M. Cloutier, A. Delâge, K. Dossou, L. Erickson, M. Gao, P. Krug *et al.*, "Planar waveguide echelle gratings in silica-on-silicon," Photonics Technology Letters, IEEE **16**, 503–505 (2004).

[150] Y. Hibino, "Recent advances in high-density and large-scale AWG multi/demultiplexers with higher index-contrast silica-based PLCs," Selected Topics in Quantum Electronics, IEEE Journal of **8**, 1090–1101 (2003).

[151] H. Kosaka, T. Kawashima, A. Tomita, M. Notomi, T. Tamamura, T. Sato, and S. Kawakami, "Superprism phenomena in photonic crystals: toward microscale lightwave circuits," Journal of lightwave technology **17**, 2032 (1999).

[152] B. Momeni, J. Huang, M. Soltani, M. Askari, S. Mohammadi, M. Rakhshandehroo, and A. Adibi, "Compact wavelength demultiplexing using focusing negative index photonic crystal superprisms," Opt. Express **14**, 2413–2422 (2006).

[153] B. Momeni, M. Chamanzar, E. Shah Hosseini, M. Askari, M. Soltani, and A. Adibi, "Strong angular dispersion using higher bands of planar silicon photonic crystals," Optics Express **16**, 14213–14220 (2008).

[154] B. Momeni and A. Adibi, "An approximate effective index model for efficient analysis and control of beam propagation effects in photonic crystals," Journal of Lightwave Technology **23**, 1522 (2005).

[155] B. Momeni and A. Adibi, "Preconditioned superprism-based photonic crystal demultiplexers: analysis and design," Applied optics **45**, 8466–8476 (2006).

[156] B. Momeni, M. Askari, E. Hosseini, A. Atabaki, and A. Adibi, "An on-chip silicon grating spectrometer using a photonic crystal reflector," Journal of Optics **12**, 035501 (2010).

[157] T. Baba and D. Ohsaki, "Interfaces of photonic crystals for high efficiency light transmission," Japanese Journal of Applied Physics **40**, 5920 (2001).

[158] B. Momeni and A. Adibi, "Adiabatic matching stage for coupling of light to extended Bloch modes of photonic crystals," Applied Physics Letters **87**, 171104 (2005).

[159] K. Okamoto, *Fundamentals of optical waveguides* (Academic press, 2006).

[160] M. Notomi, "Theory of light propagation in strongly modulated photonic crystals: Refractionlike behavior in the vicinity of the photonic band gap," Physical Review B **62**, 10696–10705 (2000).

[161] M. Smit, "New focusing and dispersive planar component based on an optical phased array," Electronics Letters **24**, 385 (1988).

[162] H. TAKAHASHI, S. SUZUKI, K. KATO, and I. NISHI, "Arrayed-waveguide grating for wavelength division multi/demultiplexer with nanometre resolution," Electronics letters **26**, 87–88 (1990).

[163] C. Dragone, "An< e 1> N</e 1> x< e 1> N</e 1> optical multiplexer using a planar arrangement of two star couplers," IEEE Photonics Technology Letters **3**, 812–815 (1991).

[164] P. Dumon, W. Bogaerts, D. Van Thourhout, D. Taillaert, V. Wiaux, S. Beckx, J. Wouters, and R. Baets, "Wavelength-selective components in SOI photonic wires fabricated with deep UV lithography," in "Group IV Photonics, 2004. First IEEE International Conference on," (IEEE, 2005), pp. 28–30.

[165] G. Kurczveil, M. Heck, J. Peters, J. Garcia, and J. Bowers, "A fully integrated hybrid silicon AWG based multiwavelength laser," in "Semiconductor Laser Conference (ISLC), 2010 22nd IEEE International," (IEEE), pp. 141–142.

[166] R. März, *Integrated optics: design and modeling* (Artech House Publishers, 1995).

[167] M. Smit and C. Van Dam, "PHASAR-based WDM-devices: Principles, design and applications," IEEE Journal of Selected Topics in Quantum Electronics **2**, 236–250 (1996).

[168] Z. Xia, M. Soltani, A. Eftekhar, Q. Li, M. Chamanzar, S. Yegnanarayanan, B. Momeni, and A. Adibi, "Demonstration of high resolution SOI spectrometer with miniaturized disks," in "Group IV Photonics (GFP), 2010 7th IEEE International Conference on," (IEEE), pp. 252–254.

[169] B. Kyotoku, L. Chen, and M. Lipson, "Sub-nm resolution cavity enhanced microspectrometer," Optics Express **18**, 102–107 (2010).

[170] K. Okamoto and A. Sugita, "Flat spectral response arrayed-waveguide grating multiplexer with parabolic waveguide horns," Electronics letters **32**, 1661 (2002).

[171] A. Sugita, A. Kaneko, K. Okamoto, M. Itoh, A. Himeno, and Y. Ohmori, "Very low insertion loss arrayed-waveguide grating with vertically tapered waveguides," IEEE Photonics Technology Letters **12**, 1180–1182 (2000).

[172] B. Luff, J. Wilkinson, J. Piehler, U. Hollenbach, J. Ingenhoff, and N. Fabricius, "Integrated optical Mach-Zehnder biosensor," Lightwave Technology, Journal of **16**, 583–592 (2002).

[173] A. Ymeti, J. Greve, P. Lambeck, T. Wink, S. van H
"ovell, T. Beumer, R. Wijn, R. Heideman, V. Subramaniam, and J. Kanger, "Fast, ultrasensitive virus detection using a young interferometer sensor," Nano Lett **7**, 394–397 (2007).

[174] A. Armani and K. Vahala, "Heavy water detection using ultra-high-Q microcavities," Optics letters **31**, 1896–1898 (2006).

[175] R. Karlsson, "SPR for molecular interaction analysis: a review of emerging application areas," Journal of Molecular Recognition **17**, 151–161 (2004).

[176] M. Lee and P. Fauchet, "Two-dimensional silicon photonic crystal based biosensing platform for protein detection," Opt. Express **15**, 4530–4535 (2007).

[177] J. Foresi, P. Villeneuve, J. Ferrera, E. Thoen, G. Steinmeyer, S. Fan, J. Joannopoulos, L. Kimerling, H. Smith, and E. Ippen, "Photonic-bandgap microcavities in optical waveguides," Nature **390**, 143–145 (1997).

[178] B. Schmidt, V. Almeida, C. Manolatou, S. Preble, and M. Lipson, "Nanocavity in a silicon waveguide for ultrasensitive nanoparticle detection," Applied Physics Letters **85**, 4854–4856 (2009).

[179] N. Skivesen, A. Tŕtu, M. Kristensen, J. Kjems *et al.*, "Photonic-crystal waveguide biosensor," Optics Express **15**, 3169–3176 (2007).

[180] S. Fan, J. Joannopoulos, J. Winn, A. Devenyi, J. Chen, and R. Meade, "Guided and defect modes in periodic dielectric waveguides," Journal of the Optical Society of America B **12**, 1267–1272 (1995).

[181] P. Villeneuve, D. Abrams, S. Fan, and J. Joannopoulos, "Single-mode waveguide microcavity for fast optical switching," Optics letters **21**, 2017–2019 (1996).

[182] B. Song, S. Noda, T. Asano, and Y. Akahane, "Ultra-high-Q photonic double-heterostructure nanocavity," Nature materials **4**, 207–210 (2005).

[183] E. Kuramochi, M. Notomi, S. Mitsugi, A. Shinya, T. Tanabe, and T. Watanabe, "Ultrahigh-Q photonic crystal nanocavities realized by the local width modulation of a line defect," Applied Physics Letters **88**, 041112 (2006).

[184] P. Lalanne and J. Hugonin, "Bloch-wave engineering for high-Q, small-V microcavities," Quantum Electronics, IEEE Journal of **39**, 1430–1438 (2003).

[185] C. Sauvan, G. Lecamp, P. Lalanne, and J. Hugonin, "Modal-reflectivity enhancement by geometry tuning in Photonic Crystal microcavities," Quantum Electron **39**, 1430–1438 (2003).

[186] P. Velha, J. Rodier, P. Lalanne, J. Hugonin, D. Peyrade, E. Picard, T. Charvolin, and E. Hadji, "Ultra-high-reflectivity photonic-bandgap mirrors in a ridge SOI waveguide," New Journal of Physics **8**, 204 (2006).

[187] P. Velha, E. Picard, T. Charvolin, E. Hadji, J. Rodier, P. Lalanne, and D. Peyrade, "Ultra-high Q/V Fabry-Perot microcavity on SOI substrate," Opt. Express **15**, 16090–16096 (2007).

[188] A. Zain, N. Johnson, M. Sorel, and R. De La Rue, "Ultra high quality factor one dimensional photonic crystal/photonic wire micro-cavities in silicon-on-insulator (SOI)," Quantum Electron **39**, 1430–1438 (2003).

[189] B. Ahn, J. Kang, M. Kim, J. Song, B. Min, K. Kim, and Y. Lee, "One-dimensional parabolic-beam photonic crystal laser," Optics Express **18**, 5654–5660 (2010).

[190] P. Barclay, K. Fu, C. Santori, and R. Beausoleil, "Hybrid photonic crystal cavity and waveguide for coupling to diamond NV-centers," Optics Express **17**, 9588–9601 (2009).

[191] A. F. Oskooi, D. Roundy, M. Ibanescu, P. Bermel, J. D. Joannopoulos, and S. G. Johnson, "MEEP: A flexible free-software package for electromagnetic simulations by the FDTD method," Computer Physics Communications **181**, 687–702 (2010).

[192] M. Makarova, J. Vuckovic, H. Sanda, and Y. Nishi, "Silicon-based photonic crystal nanocavity light emitters," Applied Physics Letters **89**, 221101 (2009).

[193] M. Barth, J. Kouba, J. Stingl, B. Löchel, and O. Benson, "Modification of visible spontaneousemission with silicon nitride photoniccrystal nanocavities," Opt. Express **15**, 17231–17240 (2007).

[194] J. Jewell, J. Harbison, A. Scherer, Y. Lee, and L. Florez, "Vertical-cavity surface-emitting lasers: design, growth, fabrication, characterization," Quantum Electronics, IEEE Journal of **27**, 1332–1346 (2002).

[195] E. Istrate and E. Sargent, "Photonic crystal heterostructures and interfaces," Reviews of Modern Physics **78**, 455–481 (2006).

[196] P. Anderson, "Absence of diffusion in certain random lattices," Physical Review **109**, 1492–1505 (1958).

[197] J. Feldmann, K. Leo, J. Shah, D. Miller, J. Cunningham, T. Meier, G. Von Plessen, A. Schulze, P. Thomas, and S. Schmitt-Rink, "Optical investigation of Bloch oscillations in a semiconductor superlattice," Physical Review B **46**, 7252–7255 (1992).

[198] Q. Xu and M. Lipson, "Carrier-induced optical bistability in silicon ring resonators," Optics letters **31**, 341–343 (2006).

[199] P. Alipour, E. S. Hosseini, A. A. Eftekhar, B. Momeni, and A. Adibi, "Athermal performance in high-q polymer-clad silicon microdisk resonators," Opt. Lett. **35**, 3462–3464 (2010).

[200] R. Amatya, C. Holzwarth, H. Smith, and R. Ram, "Efficient Thermal Tuning for Second-order Silicon Nitride Microring Resonators," in "Photonics in Switching, 2007," (IEEE, 2007), pp. 149–150.